INAUGURAL DISSERTATION

for
obtaining the doctoral degree
of the
Combined Faculty of Mathematics, Engineering, and Natural Sciences
of the
Ruprecht - Karls - University
Heidelberg

presented by

Joel Christian M.Sc.

born in Tenggarong, Indonesia
Oral examination: 04.11.2022

Role of Traction Forces in Initiating Clathrin-Mediated Endocytosis of Nanoparticles at the Cellular Ventral Side

Referees

1. Prof. Dr. Joachim Spatz
2. Prof. Dr. Christine Selhuber-Unkel

Parts of this thesis are published in the following journals :

- **Christian J**, Blumberg JW, Probst D, Giudice CL, Sindt S, Selhuber-Unkel C, Schwarz US, and Cavalcanti-Adam EA, “Control of cell adhesion using hydrogel patterning techniques for applications in traction force microscopy”, Journal of Visualized Experiments, vol. 179, no. e63121, pp. 1–17, 2022. **doi: 10.3791/63121**
- **Christian J** and Cavalcanti-Adam EA, “Micro- and Nanopatterned Substrates for Studies on the Mechanobiology of Cell–Matrix adhesions”, In : **Material-Based Mechanobiology** : Royal Society of Chemistry page 135-151, 2022. **doi: 10.1039/9781839165375**
- Zambarda C, ... **J. Christian**, ... , Cavalcanti-Adam EA,“The epithelial cell cluster size affects force distribution in responses to EGF-induced collective contractility”, Submitted.
- Levario-Diaz V, ... **J. Christian**, ..., Cavalcanti-Adam EA, “1D micro-nanopatterned integrin surfacs as tool to modulate cell front and rear coordination for directed migration”, Submitted.
- **Christian J** et al, “Role of traction force in stabilizing clathrin mediated endocytosis”, in preparation.

Table of Contents

Table of Contents i

Acknowledgments iii

List of Figures vi

List of Tables xviii

Summary 1

Zusammenfassung 3

1 Part I: Development of local ultraviolet illumination traction force microscopy combined with surface patterning **5**

1.1 Introduction 5

1.1.1 Motivation 6

1.2 State of the art 8

1.2.1 Traction force microscopy 8

1.2.2 Material response to mechanical loading 11

1.2.3 Linear elastic/viscoelastic materials for TFM applications 14

1.2.4 Surface modification of elastic/viscoelastic materials for TFM applications 15

1.3 Materials and methods 22

1.3.1 Pattern production for maskless photolithography 22

1.3.2 Surface micropatterning 23

1.3.3 Surface nanopatterning 23

1.3.4 Preparation of micropatterned polyacrylamide substrate for traction force microscopy 25

1.3.5 Preparation of nanopatterned polyacrylamide substrate for traction force microscopy 26

1.3.6 Preparation of micropatterned high-refractive index silicon elastomer for traction force microscopy . . . 28
1.3.7 Sample preparation for 3D-traction force microscopy . . . 29
1.3.8 Local ultraviolet illumination traction force microscopy . . . 29
1.3.9 Measurement and calculation of the Young's modulus by nanoindentation experiments 29
1.3.10 Cell Culture . . . 29
1.3.11 Immunostaining . . . 30
1.3.12 Statistical analysis . . . 30
1.4 Results and Discussion . . . 31
1.4.1 Mechanical characterization of elastic/viscoelastic substrates . . . 31
1.4.2 Micropatterning on the surface of deformable substrates . . . 38
1.4.3 Nanopatterning on the surface of deformable substrates . . . 42
1.4.4 Light based traction force microscopy . . . 46
1.5 Summary . . . 57
1.6 Outlook . . . 58

2 Part II : Role of Traction Forces in Initiating Clathrin-Mediated Endocytosis of Nanoparticles at the Cellular Ventral Side 60
2.1 Introduction . . . 60
2.1.1 Related previous discoveries . . . 60
2.1.2 What is the gap in previous discoveries? Why is it important? . . . 61
2.1.3 Motivation . . . 62
2.2 Theoretical Background . . . 63
2.2.1 Integrins . . . 63
2.2.2 Clathrin-mediated endocytosis . . . 63
2.2.3 Role of integrin-mediated cellular adhesion in the formation of clathrin coated structures . . . 65
2.3 Materials and Methods . . . 68
2.3.1 Cell Culture . . . 68
2.3.2 Immunostaining . . . 68
2.3.3 F-actin labelling for the fluorescent live imaging . . . 69
2.3.4 Image acquisition . . . 69
2.3.5 Biofunctionalization of the surface . . . 70
2.3.6 Immobilization of nanoparticles on the surface . . . 71
2.3.7 SEM imaging of critical point dried cells . . . 72
2.3.8 TEM sample preparation and imaging . . . 72
2.4 Results and Discussion . . . 73

2.4.1 Traction forces exerted by cells result in removal of electrostatically immobilized nanoparticles from the surface 73

2.4.2 Controlled distribution of focal adhesion and endocytic clusters by micropatterning 75

2.4.3 Controlled distribution of traction forces by micropatterning 78

2.4.4 Traction forces alone were insufficient to remove nanoparticles 79

2.4.5 AP2 clusters were highly distributed at the cell edge at 4 hours post-seeding 83

2.4.6 AP2 lifetime was independent on the substrate rigidity 85

2.4.7 AP2 clusters were spatially-colocalized with the normal component of traction forces 87

2.5 Summary 90

2.6 Outlook 91

Appendix - Supplementary Figures **I**

Appendix - Script **VII**

Glossary **XI**

Bibliography **XIV**

Acknowledgments

The acknowledgment part begins this doctoral dissertation, but I can bet that most people wrote it at the very end as a way to recapitulate their doctoral journey. It has been long and exhaustive months which undoubtedly brought mixed emotions, until I was finally able to write this. Nonetheless, by the grace of God, I finished my doctoral dissertation with a proud feeling.

But seriously, this achievement would not be possible without the support of many incredible people. First, I want to thank Prof. Dr. Joachim Spatz for being a "Doktorvater" and allowing me to be a doctoral student in his group. It is an absolute honor and an extraordinary research experience for me to be part of such an inspiring interdisciplinary group.

I thank Prof. Dr. Christine Selhuber-Unkel, who replied positively to my email within minutes when I asked to be the second referee of my doctoral thesis.

I am deeply indebted to PD Dr. Dr. E. A. Cavalcanti-Adam for her unwavering support and care throughout my doctoral study. Thanks for trusting me, a curious engineer by training with a little bit of cell-biology-related background, to work with you in the field of mechanobiology four years ago.

I sincerely thank Prof. Dr. Ulrich Schwarz for continuously supporting my doctoral project by being my TAC member committee and providing the TFM analysis code. A special shoutout should be given to Dr. Dimitri Probst and Johannes Blumberg, who generated the code.

I appreciate the invaluable discussions and trainings from many scientists, including Dr. Steeve Boulant, Dr. Ilia Platzmann, Dr. Dimitris Missirlis, Dr. Wenqian Feng, Dr. Kerstin Göpfrich, Dr. Kevin Jahnke, Dr. Oskar Staufer, Dr. Cornelia Zapp, Dr. Désirée Sauter, and Dr. Martin Schröter.

My utmost respect to all lab technicians who undeniably had a vital role in this achievement. Kuddos to Sabine Grünewald for taking care of my orders and helping me maintain cells. Raimund Jung for helping in sorting fluorescent-tagged MEF cells, for all suggestions concerning SDS-PAGE, and for proofreading this dissertation. Johannes Hirte for preparing block copolymer solutions. Ioanis Grigoridis for countless sessions of SEM, cryoSEM, and CPD. Conny Weber, Carmen Sahm, Annette Fautsch, and Felix Hybel for their help.

During my doctoral, I had a wonderful time supervising and working with several master and bachelor students. I thank Rebecca Alvarado for her contribution to establishing the hydrogel micropatterning protocol and for being a voice-over of my first ever published protocol. Daniel Eggmeier, for his contribution to establishing the link between the uptake project and the synthetic cell approach. Nisha Veits, for her contribution to investigating the proteins related to particle uptake and adhesions. Jonah Voigt, for his contribution to particle labeling and elastomer production. Jens Timmer, for his contribution to AAV2 particle labeling. Thank you for bringing positivity to the project.

Cheers to my colleagues in the “Growth-factor mechanobiology” group, especially the “older” generation of the group including Dr. Wenqian Feng, Dr. Francesca Posa, Dr. Anna Grab, Federica Pennarola, and Niranjan Srikanth, who were really helpful during my early time as a doctoral student. Also, to “new” generation, Dr. Cristina Lo Giudice for doing AFM experiments together, Dr. Sam Barnett and Dr. Victoria Levario Diaz for proofreading this dissertation, Fatima Noureddine, Andy Fink for kindly giving me a bicycle, and Grégoire Lemahieu for kindly providing me spheroids for initial 3D-TFM tests.

Also, for collaborators, Dr. Laurent Limozin, Dr. Kheya Sengupta, and Rémy Torro for hosting my lab visit in Marseille. Prof. Dr. Dirk Grimm and Ning Meng for providing AAV2 particles. Prof. Dr. Barbara Müller and Sandra Schifferdecker for providing HIV particles. Dr. Elisa D’Este for the assistance with STED imaging. Dr. Birgit Koch for the assistance with FLIM imaging, Dr. Ulrike Engel for the assistance with the TIRF imaging, and Dr. Charlotta Funaya for the assistance with the TEM imaging.

Last but not least, I want to express my gratitude to my family for the support. Terima kasih bapak, janji 8 tahun lalu sudah terpenuhi! Terima kasih kepada ibu terkasih Bu Vincentia Mayan, istriku Sherly Rosalina, saudara-saudara, keluarga besar, dan teman-teman atas semua bentuk dukungan selama ini. Semoga kalian semua bangga.

.

List of Figures

1.1 Venn's diagram showing four main aspects that are considered for the alternative TFM method: material, imaging, flexibity, and handling. The novelty of this TFM method comes from the handling aspect. The method aims to provide a tool that can be easily used even by beginners to study a biology-related phenomenon (i.e., mechanobiology of cell-matrix interaction). 6

1.2 General overview of TFM. Reproduced from Ref. [11] under the terms of the Creative Commons Attribution License (https://creativecommons.org/licenses/by/4.0/). (**A**) Images of the deformed state and the undeformed state are drift-corrected and processed to obtain the deformation field. The cellular traction field is estimated from the displacement field. (**B**) Two fundamentally different methods to reconstruct the traction from the displacement in TFM. The inverse method estimates a force distribution resulting in an optimum match for the displacement field. Fast fourier transform is used in FTTC. A regularization scheme is introduced to address the fact that determining the traction field from the displacement field is mathematically ill-posed. In the direct method, point-wise computational methods are used to determine the stress tensor locally. 9

1.3 The relation among complex shear modulus (G^*), real storage modulus (G'), imaginary loss modulus (G''), and phase difference (tan δ). The image is courtesy of journals.sagepub.com 12

1.4 (**a**) Linear elastic model. (**b**) Kelvin-Voigt viscoelastic model. Images are courtesy of journals.sagepub.com 13

1.5 The chemical structure of PA. The structure image is courtesy of Wikipedia. 14

1.6 The chemical structure of PDMS. The structure image is courtesy of Wikipedia. 14

1.7 Schematic representation of the sequential protein exchange on a surface (the Vroman Effect). Reproduced with permission from Ref. [32]. Copyright 2003 John Wiley and Sons. . 17

1.8 General mechanisms of protein-surface interactions. The ionic or charge-based interactions yield moderate adsorption and depend on the ionic state (I.S) and the pH of the surrounding buffer. The polar hydrophilic interactions yield weak adsorption. The hydrophobic interactions yield strong adsorption. The covalent interactions generate the strongest bond among all types of interactions. The Vroman effect describes that proteins with higher affinity to the surface can replace lower affinity proteins already adsorbed to the surface. Reproduced with permission from Ref. [101]. Copyright 2016 Elsevier. 18

1.9 Mean-field phase diagram showing stable morphologies in diblock copolymer melts. χN represents the degree of microseparation, f_1 is the volume fraction of block A (the red block in the picture). SPH = sphere, CYL = cylinder, LAM = lamellae, GYR = gyroid. Reproduced with permission from Ref. [58]. Copyright 2006 Elsevier. 20

1.10 (**A**) Structural formula of polystyrene-b-poly(2-vinyl-pyridine) block copolymer. (**B**) Loading process of the gold salt $HAuCl_4$ to the core of the micelle [111]. 22

1.11 (**A**) Images showing the initial diameter of PA (i.e., Acrylamide = 10 % Bisacrylamide = 0.1 %) compared to the diameter after 35 days inside PBS. (**B**) The swelling of PA with different monomer concentration. (**C**) The functionalisation of 1 μg/cm^2 FN did not increase the stiffness of PA. n from left to right = 16, 16, 16, 10, 16, 10. The stiffness of PA was measured with nanoindentation experiments using a fiber optic probe (stiffness = 0.24 N/m, radius = 21.5 μm). Bars show mean ± S.E.M (two-tailed t-tests, **** $P < 0.0001$, *** $P < 0.001$, ** $P < 0.01$, * $P < 0.05$, ns $P \leq 0.5$). **Please click here to view a full size version of this figure.** 31

1.12 Box and whiskers plots (10-90 percentile) showing Young's modulus and dissipation factors of PA prepared using various Acrylamide and Bisacrylamide contents. n= 10 for each condition. The statistical analysis was done using the ordinary one-way ANOVA, **** $P < 0.0001$, *** $P < 0.001$, ** $P < 0.01$, * $P < 0.05$, ns $P \leq 0.5$.). **Please click here to view a full size version of this figure.** 35

1.13 (**A**) Micrograph showing the projection of a 200 μm circle-shaped pattern on the surface of A10B0.1 PA (red-dashed line). The white square line shows the indentation area. Scale bar = 100 μm. (**B**) 3D maps of the Young's modulus before and after near UV (UVA) light illumination. The measurements were carried out using a spherical-probe with stiffness = 0.43 N/m and radius = 54 μm. (**C**) Young's modulus of the PA surface before and after illumination is non-significantly different. n of each condition = 25. (two-tailed t-tests, **** $P < 0.0001$, *** $P < 0.001$, ** $P < 0.01$, * $P < 0.05$, ns $P \leq 0.5$). **Please click here to view a full size version of this figure.** 36

1.14 (**A**) Young's moduli of the elastomer surface, the elastomer surface after deep UV illumination for 5 minutes, and the elastomer surface after the oxygen plasma treatment (100 W, 0,4 mbar for 20 s). (**B**) Dissipation factors of the elastomer surface, the elastomer surface after deep UV illumination for 5 minutes, and the elastomer surface after the oxygen plasma treatment (100 W, 0,4 mbar for 20 s). Bars show mean ± S.E.M (ordinary one-way ANOVA, **** $P < 0.0001$, *** $P < 0.001$, ** $P < 0.01$, * $P < 0.05$, ns $P \leq 0.5$). **Please click here to view a full size version of this figure.** 38

1.15 (**A**) Workflow of maskless photolithography based micropatterning. (1) A glass coverslip was cleaned by using oxygen plasma (200 W, 0.4 mbar for 2 minutes). (2) Then, antifouling PLL-PEG brushes were coated on the glass surface. (3) The photo-initiator reagent was added. (4-5) The reagent absorbed energy from UV laser beam creating radicals for a rapid degradation of PEG polymers from the surface. (6) ECM proteins like fibronectin or collagen were added on the surface. The proteins bound to unprotected PLL layer. (7) Cells were seeded on the surface. (**A'**) The optical schematic of DMD-based maskless photolithography. Reproduced with permission from Ref. [116]. Copyright 2015 John Wiley and Sons. (**B**) 8-bit tiff file of a crossbow pattern was used to make a 100 μm diameter crossbow *via* 20x air NA = 0.45 lens. (**C**) A SEM micrograph of a crossbow pattern produced with 30 mJ/mm^2 UV dose on the glass surface made using the image from (B). Scale bar = 20 μm. (**D**) A SEM micrograph of a (critically point dried) patterned single cell on the glass surface made using the image from (B). Scale bar = 20 μm. **Please click here to view a full size version of this figure.** 39

1.16 Scheme of a patterned ECM substrate for TFM. (**A**) The solution for the bottom layer was pipetted on a methacrylated surface. (**B**) A smaller clean coverslip was carefully placed on the pre-polymer droplet. (**C**) The polymerization took 45 minutes. (**D**) The top coverslip was detached. The bottom layer is ready. (**E**) The solution for the top layer was pipetted on the hydrogel. (**F**) The micro/nano-patterned coverslip was carefully placed on the pre-polymer droplet. (**F'**) The micropatterning of adhesive proteins on glass was produced by maskless-based patterning and then transferred from glass to a PA hydrogel. The free amine groups of adhesive proteins, e.g., fibronectin, were bound covalently to aldehyde groups on the PA. (**G**) The polymerization took 45 minutes. (**H**) The top coverslip is detached. The patterned PA hydrogel was ready. (**I**) A 3D representation of a confocal xyz micrograph showing a high density of fiducial beads near the surface. (**J**) A micrograph of fluorescently labeled fibronectin (magenta) on the surface of PA (A10B0.5) with embedded fluorescent beads (green), overlayed with a bright field image of cells. (**K**) Indirect immunofluorescence microscopy imaging of a single cell adhering to a circle-shaped fibronectin micropattern (100 μm). Nucleus (blue), paxillin (red). Reproduced with permission from Ref. [25]. Copyright 2022 the Journal of Visualized Experiments. **Please click here to view a full size version of this figure.** 41

1.17 Micrographs of micropatterns labeled with 1 μg/cm^2 fibrinogen conjugated with Alexa488 on the surface of QGel920 elastomer (3 kPa). (**A**) Circle patterns. (**B**) Crossbow patterns. (**C**) Square patterns. Scale bar = 100 μm. **Please click here to view a full size version of this figure.** 42

1.18 (**A**) Schematic showing the preparation of nanopatterned glass. (1) A glass surface after cleaning with the piranha solution. (2) The micellar solution was spin-coated onto the surface. (3) The micelles self-assembled into groups resembling quasi-hexagonal patterns after the non-polar solvent evaporated from the surface. (4) The removal of polymer matrices and the reduction of the metal precursor salts ($HAuCl_4$ or AgOAc) to elemental gold and silver, respectively upon the exposure to the hydrogen plasma (150 W, 0.4 mbar, 20 minutes). (5) The gold nanopatterned surface was used for PA nanopatterning template. (**B**) **Left** A SEM micrograph showing a region of gold nanopatterned glass surface prepared by using polymer P4921-S2VP (L = 0.25, C = 2 mg/ml, spin-coated with 3000 rpm). Scale bar = 100 nm. **Right** A SEM micrograph showing a region of silver nanopatterned glass surface prepared by using polymer P4921-S2VP (L = 0.25, C = 5 mg/ml, spin-coated with 5000 rpm). Scale bar = 100 nm. (**C**) The transmission as a function of wavelength on various substrates. In general, the light transmission on nanopatterned glass surfaces fabricated using polymer P4708-S2VP (i.e., 154), P4705-S2VP (i.e., 288), and P4921-S2VP (i.e., 1018), respectively was reduced. **Please click here to view a full size version of this figure.** 43

1.19 (**A**) Schematic showing the preparation of nanopatterned PA using a nanopatterned glass surface as the template (the continuation from Figure 1.18). (7) The nanopatterned glass surface was activated in the solution containing 2 μM BAC and 5 μM $NaBH_4$ in ethanol for 2 h. (8) The activated glass surface was put on a droplet of the hydrogel precursor. (9) The gold nanopatterned PA. (**B**) (**Left**) A SEM micrograph showing the nanopatterned gold array on the surface of the glass (before transfer). (**Center**) A SEM micrograph showing the successful removal of nanopatterned gold array from the surface of the glass. (**Right**) A cryo-SEM micrograph showing a region of nanopatterned PA (A10B0.2) surface. Table 1.7 shows the result of transfer experiments using different monomer and crosslinker concentrations. **Please click here to view a full size version of this figure.** 45

1.20 (**A**) Schematic showing the workflow of LUVI-TFM. (1) An adherent cell deforms the underlying substrate. (2) The cell is killed using a high dose of near UV light. The cell experiences acute oxidative stress leading to the release of traction force on the substrate. (3) The substrate is no longer deformed. The release can be tracked by comparing bead images of (1) and (3). Reproduced with permission from Ref. [25]. Copyright 2022 the Journal of Visualized Experiments. (**B**) Micrographs showing micropatterned cells (green dashed line) before and after the exposure of the high dose of near UV (UVA) light (red dashed line: cross sectional areas of the light). Micropatterned cells on 50, 150, and 200 μm patterns were illuminated with 200 μm of UVA light. Micropatterned cells on 100 μm patterns were illuminated with 100 μm of UVA light. Micropatterned cells on 300 μm patterns were illuminated with 300 μm of UVA light. The substrate deformation was calculated by PIV analysis. Scale bar = 100 μm. **Please click here to view a full size version of this figure.** 47

1.21 (**A**) Near UV light (UVA) illumination (6000 mJ/mm^2, red-dashed line) on a patterned cell cluster led to an elevated ROS (i.e., oxidative stress) measured by a commercially available reagent (i.e., CellRox). It was indicated by an increasing signal intensity after the illumination. Scale bar = 200 μm. (**B**) Near UV light (UVA) illumination (6000 mJ/mm^2) on patterned cell clusters possibly caused cell death due to the oxidative stress. Illuminated cells died and were easily detached by several washing steps during immunostaining steps compared to non-illuminated cells. Nuclei = blue, grey = cells in brightfield. **Please click here to view a full size version of this figure.** 48

1.22 (**A**) Micrographs showing different treatments to get undeformed images in LUVI-TFM (the illumination is depicted with a red dashed line) and the conventional TFM using trypsin. (**B**) Full release of cellular tractions 15 minutes after exposure to a high dose of near UV light was non-significantly different from tractions recorded 20 minutes after trypsin treatment. The measurements were conducted on PA with E = 1.7 kPa (A4B0.1). Bars show mean ± S.E.M (ordinary one-way ANOVA, **** $P < 0.0001$, *** $P < 0.001$, ** $P < 0.01$, * $P < 0.05$, ns $P \leq 0.5$.). **Please click here to view a full size version of this figure.** . . . 49

1.23 (**A**) Cells adhering to a 100 μm FN micropattern slowly released their traction on the surface of PA (A10B0.06) after high-dose near UV (UVA) exposure (red dashed line). The deformation was tracked by PIV. PIV (t_0) is PIV of the surface deformation right after the illumination. PIV (t_0+15), PIV (t_0+30), PIV (t_0+45), and PIV (t_0+60) are PIVs of the surface deformation at 15, 30, 45, and 60 minutes post-exposure, respectively. Traction stresses were reconstructed using regularized Fourier Transform Traction Cytometry[103] with a regularization parameter acquired by Generalized Cross Validation[50]. (**B**) Full release was achieved 15 minutes post-exposure (i.e., the traction force curve reaches the saturation). **Please click here to view a full size version of this figure.** 50

1.24 (**A**) Polarized light images, PIV images, displacement fields, and stress fields of a live single MEF cell adhered to the surface of nanopatterned PA (E = 8.34 kPa, the interparticle distance is around 100 nm) functionalized with 25 μM of cRGD-thiol. The cell was seeded in medium without serum. Scale bar = 20 μm. (**B**) The force and energy of the single MEF were measured every 5 minutes for 1 h. **Please click here to view a full size version of this figure.** 52

1.25 (**A**) Micrographs showing LUVI-TFM performed on micropatterned cells seeded on PA (A4B0.1, E = 1.7 kPa) using a 20x NA = 0.45 air objective lens. Tangential components (i.e., x and y) and a normal component (i.e., z) were acquired by comparing the 3D deformation of beads between undeformed and deformed image stacks. Scale bar = 100 μm. (**B**) Micrographs showing LUVI-TFM performed on a single cell seeded on PA (A5B0.3, E = 11.3 kPa) using a 40x NA = 0.95 air objective lens. Scale bar = 50 μm. The image of UV illumination seems brighter on the 20x setup because I used green fluorescent beads that were excited using a blue light. In comparison, in the 40x setup, I used far-red fluorescent beads that were excited using a red light. **Please click here to view a full size version of this figure.** 54

1.26 LUVI-TFM was performed on a cell spheroid in a hydrogel. **A**) Micrographs showing a 3D cell cluster before and after the exposure of high dose near UV (UVA) light (40000 mJ/mm^2) followed by 15 minutes of waiting. The imaging and illumination were performed using a 40x NA = 0.95 air objective lens. Scale bar = 100 μm. (**B**) Fluorescent micrographs (maximum intensity projection) showing the embedded beads before and after the exposure of the high-dose UVA laser. Scale bar = 100 μm. (**B'**) The bead movement indicated the cell cluster exerted traction forces inside the gelatin methacrylate hydrogel (Young's modulus = 0.3 kPa). Cell spheroids courtesy G. Lemahieu. **Please click here to view a full size version of this figure.** 55

1.27 Integrated bioengineering toolbox to study the cell-matrix interaction. (**A**) The toolbox includes surface patterning strategies, substrates production protocol, and LUVI-TFM protocol. All images were created with BioRender.com. Micropatterning and nanopatterning images are reproduced with permission from Ref. [26]. Copyright 2022 Royal Society of Chemistry. 2D-LUVI-TFM schematic is reproduced with permission from Ref. [25]. Copyright 2022 the Journal of Visualized Experiments. (**B**) Every box represents a single tool that can be used to study the cell-matrix interaction. A single solid line connecting two boxes indicates a combination of both tools that has be used in this work. **Please click here to view a full size version of this figure.** 59

2.1 The family of integrin receptors. There are known 24 distinct integrins comprising of 8 β and 16 α subunits. Integrin pairs are restricted into several groups based on their receptor-ligand specificity. Reproduced with permission from Ref. [61]. Copyright 2002 Elsevier. 64

2.2 Steps of clathrin-coated vesicles production in CME. Adapted with permission from Ref. [88]. Copyright 2011 Springer Nature. 65

2.3 Comparing the consensus adhesome of canonical adhesion complexes to the reticular adhesome and the clathrin interactome. Most proteins in the consensus adhesome are distinct from the other adhesomes. However, the reticular adhesome and the clathrin interactome share many proteins. Therefore, they are highly analogous. Adapted with permission from Ref. [81]. Copyright 2019 Rockefeller University Press. 66

2.4 (**A**) Schematic of live 2D-LUVI-TFM during the uptake of nanoparticles at the cellular ventral side. Fiducial beads for tracking the deformation were embedded inside PA close to the surface. Beads for uptake were immobilized electrostatically on the surface. Image is created with BioRender.com (**B**) Traction force heatmap during particle uptake around 4 hours post seeding. A single HeLa cell was seeded on a 5.7 kPa PA substrate coated with fibronectin. The electrostatically immobilized particles are shown in cyan. (**C**) Kymographs show the movements of different nanoparticles in the region of interest 1 and 2. Two upper kymographs describe the movement of the different nanoparticles inside the ROI 1 and 2, whereas the lower kymographs describe the traction force values inside the ROI 1 and 2. In ROI 1, an electrostatically immobilized nanoparticle was removed from the surface under cellular traction forces. (**D**) The graph showing total forces exerted by the cell over 1200 s. (**E**) The graph showing the energy transferred from the cell to the substrate over 1200 s. (**F**) Traction forces exerted by a single HeLa cell on 3 kPa (n = 25), 5.7 kPa (n = 20), and 22 kPa (n = 22) substrates. Bars show mean ± S.E.M (ordinary one-way ANOVA, **** $P < 0.0001$, *** $P < 0.001$, ** $P < 0.01$, * $P < 0.05$, ns $P \leq 0.5$). **Please click here to view a full size version of this figure.** 74

2.5 (**A**) Fluorescent micrograph of a micropatterned MEF cell expressing stable AP2 tagged with eGFP and clathrin light chain A (CLTA) (CLTA signals were not shown because they were very low in this image). AP2 density was higher in the patterned region. Scale bar = 50 μm. (**B**) Fluorescent micrographs, including the insets, showing AP2 clusters were excluded from focal adhesion clusters signified by β3-integrin, paxillin, and β1 integrin. MEF cells were seeded on the patterns coated with vitronectin (1 μg/cm^2) for β3-integrin staining. For paxillin and β1-integrin, MEF cells were seeded on the patterns coated with fibronectin (1 μg/cm^2). Scale bar = 50 μm. (**C**) (**C**) FA protein clusters (i.e., β3-integrin (n=423), paxillin (n=155), and β1 integrin(n=509)) were used as the masks, whose the area, the major, and the minor axis were quantified. Furthermore, by detecting the AP2 signal occupancy inside the mask, the area covered by AP2 could be quantified. Focal adhesion clusters excluded AP2 clusters since less than 5 % of the mask was covered by the AP2. Bars show mean ± S.E.M (ordinary one-way ANOVA, **** $P < 0.0001$, *** $P < 0.001$, ** $P < 0.01$, * $P < 0.05$, ns $P \leq 0.5$). **Please click here to view a full size version of this figure.** 76

2.6 High traction forces in the side arc and tail regions. (**A**) Phase contrast image of micropatterned MEF on a 5.4 kPa PA hydrogel. Scale bar = 20 μm. (**B**) After releasing the traction forces *in situ* with a near UV (UVA) light, the substrate deformation was tracked with PIV. (**C**) The displacement field. (**D**) The reconstructed stress field. **Please click here to view a full size version of this figure.** 78

2.7 (**A**) Fluorescent micrographs of a micropatterned MEF expressing AP2 tagged with eGFP and CLTA tagged with RFP cell taken with live-TIRF. Scale bar = 20 μm. Inset (1) shows AP2 (green) and clathrin-light chain A CLTA (magenta) clusters above immobilized nanoparticles in the side arc region. Inset (2) shows random AP2 (green) and CLTA (magenta) clusters. (**B**) Kymograph showing the recruitment of AP2 and CLTA clusters above immobilized nanoparticles in the side arc region. (**C**) Kymograph showing the kinetics of random AP2 and CLTA clusters. (**D**) Quantification of signal intensity of the background (n=10), AP2 and CLTA clusters above immobilized nanoparticles in the side arc region (n=10), and arbitrary AP2 and CLTA clusters (n=10). Schematics were created with BioRender.com. Bars show mean ± S.E.M (ordinary one-way ANOVA, **** $P < 0.0001$, *** $P < 0.001$, ** $P < 0.01$, * $P < 0.05$, ns $P \leq 0.5$). **Please click here to view a full size version of this figure.** 80

2.8 (**A**) Micrographs of a micropatterned MEF cell above electrostatically immobilized nanoparticles were taken with live-RICM. A darker RICM signal along the crossbow arc indicated that the ventral membrane (marked with the red square) was intimately linked to the matrix. Scale bar = 20 μm. Insets show that a nanoparticle was linked to the membrane but could not be removed from the surface. (**B**) TEM images from ultrathin section of a micropatterned MEF cell that was seeded above electrostatically immobilized 300 nm gold nanoparticles (Au). The cross section was taken from the central part connecting the arc and the tail of the crossbow. Scale bar of the cell cross section = 5 μm. Scale bar of the cross section showing a gold deforming the ventral membrane = 200 nm. **Please click here to view a full size version of this figure.** 82

2.9 (**A**) A spreading fibroblast cell on a fibronectin-coated substrate undergoes several distinct phases. (P0) The formation of initial integrin clusters. (P1) Expanding membrane surface and fast actin polymerization. (P2) The initial contractility (i.e., protrusion-retraction). Adapted with permission from Ref. [122]. Copyright 2014 Elsevier. (**B**) SEM image of a critically dried "bulls-eye egg" cell on the glass around 4 hours post-seeding. (**C**) TIRF images of HeLa cells stably expressing AP2 tagged with eGFP. AP2 clusters were highly distributed at the cell periphery. The upper left image describes the cell adhered to the glass coated with fibronectin (without cargo). The lower left image describes the cell adhered to the glass coated with covalently immobilized nanoparticles and fibronectin (cargo). The red line indicates the shape of the cell. Scale bars = 20 μm. To quantify the spatial distribution of AP2, AP2 clusters from "cargo" and "without cargo" images were segmented by an image processing software (i.e., ilastik) and were analyzed to measure the distance between each cluster and the cell centroid with a custom-made Matlab script. The upper center and lower center images show the output images of the script. The upper right and lower right graphs show the histogram of AP2 clusters as a function of distance from the cell centroid. The spatial distribution of AP2 is mainly at the cell periphery, irrespective of the presence of immobilized nanoparticles (cargo). **Please click here to view a full size version of this figure.** 84

2.10 (**A**) Fluorescent micrographs of HeLa cells stably expressing AP2 tagged with eGFP (green) at 4 hours post-seeding on the surface of the glass, which was already immobilized covalently with 200 nm nanoparticles (magenta) and biofunctionalized with fibronectin. Scale bars = 50 μm. Red squares on both channels indicate the recruitment of AP2 on a single bead. The insets show the evolution of AP2 intensity above a single bead. The intensity over time is depicted in the graph on the right. (**B**). Similar analysis like (A) but on a 3 kPa QGel920 substrate. (**C**) (Left) Comparison of AP2 cluster area between 3 kPa PDMS elastomer (n=143) and glass (n=243). (Right) Comparison of AP2 cluster lifetime above a nanoparticle between a 3 kPa PDMS elastomer (n=26) and glass (n=22). Bars show mean ± S.E.M (unpaired t-test (two-tailed), **** $P < 0.0001$, *** $P < 0.001$, ** $P < 0.01$, * $P < 0.05$, ns $P \leq 0.5$). **Please click here to view a full size version of this figure.** . 86

2.11 (**A**) Tangential (x, y) and normal (z) components of traction forces exerted by HeLa cells on a 3 kPa fibronectin-coated PA hydrogel at around 4 hours post-seeding. (**B**) The normal component of traction forces, fluorescent micrographs of AP2, and electrostatically immobilized nanoparticles. The cell indented the substrate indicated by negative stress values at the cell periphery area. Scale bar = 50 μm. (**C**) Inset shows the spatial correlation between AP2 and electrostatically immobilized beads in the region where the cell indented the substrate. Scale bar = 10 μm. **Please click here to view a full size version of this figure.** 87

2.12 (**A**) Fluorescent micrographs of the covalently immobilized nanoparticles and AP2-eGFP of a single HeLa 4 hours post-seeding taken with a TIRF microscope. Scale bar = 20 μm. The inset shows the clustering of AP2 above a covalently bound nanoparticle. (**B**) Displacement and stress fields (x, y, and z) overlaid with AP2 clusters (white, thresholded). The ring of AP2 clusters was spatially-correlated with the normal component (z) of the stress field. **Please click here to view a full size version of this figure.** 88

2.13 Flow cytometry analysis of the cellular uptake of fluorescent 200 nm carboxylated nanoparticles at the ventral side after 4 hours seeding. The median of APC-A in the first experiment, 0.4 kPa = 9014, 50 kPa = 7269. In the s experiment, 0.4 kPa = 14151, 50 kPa = 9470, and third experiment, 0.4 kPa = 13083, 50 kPa = 8281. Flow cytometry data courtesy of Mr. Jonah Voigt. 91

2.14 Fluorescent micrographs of MyosinVI, Dab2, PIP_2 signals, and 200 nm fluorescent nanoparticles. MEF cells expressing MyosinVI-eGFP were seeded on glass, fixed at 1 hour post-seeding, and stained for Dab2 (clathrin adaptor protein) and PIP_2. Before cell seeding, the glass surface was first covalently immobilized with nanoparticles and coated with fibronectin. Scale bar = 20 μm. Insets show colocalizing MyosinVI, Dab2, and PIP_2 clusters above immobilized nanoparticles. Scale bar = 2 μm. 92

2.15 **Flow cytometry experiments indicated that electrostatically immobilized 40 nm nanoparticles were internalized more on the softer than the stiffer PDMS elastomer**. Flow cytometry analysis of the cellular uptake of fluorescent 40 nm carboxylated nanoparticles at the ventral side after 4 hours seeding. The median of APC-A in the first experiment, 0.4 kPa = 10341, 50 kPa = 9385. In the second experiment, 0.4 kPa = 15030, 50 kPa = 12934, and third experiment, 0.4 kPa = 12184, 50 kPa = 10364. Flow-cytometry data courtesy of Mr. Jonah Voigt. I

2.16 **Flow cytometry experiments indicated that electrostatically immobilized AAV2 particles were internalized more on the softer than the stiffer PDMS elastomer**. (**A**) SEM and STED image of non-labelled and Atto647N-labelled AAV2. Scale bar of the SEM image = 100 nm. Scale bar of the STED image = 200 nm. (**B**) Flow cytometry analysis of the cellular uptake of TFP ester Alexa647 labelled AAV2 at the ventral side after 4 hours seeding. The median of APC-A in the first experiment, 0.4 kPa = 3427, 50 kPa = 2033. In the second experiment, 0.4 kPa = 1828, 50 kPa = 890, and third experiment, 0.4 kPa = 1112, 50 kPa = 839. Flow-cytometry data courtesy of Mr. Jens Timmer. II

2.17 **MyosinVI clusters were highly distributed at the cell periphery**. (**A**) Fluorescent micrographs of a HT1080 stained for F-actin and MyosinVI protein. MyosinVI clusters were highly distributed at the cell periphery where the electrostatically particles (cyan) were removed from the surface. Scale bar = 50 μm. (**B**) Quantification of the distance between each MyosinVI cluster from the cell centroid. The graph shows that MyosinVI clusters were highly distributed at the cell periphery. III

2.18 **Colocalizing MyosinVI-PIP$_2$ clusters linked to actin stress fibers at the cell periphery**. MEF cells expressing MyosinVI-eGFP were seeded on fibronectin-coated glass, fixed at 1 hour post-seeding, and stained for F-actin and PIP$_2$. Scale bar = 20 μm. Insets show that MyosinVI clusters were colocalized with PIP$_2$. Colocalizing MyosinVI/PIP$_2$ clusters linked to actin stress fibers at the cell periphery. As PIP$_2$ recruitment on the membrane is vital for the early stages for CME (i.e., Dab2-PIP$_2$ colocalization, Figure 2.14), these images strongly indicate that actin, MyosinVI, and PIP$_2$ are the governing proteins for CME of nanoparticles at the cellular ventral side. Scale bar = 2 μm. IV

2.19 **MyosinVI-PIP$_2$ clusters seemed to be influenced by matrix rigidity**. MEF cells expressing MyosinVI-eGFP were seeded on fibronectin-coated substrates (i.e., glass, rigid PDMS elastomer = 50 kPa, and soft PDMS elastomer = 0.4 kPa), fixed at 1 hour post-seeding, and stained for F-actin and PIP$_2$. Scale bar = 20 μm. V

2.20 **PIP$_2$ clusters also seemed to be associated with cellular adhesion**. MEF cells were seeded on fibronectin-coated substrates (i.e., glass, rigid PDMS elastomer = 50 kPa, and soft PDMS elastomer = 0.4 kPa), fixed at 1 hour post-seeding, and stained for zyxin, F-actin and PIP$_2$. PIP$_2$ clusters colocalize with zyxin clusters at the cell boundary. Scale bar = 20 μm. VI

.

List of Tables

1.1 The list of diblock copolymers used in this thesis. 24

1.2 PA stock solution composition used in this thesis. A = Acrylamide, B = Bisacrylamide. . 26

1.3 The swelling experiment of thick PA. w_b = the weight of the freshly made thick PA. w_a = the weight of the dehydrated PA after 120 h. Q = Swelling ratio. 32

1.4 The swelling experiment of thick PA after 120 hours inside PBS. w_{b2} = the weight of thick PA after 2 weeks in PBS. w_a = the weight of the dehydrated PA after 120 hours. Q = Swelling ratio. 33

1.5 The mechanical characterization of PA surface with the nanoindentation experiments (k = 0.2 N/m, r = 54 μm). A = Acrylamide, B = Bisacrylamide, E_1 = Young's modulus (before UV exposure), tan δ_1 = dissipation factor before UV exposure, E_2 = Young's modulus (after UV exposure), tan δ_2 = dissipation factor after UV exposure. 34

1.6 The mechanical characterization of elastomer surface with the nanoindentation experiments (k = 0.2 N/m, r = 54 μm). 37

1.7 Transfer of gold nanopatterned arrays from glass to PA experiments. **1** = AuNPs were absent from the glass surface verified by SEM. **2** = AuNPs were present from the PA surface verified by cryo-SEM. **3** = Cells attached on the surface of nanopatterned PA functionalized with 25 μM SH-cRGD. nt = not-tested. 46

1.8 Overview about the existing TFM methods in the lab. 57

1.9 Overview about substrates used in this work. 57

2.1 Primary antibodies. 69

2.2 Secondary antibodies and fluorescent affinity binders. 69

Summary

Clathrin-mediated endocytosis (CME) is one of the main uptake processes in cells. The biomechanical study of the formation of clathrin-coated structures has been attracting more attention since the first discovery of the clathrin protein more than 50 years ago. For CME to occur, adhesion energy between the cell and cargo must overcome an energy barrier produced by turgor pressure, membrane tension, and bending energy. While the molecular force mechanism of CME is relatively better understood, the role of cellular forces by rigidity sensing in supporting CME from the ventral side is less studied.

My doctoral thesis aimed to elucidate how the cellular adhesion forces to the extracellular matrix (ECM) contribute to the CME of nanoparticles at the cellular ventral side. The experimental setup entails the immobilization of nanoparticles on substrates coated with an ECM protein such as fibronectin. Next, cells expressing CME adaptor protein 2 (AP2) tagged with e-GFP (i.e., MEF, HeLa) were seeded on the substrate and were subsequently analyzed at around 4 hours post-seeding. Traction force microscopy (TFM) was used to quantify the ability of cells to generate traction forces.

As TFM requires a substrate that can be deformed by adherent cells, I described in the first part the preparation of elastic polyacrylamide (PA)/viscoelastic polydimethylsiloxane (PDMS) substrates and their mechanical characterization using nanoindentation experiments. Additionally, I investigated the response of materials upon the exposure to ultraviolet light (both PA and PDMS) and oxygen plasma (only PDMS elastomer). Next, I described the surface patterning on the substrate, including micropatterning (both PA and PDMS) using the maskless photolithography method and nanopatterning (only PA hydrogel) using the block-copolymer micellar nanolithography (BCMN) method. Finally, I described the development of an integrated bioengineering toolbox that includes a novel method called "Local Ultraviolet Illumination Traction Force Microscopy (LUVI-TFM)" that could be combined with micro- and nanopatterned substrates to perform 2D- and 2.5D-TFM on a single cell or multicellular clusters. This toolbox was devised so users could choose a single tool or a combination of multiple tools to study cell-matrix interaction.

In the second part, I described the use of the bioengineering tools established in the previous part to study the role of traction forces in initiating CME of nanoparticles at the cellular ventral side. First, I observed that electrostatically immobilized nanoparticles were removed under cellular traction forces

by using live 2D-LUVI-TFM. However, it was unclear if traction forces caused the particle removal. To elucidate it, I employed micropatterning to control the size and shape, thereby the traction force hotspots of a single cell. I could also immobilize nanoparticles in regions where the cell exerted high traction forces. On micropatterned cells, I observed a low spatial correlation between the clathrin adaptor protein 2 (AP2) clusters and focal adhesion marker clusters (paxillin, $\beta 1$ integrin, and $\beta 3$ integrin). Furthermore, I observed that traction forces alone were insufficient to remove nanoparticles from the surface. Despite no removal, I observed immobilized nanoparticles initiated CME in high traction force regions.

Concerning the role of traction force in initiating CME of nanoparticles at the cellular ventral side, I focused on cells that were transitioning between the early adhesion phase and the initial contractility at around 4 hours post-seeding. In this phase, cells exhibited the shape of a symmetric "bulls-eye egg" and were easier to be compared. I observed that AP2 clusters were highly distributed at the cell periphery, irrespective of the presence of covalently immobilized nanoparticles and substrate rigidity. Furthermore, I observed no significant difference between cells growing on the 3 kPa substrate and the glass concerning the cluster area and the signal lifetime of AP2. Lastly, I observed that the cell pushed down the substrate at the cell periphery, and AP2 clusters were found highly distributed inside the indentation area. Eventually, AP2 clusters were recruited above covalently immobilized nanoparticles in the indentation area. This result strongly suggested that the normal component of traction forces plays an undeniably important role in initiating CME of nanoparticles at the cellular ventral side.

Zusammenfassung

Die Clathrin-vermittelte Endozytose (CME) ist einer der wichtigsten Aufnahmeprozesse in Zellen. Seit der ersten Entdeckung des Clathrin-Proteins vor mehr als 50 Jahren hat die biomechanische Untersuchung der Bildung von Clathrin-beschichteten Strukturen immer mehr Aufmerksamkeit erregt. Damit CME stattfinden kann, muss die Adhäsionsenergie eine Energiebarriere überwinden, die durch Turgordruck, Membranspannung and Biegeenergie entsteht. Während der molekulare Kraftmechanismus von CME relativ gut verstanden ist, ist die Rolle der zellulären Kräfte durch Steifigkeitssensorik bei der Unterstützung von CME von der ventralen Seite her weniger untersucht.

In meiner Doktorarbeit wollte ich herausfinden, wie die zellulären Adhäsionskräfte an der extrazellulären Matrix (ECM) zur CME von Nanopartikeln an der Zellventralseite beitragen. Der Versuchsaufbau sieht die Immobilisierung von Nanopartikeln auf Substraten vor, die mit einem ECM-Protein wie Fibronektin beschichtet sind. Anschließend wurden Zellen, die das mit e-GFP markierte Adaptorprotein 2 (AP2) exprimieren (z.B., MEF, HeLa), auf dem Substrat ausgesät und anschließend etwa 4 Stunden nach der Aussaat analysiert. Mit Traktionskraft-Mikroskopie (TFM) wurde die Fähigkeit der Zelle, Traktionskräfte zu erzeugen, quantifiziert.

Da TFM ein Substrat benötigt, dass durch anhaftende Zellen verformt werden kann, beschrieb ich im ersten Teil die Herstellung elastischer Polyacrylamid (PA)- sowie viskoelastischer Polydimethylsiloxane (PDMS) Substrate und ihre mechanische Charakterisierung durch Nanoindentationsexperimente. Außerdem untersuchte ich die Reaktion der Materialien auf die Bestrahlung mit ultraviolettem Licht (sowohl PA als auch PDMS) und Sauerstoffplasma (nur PDMS-Elastomer). Als Nächstes beschrieb ich die Oberflächenstrukturierung auf dem Substrat, einschließlich das Mikropatterning (sowohl PA als auch PDMS) unter Verwendung der maskenlosen Fotolithografiemethode und das Nanopatterning (nur PA Hydrogel) unter Verwendung der mizellaren-Block-Copolymer-Nanolithographie-Methode (BCMN). Schließlich beschrieb ich die Entwicklung einer integrierten Bioengineering-Toolbox, die eine neuartige Methode namens „Lokale Ultraviolett-Beleuchtung Traktionskraft-Mikroskopie (LUVI-TFM)“ umfasst, die mit mikro- und nanostrukturierten Substraten kombiniert werden kann, um 2D- und 2.5D-TFM an einer einzelnen Zelle oder multizellulären Clustern durchzuführen. Diese Toolbox wurde entwickelt, damit

die Benutzer ein einzelnes Tool oder eine Kombination mehrerer Tools zur Untersuchung der Zell-Matrix-Interaktion wählen können.

Im zweiten Teil beschrieb ich die Verwendung der im vorigen Teil etablierten Bioengineering-Tools, um die Rolle von Traktionskräften bei der Initiierung der CME von Nanopartikeln an der ventralen Seite der Zelle zu untersuchen. Zunächst beobachtete ich, dass elektrostatisch immobilisierte Nanopartikel unter zellulären Traktionskräften entfernt wurden, indem ich lebende 2D-LUVI-TFM verwendete. Es war jedoch unklar, ob die Traktionskräfte die Entfernung der Partikel verursachten. Um dies zu klären, habe ich durch Mikropatterning die Größe und Form und damit die Traktionskraft-Hotspots einer einzelnen Zelle kontrolliert. Außerdem konnte ich Nanopartikel in Bereichen immobilisieren, in denen die Zelle hohe Traktionskräfte ausübte. Auf mikrostrukturierten Zellen beobachtete ich eine geringe räumliche Korrelation zwischen den Clathrin-Adapter protein-2-Clustern (AP2) und den Clustern der fokale Adhäsionsmarker (Paxilin, $\beta 1$ Integrin, und $\beta 3$ Integrin). Außerdem konnte ich feststellen, dass die Traktionskräfte allein nicht ausreichten, um die Nanopartikel von der Oberfläche zu entfernen. Obwohl keine Entfernung stattfand, beobachtete ich, dass immobilisierte Nanopartikel in Regionen mit hoher Traktionskraft CME initiierten.

Was die Rolle der Traktionskraft bei der Initiierung von Nanopartikeln an der ventralen Seite der Zellen betrifft, so konzentrierte ich mich auf Zellen, die etwa 4 Stunden nach der Aussaat zwischen der frühen Adhäsionsphase und dem Beginn der Kontraktionsfähigkeit übergingen. In dieser Phase wiesen die Zellen die Form eines symmetrischen „Bullauges“ auf und waren leichter zu vergleichen. Ich beobachtete, dass AP2-Cluster in hohem Maße and der Zellperipherie verteilt waren, unabhängig vom Vorhandensein kovalent immobilisierter Nanopartikel und der Substratsteifigkeit. Außerdem konnte ich keinen signifikanten Unterschied zwischen Zellen, die auf dem 3 kPa-Substrat wuchsen, und Zellen, die auf Glass wuchsen, in Bezug auf die Clusterfläche und die Signallebensdauer von AP2 feststellen. Ich beobachtete, dass die Zelle das Substrat and der Zellperipherie nach unten drückte, und AP2-Cluster waren im Bereich der Vertiefung stark verteilt. Schließlich wurden AP2-Cluster über kovalent immobilisierten Nanopartikeln im Bereich der Vertiefung rekrutiert. Dieses Ergebnis deutet stark darauf hin, dass die normale Komponente von Traktionskräften eine unbestreitbar wichtige Rolle bei der Initiierung von Nanopartikeln an der ventralen Seite der Zelle spielt.

1

Part I: Development of local ultraviolet illumination traction force microscopy combined with surface patterning

1.1 Introduction

Mechanical force is vital in nature. At the organism level, mechanical force sometimes relates to survivability. For example, a peacock mantis shrimp (*Odontodactylus scyllarus*) uses up to 1 kN cavitation force of its raptorial appendages to destroy the shell of its hard-shelled prey before devouring it [94]. Meanwhile, the mechanical force at around 10-30 pN is required at the molecular level to maintain the linkage between a single integrin and its ligand (i.e., the catch bond) [72]. At the cellular level, mechanical force relates to the traction force. Traction force is involved in many cellular functions, including maintaining cell shape, migration, and reorganizing the extracellular matrix (ECM) [119]. Traction forces occur due to the force transmission and transduction in response to matrix rigidity. They can be explained with the molecular clutch model where Myosin II, F-actin, Talin, Integrin, and Fibronectin are generators of traction forces [38].

It is generally accepted that Traction Force Microscopy (TFM) is the main method used in mechanobiology to measure cell-ECM forces *in vitro* (i.e., traction forces) [102]. To perform TFM, one requires a combination of a linearly elastic polymeric substrate, fluorescent markers, and solving the inverse problem of linear elasticity [18, 109, 103, 95]. TFM is typically performed using substrate like polyacrylamide (PA) embedded with fluorescent nanoparticles/beads to track the deformation caused by contracting cells. Using fluorescent microscopy, deformed and undeformed/reference/null-force bead images are taken and processed to obtain the deformation field. With prior knowledge of the mechanical properties such as the substrate stiffness, the cellular traction can be reconstructed using several methods, for example, Fourier Transform Traction Cytometry (FTTC) with regularization [103].

In conventional TFM, enzymatic detachment using trypsin is typically used to release the cell traction and subsequently to get the reference image [91, 15, 109, 103, 29, 38, 92, 35, 28]. Trypsinization leads to a simultaneous and rapid release of all cells on the substrate. However, it poses a detrimental effect as one tiny mistake in handling can lead to “sample-loss”, especially in single-cell experiments where a high magnification lens with a shallow depth of focus is often used. Also, introducing trypsin to detach cells necessitates careful handling of samples on the microscopy stage. Activities like opening the heating chamber stage, opening the lid of the dish, aspirating medium, rinsing, pipetting in trypsin, closing the lid of the dish, and closing the heating chamber without disturbing the sample represent a challenge even for experienced users. These procedures are a significant source of the drift in xyz axes, resulting in a loss in position and focus.

The estimation of force distribution using the inverse method like FTTC is mathematically ill-posed. Slight experimental noise can easily trigger a significant error in the traction field. A specific issue such as a small lateral drift typically can be solved with image processing plugins (e.g., StackReg and TurboReg in ImageJ). However, the change in the signal intensity due to defocus is impossible to recover. Comparing images, in this case, will produce a very noisy force map and overestimated cellular forces. Regularization introduces a more rigorous treatment to tackle the experimental noise issue. However, as it is well-described with the adage “garbage in, garbage out”, the quality of the output is determined by the quality of input. Therefore, combining high-quality displacement fields with proper data handling, including regularization, are essential in doing TFM.

1.1.1 Motivation

Development of an alternative TFM method

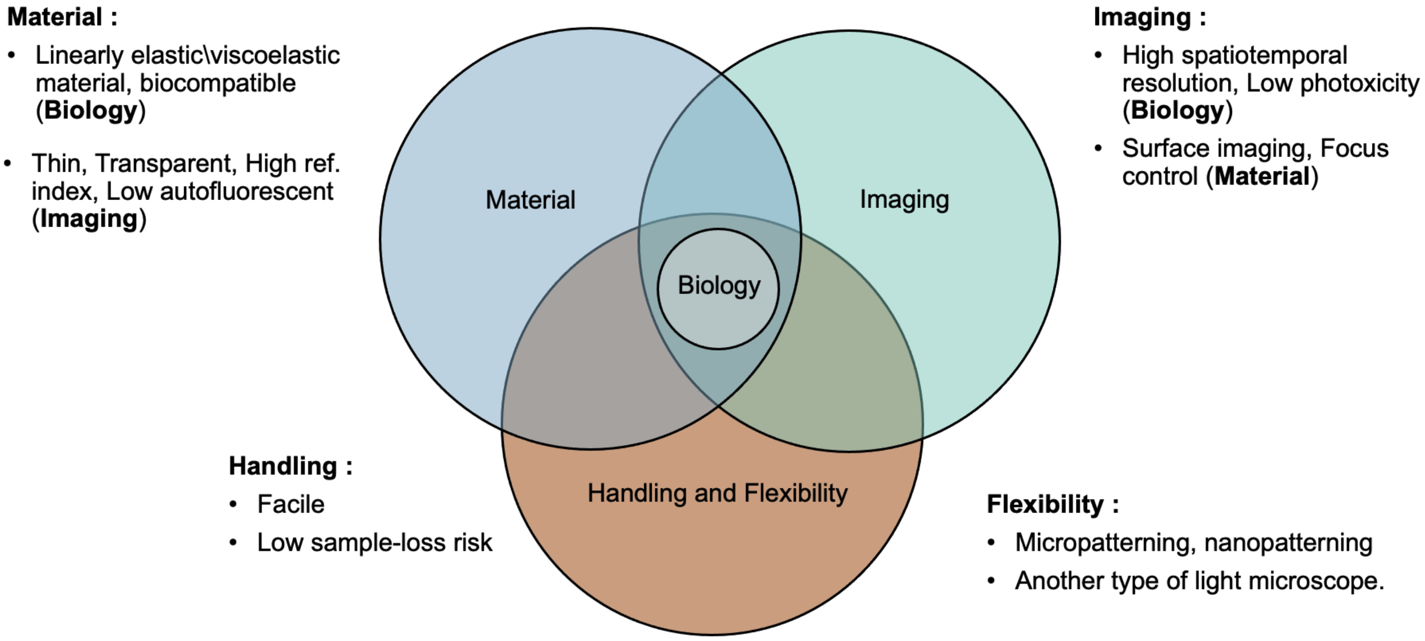
Material :
• Linearly elastic\viscoelastic material, biocompatible **(Biology)**
• Thin, Transparent, High ref. index, Low autofluorescent **(Imaging)**
Imaging :
• High spatiotemporal resolution, Low photoxicity **(Biology)**
• Surface imaging, Focus control **(Material)**
Material
Imaging
Biology
Handling and Flexibility
Handling :
• Facile
• Low sample-loss risk
Flexibility :
• Micropatterning, nanopatterning
• Another type of light microscope.

Figure 1.1: Venn’s diagram showing four main aspects that are considered for the alternative TFM method: material, imaging, flexibity, and handling. The novelty of this TFM method comes from the handling aspect. The method aims to provide a tool that can be easily used even by beginners to study a biology-related phenomenon (i.e., mechanobiology of cell-matrix interaction).

There have been increasing biology-related questions on single cells researchers try to answer with the help of TFM experiments. Unfortunately, some experiments are cumbersome to be conducted with the conventional trypsin-based TFM. After working with single-cell TFM for several years, I realized that there was an urgency to have an alternative protocol aiming at the facile production of high-quality displacement fields. Many labs have developed solutions regarding high-throughput TFM methods. However, it is mainly challenging to apply established protocols from other labs due to limited access to setups, backgrounds of users, and skills. Furthermore, I felt that it was more encouraging to build a setup based on the available equipment in the lab rather than applying established protocols from other labs.

As shown in Figure 1.1, the alternative protocol aims to provide a method that can be easily used even by beginners to study a biology-related phenomenon (i.e., mechanobiology of cell-matrix interaction). To this end, four main aspects are considered: material, imaging, flexibility, and handling. The material aspect describes the use of linearly elastic/viscoelastic materials that should be biocompatible and can be used for imaging by fluorescence microscopy (i.e., thin, transparent, glass-matching refractive index). The imaging aspect describes the strategies for quantifying the cellular forces and detecting the proteins responsible for the process without too much harming the cells. The flexibility aspect describes surface patterning methods (e.g., micropatterning and nanopatterning) and other microscopy techniques that can be applied to the method. In this alternative protocol, those three aspects (i.e., material, imaging, and flexibility) are adapted from several reported works [92, 121, 105, 25, 26, 28, 78, 107].

The novelty of this alternative protocol comes from the handling aspect. As mentioned before, the alternative protocol aims to provide a method that is flexible, easy to handle, and allows to record traction forces from several cells efficiently. To this end, I focus on releasing traction forces by killing the cells with light illumination. Overexposing high-dose ultraviolet light to cells is known to cause oxidative distress, leading to phototoxicity and cell death [1, 113]. Dead cells release traction from the underlying substrate as they lose their ability to maintain adhesion and cytoskeletal integrity. By treating cells with light to release their traction *in situ*, the need for activities such as opening the stage, opening the dish, aspirating, and pipetting trypsin could be eliminated. Ideally, the light should only kill the cells without changing any physical properties of the underlying elastic substrate.

Development of an integrated bioengineering toolbox to study cell-matrix interaction

Finally, the alternative TFM protocol should be integrated with existing surface patterning methods such as micropatterning and nanopatterning to provide users with a versatile bioengineering toolbox. With this toolbox, users can choose a single tool or a combination of multiple tools to study cell-matrix interaction.

1.2 State of the art

1.2.1 Traction force microscopy

Traction force microscopy (TFM) is a highly interdisciplinary technique borrowing its key concepts from optical microscopy, polymer chemistry, soft-matter physics, and computer sciences [95]. To date, TFM is the main method used in mechanobiology to measure cell forces. In their typical environment, mammalian cells exert three-dimensional forces. Some cell types have comparable normal force component to in-plane/parallel force components (e.g., ameboid cells) [8]. However, two-dimensional TFM is still highly applicable for experiments on most adherent cell types to measure cellular forces on the nanonewton scale. Events that produce piconewtons forces, such as the molecular extension of integrins and talin unfolding can not be measured with 2D-TFM and require an alternate approach such as tension sensors [102].

In 2D-TFM, a thick polymer substrate embedded with fiducial markers is seeded with cells [91, 103, 97]. Bead images of cells deforming the substrate are acquired, followed by a zero-traction reference image after the cell removal. The images of the cell deforming the substrate are mapped onto the reference image to produce displacement vectors indicating how the substrate has been deformed. If the density of the marker is high, one can use Particle Image Velocimetry (PIV), a well-established cross-correlation function to derive local motion. Otherwise, one can use Particle Tracking Velocimetry (PTV). Finally, cellular traction is reconstructed using the most efficient and reliable method for 2D-TFM, namely Fourier Transform Traction Cytometry (FTTC) with regularisation [17, 103].

For a single cell TFM using a high magnification lens (e.g., 60x) that has a short working distance, a certain thickness (e.g., 30 μm) has to be applied not only to ensure cells are only subjected to the stiffness of the polymer substrate but also to allow high-resolution imaging of the sample [95]. For PA hydrogel, fluorescent nanoparticles are embedded close to the surface during the hydrogel polymerization through centrifuged-based sedimentation or the formation of two layers [15, 25]. For PDMS elastomer, carboxylated fluorescent nanoparticles are covalently-conjugated on the aminated elastomer surface [6].

The standard workflow of a TFM analysis for planar elastic substrates is shown in Figure 1.2 [11]. The traditional 2D-TFM approach is the inverse method, which minimizes the difference between the experimental and the estimated displacement fields. Meanwhile, the direct method uses a direct calculation from the displacement field, including differentiation and (linear) transformation between strain and stress. The direct method cannot be used in a purely 2D setup but requires 3D image data. Schwarz et al. described that methods in reconstructing traction forces, namely the inverse method and the direct method require elements of the elasticity theory [109, 11].

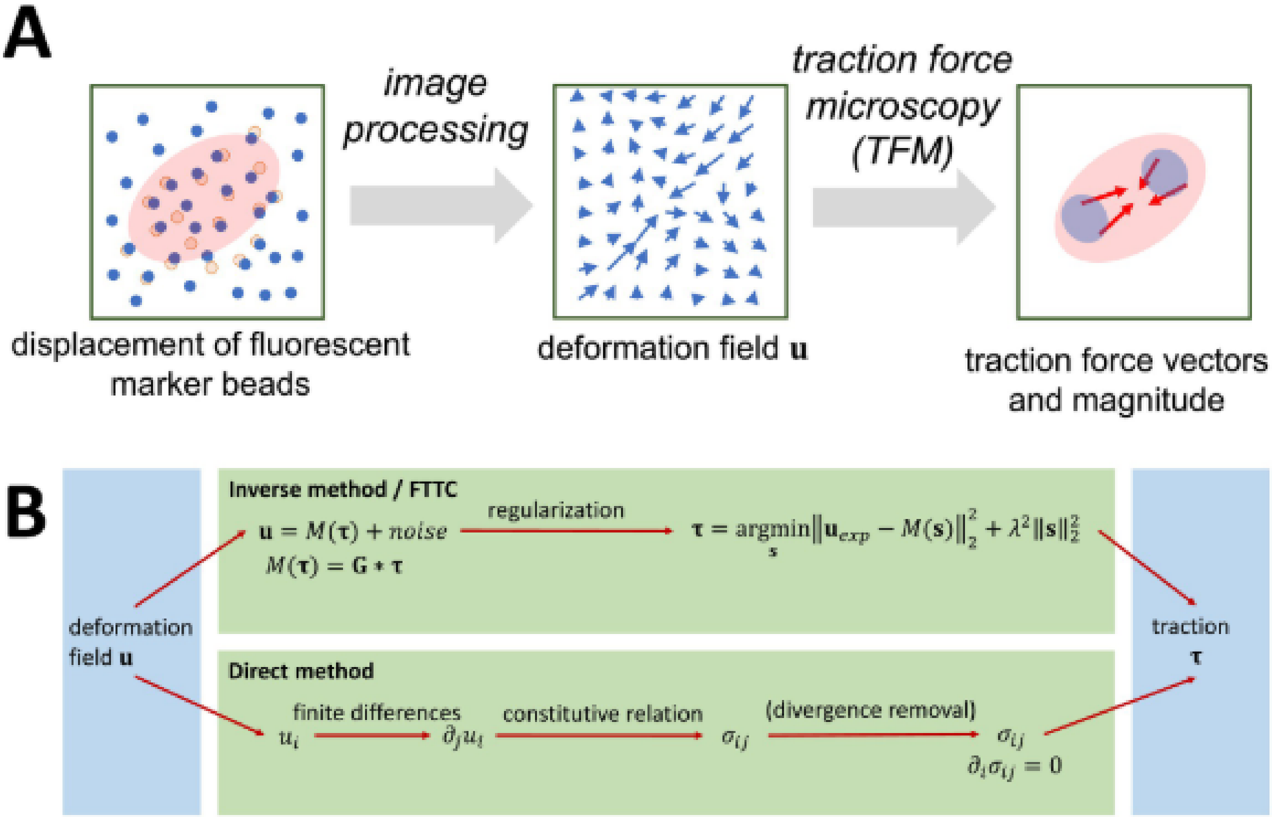
A
image processing
traction force microscopy (TFM)
displacement of fluorescent marker beads
deformation field **u**
traction force vectors and magnitude
B
Inverse method / FTTC
$\mathbf{u} = M(\boldsymbol{\tau}) + noise$
$M(\boldsymbol{\tau}) = \mathbf{G} * \boldsymbol{\tau}$
regularization
$\boldsymbol{\tau} = \operatorname{argmin}_{\mathbf{s}} \|\mathbf{u}_{exp} - M(\mathbf{s})\|_2^2 + \lambda^2 \|\mathbf{s}\|_2^2$
deformation field **u**
traction $\boldsymbol{\tau}$
Direct method
finite differences
constitutive relation
(divergence removal)
u_i
$\partial_j u_i$
σ_{ij}
σ_{ij}
$\partial_i \sigma_{ij} = 0$

Figure 1.2: General overview of TFM. Reproduced from Ref. [11] under the terms of the Creative Commons Attribution License (https://creativecommons.org/licenses/by/4.0/). (**A**) Images of the deformed state and the undeformed state are drift-corrected and processed to obtain the deformation field. The cellular traction field is estimated from the displacement field. (**B**) Two fundamentally different methods to reconstruct the traction from the displacement in TFM. The inverse method estimates a force distribution resulting in an optimum match for the displacement field. Fast fourier transform is used in FTTC. A regularization scheme is introduced to address the fact that determining the traction field from the displacement field is mathematically ill-posed. In the direct method, point-wise computational methods are used to determine the stress tensor locally.

Elasticity theory

Traction forces are forces acting on the boundary of elastic solids. They are quantified by a three-component vector field τ, which is defined for all points at a surface and describes the area density of the force. Its component normal to the surface describes the pressure balance between the solid and its surroundings. In contrast, the in-plane/parallel/tangential components describe shear forces.

The stress tensor σ describes the force per area acting on any (real or fictitious) surface of the system. It is defined by the relation:

$$\boldsymbol{\tau_S} = \boldsymbol{\sigma n_S} \tag{1.1}$$

The left hand side represents the surface force density for a given surface ($\boldsymbol{S}$). The vector $\boldsymbol{n_S}$ is the unit normal vector of $\boldsymbol{S}$. In the case of a solid which is delimited by a planar surface at the $z = 0$ plane and whose outwards normal is defined in negative z direction, the traction stress reads:

$$\boldsymbol{\tau} = -(\sigma_{13}, \sigma_{23}, \sigma_{33})|_{z=0} \tag{1.2}$$

This means that by determining the stress tensor in a region close to the surface, the surface traction is known.

Stresses leading to the material movement and are described by the deformation gradient tensor **F**, which is the Jacobian of the coordinate transformation between deformed and undeformed configurations. Alternatively, the movement can be described by the deformation field **u**, which is related to the deformation gradient tensor by

$$F_{ij} = \delta_{ij} + \frac{\partial u_i}{\partial x_j} \tag{1.3}$$

Stresses within the material and changes in its configuration are related by a constitutive equation $\sigma = \sigma(\mathrm{F})$. For relatively stiff, homogeneous and isotropic material, a linear approximation can be used that is given by (in terms of displacement field)

$$\sigma_{ij} = \frac{E}{2(1+\nu)} \left(\frac{\partial u_i}{\partial x_j} + \frac{\partial u_i}{\partial x_j} + \frac{2\nu}{1-2\nu} (\boldsymbol{\nabla u}) \delta_{ij} \right) \tag{1.4}$$

The material constants E and ν are known as the Young's modulus and the Poisson's ratio. E and ν describe the stiffness and the compressibility of the material. A substrate is considered stiff or soft by the relation between the typical traction force amplitude and the Young's modulus. The substrate is soft if the magnitude of the traction forces is much larger than substrates Young's modulus. The linear approximation (equation 1.4) does not apply anymore and might need to be replaced by a non-linear mapping. For typical TFM-experiments with a substrate having E = 10 kPa, cells exert traction stresses in the range of 1 kPa, therefore the linear relation is satisfied. Both PA and PDMS are considered to be close to incompressible ($\nu = 0.5$). The incompressibility also implies $\boldsymbol{\nabla u} = 0$ in the linear case in the equation 1.4.

Assuming small deformations and a linear material law, the traction forces can be related to deformations directly using a convolution relation:

$$\boldsymbol{u}(x, y, z) = \int_s (G)(x - x', y - y', z) \cdot \boldsymbol{\tau}(x', y') dx'dy' \tag{1.5}$$

where the coordinate system is chosen in such a way that the traction stresses are exerted on the z =

0 plane and the substrate is confined to the z > 0 halfspace. Given the experimental displacement $\boldsymbol{u}$(x, y, z) and the Green's function, the equation 1.5 can be inverted to obtain the desired traction $\boldsymbol{\tau}$. The Green's function $\boldsymbol{G}$ is known analytically for an elastic halfspace (*Boussinesq solution*) [75]:

$$\frac{2\pi E}{1+\nu}\boldsymbol{G}(x,y,z) = \begin{pmatrix} \frac{2(1-\nu)r+z}{r(r+z)} + \frac{(2r(\nu r+z)+z^2)x^2}{r^3(r+z)^2} & \frac{(2r(\nu r+z)+z^2)xy}{r^3(r+z)^2} & \frac{xz}{r^3} - \frac{(1-2\nu)x}{r(r+z)} \\ \frac{(2r(\nu r+z)+z^2)xy}{r^3(r+z)^2} & \frac{2(1-\nu)r+z}{r(r+z)} + \frac{(2r(\nu r+z)+z^2)y^2}{r^3(r+z)^2} & \frac{yz}{r^3} - \frac{(1-2\nu)y}{r(r+z)} \\ \frac{(1-2\nu)x}{r(r+z)} + \frac{xz}{r^3} & \frac{(1-2\nu)y}{r(r+z)} + \frac{yz}{r^3} & \frac{2(1-\nu)}{r} + \frac{z^2}{r^3} \end{pmatrix}$$

with $r = \sqrt{x^2+y^2+z^2}$. The 1/r-dependence of this Green's function reveals the long-ranged nature of traction forces and is the reason why the inverse problem is ill-posed [103, 11]. This means the addition of a small amount of measurement noise in the displacement field can lead to a large error in the traction field [103, 110].

Inverse problem and regularization

In principle, a traction field can be acquired by inverting equation 1.5. However, it ignores the fact that the inverse problem of elasticity is ill-posed because the elastic effects are long-ranged. The local changes in the traction will induce non-negligible effects on the displacement even over a larger distance [11]. Experimental noise sources, including elastic inhomogeneities in the substrate, weakly bound marker beads, non-optimum optical setup, lack of accuracy in the tracking routines, and also the user handling may heavily influence the traction estimation.

To overcome the experimental noise problem in generating suitable traction fields, Schwarz et al. reported the use of a regularization scheme such as the 0^{th} order Tikhonov regularization [109, 103]. The regularization parameter λ is chosen by the generalized cross validation (GCV) technique to avoid the subjectiveness of users [50] in producing the traction field. If λ is chosen too large, the traction field will lose accuracy and resolution. Whereas when λ is chosen too small, the traction field will be dominated by noise [110].

1.2.2 Material response to mechanical loading

Materials can be categorized by how they deform in response to mechanical loading, typically in a stress-strain test [22]. Strain is a normalized measure of deformation. Force per area defines the mechanical stress, with units of pascals (N/m^2), and can be shear and normal.

Linear elasticity Material can be grouped as linearly elastic when stress is linearly related to strain for minor strains, with no loss of mechanical energy and reversible deformations. For an elastic material, the relationship between stress (σ) and strain (ϵ) can be expressed in the following form

$$\sigma = f\epsilon \tag{1.6}$$

Non-linear elasticity Material can be grouped as non-linearly elastic when stress is non-linearly related even for small strains, with no loss of mechanical energy and reversible deformations.

Viscoelasticity Material can be grouped as viscoelastic when it exhibits a combination of storage of elastic energy as a solid, and a loss of mechanical energy, as a Newtonian fluid. Viscoelastic materials exhibit stress relaxation in response to a constant deformation, and increased strain, or creep, in response to constant stress [22]. Stress, temperature, frequency, and other factors play role in the viscoelastic properties of polymers. For a viscoelastic material, the relationship between stress (σ) and strain (ϵ) can be expressed in the following form

$$\sigma = f(\epsilon, \dot{\epsilon}) \tag{1.7}$$

In comparison to the linear elasticity, the stress is not only a function of strain, but also a function of strain rate ($\dot{\epsilon} = d\epsilon/dt$, where t is the time). Therefore, the stress is also dependent upon the rate at which the strain is developed in the material.

Complex shear modulus As shown in Figure 1.3, the relation among complex shear modulus (G^*) obtained from a dynamic mechanical test, storage modulus (G'), and loss modulus (G'') can be expressed as follows

$$G^* = G' + iG'' \tag{1.8}$$

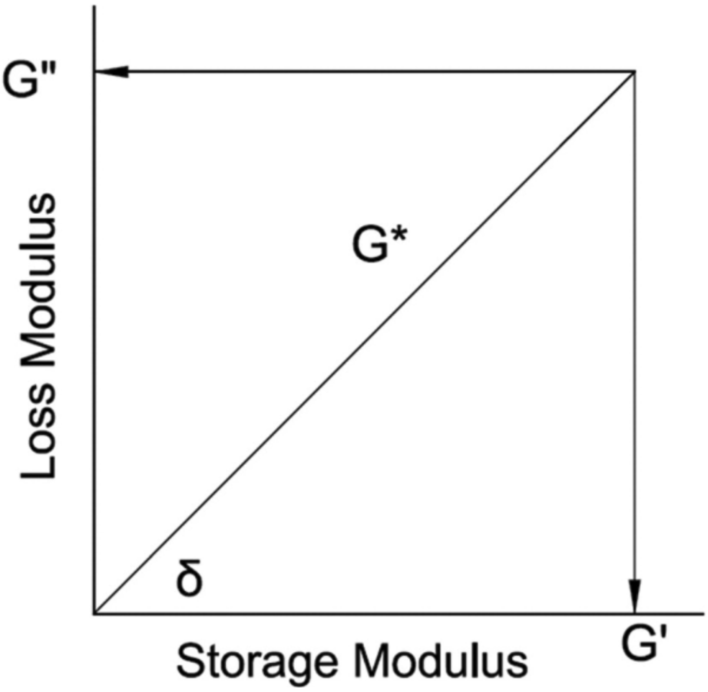

Figure 1.3: The relation among complex shear modulus (G^*), real storage modulus (G'), imaginary loss modulus (G''), and phase difference (tan δ). The image is courtesy of journals.sagepub.com

In addition, the dissipation factor or loss tangent (tan δ) can be expressed as follows

$$tan(\delta) = \frac{G''}{G'} \tag{1.9}$$

Elastic and viscoelastic modeling As shown in Figure 1.4, the schematic illustrations of the linear elastic and the viscoelastic are represented by the spring and the Kelvin-Voigt model involving a paralled spring-dashpot element.

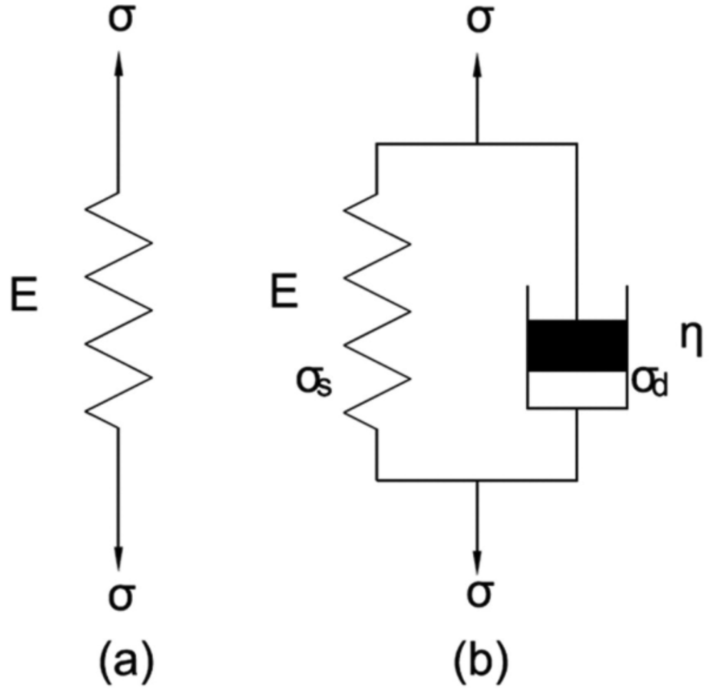

Figure 1.4: (**a**) Linear elastic model. (**b**) Kelvin-Voigt viscoelastic model. Images are courtesy of journals.sagepub.com

The total stress in the system (σ) and the strain of the system (ϵ) can be expressed as follows

$$\sigma_s = E\epsilon_s \tag{1.10}$$

$$\sigma_d = \eta\dot{\epsilon_d} \tag{1.11}$$

$$\sigma = \sigma_s + \sigma_d \tag{1.12}$$

$$\epsilon = \epsilon_s = \epsilon_d \tag{1.13}$$

From all equations above, we can express the total stress as

$$\sigma = E\epsilon + \eta\frac{d\epsilon}{dt} \tag{1.14}$$

Equation 1.14 tells us about the stress-strain relationship and the strain rate for two parameters (E and η) of the viscoelastic model. E represents the elasticity which describes the elastic behavior of the single spring and η represents the dynamic viscosity which describes the viscous behavior of the single dashpot in the Kelvin-Voigt model. The relationship between dynamic viscosity (η) and the loss modulus (G'') can be expressed as follows

$$\eta = \frac{G''}{\omega} \tag{1.15}$$

where ω is the oscillation frequency of measurement.

1.2.3 Linear elastic/viscoelastic materials for TFM applications

Polyacrylamide Polyacrylamide (PA) is a water-soluble polymer PA and is highly water-absorbent [54, 34]. Therefore, it is most widely used in water treatments. In biological applications, PA is used as a medium for electrophoresis of proteins and nucleic acids. PA poses low toxicity, but unpolymerized Acrylamide is highly neurotoxic and carcinogenic [115, 73]. PA is chemically inert, electrically neutral, hydrophilic, and transparent for wavelengths greater than 250 nm.

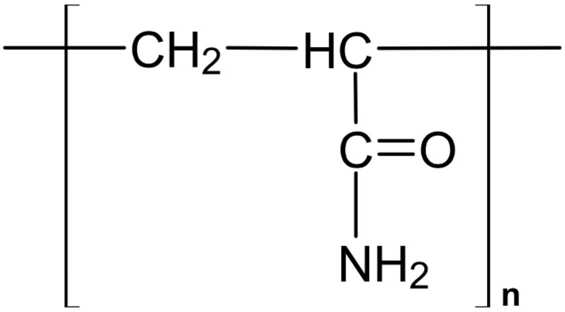

Figure 1.5: The chemical structure of PA. The structure image is courtesy of Wikipedia.

The chemical formula for PA is (-$CH_2CHCONH_2$-) and PA is a linearly elastic material because it exhibits a constant storage modulus throughout a wide range of strains [100, 34].

Polydimethylsiloxane Polydimethylsiloxane (PDMS) is the most widely used silicon-based organic polymer [84]. Its applications range from contact lenses, medical devices, lubricating oils, heat resistant tiles, and elastomers. PDMS is optically clear, inert, non-toxic, and non-flammable.

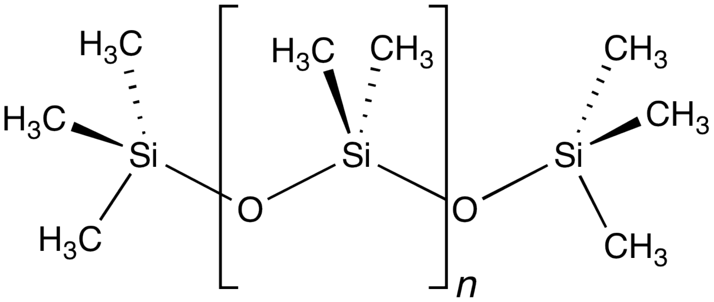

Figure 1.6: The chemical structure of PDMS. The structure image is courtesy of Wikipedia.

The chemical formula for PDMS is $(H_3C)_3[Si(CH_3)_2O]_nSi(CH_3)_3$, where n is the number of repeating monomer [Si$(CH_3)_2$O] units. The siloxane functional group forms the backbone of PDMS (Figure 1.6). PDMS is viscoelastic, which means at long flow times or high temperatures, it acts as a viscous liquid. Whereas at short flow times or low temperatures, it acts like an elastic solid.

Solid PDMS substrates have a hydrophobic surface chemistry, and it is not easy to wet the surface using polar solvents such as water. Silanol (SiOH) groups can be added *via* plasma oxidation treatment to render the surface hydrophilic. However, the oxidized surface will not be stable permanently, and the material will recover its hydrophobicity regardless of the surrounding medium [84].

1.2.4 Surface modification of elastic/viscoelastic materials for TFM applications

General on ECM proteins

The extracellular matrix is a non-cellular component in all tissues and organs [42]. It provides the physical environment for the cells and plays a vital role in determining the assembly of tissues, differentiation, and homeostasis. Defects in the ECM may cause cellular and tissue alterations leading to disease. To date, pharmacotherapy targeting ECM has been attracting more attention due to its vital role in disease progression [63].

Two main classes of macromolecules in ECM are proteoglycans (PGs) and fibrous proteins [42]. PGs are the principal substance of the extracellular interstitial space within a tissue. They serve various functions reflecting their unique buffering, hydration, binding, and force-resistant properties. The main fibrous proteins of ECM are collagens, elastins, fibronectins, and laminins. The most abundant protein, collagen, contributes to almost 30 % of the total protein mass of a multicellular animal [112]. As the main element of ECM, collagen provides tensile strength, regulates cell adhesion, supports chemotaxis, controls adhesion, and directs tissue development. Elastin fibers, also tightly associated with collagen, mainly provide recoil to tissues undergoing stretches [120]. Fibronectin directs the organization of the interstitial ECM and cell attachment [114, 104]. It presents integrin binding sites such as the RGD loop and binding sites for other ECM proteins [61]. Fibronectin is a large, dimeric protein with more than 50 repeating subunits and is typically in an equilibrium folded state, hiding some of its cryptic binding sites. Cellular traction forces can unfold fibronectin fibers up to 5-fold of their resting length [114]. The force-dependent unfolding of fibronectin also implicates fibronectin as an extracellular mechano-regulator [44]. The last main protein of ECM, laminin, is a heterotrimeric protein composed of α-, β-, and γ-subunits [53]. Laminin involves in cell adhesion, migration, differentiation, and proliferation.

Engineering surface-ECM interaction

Polymeric substrates (e.g., PA hydrogel and PDMS silicon elastomer) are chemically inert, which means that the substrates need to be biofunctionalized with ECM proteins to allow cell-surface interactions

[42, 25, 26]. Therefore, the interaction between functionalized ECM proteins and the substrates is the main regulator in generating stable cell adhesion when doing TFM [15]. It is widely known that the physical and chemical properties of the surface can be changed to enhance ECM-surface interaction, thereby improving cell adhesion for TFM applications [32, 101].

In 2003, Dee et al. described that ECM-surface interactions depend on the properties of both the protein and the surface [32].

Properties of a protein that influences the interaction with the surface

1. (**Size**) Large molecules can have more contact sites with the surface.
2. (**Charge**) Molecules near the isotropic point adsorb more on the surface.
3. (**Stability**) Less stable proteins (i.e., less intramolecular cross-linking) can be more unfolded and form more contact points with the surface.
4. (**Unfolding rate**) Molecules that unfold rapidly can establish more contact points with the surface more quickly.

Properties of surfaces that influences the interaction with ECM proteins

1. (**Topography**) Greater texture exposes more surface area for interaction with proteins.
2. (**Composition**) Surface chemistry will determine the intermolecular force governing interaction with proteins (e.g., hydrophobic surfaces tend to bind more protein).
3. (**Heterogeneity**) Surfaces that are not uniform can interact differently with proteins.
4. (**Potential**) Surface potential will determine the distribution of ions and interaction with proteins.

Adsorption and desorption Adsorption is the process in which molecules adhere to a solid surface [32]. In contrast, desorption is when molecules detach from a solid surface and return to the bulk phase. Besides the properties of the protein and the surface, molecules can be brought to the surface by four main mechanisms: diffusion, thermal convection, flow, and coupled transport (i.e., a combination of thermal convection and diffusion). For all mechanisms, the molecular size, concentration, and velocity determine the arrival of protein molecules at the surface.

Simple diffusion can be described by the following equation:

$$\frac{\delta C}{\delta t} = D\frac{\delta^2 C}{\delta x^2} \tag{1.16}$$

where C is concentration, D is the diffusion coefficient, and x is distance. At short times and under conditions in which the rate of adsorption equals the rate of diffusion

$$\frac{\mathrm{d}n}{\mathrm{d}t} = C_0\left(\frac{D}{\pi t}\right)^{1/2} \tag{1.17}$$

where n is the protein surface concentration, C_0 is the protein bulk concentration, and t is time. Under convective diffusion, the treatment now depends on the geometry of interface. For flow in a thin channel:

$$\frac{\delta C}{\delta t} = V(y)\frac{\delta C}{\delta x} + D\frac{\delta^2 C}{\delta y^2} \tag{1.18}$$

where

$$V(y) = \gamma y\left(1 - \frac{y}{b}\right) \tag{1.19}$$

where V is the velocity of flow, x is the distance down the channel, y is the location within the channel height (b), and γ is the wall shear rate.

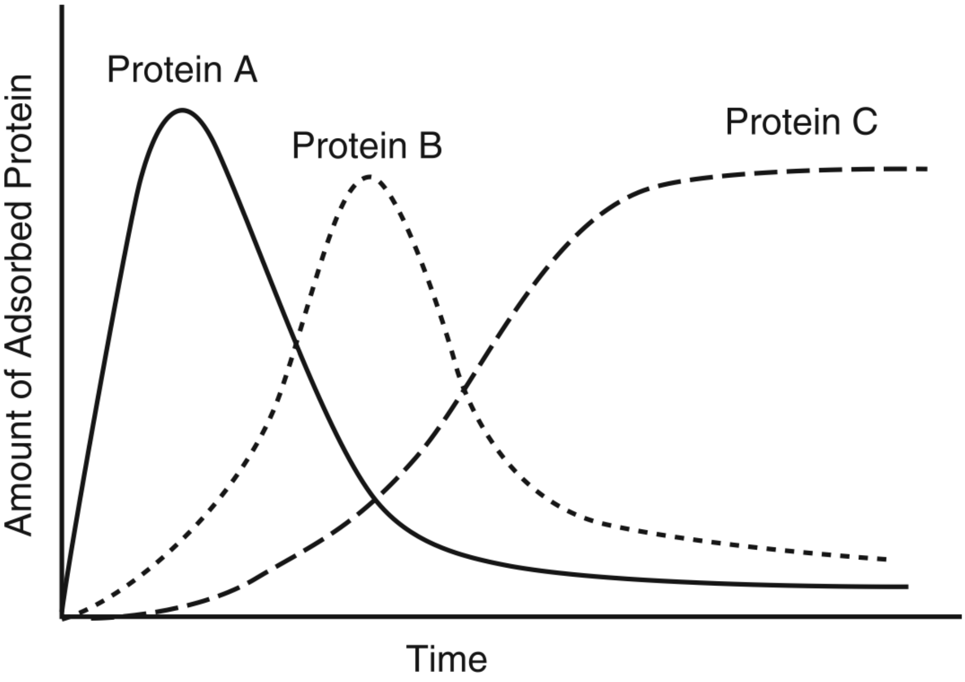

Figure 1.7: Schematic representation of the sequential protein exchange on a surface (the Vroman Effect). Reproduced with permission from Ref. [32]. Copyright 2003 John Wiley and Sons.

The Vroman Effect The Vroman effect describes the mechanism regulating the protein interaction. As shown in Figure 1.7, proteins with low diffusion coefficient and higher affinity to a surface can replace proteins with high diffusion coefficient and low affinity already adsorbed to the surface [32].

General mechanism governing protein-surface interactions As shown in Figure 1.8, Ribeiro et al. described the general mechanism governing the interactions between the protein and the surface [101]. The interactions are highly dependent on the properties of the protein and the surface. Charge-based interactions typically yield moderate adsorption (i.e., 3-7 kCal/mol), which is unstable and dependent

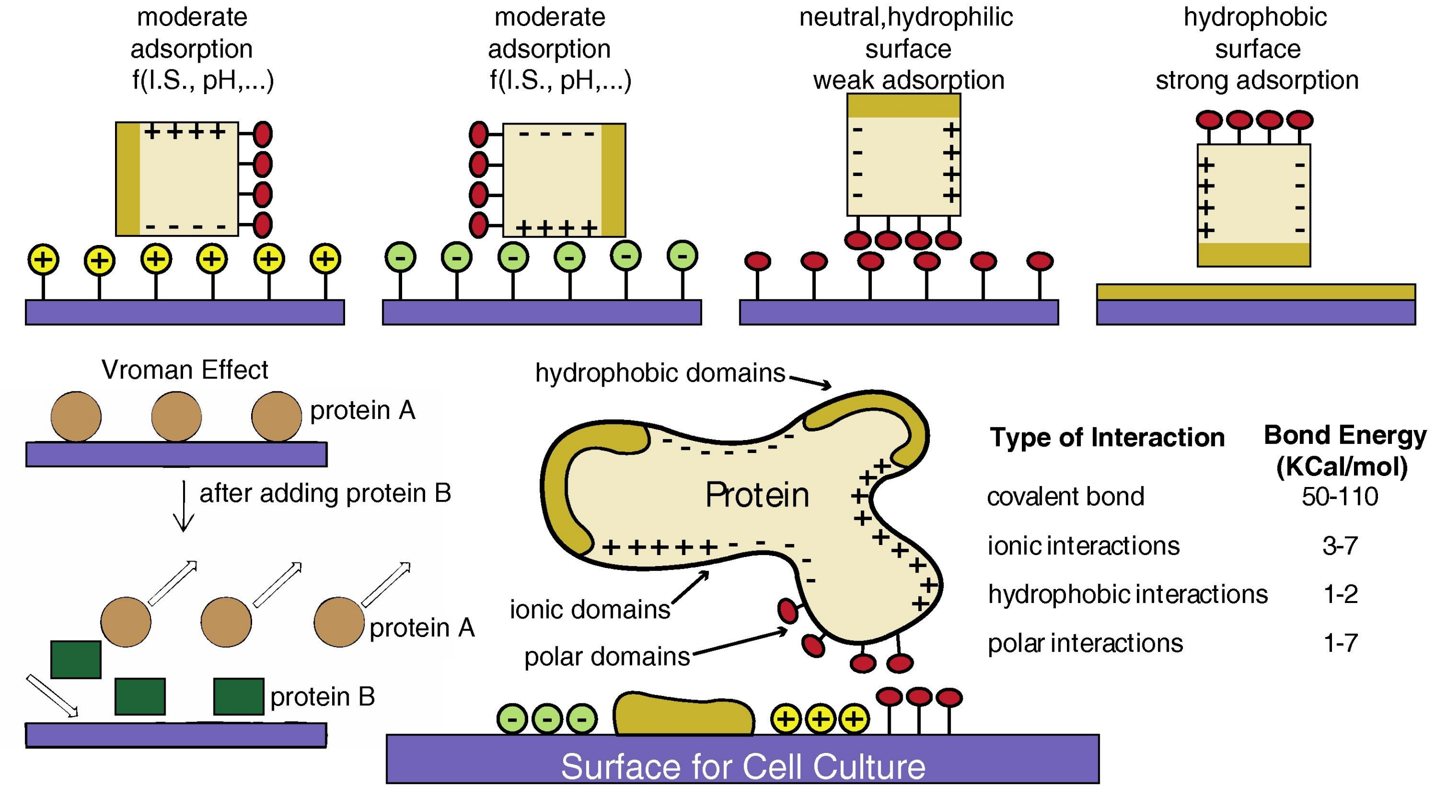
moderate adsorption f(I.S., pH,...)
moderate adsorption f(I.S., pH,...)
neutral,hydrophilic surface weak adsorption
hydrophobic surface strong adsorption
Vroman Effect
protein A
after adding protein B
protein A
protein B
hydrophobic domains
Protein
ionic domains
polar domains
Surface for Cell Culture

Type of Interaction	Bond Energy (KCal/mol)
covalent bond	50-110
ionic interactions	3-7
hydrophobic interactions	1-2
polar interactions	1-7

Figure 1.8: General mechanisms of protein-surface interactions. The ionic or charge-based interactions yield moderate adsorption and depend on the ionic state (I.S) and the pH of the surrounding buffer. The polar hydrophilic interactions yield weak adsorption. The hydrophobic interactions yield strong adsorption. The covalent interactions generate the strongest bond among all types of interactions. The Vroman effect describes that proteins with higher affinity to the surface can replace lower affinity proteins already adsorbed to the surface. Reproduced with permission from Ref. [101]. Copyright 2016 Elsevier.

on the ionic state (I.S.) and the pH of the surrounding buffer. Interactions between the protein and surface hydrophilic polar domains generate the weakest bonding energy (i.e., 1-7 kCal/mol), resulting in weak adsorption. In contrast, the hydrophobic domain interactions lead to stronger adsorption. Covalent interactions generate the strongest bonding energy (i.e., 50-110 kCal/mol). One way to introduce a covalent binding of protein-surface is by silanizing glass using (3-aminopropyl)triethoxysilane. In 2014, Masuda et al. reported that silanized glass stabilized coated fibronectin molecules [86]. The covalent binding was likely caused by amine groups (-NH_2) on the silanized glass surface interacting with the carboxylic acid (-COOH) of the ECM protein. Masuda et al. also reported that the silanized glass surface was more hydrophobic than the untreated glass. This treatment can also be applied to the surface of PDMS elastomer [6, 64, 78]. For PA, proteins and the surface can be covalently linked by incorporating aldehyde groups in the hydrogel precursor (-CHO) [105, 25]. Alternatively, sulfosuccinimidyl-6 (4'-azido-2'nitrophenylamino) hexanoate (sulfoSANPAH) can be used. It is a photoactivatable heterobifunctional reagent with a phenylazide group at one end that reacts with PA during the photoactivation process, and a sulfosuccinimidyl group (-NHS) that can bind the primary amine of proteins [67].

Micropatterning of matrix proteins to direct cell shape and architecture

It is well known that the interactions between cells and their extracellular matrix (ECM) are among the most vital processes determining cellular functions [42]. Among families of adhesion molecules, integrins are principal receptors in metazoan cells and can bind to almost all of ECM proteins [61].

ECM provides unique chemical and physical properties for each tissue. The uniqueness comes not only from the composition but also the density and organization of proteins. The distribution of chemical and mechanical cues within the ECM is vital in regulating cell shape, adhesion, migration, and proliferation.

Since its first invention more than 50 years ago, micropatterning has attracted widespread interest in maintaining control over cell adhesion and shape [26]. To date, there are several micropatterning methods of matrix proteins, and the most popular is microcontact printing [118]. Microcontact printing typically works by stamping pre-deposited matrix proteins onto the surface of a glass coverslip. A PDMS master made by etching is generally used as the stamp. Another method involves the cleavage of cell-repellent polymeric brushes by using deep-ultraviolet illumination. This method requires a photomask that is placed between the deep-ultraviolet light source and the polymer PEG-coated substrate. Recently, the need for photomasks has been eliminated by digital micromirror-based (DMD)-photolithography [116]. DMD is a spatial light modulator and can be used for protein printing. This method works by generating grayscale patterns of light and requires a well-collimated light source to reach micrometer resolution over the entire field of view. Current near-UV photodiodes can generally only provide a few mW/mm^2 of power. Thus, efficient patterning requires very sensitive grafting photochemistry. Compared to deep-ultraviolet illumination, this method uses a low dose of near-UV light to efficiently cleave polymeric brushes due to the presence of a photoinitiator.

Nanopatterning of matrix ligands to control receptor clustering

The ECM has a complex and very dynamic structure that is constantly being remodeled [42, 26]. It is technically high-demanding to obtain information on the spatial distribution of single binding sites between cells and ECM proteins. For greater specificity, peptides derived from ECM proteins containing cellular binding sites can be used instead of full-length ECM proteins. For example, RGD (arginine-glycine-aspartic acid) is known to be a recognition sequence for several different integrins [96, 61]. Furthermore, it is also possible to enhance selectivity of specific integrins by using peptidomimetic ligands [68].

Block copolymer method It is worth describing the block copolymer technology as it can be applied in surface nanopatterning. Block copolymers (BCPs) are polymers with two or more chemically distinct homogenous building blocks that are covalently bound together [9]. The simplest BCPs are linear A-b-B diblock copolymers. Block A and B represent two different homopolymers joined together *via* a covalent bond.

Bates and Fredrickson described three experimentally controllable parameters that cause microphase separation in block copolymers, leading to the formation of diverse morphologies. These include the total degree of polymerization (N), the volume fraction of block A (f_A), and the Flory-Huggins (A-B) interaction parameter of two blocks (χ) [9, 60]. The polymer stoichiometry influences the polymerization degree and the volume fraction of block A, whereas the choice of the A-B pair determines the Flory-Huggins parameter. χ represents the incompatibility between two blocks. Therefore the segregation product χN determines the degree of microseparation.

$$N = N_A + N_B \tag{1.20}$$

$$f_A = 1 + f_B \tag{1.21}$$

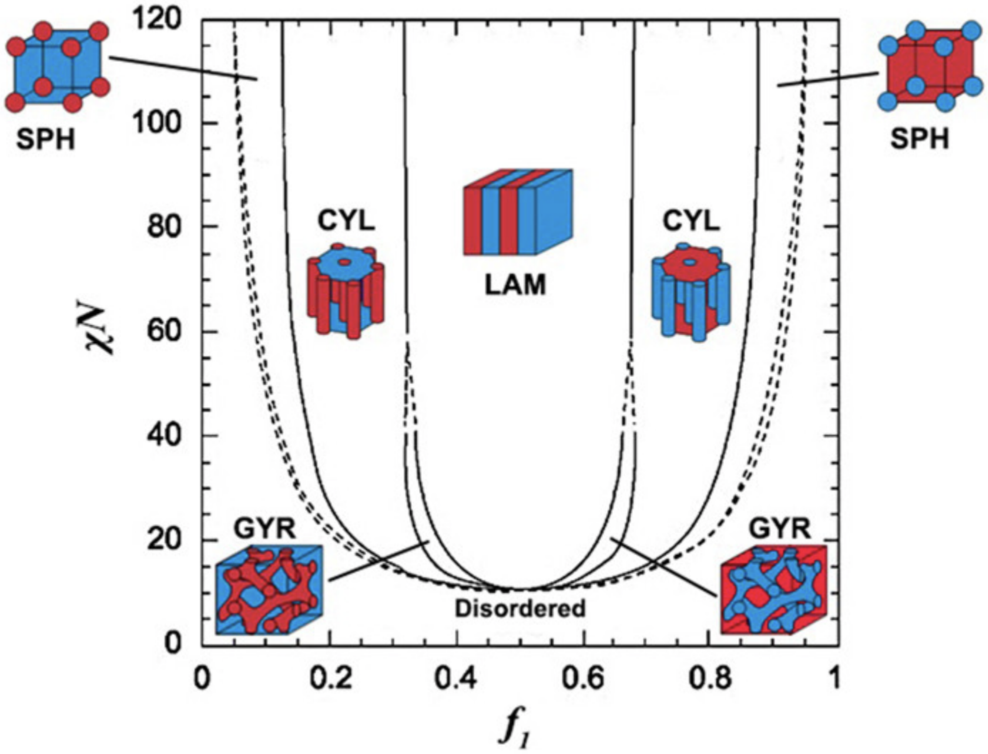

Figure 1.9: Mean-field phase diagram showing stable morphologies in diblock copolymer melts. χN represents the degree of microseparation, f_1 is the volume fraction of block A (the red block in the picture). SPH = sphere, CYL = cylinder, LAM = lamellae, GYR = gyroid. Reproduced with permission from Ref. [58]. Copyright 2006 Elsevier.

Figure 1.9 shows us that the minimum degree of microseparation to get a microphase formation of ordered equilibrium structures is 10.5. When χN exceeds 10.5 and depending on f_A, the BCP microphase separates and self-assembles into ordered morphologies, including spheres, cylinders, gyroids, and lamellae. The arrangement of an ordered morphology between the A-B pair can be theoretically inverted by swapping the ratio of A and B monomers at an identical χN. To achieve a small microphase like a nanometric sphere, one has to have a high χN, specifically high χ and low N.

Block copolymer micelle nanolithography Nanopatterning of regularly spaced gold dots on the glass surface can be achieved by using the block copolymer micelle nanolithography (BCMN) method [2]. To form micelles, block copolymers of polystyrene (PS) and poly-2-vinyl-pyridine (PVP) blocks dissolved in a non-polar solvent such as toluene have been widely used [48, 19, 20, 92]. Upon dissolving inside toluene, the polar PVP block aggregates in the center, forming the core of a micelle. In comparison, the non-polar PS block forms the surrounding shell. Then, depending on the application, the hydrophilic core can be loaded with various metals, alloys, or oxides [14, 48, 40]. The formation of micelles is only possible when the surfactant concentration is above the critical micelle concentration (CMC). Furthermore, the addition of inorganic materials will stabilize the micelles. For cell experiments, the use of gold metal typically generates the most interest mainly due to the low toxicity and its surface chemistry [48, 19, 20, 3, 92].

$$L = \frac{n[HAuCl_4]VP}{mVP} \tag{1.22}$$

Gold-loaded micelles are produced by adding tetrachloroauric(III)acid ($HAuCl_4$) as shown in Figure 1.10B according to the Equation 1.22. To produce gold nanopatterns on the glass surface, the gold-loaded micelles need to be transferred to the substrate. This can be done by using spin-coating or dip-coating techniques [48, 19, 20, 2]. Finally, the micellar polymer shells around particles are removed by using hydrogen plasma. The hydrogel plasma treatment also reduces the gold salts $HAuCl_4$ to elemental gold dots on the glass surface. The interparticle spacing of gold dots is dependent on the molecular weight of the block copolymer, the concentration of polymer solution, and the speed during spin-coating/dip-coating treatments. The size of a gold dot is highly dependent on the concentration of the gold salt $HAuCl_4$.

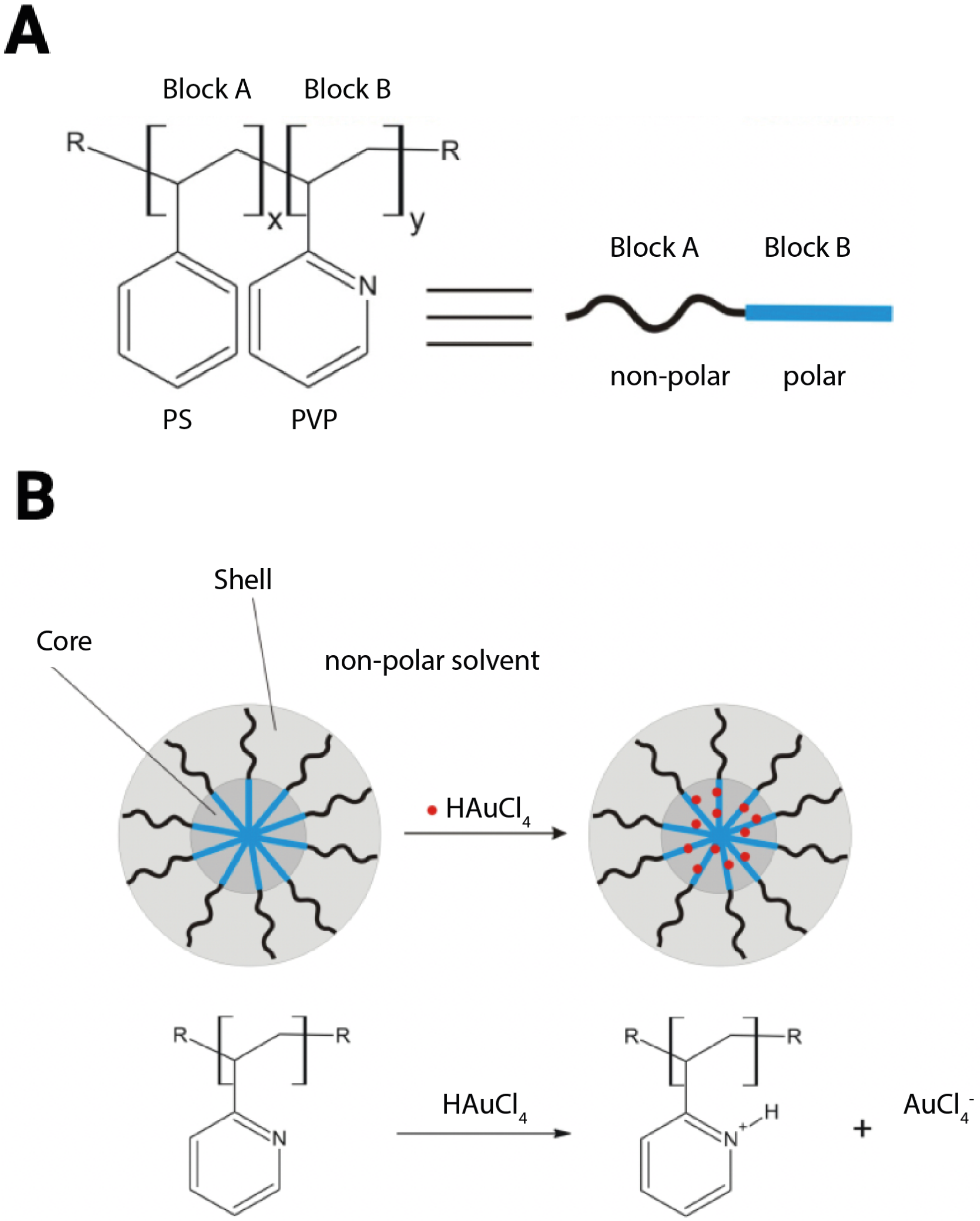
A
Block A
Block B
R
x
y
R
N
PS
PVP
Block A
Block B
non-polar
polar
B
Shell
Core
non-polar solvent
HAuCl4
R
R
N
HAuCl4
R
R
N+
H
+
AuCl4-

Figure 1.10: (**A**) Structural formula of polystyrene-b-poly(2-vinyl-pyridine) block copolymer. (**B**) Loading process of the gold salt $HAuCl_4$ to the core of the micelle [111].

1.3 Materials and methods

1.3.1 Pattern production for maskless photolithography

For maskless photolithography-based patterning of adhesive proteins or hydrogels, pattern files (i.e., 8-bit tiff) were prepared using an open source software (e.g., Inkscape or ImageJ). The canvas was set to 1824 x 1140 pixels to mirror the size of the Digital Micromirror Device (DMD). The background was set to black (i.e., grey level = 0) and desired patterns were set to white (i.e., grey level = 255). To control the size, patterns were designed by using the pixel ratio of the lens (1.4 μm/px, 0.28 μm/px, 0.14 μm/px for 4x, 20x, and 40x lenses respectively).

1.3.2 Surface micropatterning

Surface Micropatterning by UV-Ozone Cleaner

Surface patterns were prepared with the deep UV photomasking method [118]. Briefly, 15 mm round coverslips (Assistent, #41001115) were clean-wiped with 70% ethanol and activated in UVO cleaner (Jelight, #342-220) for 10 minutes. Then, the coverslips were incubated (1h, RT) in 50 μl of 100 μg/ml poly(L-lysine)-graft-poly(ethylene glycol) co-polymer (SuSoS, #PLL(20-g[3.5]-PEG(2)) in 10 mM HEPES pH 7.5. Next, coverslips were rinsed thoroughly with ddH$_2$O, dried, and placed on the chromium side of the photomask covering the light pass regions (Toppan Photomasks, custom made). Before placing coverslips on the photomask, the photomask was cleaned with isopropanol and acetone and was subsequently dried with an air gun. To ensure coverslips stick to the photomask and remain hydrated during the patterning process, 5 μl of ddH$_2$O was sandwiched between the glass and the chromium side of the photomask. Then, the photomask with coverslips was placed in the UVO cleaner with the glass side of the photomask facing the light source for 10 mins. After that, coverslips were gently detached from the photomask and rinsed. Finally, patterned coverslips were incubated with 1 μg/cm^2 fibronectin (Sigma, #F1141) and 1 μg/cm^2 fibrinogen conjugated with Alexa488 (Invitrogen, #F13191) in PBS for 1 h in RT. The patterned coverslips were rinsed and stored in PBS at RT.

Surface Micropatterning by maskless photolithography

Alternatively, micropatterned glass surfaces by the maskless photolithography were prepared as described [116]. Briefly, 15 mm round coverslips (Assistent, #41001115) were cleaned by oxygen plasma treatment (0.4 mbar, 200 W) in a plasma cleaner (TePla, #100-E) for 2 minutes. Then, coverslips were treated with 0.01% of poly-L-lysine solution (Sigma Aldrich, #P4832) for 30 minutes. Afterward, coverslips were rinsed and incubated with 5 mg of mPEG-SVA (Laysan Bio, #MPEG-SVA-5000) in 0.1 ml of 10 mM HEPES pH 8.5 for 1 hour. Coverslips were then gently rinsed, dried, and incubated with 3 μl of PLPP gel (Alveole, #PLPPgel) diluted in 60 μl of pure ethanol for 5 minutes. Then, coverslips were patterned with UV-A illumination ($\lambda = 375$ nm, 30 mJ/mm^2) using a widefield microscope (Nikon, Nikon Eclipse Ti2E) equipped with a patterning module (Alveole, Primo) and dedicated software (Alveole, Leonardo). Finally, patterned coverslips were rinsed and incubated with a mixture of 1 μg/cm^2 fibronectin and 1 μg/cm^2 fibrinogen conjugated with Alexa488 in PBS for 1 h in RT.

1.3.3 Surface nanopatterning

Preparation of BCMN solution

Table 1.1 shows diblock polymers used in this thesis. Block copolymers (Polymer Source) were dissolved in o-Xylene (5 mg/ml) and were stirred for 24 h at RT. An exception applied to polymer P4921-S2VP, which was dissolved in 2 mg/ml. Then, the gold salt ($HAuCl_4$; $M = 393.83$ gmol^{-1}) was added into the solution according to Equation 1.23 with the loading parameter ($L = 0.25$). Afterward, the metal precursor salt was further dissolved for another 24 h. The micellar solution was filtered using a polytetrafluoroethylene (PTFE) filter with a pore size of 0.22 μm (Milipore, Eschborn). The solutions were stored in the dark at RT.

$$m(HAuCl_4) = \frac{m(Polymer) \cdot M(HAuCl_4 \cdot 3H_2O) \cdot PVP_{units} \cdot L}{M(polymer)} \tag{1.23}$$

Table 1.1: The list of diblock copolymers used in this thesis.

Product ID	M_N (PS) (g/mol)	M_N (PVP) (g/mol)	PS_{units}	PVP_{units}
P4708-S2VP	16000	3500	154	33
P4705-S2VP	30000	12500	288	119
P4707-S2VP	52200	34000	501	323
P4921-S2VP	106000	75000	1018	713

Surface cleaning and activation

Coverslips (Carl Roth, #1.5 glass) were cleaned by using the piranha solution (i.e., 3:1 mixture of H_2SO_4 and H_2O_2). First, the 15 mm or 24 mm round coverslips were put inside a custom-made polytetrafluorethylene rack and placed in a crystalizing dish. The solution was prepared with a great care (i.e., use of safety polychloropren gloves, adding H_2O_2 to H_2SO_4 slowly, never in reversed order). The coverslips were put inside the piranha solution for 30 minutes and followed by rinsing with huge amount of water (i.e., 20 mililiters of water per 1 militer of the piranha solution) and then ultrasonication for 5 minutes. The activated coverslips were stored in ddH_2O at RT.

Gold nanopatterning on glass

The nanopattering was conducted by spin-coating 20 μl of BCMN solution on activated glass coverslips. PS4708-S2VP, PS4705-S2VP, PS4707-S2VP, and PS4921-S2VP were spin-coated at 3000-10000 rpm for 60 s (Laurell, #WS650 Mz-23M), respectively. Afterward, nanopatterned glass coverslips were treated with hydrogen plasma (150 W, 0.4 mbar) for 20 minutes.

SEM imaging of the nanopatterned glass surface

To validate the gold dots on the glass surface, SEM imaging of nanopatterned glass samples was conducted using a Zeiss Ultra 55 and a LEO 1530 field emission gun scanning electron microscope (Zeiss, Oberkochen, Germany) at around 5-6 mm working distance and 5 kV acceleration voltage. Signals were detected by the in-lens detector. The carbon-layer coating was deposited on the sample (7 nm) using a carbon coater to reach conductivity.

1.3.4 Preparation of micropatterned polyacrylamide substrate for traction force microscopy

Preparation of methacrylated glass surfaces

Methacrylated glass surfaces were prepared as described [92]. Briefly 24 mm round coverslips (Assistent, #41001124) were prepared by 15 minutes incubation in a solution of acetic acid (Honeywell #33209), 3-(Trimethoxysilyl) propyl methacrylate (Sigma Aldrich #440159), and 96% of ethanol with the ratio of 1:1:14, respectively. The coverslips were rinsed thrice with pure ethanol (Carl Roth #9065.3) and dried with the air gun. Methacrylated glass surfaces were kept in the dark at RT for up to 1 month before use.

Preparation of oxidized HEA

Oxidized HEA solution was prepared as described [105]. Briefly, 50 mg/ml of N-Hydroxyethyl Acrylamide (Aldrich #697931) and 20 mM sodium (meta)periodate (Sigma-Aldrich #S1878) were mixed in ddH$_2$O and stirred for 4 hours in dark at RT before use.

Production of ECM coated PA

For TFM experiments, the dual-layer PA was implemented as the substrate. It consists of two layers where the lower layer provides a separation layer between cells and the glass, whereas the thin upper layer close to the cell surface is loaded with a high density of beads. The lower layer solution was produced by mixing 99.3 μl of stock solution (Table 1.2), 0.5 μl of 10% m/v APS (Sigma, #A3678), and 0.2 μl TEMED (Thermo Scientific, #17919). For the upper layer, the mixture was 93.3 μl of stock solution, 1 μl of oxidized HEA solution, 5 μl of 200 nm beads (Invitrogen, #F8805/ #F8848/ #F8810/ #F8807), 0.5 μl of 10% m/v APS, and 0.2 μl TEMED. APS 10% and TEMED were always added at the last step. The hydrogel substrate was prepared by placing 5 μl of the lower layer solution on top of the 24 mm round methacrylated glass, covered with a 15 mm round coverslip, and kept at RT for 30-45 minutes to polymerize. Then, the 15 mm coverslip was detached by using a scalpel. Next, 5 μl of upper layer solution was directly placed on the lower layer, covered with the 15 mm ECM-patterned round coverslip (Section 1.3.2), and also kept at RT for 30-45 minutes to polymerize. Finally, the top coverslip was detached and the substrate was glued on the bottom of a custom-drilled 6 well-plate with dental glue (Picodent, #1300 100).

Table 1.2: PA stock solution composition used in this thesis. A = Acrylamide, B = Bisacrylamide.

A (%)	**B (%)**	**40% A (ml)**	**2% B (ml)**	**ddH_2O (ml)**
4	0.03	1	0.15	8.85
4	0.1	1	0.5	8.5
4	0.3	1	1.5	7.5
4	0.5	1	2.5	6.5
5	0.03	1.25	0.15	8.6
5	0.1	1.25	0.5	8.25
10	0.02	2.5	0.1	7.4
10	0.04	2.5	0.2	7.3
10	0.06	2.5	0.3	7.2
10	0.08	2.5	0.4	7.1
10	0.1	2.5	0.5	7
10	0.2	2.5	1	6.5
10	0.3	2.5	1.5	6
10	0.4	2.5	2	5.5
10	0.5	2.5	2.5	5
20	0.02	5	0.1	4.9
20	0.04	5	0.2	4.8
20	0.06	5	0.3	4.7
20	0.08	5	0.4	4.6

1.3.5 Preparation of nanopatterned polyacrylamide substrate for traction force microscopy

Preparation of transfer solution and activation of nanopatterned glass substrate

Preparation of the gold nanoparticle (AuNP) decorated PA was conducted as described with a slight modification [92]. Briefly, 2 μM BAC (Alfa Aesar, #44132) and 5 μM $NaBH_4$ (Sigma Aldrich, #452882) were mixed in ethanol. The solution was stirred overnight in dark at RT before use. The nanopatterned glass coverslips were activated with the hydrogen plasma (0.4 mbar, 150 W) in a plasma cleaner (TePla, #100-E) for 20 minutes. Next, the activated glass coverslips were incubated in the transfer solution for 2 hours in the dark at RT. Finally, the glass coverslips were carefully rinsed with ethanol and ddH_2O and stored in ddH_2O at RT.

Direct transfer of nanopattern from glass to hydrogel

Dual-layer PA was used as the elastic substrate for TFM. The lower layer solution was produced by mixing 99.3 μl of stock solution (Table 1.2), 0.5 μl of 10% m/v APS (Sigma, #A3678), and 0.2 μl TEMED (Thermo Scientific, #17919). For the upper layer, the mixture was 94.3 μl of stock solution, 5 μl of 200 nm beads (Invitrogen, #F8805/ #F8848/ #F8810/ #F8807), 0.5 μl of 10% m/v APS, and 0.2 μl TEMED. APS 10% and TEMED were always added at the last step. The substrate was prepared by placing 5 μl of the lower layer solution on top of 24 mm round methacrylated glass, covered with a 15 mm round coverslip, and kept at RT for 30-45 minutes to polymerize. Then, the 15 mm coverslip was detached by using a scalpel. Next, 5 μl upper layer solution is directly placed on top of the lower layer, covered with the 15 mm nanopatterned glass that had been activated (Section 1.3.3), and also kept at RT for 30-45 minutes to polymerize. The nanopattern transfer process was further extended by incubating the substrate inside PBS for 3 days at 37 degrees Celsius. Exposure to PBS for extended periods of time causes the top coverslip to detach by itself. If the top coverslip remains attached, carefully detach it with a scalpel.

Functionalisation of nanopatterned PA

Briefly, the AuNP decorated PA was incubated with 25 μM of cRGD-thiol (cyclo(Arg-Gly-Asp-D-Phe-Lys(Ahx Mercaptopropionic Acid)) (#PCS-31062-PI, Peptide International) for 4h at RT. Next, the hydrogel was rinsed thrice with PBS and stored in PBS at RT.

Cryo-SEM imaging of nanopatterned PA

Production of thick PA For the easier handling during the cryo-SEM imaging, a thick AuNP decorated PA hydrogel (i.e., 2 mm) was prepared. A thicker PA is easier to cut to the correct shape for the liquid nitrogen-cooled stage size. To prepare a 20 mm diameter and 2 mm thick PA hydrogel, 645.45 μl, 3.25 μl, 1.3 μl of the stock solution (Table 1.2), APS 10%, and TEMED respectively were mixed. Then, 650 μl of the mixture solution was placed dropwise into the groove (depth = 2 mm, diameter = 20 mm) of a custom-made polytetrafluorethylene slab. Then, a nanopatterned coverslip (activated, 24 mm diameter) with the gold surface facing down was placed on top of the droplet. The gelation process was carried out for 45 minutes at RT followed by additional 72 hours incubation (in PBS, 37 degrees Celsius). Exposure to PBS for extended periods of time stimulates detachment of the top coverslip. The thick hydrogel was carefully removed from the groove and stored in PBS at RT.

Imaging of thick nanopatterned PA Prior to the nitrogen-cooling, the thick AuNP decorated PA hydrogel was cut into into the size of 18 mm in length and 6 mm in width using a clean scalpel. The specimen was carefully placed on the liquid nitrogen-cooled stage and followed by the vitrification process in which the sample was immersed in the liquid nitrogen. Then, the hydrogel specimen was transferred to the BAL-TECH MED 020 (BAL-TEC AG, Balzers, Liechenstein) preparation device *via* an evacuated liquid nitrogen-cooled shuttle BAL-TECH VLC 100 (BAL-TEC AG, Balzers, Liechenstein). The hydrogel specimen was fractured in the 10^{-5}-10^{-6} mbar vaccum chamber at -160 degrees Celsius. Then, the sample was heated slowly to -90 degrees Celsius and kept in the vacuum for 30-45 minutes to allow sublimation of water on the interface and to carbon coat the sample. The sample was immediately transferred to the SEM chamber *via* the evacuated liquid nitrogen-cooled shuttle. The imaging of nanopatterned PA specimen was conducted under a low temperature condition (-130 degrees Celsius) using a Zeiss Ultra 55 field emission SEM (Zeiss, Oberkochen, Germany) at around 2.5-3 mm working distance and 2-3 kV acceleration voltage. Signals were detected by the in-lens detector.

1.3.6 Preparation of micropatterned high-refractive index silicon elastomer for traction force microscopy

Production of high-refractive index silicon elastomer

Glass coverslips (Carl Roth, #0 glass, 24 mm round) were cleaned with the piranha solution (see Section 1.3.3 Surface cleaning and activation). Part A and part B of QGel920 were mixed according the ratio given in Table 1.6 and were degassed for 10 minutes to eliminate air bubbles. 100 μl of mixture was deposited on the cleaned glass and spin-coated at 5000 rpm for 10 s followed by curing at 70 degrees Celsius overnight.

Covalent attachment of fluorescent beads to the surface of the elastomer

The attachment solution was prepared by mixing 0.1 mg/ml EDC and 1 % v/v carboxylated fluorescent beads (Invitrogen, #F8805/ #F8848/ #F8810/ #F8807) in ddH$_2$O. The surface elastomer was cleaned using the oxygen plasma (100 W, 0.4 mbar) for 20 s. Then, the surface of the elastomer was conjugated with 10 % v/v of 3-aminopropyl trimethoxysilane in ethanol for 5 minutes followed by rinsing with ethanol once and twice with ddH$_2$O. The attachment solution was placed on the surface of the elastomer and was incubated for 30 minutes. Finally, the elastomer was rinsed twice with ddH$_2$O and stored in ddH$_2$O at RT.

Maskless photolithography on the surface of elastomer

To perform micropatterning on the surface of QGel920 elastomer, the surface was cleaned using the oxygen plasma (100 W, 0.4 mbar) for 20 s followed by conjugating 0.01% of poly-L-lysine solution (Sigma Aldrich, #P4832) on the surface for 30 minutes. Afterward, the surface was rinsed with 10 mM HEPES pH 8.5 and incubated with a freshly prepared solution of 5 mg of mPEG-SVA (Laysan Bio, #MPEG-SVA-5000) in 0.1 ml of 10 mM HEPES pH 8.5 for 30 minutes. Next, the elastomer was placed on a custom-made bottom hole petri dish (35 mm) followed by depositing 3 μl of PLPP gel (Alveole) + 1.85 μl of the surfactant mix (Alveole) in the center area of the surface. Next, 30 μl ethanol was added on top of the droplet and was carefully distributed by manual tilt and rotation of the petri dish. The gel was left to polymerize on the surface for 5 minutes at RT. Then, the surface was patterned with UV-A illumination (λ = 375 nm, 30 mJ/mm^2) using a widefield microscope (Nikon, Nikon Eclipse Ti2E) equipped with a patterning module (Alveole, Primo) and a dedicated software (Alveole, Leonardo). Finally, the patterned coverslip was rinsed and incubated with a mixture of 1 μg/cm^2 fibronectin and 1 μg/cm^2 fibrinogen conjugated with Alexa488 in PBS for 30 minutes at RT.

1.3.7 Sample preparation for 3D-traction force microscopy

MCF10A cells were allowed to grow and form spheroids inside ultra-low attachment well plates (Corning, #3473) for several days. Next, spheroids were harvested, spun-down, and suspended in a solution of 10 % w/v GelMa (Sigma Aldrich, #CC323-3) in PBS containing 0.5 mg/ml of a photoinitiator Irgacure 2959 (Sigma Aldrich, #410896) and 1 % v/v fluorescent beads (1 μm in diameter). Then, 200 μl of the solution was placed inside a groove (13 mm diameter, 1 mm depth) of a custom teflon mold covered with a 24 mm methacrylated glass coverslip (see Section 1.3.4). Crosslinking with UV-A (λ = 365 nm, I = 2.23 mW/cm^2) occured for 3 minutes (Vilber, Bio-Link 365 and T-8.L).

1.3.8 Local ultraviolet illumination traction force microscopy

Substrates with seeded cells were placed on an epifluorescence microscope (Nikon, #Eclipse Ti2) equipped with a custom-made incubation chamber (EMBLEM), an sCMOS camera (Hamamatsu, #C11440 - 42U30), a patterning module (Alveole, #PRIMO), and a dedicated software (Alveole, #Leonardo). An image of the marker beads in the undeformed state was acquired after illuminating cells with 6000 mJ/mm^2 of UV-A laser through a 20x air objective NA = 0.45 (Nikon, #MRH08230). Bead images were then drift corrected with respect to the image acquired after UV illumination using the StackReg plugin on ImageJ (P. Thévenaz, Swiss Federal Institute of Technology Lausanne). Drift-corrected images were then processed with particle image velocimetry to create a regular field of displacement vector with grid spacing of 10.5 μm. Displacement vectors were interpolated with cubic splines. Traction stresses were reconstructed using regularized Fourier Transform Traction Cytometry [103] with a regularization parameter acquired by Generalized Cross Validation [50].

1.3.9 Measurement and calculation of the Young's modulus by nanoindentation experiments

The mechanical properties of the substrate were measured by indentation experiments. The substrate was indented 2 μm with a cantilever (stiffness = 0.24 N/m) tipped with a spherical glass bead (radius = 21.5 μm). The Young's modulus was calculated with the Hertz model and by taking the slope of the load-displacement curve (5 - 20% of the load peak (P_{max})). The dissipation factor (tan δ) was acquired by the ratio between the loss and the storage modulus. It was measured by the dynamic mechanical analysis, which means indenting the substrate with the frequency of 5-10 Hz and the amplitude of 300 nm.

1.3.10 Cell Culture

Mouse embryonic fibroblast Mouse embryonic fibroblasts (MEFs) were purchased from ATCC (ATCC, #CRL-2991) and were cultured in DMEM (Thermo Fisher, #41965) supplemented with 10 % FBS South

America Origin (Biowest, #S181T) and 1 % penicillin streptomycin (Gibco, #15140-122).

HeLa HeLa cells were purchased from ATCC (ATCC,#CCL-2) and cultured in DMEM (Thermo Fisher, #41965) supplemented with 10 % FBS (Sigma Aldrich, #F7524) and 1 % penicillin streptomycin.

All cells were cultured inside an incubation chamber at 37 degrees Celsius, 5 % CO_2, and 95 % RH. For all experiments, cells were rinsed with PBS, trypsinized with 0.05 % trypsin, resuspended in media with serum, and seeded on substrates. All cells tested negative for the mycoplasma contamination.

1.3.11 Immunostaining

For staining, cells were washed once with PBS followed by the fixation using 4 % PFA for 10 minutes. Next, cells were washed with 0.1 % v/v Triton X-100 in PBS (3 x 5 mins). Afterward, cells were treated with 1 % m/v BSA in PBS for 1 h at RT. Cells were then washed with PBS followed by the incubation with the primary antibodies diluted in 1 % m/v BSA in PBS for 1 h at RT. Afterward, cells were washed again with 0.1 % v/v Triton X-100 in PBS (3 x 5 mins). Cells were washed with PBS followed by incubation with the secondary antibodies diluted in 1 % m/v BSA in PBS for 1 h at RT or overnight at 4 degrees Celsius. Finally, cells were washed with PBS. Each coverslip was mounted on a microscopy glass slide by using Mowiol and let dry at RT overnight.

1.3.12 Statistical analysis

Prism 9 for macOS (i.e., Version 9.0.0) was used for statistical analysis. Ordinary one-way ANOVA was utilized for comparing multiple cases. Meanwhile, parametric unpaired t-tests (two-tailed) was used for comparing two cases. The data distribution was assumed to follow the Gaussian distribution and equal standard deviations. **** $P < 0.0001$, *** $P < 0.001$, ** $P < 0.01$, * $P < 0.05$, ns $P \leq 0.5$.

1.4 Results and Discussion

1.4.1 Mechanical characterization of elastic/viscoelastic substrates

I started with the mechanical characterization of the substrate, including the stiffness and the viscosity. In this work, I used elastic polyacrylamide (PA) and viscoelastic polydimethylsiloxane (PDMS) as substrates. Subsequently, I coated the substrate with matrix proteins, mainly fibronectin. As I focused on cellular interaction between the cell and the matrix protein, the term matrix stiffness/matrix rigidity refers to the stiffness of the underlying substrate.

As a substrate, PA provided features such as affordable, easy in handling, and high flexibility in tuning the stiffness. In comparison, PDMS QGel920 provided an important feature such as a glass-matching refractive index. Thus, PDMS can be used to increase the imaging quality of proteins on the cell-matrix interface using surface-based microscopy like TIRF when coated on soft substrates.

Mechanical characterization of PA substrates

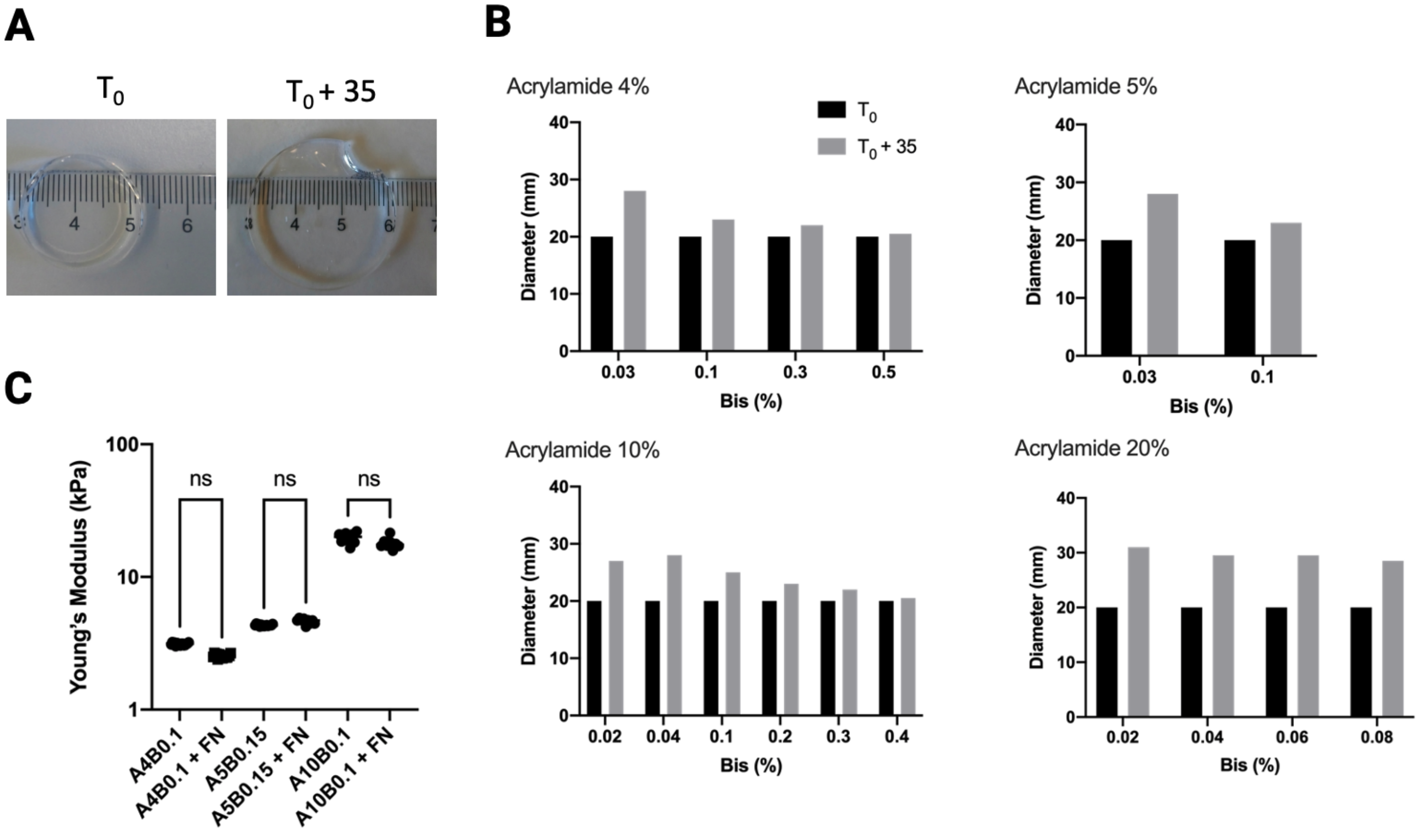

Figure 1.11: (**A**) Images showing the initial diameter of PA (i.e., Acrylamide = 10 % Bisacrylamide = 0.1 %) compared to the diameter after 35 days inside PBS. (**B**) The swelling of PA with different monomer concentration. (**C**) The functionalisation of 1 μg/cm^2 FN did not increase the stiffness of PA. n from left to right = 16, 16, 16, 10, 16, 10. The stiffness of PA was measured with nanoindentation experiments using a fiber optic probe (stiffness = 0.24 N/m, radius = 21.5 μm). Bars show mean ± S.E.M (two-tailed t-tests, **** $P < 0.0001$, *** $P < 0.001$, ** $P < 0.01$, * $P < 0.05$, ns $P \leq 0.5$). **Please click here to view a full size version of this figure.**

For the PA substrates, in all mixtures I used only a low percentage of cross-linker concentration (i.e., below 1 %) as it has been reported that high-cross linker concentrations (i.e., above 5 %) lead to a transition in the structure from an ideal to a clustered PA gel [34]. As they were all ideal hydrogels, I assumed all tetrafunctional Bisacrylamide molecules were connected to four of the nearest neighboring Acrylamide groups and therefore exhibited maximal elasticity.

Softer hydrogels swell more than stiffer hydrogels The result of the mechanical characterization of PA substrate is shown in Figure 1.11. The initial verification was carried out with the swelling experiment. A thick PA hydrogels (i.e., diameter = 20 mm, thickness = 2mm) were made and kept in PBS for 35 days. Figure 1.11A shows that the swelling was observed on a PA hydrogel produced with 10 Acrylamide and 0.1 % Bisacrylamide (A10B0.1). In Figure 1.11B, I investigated the swelling of PA hydrogels produced with different Acrylamide and Bisacrylamide concentrations. The results strongly show that the more the crosslinker (Bisacrylamide) concentration in PA hydrogel, the less ability of PA to swell or to absorb water.

The larger the gel can swell correlates inversely to the stiffness of the gel, as can be seen from Table 1.4 and Table 1.5. From Table 1.4, A10B0.1 and A10B0.4 hydrogels exhibited swelling ratios (Q) of 15.39 and 9.47 after being submerged for 120 hours inside PBS. By using nanoindentation experiments (Table 1.4), A10B0.1 and A10B0.4 hydrogels exhibited Young's moduli (E) of 8.43 and 16.28 kPa. Therefore, hydrogels with higher Q are typically softer.

I argue that the lower the crosslinker concentration, the larger the linear distance between adjacent crosslinks or mesh size could be expanded. It could not be too low either; otherwise, no polymerization could occur. A hydrogel with a larger mesh size would accommodate more water inside it. Thus, PA with less Bisacrylamide concentration expanded more. In 2016, Bhadani and Kumar also reported that swellability of PA decreases with the increasing concentration of crosslinker [10].

PA hydrogels are highly elastic From the nanoindentation experiments, the majority of PA substrates produced with varied concentrations of Acrylamide and Bisacrylamide (except A5B0.03) had low dissipation factors (tan δ) as shown in Table 1.5 and Figure 1.12. High dissipation factor value (i.e. high viscosity) on A5B0.03 PA hydrogel might occur due to high water content inside the hydrogel (i.e., A5B0.03 had 86 % water). Water is known to be a standard reference substance for viscosity [69]. This result indicates that an extremely soft hydrogels (i.e., A5B0.03 = 0.02 kPa) behave as a viscoelastic material.

Table 1.3: The swelling experiment of thick PA. w_b = the weight of the freshly made thick PA. w_a = the weight of the dehydrated PA after 120 h. Q = Swelling ratio.

A (%)	**B (%)**	w_b **(mg)**	w_a **(mg)**	Q
10	0.1	634	80.2	7.91
10	0.2	639	81.8	7.81
10	0.4	635	84.25	7.53

Table 1.4: The swelling experiment of thick PA after 120 hours inside PBS. w_{b2} = the weight of thick PA after 2 weeks in PBS. w_a = the weight of the dehydrated PA after 120 hours. Q = Swelling ratio.

A (%)	**B (%)**	w_{b2} **(mg)**	w_a **(mg)**	Q
10	0.1	1237	80.4	15.39
10	0.2	1022	81.91	12.48
10	0.4	798	84.3	9.47

PA hydrogels need to be freshly prepared before experiments Concerning the preparation of PA substrates, my goal was to determine whether it might be necessary to prepare samples just before conducting the cell experiments, or if hydrogels would be stable even after several days. To answer this, I prepared pair of thick PA hydrogels. For one hydrogel, I measured its mass, let it dehydrate for 120 hours at 37 degrees Celsius, and measured its mass again in the dried form. For the other hydrogel, I measured its mass, incubated it inside PBS for two weeks, let it dehydrate for 120 hours at 37 degrees Celsius, and measured its mass again in the dried form. For the PA hydrogel produced by 10 % Acrylamide and 0.1 % Bisacrylamide, the dry PA after 120 hours of the dehydration step weighted 80.2 mg from its initial weight 634 mg. By using Equation 1.24 [56], the swelling ratio (Q) of this hydrogel was 7.91. By increasing the crosslinker to 0.2 and 0.4 %, the swelling ratios of these gels decreased to 7.81 and 7.53, as shown in Table 1.3. As mentioned previously, I observed that the higher the crosslinker concentration, the less the swelling ratio. Furthermore, I investigated the ability of the hydrogel to store water after being inside water for an extended time. For the PA hydrogel produced by 10 % Acrylamide and 0.1 % Bisacrylamide, the PA hydrogel weighted 1237 mg after 2 weeks inside water. After 120 hours of the dehydration step, the dry PA weighted 80.4 mg, and the swelling ratio of this hydrogel was 15.39. For 0.2 and 0.4 % crosslinker concentration, the swelling ratios decreased to 12.48 and 9.47, as shown in Table 1.4. As mentioned before, I observed that the higher the crosslinker concentration, the more water the hydrogel could absorb. It means the soft hydrogels can hold more water and therefore become even softer after being submerged inside water for an extended period of time. Hereinafter, I always prepared fresh PA for the experiments.

$$Q = \frac{V_{fresh}}{V_{dried}} = \frac{\frac{w_{fresh}}{\rho}}{\frac{w_{dried}}{\rho}} \tag{1.24}$$

Fibronectin coating do not change the stiffness of the PA surface As shown in Figure 1.11C, Young's moduli of PA substrates coated with fibronectin (1 μg/cm^2) were not significantly different from the plain PA substrates. PA hydrogels were produced with A4B0.1 (4 % Acrylamide and 0.1 % Bisacrylamide), A5B0.15, and A10B0.1. As I used 500 kDa fibronectin with 1 μg/cm^2 for the coating, I argue that it might add several nanometers in thickness. In comparison, during nanoindentation experiments to measure rigidity, a several micrometers spherical probe typically indented 1-2 micrometers to acquire a force-displacement curve. The possible difference probably could not be resolved with this type of measurement.

Table 1.5: The mechanical characterization of PA surface with the nanoindentation experiments (k = 0.2 N/m, r = 54 μm). A = Acrylamide, B = Bisacrylamide, E_1 = Young's modulus (before UV exposure), tan δ_1 = dissipation factor before UV exposure, E_2 = Young's modulus (after UV exposure), tan δ_2 = dissipation factor after UV exposure.

A (%)	**B (%)**	**E_1 (kPa)**	**tan δ_1 (5 Hz)**	**E_2 (kPa)**	**tan δ_2 (5 Hz)**
4	0.03	unresolvable			
4	0.1	1.72 ± 0.083	0.118 ± 0.008	1.85 ± 0.071	0.114 ± 0.006
4	0.3	4.32 ± 0.241	0.094 ± 0.007	6.47 ± 0.484	0.107 ± 0.006
4	0.5	2.56 ± 0.229	0.127 ± 0.004	2.27 ± 0.199	0.173 ± 0.027
5	0.03	0.02 ± 0.001	1.113 ± 0.018	0.02 ± 0.002	0.861 ± 0.071
5	0.1	3.27 ± 0.06	0.057 ± 0.002	3.06 ± 0.052	0.059 ± 0.003
10	0.02	2.26 ± 0.058	0.091 ± 0.002	2.24 ± 0.078	0.091 ± 0.005
10	0.04	2.93 ± 0.058	0.092 ± 0.002	3.21 ± 0.099	0.091 ± 0.004
10	0.06	5.29 ± 0.162	0.076 ± 0.002	6.28 ± 0.188	0.068 ± 0.006
10	0.08	8.36 ± 0.126	0.061 ± 0.006	7.33 ± 0.291	0.065 ± 0.004
10	0.1	8.43 ± 0.158	0.071 ± 0.006	8.75 ± 0.148	0.061 ± 0.006
10	0.2	12.03 ± 0.402	0.074 ± 0.005	11.31 ± 0.781	0.073 ± 0.007
10	0.3	15.01 ± 0.739	0.088 ± 0.003	13.84 ± 0.415	0.083 ± 0.006
10	0.4	16.28 ± 0.615	0.091 ± 0.007	15.88 ± 1.549	0.103 ± 0.022
10	0.5	22.11 ± 0.721	0.156 ± 0.006	22.79 ± 1.384	0.181 ± 0.024
20	0.02	7.56 ± 0.511	0.105 ± 0.008	5.85 ± 0.481	0.094 ± 0.021
20	0.04	9.31 ± 0.578	0.104 ± 0.006	8.62 ± 0.512	0.102 ± 0.011
20	0.06	12.58 ± 0.164	0.097 ± 0.002	11.29 ± 0.817	0.082 ± 0.004
20	0.08	12.38 ± 0.342	0.104 ± 0.004	11.31 ± 0.955	0.084 ± 0.007

Fibronectin coating do not change the stiffness of the PA surface Mechanical properties of PA hydrogels can be assesed with several methods including the swelling experiments, rheometry, and indentation using biophysical tools like AFM.

Treatment with a high dose UV light did not influence the stiffness of PA

As I planned to use light to replace trypsin to release cellular tractions, I had to be sure that the illumination of high dose UV light would not alter the mechanical properties on the surface of PA. Exposing PA substrates to deep UV (UVC) for 5 minutes did not change the stiffness, as shown in Figure 1.12 and Table 1.5. Exposing PA substrates to deep UV (UVC) was the easiest UV illumination test since I could try with many samples at once, and it represented a high energetic UV compared to the near UV (UVA) light source on the microscope. If the mechanical properties of PA substrates are not altered by the high energetic deep UV light, I assumed that the mechanical properties of PA substrates are not altered by the near UV light either.

For the softest PA produced by 5 % Acrylamide and 0.03 % Bisacrylamide, the heat caused by the long exposure might destabilize the weak crosslinking causing a significant difference in the dissipation factors [22] (Figure 1.12). As I did not measure how much heat was transferred into the gel, I could not be sure whether this altered the gel permanently or just temporarily. In comparison, all PA hydrogels produced using higher crosslinker concentrations did not show a significant difference in Young's modulus

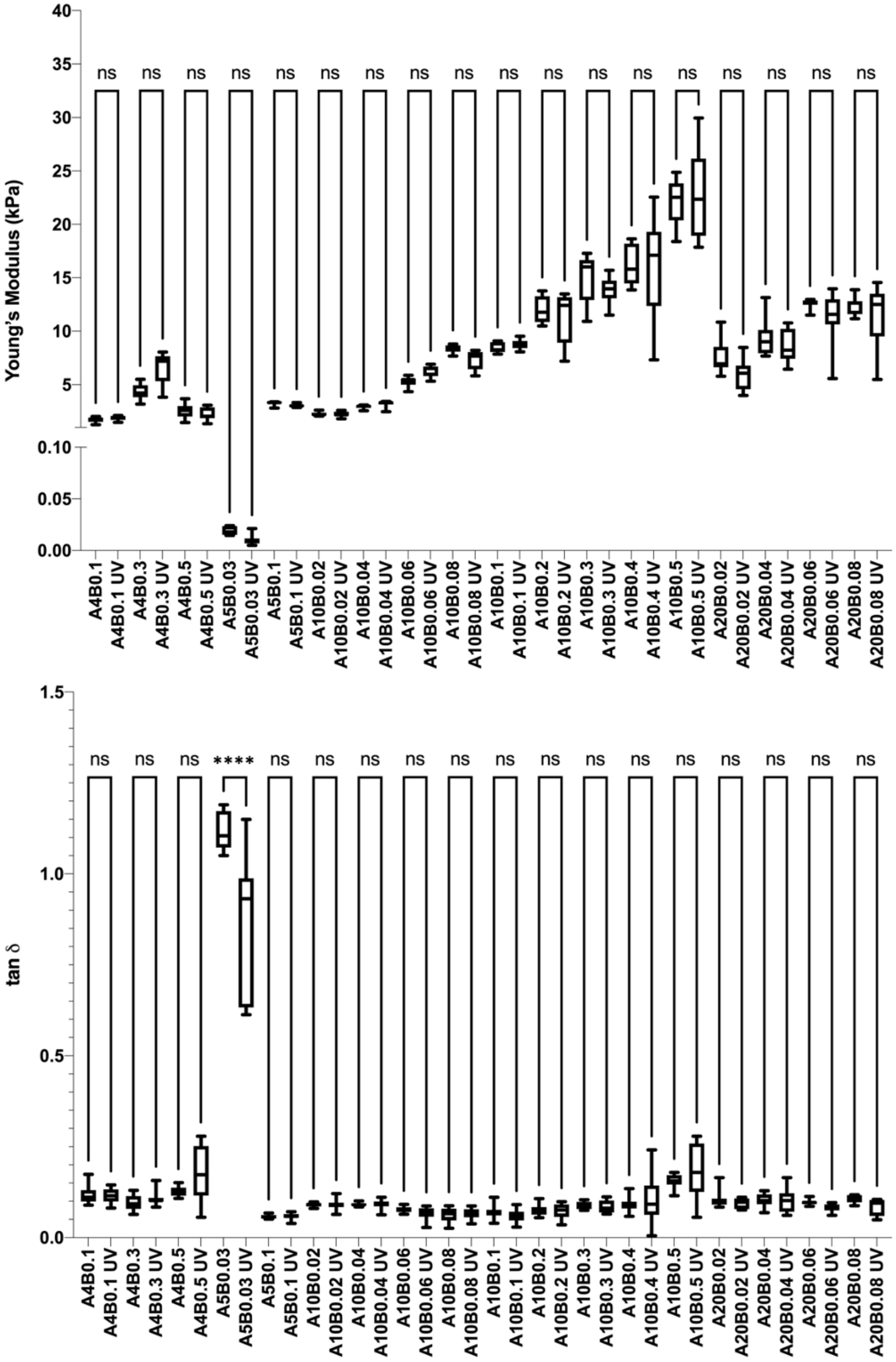

Figure 1.12: Box and whiskers plots (10-90 percentile) showing Young's modulus and dissipation factors of PA prepared using various Acrylamide and Bisacrylamide contents. n= 10 for each condition. The statistical analysis was done using the ordinary one-way ANOVA, **** $P < 0.0001$, *** $P < 0.001$, ** $P < 0.01$, * $P < 0.05$, ns $P \leq 0.5$.). **Please click here to view a full size version of this figure.**

and dissipation factors, as shown in Figure 1.12. I argue that heat caused by the exposure induced a negligible effect on gels with more stable crosslinking as more crosslinker means less water in the mixture. Exposing PA to near UV (UVA) with the dose of 6000 mJ/mm^2 did not alter the stiffness of the PA surface either as shown in Figure 1.13. In general, I argue that it is less likely I will see a significant alteration because I did not use a photoinitiator to create free radicals for the PA polymerization. Even if I used it, the remaining free radicals would be insignificant as soon as the Bisacrylamide molecules crosslink all Acrylamide molecules. Furthermore, they would likely be away as I still had 3 washing steps after the gel polymerization step. The heat caused by a long deep UV exposure might be influential to the really soft PA hydrogels (e.g., 0.03 % Bisacrylamide). To degrade PA, one needs to treat it at 175-300 degrees Celsius, which would be impossible to achieve with several milliwatts of UV laser illumination on a microscopy setup.

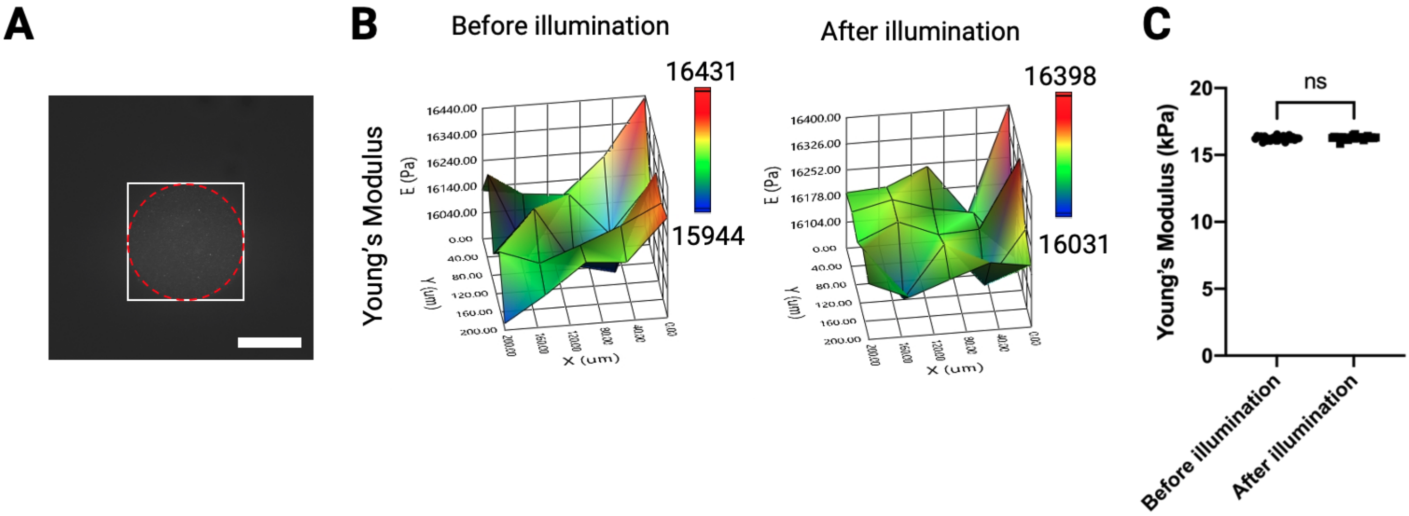

Figure 1.13: (**A**) Micrograph showing the projection of a 200 μm circle-shaped pattern on the surface of A10B0.1 PA (red-dashed line). The white square line shows the indentation area. Scale bar = 100 μm. (**B**) 3D maps of the Young's modulus before and after near UV (UVA) light illumination. The measurements were carried out using a spherical-probe with stiffness = 0.43 N/m and radius = 54 μm. (**C**) Young's modulus of the PA surface before and after illumination is non-significantly different. n of each condition = 25. (two-tailed t-tests, **** $P < 0.0001$, *** $P < 0.001$, ** $P < 0.01$, * $P < 0.05$, ns $P \leq 0.5$). **Please click here to view a full size version of this figure.**

Mechanical characterization of QGel920 substrate

I was also interested in exploiting viscoelastic substrates to study cell-ECM interactions in this doctoral thesis work. Most mechanobiology studies about cell-ECM interactions typically rely on elastic PA to mimic the stiffness of the tissue [39, 38, 92]. However, the physiological ECM and tissues exhibit stress relaxation [62, 71, 76, 80, 45]. In 2015, Chauduri et al. observed the importance of considering matrix stress relaxation to study how cells mechanically respond to ECM [23]. Using soft elastic and viscoelastic substrates with similar initial Young's modulus (i.e., 1.4 kPa), they found that cells growing on the soft viscoelastic substrate were larger than on the purely elastic substrate. This result suggests that cellular mechanosensing is not only mediated by sensing matrix rigidity but also matrix stress relaxation.

QGel920 is a silicon-based elastomer. It exhibits viscoelastic properties and provides critical features such as a glass-matching refractive index (i.e., 1.49 at 589 nm) and low autofluorescence. Thus, it could increase the imaging quality of proteins on the cell-matrix interface using surface-based microscopy like TIRF microscopy when coated on soft substrates [6, 78]. Another advantage compared to PA hydrogel is that PDMS exhibits a constant Poisson's ratio of 0.5 [64]. For storage, storing the substrate inside an aqueous solution is not required, and its mechanical properties did not degrade over time to the same extent as PA.

Table 1.6: The mechanical characterization of elastomer surface with the nanoindentation experiments (k = 0.2 N/m, r = 54 μm).

Part A	**Part B**	**E (kPa)**	**tan δ (5 Hz)**
1	1	3.026±0.48	0.491±0.031
1	2	15.26±2.51	0.241±0.011

Similarly to PA, I assessed the mechanical properties of QGel920 substrates, including Young's modulus and dissipation factors, using the nanoindentation experiments. As shown in Table 1.6, I mixed part A and part B with a particular ratio to get a stiffness. For this work, I used ratios of 1:1 and 1:2 to get 3 kPa and 15 kPa. These stiffnesses are biologically relevant as they are a typical stiffness range in tissue [16]. Compared to PA, which was a highly elastic material (the dissipation factor is close to zero), QGel920 substrates exhibited a viscoelastic behavior.

I found that the dissipation factor was smaller on the stiffer substrates. It infers that the stiffer substrate that was mixed in a ratio of 1:2 was less viscous. According to the datasheet, the viscosity of part A, part B, and the 1:1 mixing ratio is 1455 centipoise (cps), 1645 cps, and 1500 cps, respectively. Consequently, if one adequately mixed part A and part B in a ratio of 1:2, I should increase the viscosity compared to the 1:1 ratio. I argue that maybe the 1:2 mixtures were not entirely homogeneous and caused this counterintuitive observation. However, as the error (i.e., standard error) was low (see Figure 1.14), the strange reading might stem from the nanoindentation experiment itself. As the surface of the PDMS was typically quite adhesive for the spherical probe, it might influence the dynamic mechanical analysis.

Treatment with high dose UV light and the oxygen plasma altered the stiffness of QGel920 substrate

As I was interested in applying micropatterning of ECM proteins to study the cellular traction forces of confined cells on the surface of QGel920, I also checked the response of QGel920 to oxygen plasma. The plasma treatment rendered the surface of QGel920 hydrophilic due to the presence of polar silanol groups (SiOH) replacing methyl groups [33], thus allowing me to introduce a cell-repellent layer of PEG brush on the surface. I could increase the hydrophilicity of the surface. However, the stiffness increased. Similarly, when I exposed the surface to deep UV, the stiffness also increased, as shown in Figure 1.14. The UV also rendered the surface hydrophilic. As I planned to use UV light to release cellular traction, the increasing

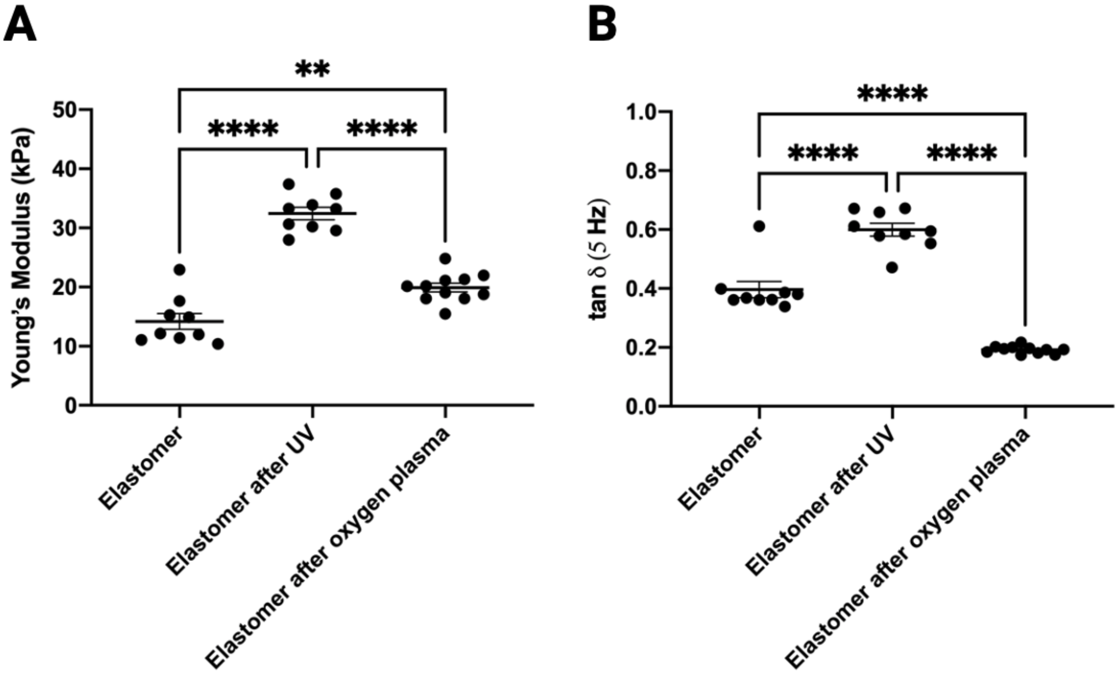

Figure 1.14: (**A**) Young's moduli of the elastomer surface, the elastomer surface after deep UV illumination for 5 minutes, and the elastomer surface after the oxygen plasma treatment (100 W, 0,4 mbar for 20 s). (**B**) Dissipation factors of the elastomer surface, the elastomer surface after deep UV illumination for 5 minutes, and the elastomer surface after the oxygen plasma treatment (100 W, 0,4 mbar for 20 s). Bars show mean ± S.E.M (ordinary one-way ANOVA, **** $P < 0.0001$, *** $P < 0.001$, ** $P < 0.01$, * $P < 0.05$, ns $P \leq 0.5$). **Please click here to view a full size version of this figure.**

stiffness of QGel920 to UV light could potentially affect the traction force reconstruction.

Many studies have already reported the hardening of PDMS due to plasma oxidation and deep UV treatments [13, 123, 117, 33, 90]. To produce a uniform rigid thin layer of PDMS to coat metals or polymers, one typically uses plasma oxidation or deep UV ozone treatment [13, 123, 117]. The interaction of ozone with PDMS produces a rigid-silica-like layer. Several studies have reported the depth of the ozone-exposed region using advanced methods such as ellipsometry, XPS, neutron reflectometry, and x-ray spectroscopy [93, 37, 57]. In 2002, Efimenko et al. reported the formation of 60 and 80 nm rigid layers for 60 and 90 minutes exposure times [37]. Interestingly, a report stated a gradient in Young's modulus of the rigid layer in the vertical direction [49].

As it was clear that both deep UV and plasma oxidation increased the stiffness of the surface, I believed that the duration of the treatment played a role in the significant difference between both treatments. However, the cause of changes in dissipation factors remained obscure. I encourage more comprehensive studies on this in the near future.

1.4.2 Micropatterning on the surface of deformable substrates

Maskless photolithography based micropatterning on glass surface

In this work, I used micropatterning to confine cells directing their shape and architecture spatially on the elastic/viscoelastic substrates. Adherent cells typically exhibit large variability of cell shapes which

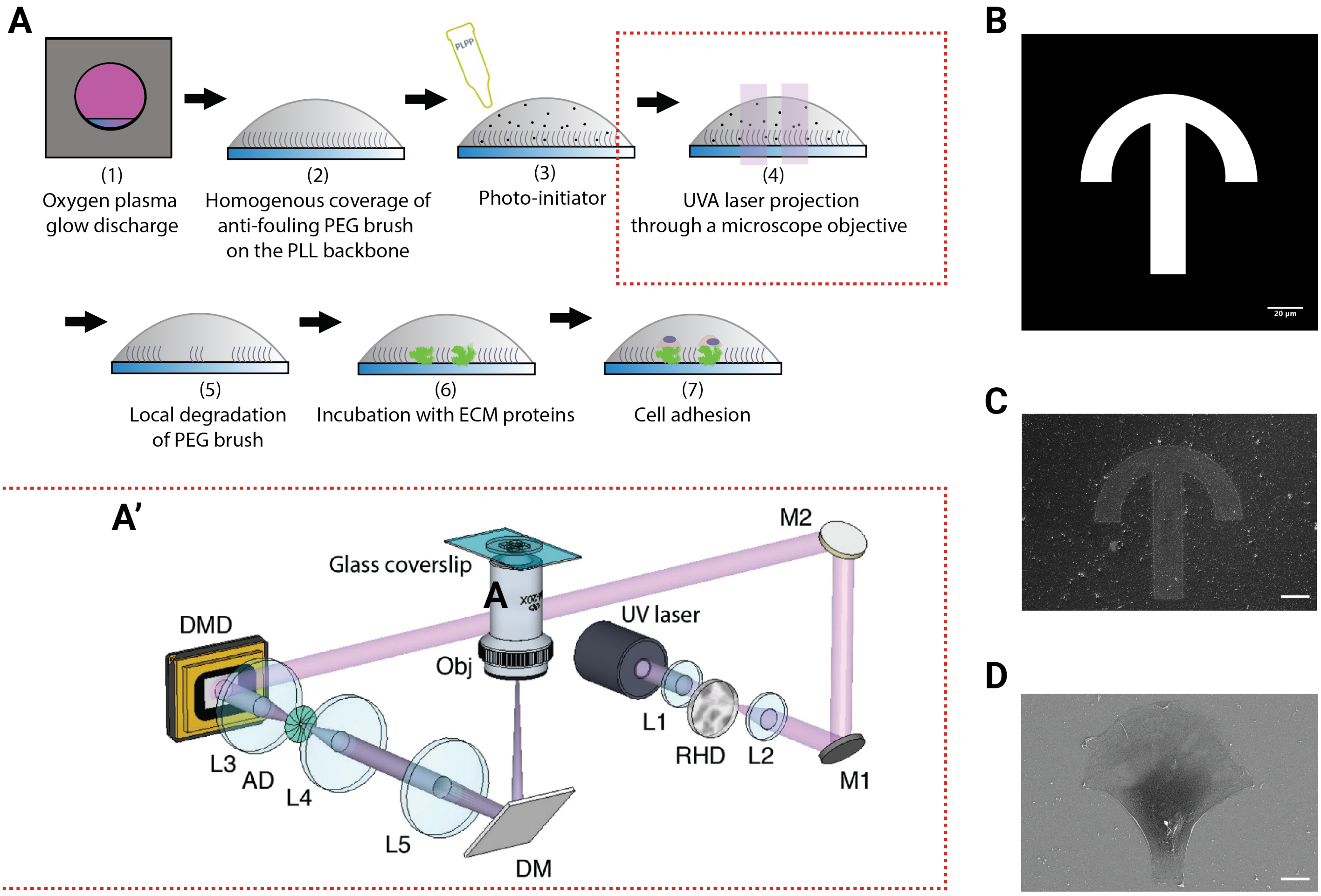
A
(1)
Oxygen plasma glow discharge
(2)
Homogenous coverage of anti-fouling PEG brush on the PLL backbone
PLPP
(3)
Photo-initiator
(4)
UVA laser projection through a microscope objective
(5)
Local degradation of PEG brush
(6)
Incubation with ECM proteins
(7)
Cell adhesion
A'
Glass coverslip
M2
DMD
A
UV laser
Obj
L1
RHD
L2
M1
L3
AD
L4
L5
DM
B
20 µm
C
D

Figure 1.15: (**A**) Workflow of maskless photolithography based micropatterning. (1) A glass coverslip was cleaned by using oxygen plasma (200 W, 0.4 mbar for 2 minutes). (2) Then, anti-fouling PLL-PEG brushes were coated on the glass surface. (3) The photo-initiator reagent was added. (4-5) The reagent absorbed energy from UV laser beam creating radicals for a rapid degradation of PEG polymers from the surface. (6) ECM proteins like fibronectin or collagen were added on the surface. The proteins bound to unprotected PLL layer. (7) Cells were seeded on the surface. (**A'**) The optical schematic of DMD-based maskless photolithography. Reproduced with permission from Ref. [116]. Copyright 2015 John Wiley and Sons. (**B**) 8-bit tiff file of a crossbow pattern was used to make a 100 μm diameter crossbow *via* 20x air NA = 0.45 lens. (**C**) A SEM micrograph of a crossbow pattern produced with 30 mJ/mm^2 UV dose on the glass surface made using the image from (B). Scale bar = 20 μm. (**D**) A SEM micrograph of a (critically point dried) patterned single cell on the glass surface made using the image from (B). Scale bar = 20 μm. **Please click here to view a full size version of this figure.**

sometimes makes it difficult to conduct a comparison study. The standardization of cell shape can be performed by micropatterning. For PA, I developed a protocol that adapted works from Sarker et al. [105] and Strale et al. [116]. First, I patterned a glass surface either with a mask-based or maskless-based patterning method (Figure 1.15A) and subsequently transferred the adhesive pattern to the PA precursor (Figure 1.16F'). For maskless-based patterning, the amount of adhesive protein patterned on the glass depends on the UV light dose [116, 89]. I used 30 mJ/mm^2 for the basic adhesive protein patterning with the commercially available photoinitiator (i.e., PLPP gel). The optical configuration for the patterning is shown in Figure 1.15A'. Typically, light from a near UV photodiode is focused on a rotary holographic diffuser before reaching the DMD chip. It is called "digital" because it projects the light by tilting its individual micromirror to two possible angles. One angle directs the light to the objective lens, whereas the other direction leads to the optical absorber. A single mirror is responsible for a single pixel. A single DMD chip contains millions of micromirrors. Consequently, I could produce a single crossbow shape (Figure 1.15B) on a passivated glass surface (Figure 1.15C) in only 1 s using UV dose of 30 mJ/mm^2 with the help of the photoinitiator. The cellular attachment was achieved by backfilling the patterned area with fibronectin (Figure 1.15D).

Transfer of pattern from glass to PA

Aldehyde-containing crosslinkers enables the physical-chemical transfer of ECM proteins from glass to PA surface To transfer the patterns from glass to the PA surface, one typically only relies on a physical transfer by stamping the patterned glass on a gel precursor. However, the method is proven to be unreliable as a significant protein fraction was not adequately transferred [105]. To overcome this issue, I incorporated reactive aldehyde groups (-CHO) in the PA precursor by adding oxidized-HEA to the mixture of conventional gel mixture (i.e., Acrylamide, Bisacrylamide, APS 10 %, and TEMED). The incorporation of aldehyde groups did not hinder the polymerization and allowed covalent binding to the primary amine groups (-NH_2) of micropatterned fibronectin on glass (Figure 1.16F'). This physical-chemical transfer yielded an efficient protein transfer from glass to the PA surface, as shown in Figure 1.16J.

The dual-layered PA method produces high-quality traction force fields PA substrates can be produced with or without TFM marker beads. Figure 1.16A-D shows the production of PA without marker beads that I typically used for rigidity sensing experiments. I could directly perform micropatterning by putting the patterned glass surface on a PA precursor (Figure 1.16B). In comparison, Figure 1.16A-H shows the production of dual-layered PA with marker beads that is used for TFM experiments.

The motivation for using the dual-layered scheme was to get a high distribution of marker beads close to the surface layer. The high distributed marker beads near the surface are crucial in reconstructing a high-quality traction force field. To produce a dual-layered PA substrate, I adopted the strategy from work

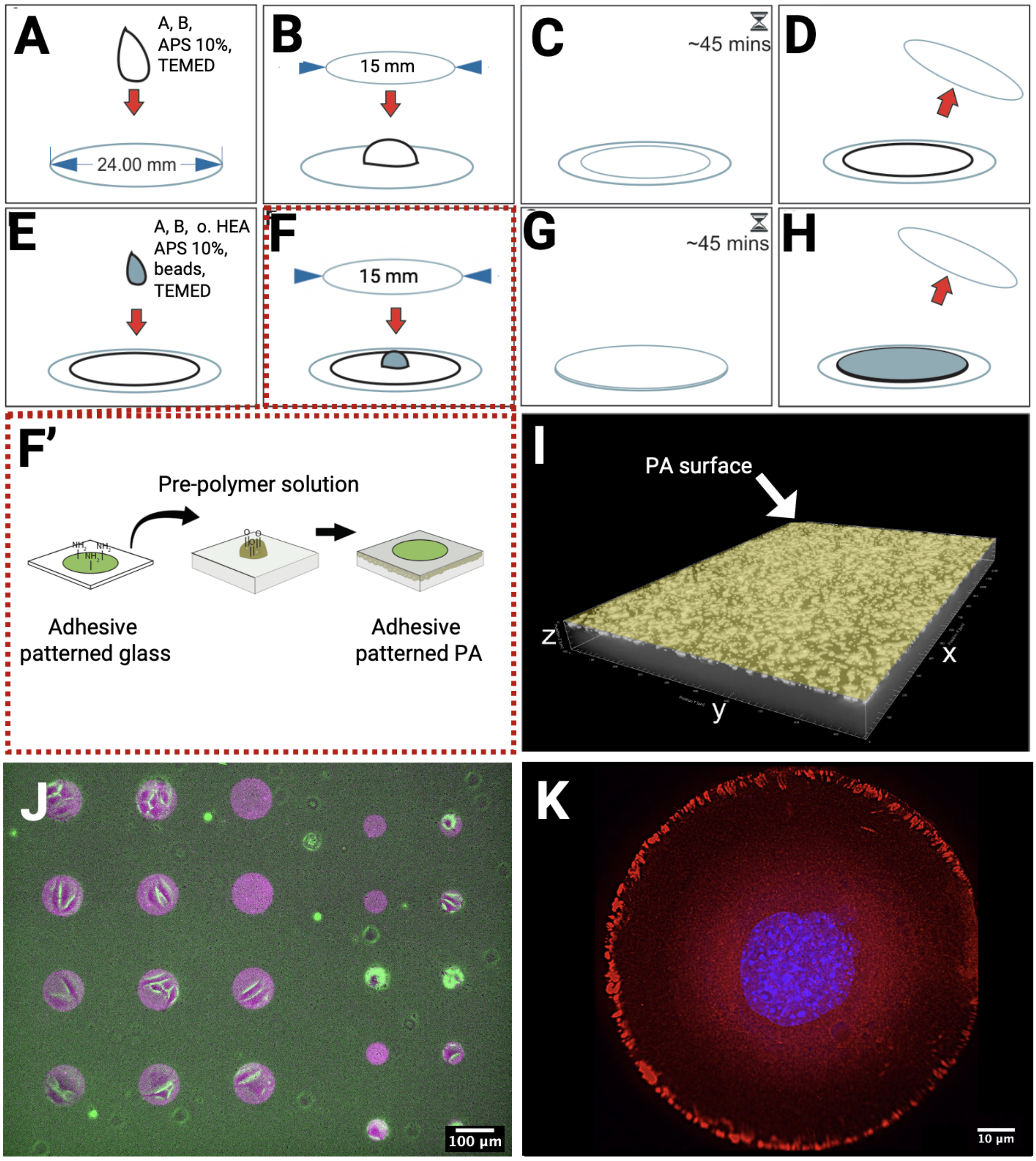
A
A, B,
APS 10%,
TEMED
24.00 mm
B
15 mm
C
~45 mins
D
E
A, B, o. HEA
APS 10%,
beads,
TEMED
F
15 mm
G
~45 mins
H
F'
Pre-polymer solution
Adhesive
patterned glass
Adhesive
patterned PA
I
PA surface
z
y
x
J
100 μm
K
10 μm

Figure 1.16: Scheme of a patterned ECM substrate for TFM. (**A**) The solution for the bottom layer was pipetted on a methacrylated surface. (**B**) A smaller clean coverslip was carefully placed on the pre-polymer droplet. (**C**) The polymerization took 45 minutes. (**D**) The top coverslip was detached. The bottom layer is ready. (**E**) The solution for the top layer was pipetted on the hydrogel. (**F**) The micro/nano-patterned coverslip was carefully placed on the pre-polymer droplet. (**F'**) The micropatterning of adhesive proteins on glass was produced by maskless-based patterning and then transferred from glass to a PA hydrogel. The free amine groups of adhesive proteins, e.g., fibronectin, were bound covalently to aldehyde groups on the PA. (**G**) The polymerization took 45 minutes. (**H**) The top coverslip is detached. The patterned PA hydrogel was ready. (**I**) A 3D representation of a confocal xyz micrograph showing a high density of fiducial beads near the surface. (**J**) A micrograph of fluorescently labeled fibronectin (magenta) on the surface of PA (A10B0.5) with embedded fluorescent beads (green), overlayed with a bright field image of cells. (**K**) Indirect immunofluorescence microscopy imaging of a single cell adhering to a circle-shaped fibronectin micropattern (100 μm). Nucleus (blue), paxillin (red). Reproduced with permission from Ref. [25]. Copyright 2022 the Journal of Visualized Experiments. **Please click here to view a full size version of this figure.**

done by Bridgman et al. in 2001 [15]. It was achieved by adding one more PA layer containing 5 % v/v fluorescent marker beads on top of a plain (i.e. containing no marker beads) PA layer, as shown in Figure 1.16E-H. The result is shown by a 3D micrograph taken with a confocal laser scanning microscope (Figure 1.16I). For dual-layered PA, I put the patterned glass surface on the upper layer PA precursor (Figure 1.16F). Figure 1.16J shows cells were adherent to micropatterned fibronectin (magenta) on a dual-layered PA with Young's modulus of 22 kPa. The green color represented fluorescent marker beads. By staining paxillin (red), a focal adhesion marker, I could see the adhesion of a single cell proven by single nuclear staining with DAPI (blue) on a pattern (Figure 1.16K).

Maskless photolithography based micropatterning on the QGel920 surface

For QGel920, I could not apply the transfer protocol I did on PA as the surface was typically tacky. However, QGel920 is a silicon-based polymer, so that I could pattern it almost like a glass surface. The main difference was the hydrophobicity of the surface of QGel920. Therefore, the main challenge in patterning QGel920 is to render the surface hydrophilic without increasing the stiffness. I could turn the surface hydrophilic with plasma treatment. However, from the mechanical characterization of the surface (Figure 1.14), plasma oxidation for 20 s increased the stiffness from 15 kPa to 20 kPa.

Despite the obvious effect on increasing the stiffness, I could in principle, also pattern the surface of QGel920 as shown in Figure 1.17. QGel920 is viscoelastic and poses a glass-matching refractive index, therefore it is a great material for future 2D and 2.5D-TFM [6, 64, 78]. I encourage more comprehensive studies on this in the near future.

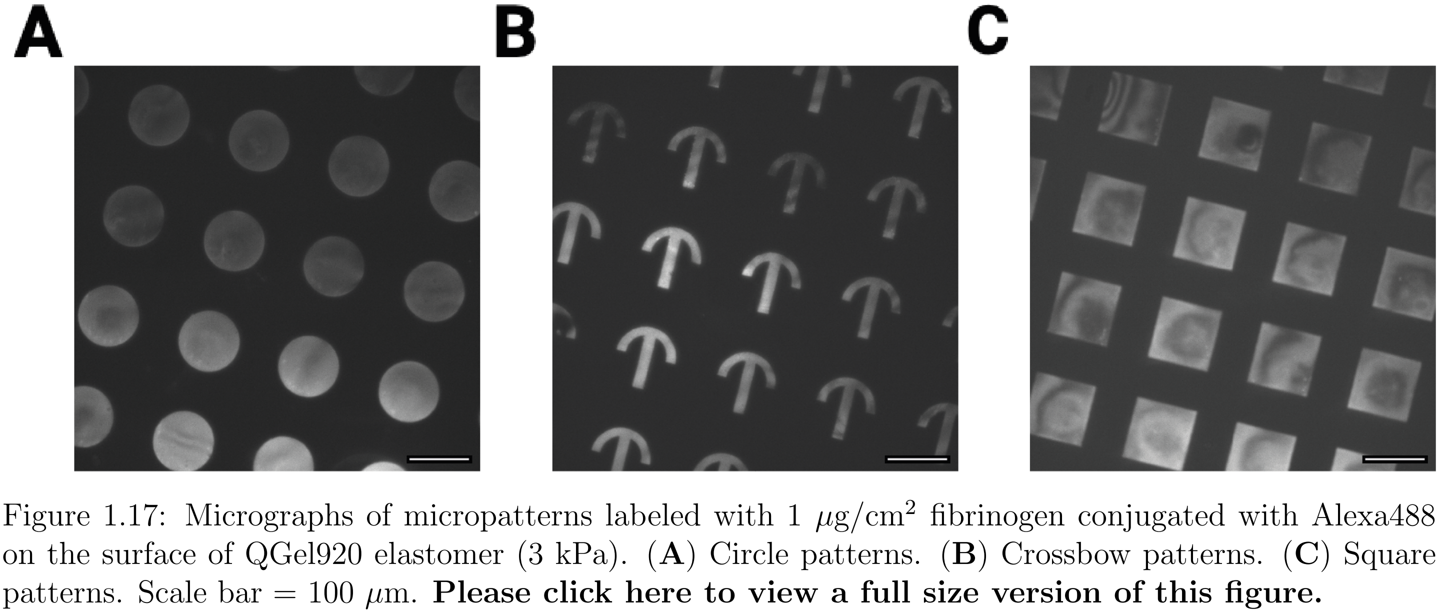

Figure 1.17: Micrographs of micropatterns labeled with 1 μg/cm^2 fibrinogen conjugated with Alexa488 on the surface of QGel920 elastomer (3 kPa). (**A**) Circle patterns. (**B**) Crossbow patterns. (**C**) Square patterns. Scale bar = 100 μm. **Please click here to view a full size version of this figure.**

1.4.3 Nanopatterning on the surface of deformable substrates

In this work, the initial interest in using nanopatterning was to provide anchor points for immobilized particles coupled to molecular force sensors and to control their distribution on PA substrate. By having

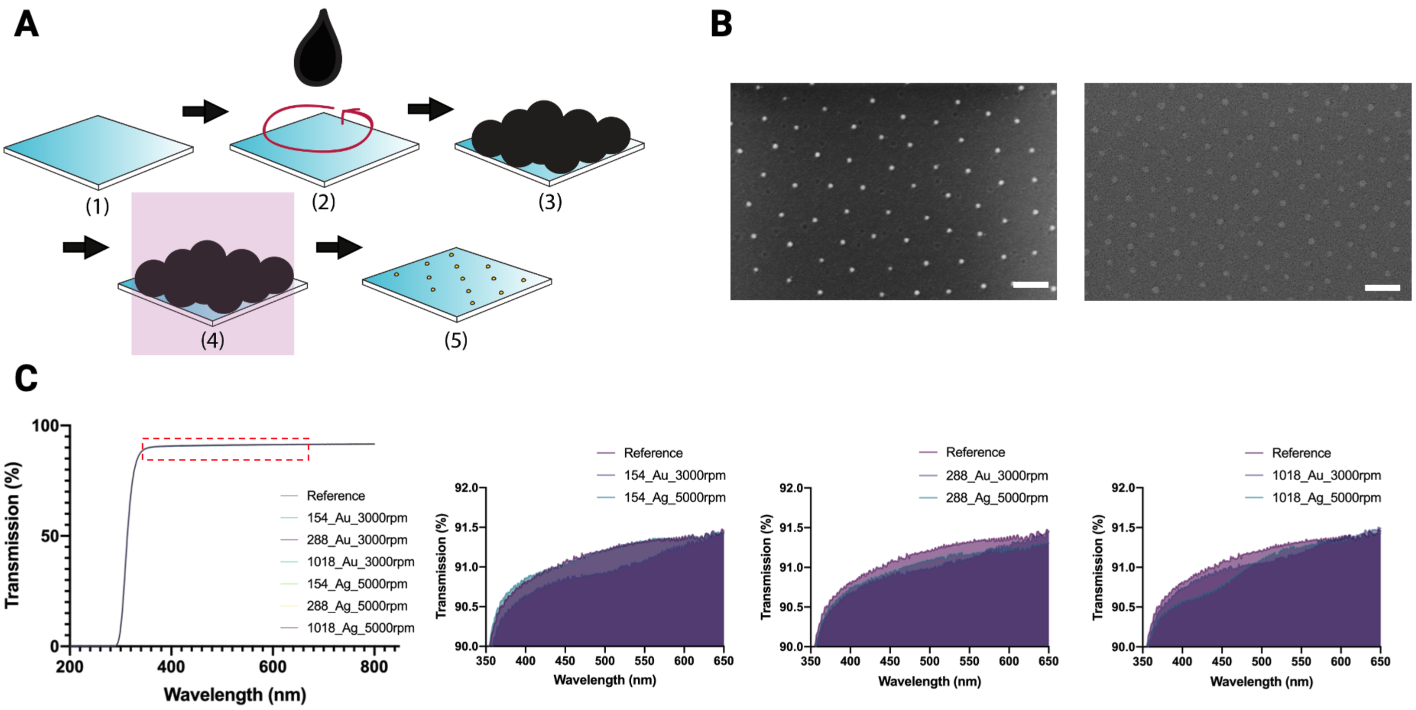

Figure 1.18: (**A**) Schematic showing the preparation of nanopatterned glass. (1) A glass surface after cleaning with the piranha solution. (2) The micellar solution was spin-coated onto the surface. (3) The micelles self-assembled into groups resembling quasi-hexagonal patterns after the non-polar solvent evaporated from the surface. (4) The removal of polymer matrices and the reduction of the metal precursor salts ($HAuCl_4$ or AgOAc) to elemental gold and silver, respectively upon the exposure to the hydrogen plasma (150 W, 0.4 mbar, 20 minutes). (5) The gold nanopatterned surface was used for PA nanopatterning template. (**B**) **Left** A SEM micrograph showing a region of gold nanopatterned glass surface prepared by using polymer P4921-S2VP (L = 0.25, C = 2 mg/ml, spin-coated with 3000 rpm). Scale bar = 100 nm. **Right** A SEM micrograph showing a region of silver nanopatterned glass surface prepared by using polymer P4921-S2VP (L = 0.25, C = 5 mg/ml, spin-coated with 5000 rpm). Scale bar = 100 nm. (**C**) The transmission as a function of wavelength on various substrates. In general, the light transmission on nanopatterned glass surfaces fabricated using polymer P4708-S2VP (i.e., 154), P4705-S2VP (i.e., 288), and P4921-S2VP (i.e., 1018), respectively was reduced. **Please click here to view a full size version of this figure.**

those structures on the surface, I aimed to simultaneously study the interplay between cellular and molecular forces during particle uptake. However, while I was finishing this thesis, the molecular force sensor was still under development. Therefore, as proof that I could produce nanopatterned PA substrates, I performed TFM on immobilized thiol-cRGD peptide on PA substrate, which will be described later.

For nanopatterning of PA substrates, I adapted the protocol described by Oria et al. [92] with a slight modification. As depicted in Figure 1.18A and described in the materials and methods part, I started by patterning the glass surface with the BCMN method. I used gold ($HAuCl_4$) and silver (AgOAc) metal salts loaded in the BCP solution. I considered silver an alternative anchor due to the quenching issue of fluorescent dyes by gold *via* a mechanism called nanosurface energy transfer (NSET) [125, 65]. As shown in Figure 1.18B, I could pattern gold and silver with the interparticle distances of 100 nm on the surface of the glass. I did not quantify the height of the dot, but it should be around 8 nm as reported by Glass et al. [48, 108].

Next, I investigated if the nanopattern of gold or silver influenced the light transmission through the glass by using a spectrometer (Agilent, #Cary 5000). Figure 1.18C shows that patterning glass with nanoarrays of metals slightly altered light transmission. At λ=500 nm, the transmission of plain glass and a gold-nanopatterned glass made with the polymer 154 were around 91.2 and 90.7 % which was 0.5 % in difference. From the global point of view, 0.5 % difference seems negligible. However, it was unclear how it would influence single molecule observation (i.e., molecular force measurements) as gold might scatter light. Gold nanopatterns with the smallest interparticle distance (i.e., 20 nm) prepared with the polymer 154 (see Table 1.1, PS_{units}) seemed to reduce the transmission more than the silver nanopattern with a similar interparticle distance. Interestingly, the curve of the silver nanopattern resembled the control glass surface without patterning. On 50 nm interparticle distance, which was prepared with the polymer 288 (see Table 1.1, PS_{units}), the reduction in transmission by silver nanopattern was comparable to gold in all wavelengths. The reduction of transmission by gold was relatively stronger from 450 to 550 nm. On 100 nm interparticle distance, which was prepared with the polymer 1018 (see Table 1.1, PS_{units}), the reduction in transmission caused by silver nanopattern was relatively stronger from 350 to 500 nm.

The silver nanopattern seemed to scatter more light than gold as the interparticle distance increased, especially from 350 to 500 nm. At around 650 nm, the influence was relatively milder. This finding was supported by the fact that silver was more used to detect low levels of biomarkers using spectroscopy compared to gold [52, 51]. However, the sensitivity of silver could be detrimental to the microscopy application, especially in single-molecule studies, if I use a silver nanopattern as an anchor. Thus, silver was discarded as an optimal anchor site in future experiments.

Transfer of pattern to PA surface

As QGel920 turned rigid when treated with plasma, I could not pattern this substrate either by BCMN or by direct transfer of patterned glass. Therefore, in this work, I only applied nanopatterning on PA substrates. To transfer the nanopattern from glass to PA, I incubated the nanopatterned glass in the solution containing BAC and $NaBH_4$. BAC is typically used as a reversible crosslinker in making PA. The chemical formula for BAC is $C_{10}F_{16}N_2O_2S_2$. By utilizing a strong reducing agent such as $NaBH_4$, I could break the disulfide linkage of BAC to thiol-containing crosslinker [36]. The presence of the thiol groups linked PA networks to the gold nanopattern on the glass surface. The covalent linkage between PA network and gold dots would generate sufficient pulling forces during the transfer. Meanwhile, the attachment of gold dots to the glass surface should not be too strong either to facilitate the transfer. Therefore, I only treated the glass with hydrogen plasma for 20 minutes at 150 W (Figure 1.18A). In comparison, I typically treated the nanopatterned glass in hydrogen plasma for 20 minutes at 150 W, followed by 72 hours of baking at 300 degrees Celsius to get strongly anchored gold nanoparticles.

The transfer process was adopted from the work of Oria et al. [92]. After the hydrogel polymerization finished, I kept the sample for another 72 hours at 37 degrees Celsius. The process of transferring the nanopattern from glass to PA is depicted in Figure 1.19A. Every step was verified with SEM imaging

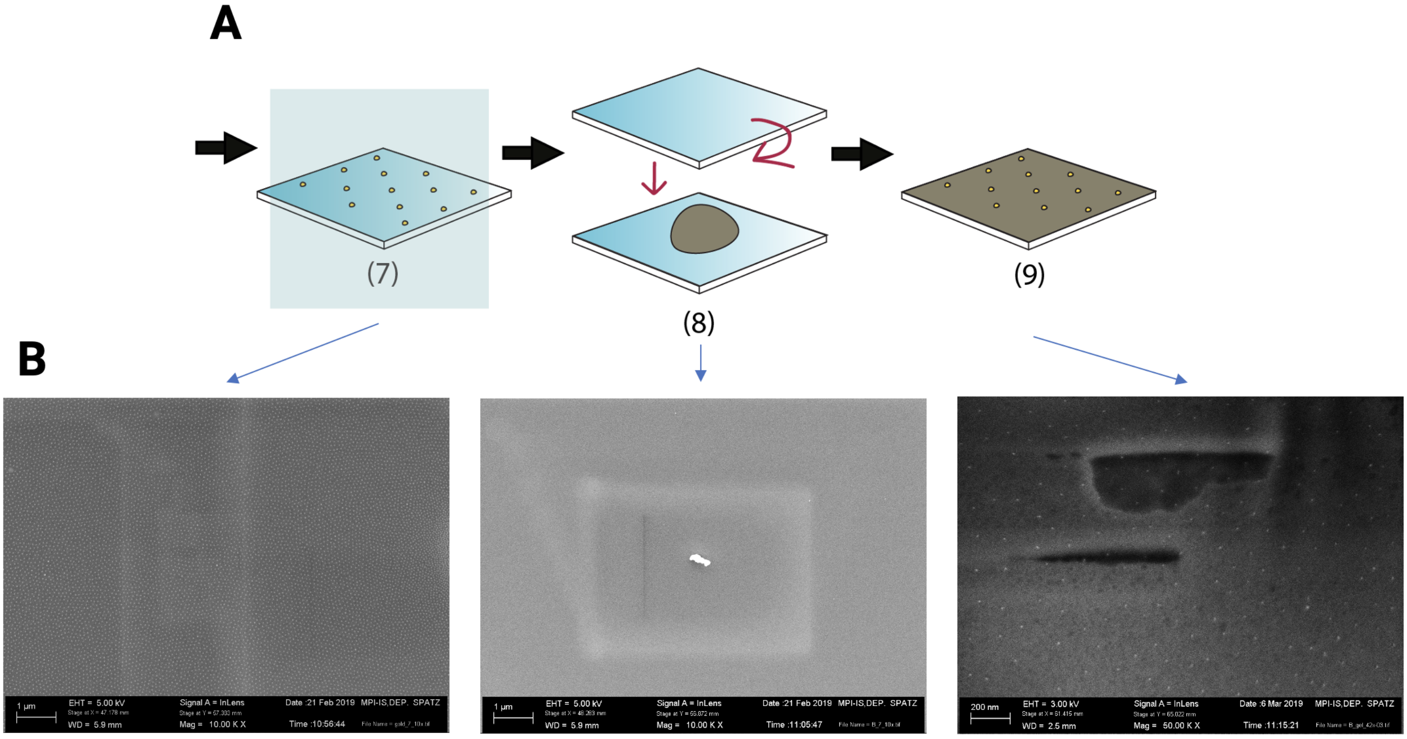
A
(7)
(8)
(9)
B
1 µm
EHT = 5.00 kV
Signal A = InLens
Date :21 Feb 2019
MPI-IS,DEP. SPATZ
WD = 5.9 mm
Mag = 10.00 K X
Time :10:56:44
1 µm
EHT = 5.00 kV
Signal A = InLens
Date :21 Feb 2019
MPI-IS,DEP. SPATZ
WD = 5.9 mm
Mag = 10.00 K X
Time :11:05:47
200 nm
EHT = 3.00 kV
Signal A = InLens
Date :6 Mar 2019
MPI-IS,DEP. SPATZ
WD = 2.5 mm
Mag = 50.00 K X
Time :11:15:21

Figure 1.19: (**A**) Schematic showing the preparation of nanopatterned PA using a nanopatterned glass surface as the template (the continuation from Figure 1.18). (7) The nanopatterned glass surface was activated in the solution containing 2 μM BAC and 5 μM $NaBH_4$ in ethanol for 2 h. (8) The activated glass surface was put on a droplet of the hydrogel precursor. (9) The gold nanopatterned PA. (**B**) (**Left**) A SEM micrograph showing the nanopatterned gold array on the surface of the glass (before transfer). (**Center**) A SEM micrograph showing the successful removal of nanopatterned gold array from the surface of the glass. (**Right**) A cryo-SEM micrograph showing a region of nanopatterned PA (A10B0.2) surface. Table 1.7 shows the result of transfer experiments using different monomer and crosslinker concentrations. **Please click here to view a full size version of this figure.**

as depicted in Figure 1.19B. Table 1.7 shows the result of transfer experiments using different monomer and crosslinker concentrations. Nanopatterning of PA substrates were successfully performed on A10B0.1, A10B0.2, A10B0.3, A10B0.4, and A10B0.5. Three different validation experiments were conducted to determine if the nanopatterning was successful. First, if the nanopatterning worked, the gold dots should no longer remain on the glass surface, which should be confirmed by SEM imaging. Second, if the gold dots should appear on the PA surface, which should be confirmed by cryo-SEM imaging. Last, cells should bind to the biofunctionalized surface. According to Table 1.5, Young's moduli for A10B0.1, A10B0.2, A10B0.3, A10B0.4, and A10B0.5 were 8.43, 12.03, 15.01, 16.28 and 22.11 kPa, respectively.

Looking at Table 1.7, it should be considered that stiffer gels would not guarantee a successful transfer. One should consider the combination of measured Young's modulus stiffness, Acrylamide concentrations, and crosslinker concentrations. Low Acrylamide concentration (e.g., 4 %) means more water in the stock solution irrespective of the crosslinker concentration. Typically it would produce gels with a non-smooth surface. I argue that the amount of Acrylamide to be crosslinked was not enough to produce a good gel. I should avoid this low concentration for transfer-based nanopatterning. Having a too low concentration of crosslinkers (i.e., 0.02 - 0.08 %) might also hinder a successful transfer as it might only crosslink the bottom part of the PA touching the methacrylated glass, thereby leaving a weaker polymer network to

Table 1.7: Transfer of gold nanopatterned arrays from glass to PA experiments. **1** = AuNPs were absent from the glass surface verified by SEM. **2** = AuNPs were present from the PA surface verified by cryo-SEM. **3** = Cells attached on the surface of nanopatterned PA functionalized with 25 μM SH-cRGD. nt = not-tested.

A (%)	B (%)	**1**	**2**	**3**
4	0.03	failed	nt	nt
4	0.1	failed	nt	nt
4	0.3	failed	nt	nt
4	0.5	failed	nt	nt
5	0.03	**successful**	nt	failed
5	0.1	**successful**	nt	nt
10	0.02	failed	nt	nt
10	0.04	failed	nt	nt
10	0.06	failed	nt	nt
10	0.08	failed	nt	nt
10	0.1	**successful**	**successful**	**successful**
10	0.2	**successful**	**successful**	**successful**
10	0.3	**successful**	**successful**	**successful**
10	0.4	**successful**	**successful**	**successful**
10	0.5	**successful**	**successful**	**successful**
20	0.02	failed	nt	nt
20	0.04	failed	nt	nt
20	0.06	failed	nt	nt
20	0.08	failed	nt	nt

pull the gold dots on the upper part of PA, as we can see on 10 % and 20 % Acrylamide concentration.

1.4.4 Light based traction force microscopy

I have shown that the maskless-based patterning method could be used to micropattern directly on the surface of the glass, QGel920, and indirectly on PA. In this part, I directly used light in TFM experiments. As shown in Figure 1.20A, I let a cell grow on a surface of biofunctionalized PA/QGel920 presenting high-density fluorescent beads on the surface. Through a series of mechanotransduction signaling, the adherent cell would exert a traction force on the underlying substrate. During this step, I acquired the image of the beads and called it a deformed state (1). Next, I applied near UV (UVA) illumination with a high dose (6000 mJ/mm^2) to selectively kill the cell. Due to acute oxidative stress, the dying or dead cell would release its traction on the surface (2). After the full release, I acquired the image of beads again and called it an undeformed state (3). I called this process ”local ultraviolet illumination traction force microscopy” or simply LUVI-TFM.

The technique is ”local” since I only released the traction force from selected cells. By setting a projection pattern on the DMD, I could vary the shape and the size of light illumination accordingly. As we can see from Figure 1.20B, I could illuminate cells on fibronectin patterns ranging from 50, 100, 150, 200, and 300 μm. In this example, I used a 20x NA = 0.45 air objective lens and varied only the size but not the shape. Shortly after illumination, I observed the release of cellular traction calculated by PIV.

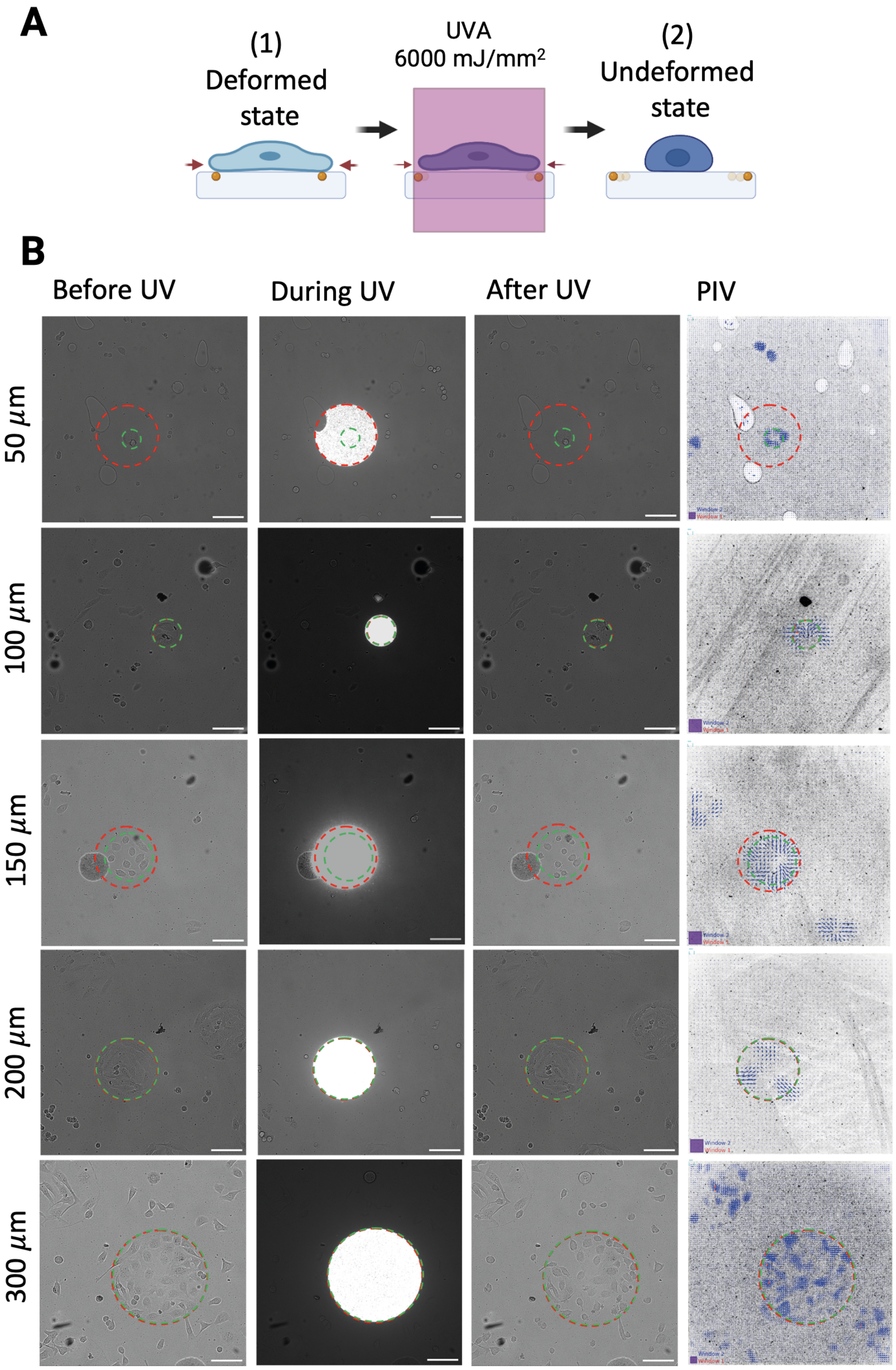

Figure 1.20: (**A**) Schematic showing the workflow of LUVI-TFM. (1) An adherent cell deforms the underlying substrate. (2) The cell is killed using a high dose of near UV light. The cell experiences acute oxidative stress leading to the release of traction force on the substrate. (3) The substrate is no longer deformed. The release can be tracked by comparing bead images of (1) and (3). Reproduced with permission from Ref. [25]. Copyright 2022 the Journal of Visualized Experiments. (**B**) Micrographs showing micropatterned cells (green dashed line) before and after the exposure of the high dose of near UV (UVA) light (red dashed line: cross sectional areas of the light). Micropatterned cells on 50, 150, and 200 μm patterns were illuminated with 200 μm of UVA light. Micropatterned cells on 100 μm patterns were illuminated with 100 μm of UVA light. Micropatterned cells on 300 μm patterns were illuminated with 300 μm of UVA light. The substrate deformation was calculated by PIV analysis. Scale bar = 100 μm. **Please click here to view a full size version of this figure.**

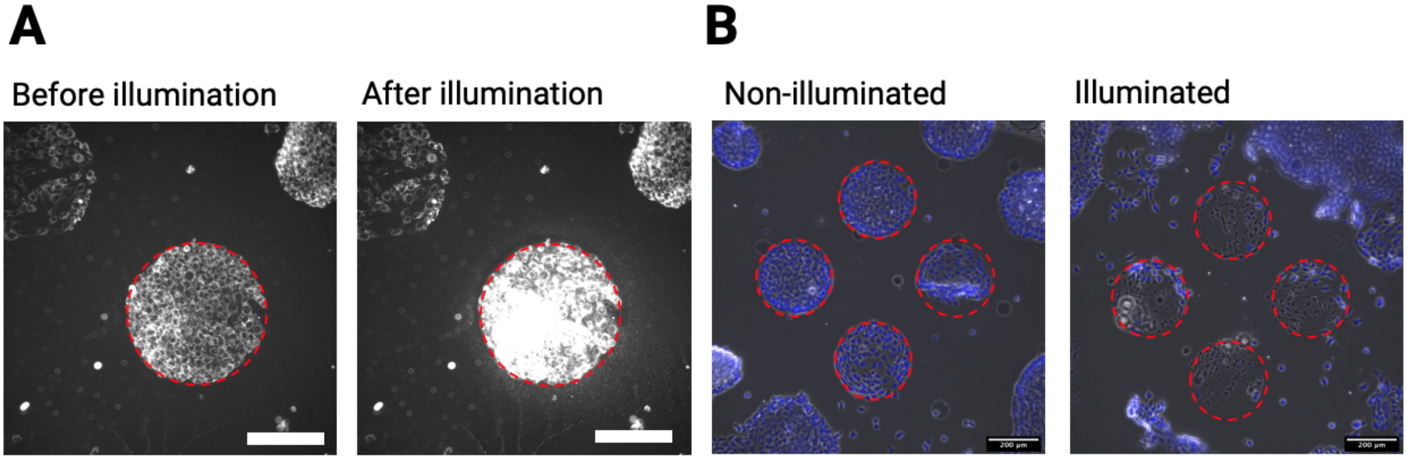

Figure 1.21: (**A**) Near UV light (UVA) illumination (6000 mJ/mm^2, red-dashed line) on a patterned cell cluster led to an elevated ROS (i.e., oxidative stress) measured by a commercially available reagent (i.e., CellRox). It was indicated by an increasing signal intensity after the illumination. Scale bar = 200 μm. (**B**) Near UV light (UVA) illumination (6000 mJ/mm^2) on patterned cell clusters possibly caused cell death due to the oxidative stress. Illuminated cells died and were easily detached by several washing steps during immunostaining steps compared to non-illuminated cells. Nuclei = blue, grey = cells in brightfield. **Please click here to view a full size version of this figure.**

The bead displacement underneath cells outside the illumination area was also detected and was relatively minor. The minor bead displacement under the cell outside the illumination area might occur due to the cell movement. It remained unclear how those cells were also affected by the light. I encourage more comprehensive studies in the near future.

By using light to release cellular tractions instead of trypsinization, it is no longer required to detach all cells to measure the cellular forces of several cells. Most importantly, opening the microscopy stage to add trypsin from outside was no longer required. That means I could eliminate one significant source of experimental failure in performing TFM.

Cell death induced by near UV light exposure

In this part, I wanted to determine the biological explanation for why cells died after exposure to a high dose of near UV light. As depicted in Figure 1.21A, using a commercially available reagent (i.e., CellRox), I observed an increasing level of reactive oxidative species (ROS) caused the illumination of near UV light (6000 mJ/mm^2). Elevated ROS might cause acute oxidative distress leading to cell death [1, 113]. As dead cells cannot maintain adhesion and cytoskeletal integrity, traction forces are released from the matrix. In Figure 1.21B, the nuclei of illuminated cells could not be marked with DAPI might indicate that the high dose of UV had caused permanent damage to DNA.

2D-LUVI-TFM

In general, cells exert three-dimensional forces. However, as most adherent cells *in vitro* turn flat during matured adhesion, one could consider using only the two-dimensional approach [110]. I used a program developed by Schwarz's group (ITP, Ruprecht-Karls-Universitaet Heidelberg) to quantify traction forces.

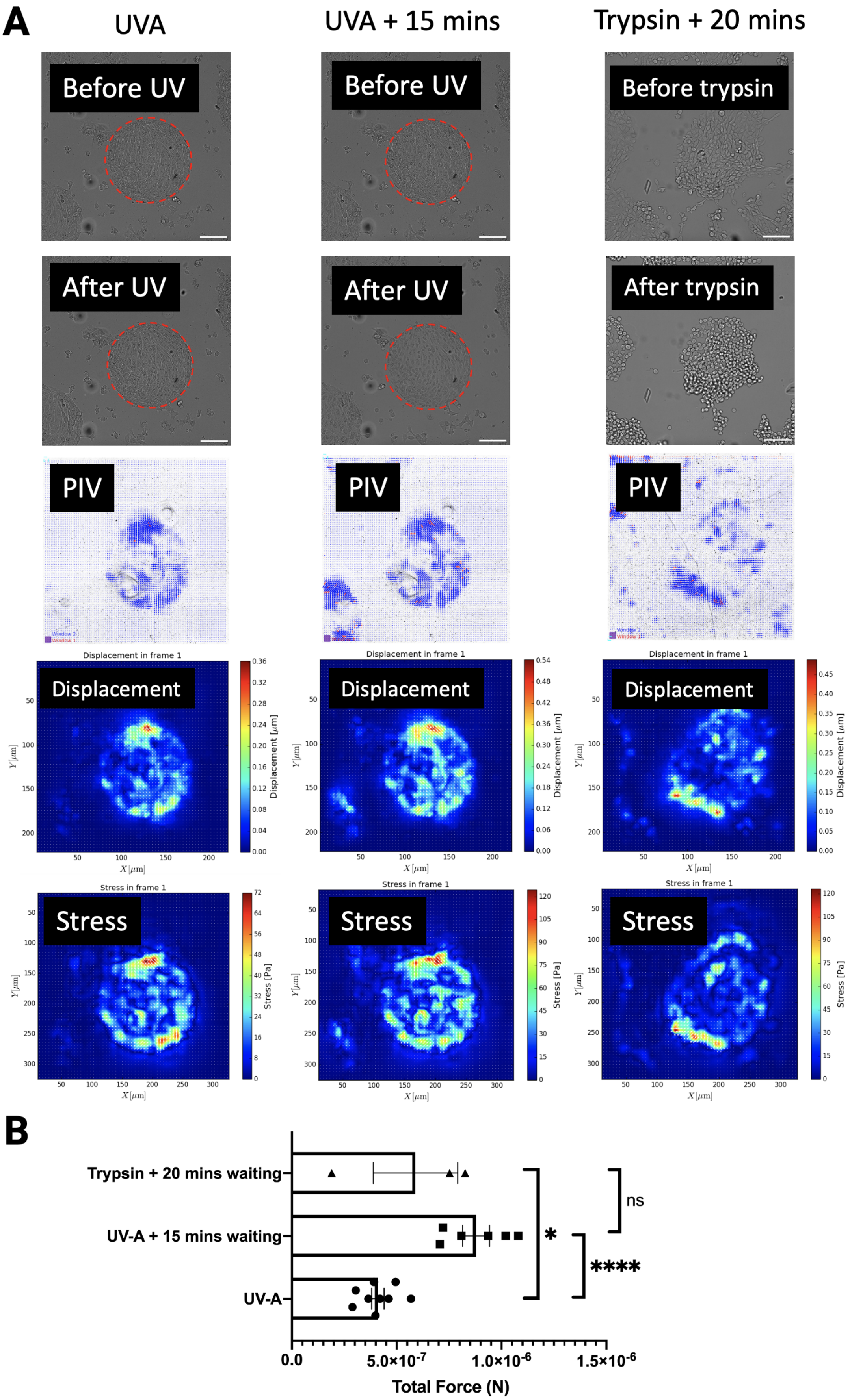

Figure 1.22: (**A**) Micrographs showing different treatments to get undeformed images in LUVI-TFM (the illumination is depicted with a red dashed line) and the conventional TFM using trypsin. (**B**) Full release of cellular tractions 15 minutes after exposure to a high dose of near UV light was non-significantly different from tractions recorded 20 minutes after trypsin treatment. The measurements were conducted on PA with E = 1.7 kPa (A4B0.1). Bars show mean ± S.E.M (ordinary one-way ANOVA, **** $P < 0.0001$, *** $P < 0.001$, ** $P < 0.01$, * $P < 0.05$, ns $P \leq 0.5$.). **Please click here to view a full size version of this figure.**

The program required drift-corrected images of the undeformed and deformed images that I acquired with the light-based protocol, Young's modulus of the substrate that was measured with nanoindentation experiments, and the μm/pixels ratio of the image. By inserting those into the program, I could generate PIV, displacement, and stress fields as shown in Figure 1.22A.

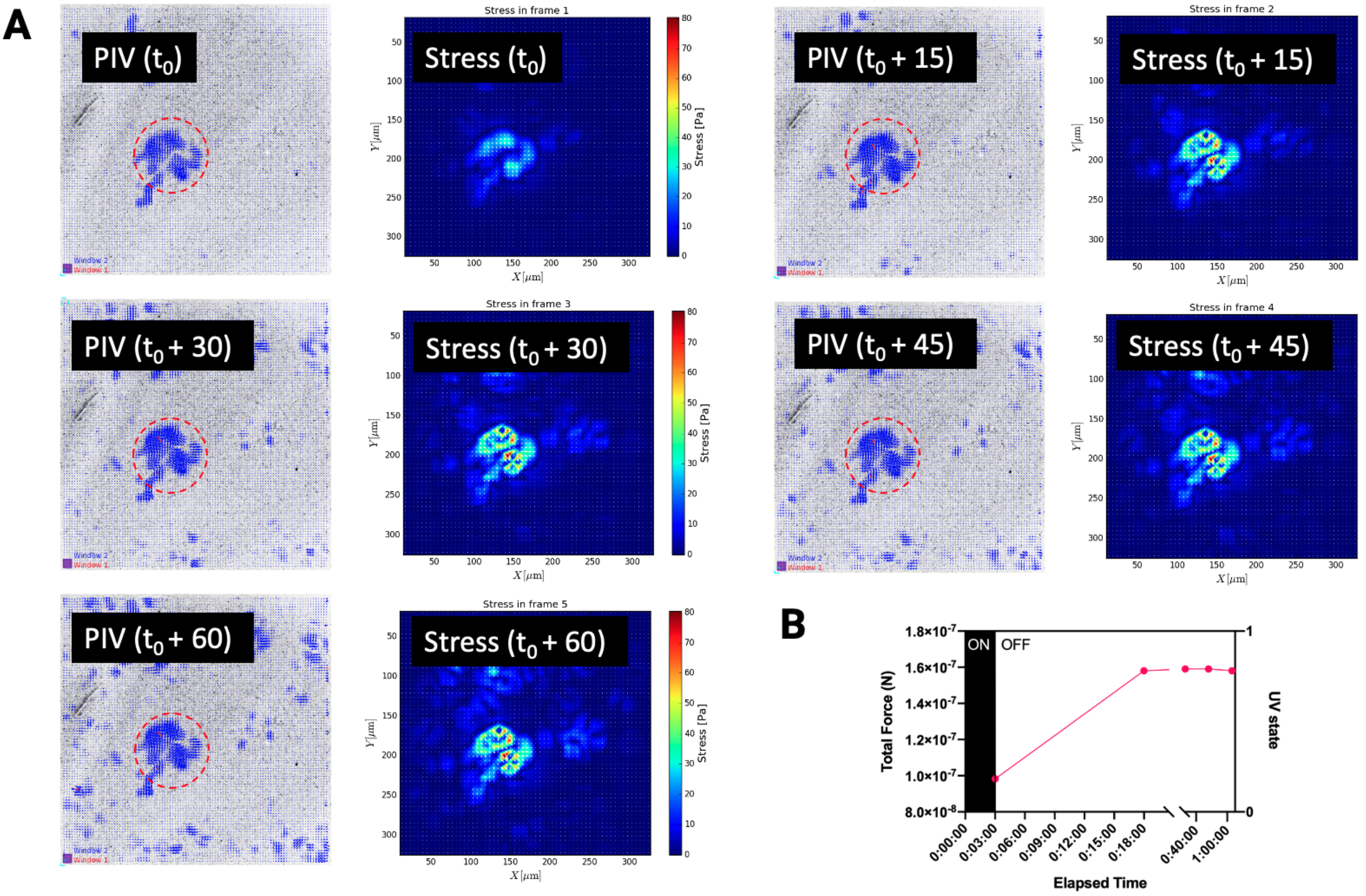

Figure 1.23: (**A**) Cells adhering to a 100 μm FN micropattern slowly released their traction on the surface of PA (A10B0.06) after high-dose near UV (UVA) exposure (red dashed line). The deformation was tracked by PIV. PIV (t_0) is PIV of the surface deformation right after the illumination. PIV (t_0+15), PIV (t_0+30), PIV (t_0+45), and PIV (t_0+60) are PIVs of the surface deformation at 15, 30, 45, and 60 minutes post-exposure, respectively. Traction stresses were reconstructed using regularized Fourier Transform Traction Cytometry[103] with a regularization parameter acquired by Generalized Cross Validation[50]. (**B**) Full release was achieved 15 minutes post-exposure (i.e., the traction force curve reaches the saturation). **Please click here to view a full size version of this figure.**

In Figure 1.22A, I compared the traction force of a cell cluster on the micropatterned PA surface acquired with three different treatments. First, I imaged the undeformed bead image after cells were illuminated by 6000 mJ/mm^2 of near UV light (UVA). It corresponded to 3 minutes of illumination using a 20x NA = 0.45 air objective lens. Second, I imaged the undeformed bead image after the illumination, followed by 15 minutes of waiting. Third, I imaged the undeformed bead image after trypsinization, followed by 20 minutes waiting time. The deformed images were taken before treatments (i.e., UV or trypsin).

As shown in Figure 1.22B, imaging immediately after illuminating the cells with 6000 mJ/mm^2 of near UV light released around 50 % of cellular traction forces on the substrate, whereas imaging 15 minutes after the illumination released entire cellular traction forces on the substrate. When I compared the performance of both light-based treatments, the illumination of a high dose of near UV light followed by 15 minutes of waiting was non-significantly different compared to the trypsinization method. It can be ensured that the difference was not due to a high discrepancy in cell numbers. I used 200 μm of circular fibronectin pattern, and I calculated that there were 71 cells inside the pattern on average.

Light-based and trypsin-based treatments exhibited different mechanisms in releasing cellular traction forces from the substrate. Even though the performance of a high dose of near UV light followed by 15 minutes of waiting was comparable to the trypsinization method, the dead cells rarely detached from the substrate after the illumination, as depicted in Figure 1.23A. In comparison, trypsinization typically breaks down adhesion proteins resulting in cell detachment from the surface. It means that in using LUVI-TFM, one always has to check if cells have already released total traction forces by looking at the shape of the cells. Cell death caused by the illumination typically were indicated by the necrotic phenotype or membrane blebbing. Alternatively, one can compare force release at different time points, as shown in Figure 1.23B. I found that the total force release reached the plateau after 15 minutes. This was the reason why I waited 15 minutes before acquiring the undeformed image.

2D-TFM of a single cell on a nanopatterned PA substrate Besides the matrix's composition, we know from *in vitro* studies that cell-ECM interactions also depend on the spatial organization of ECM, especially integrin ligands [19]. In 2006, Cavalcanti-Adam et al. reported that a distance of 58 nm between integrin ligands had to be maintained to preserve stable adhesion [19]. Beyond it, the integrin cluster collapsed, and focal adhesion marker proteins such as vinculin and zyxin only transiently colocalized with actin fibers at focal adhesions. This collapse could be quantified by TFM. Motivated by that, part I also aimed initially to build a combining assay of cellular (i.e., TFM) and molecular force measurements anchored on gold dots. By changing the underlying stiffness, it would be interesting to check if the stable adhesion maintained by 58 nm between integrin ligands would still be valid. Oria et al. have reported TFM on nanopatterned PA biofunctionalized with cRGD [92]. However, the use of a molecular force sensor to detect forces on a single integrin combined with cellular force measurement using TFM dedicated to studying the stable adhesion has not been reported yet. Despite being able in developing reliable protocols, including the production of nanopatterned PA substrate and single cell LUVI-TFM. Unfortunately, I could not achieve it yet as the molecular force sensors were still under development.

Even though I could not implement these methods for the initial plan, as shown in Figure 1.24A, I could perform live LUVI-TFM of a single cell on the nanopatterned PA surface (E = 8.34 kPa) 1 hour post-seeding. To ensure the cell adhesion was only mediated by integrin ligands anchored on gold dots with an interparticle distance of 100 nm, I functionalized the surface with 25 μM of sH-cRGD and subsequently seeded cells in medium without serum. Figure 1.24B shows the evolution of force and energy every 5 minutes for 1 hour. As the area increased, the force and energy increased as well. I did not do any further experiments related to TFM of nanopatterned PA substrates as I was unable to introduce any molecular

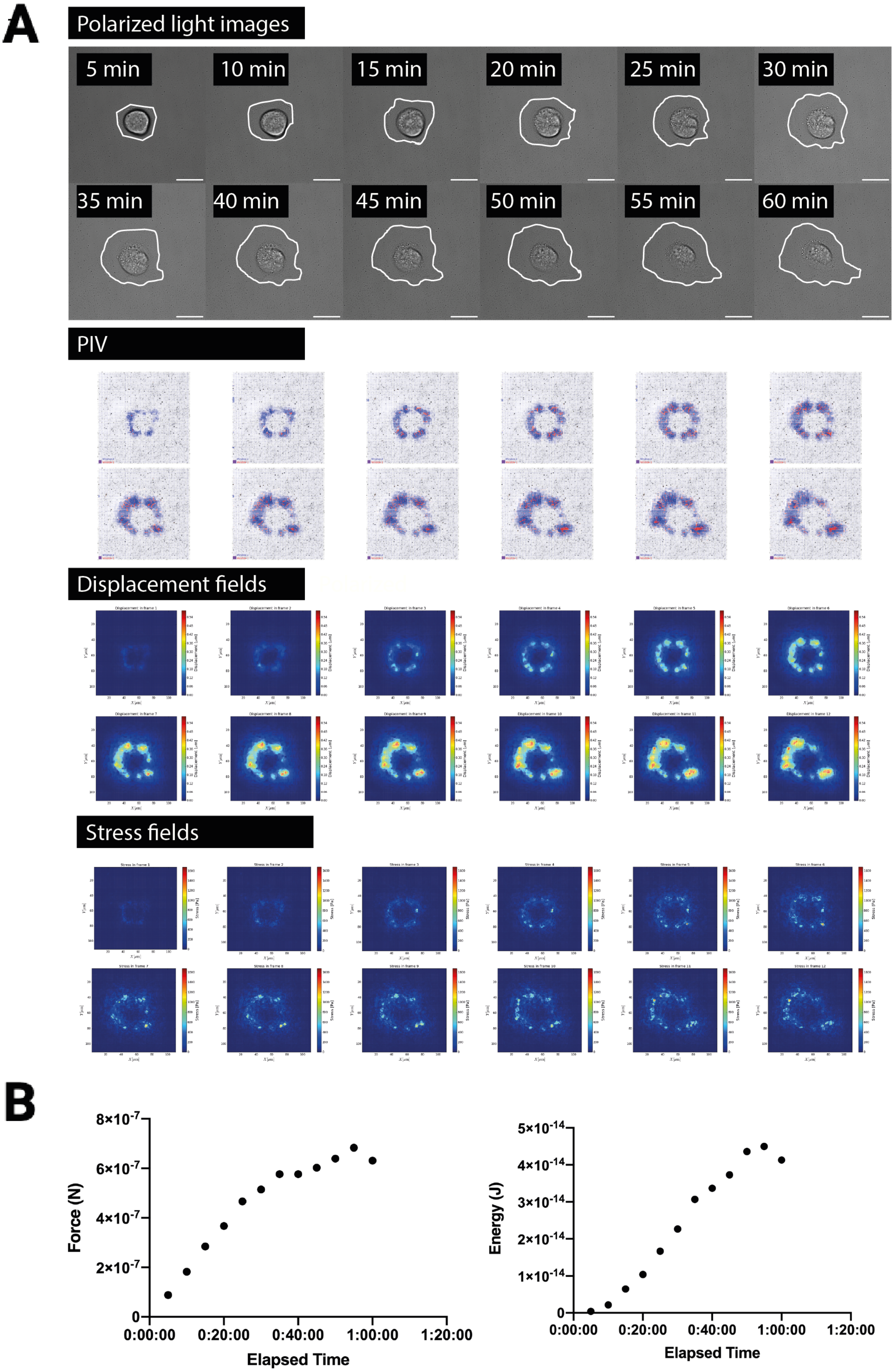

Figure 1.24: (**A**) Polarized light images, PIV images, displacement fields, and stress fields of a live single MEF cell adhered to the surface of nanopatterned PA (E = 8.34 kPa, the interparticle distance is around 100 nm) functionalized with 25 μM of cRGD-thiol. The cell was seeded in medium without serum. Scale bar = 20 μm. (**B**) The force and energy of the single MEF were measured every 5 minutes for 1 h. **Please click here to view a full size version of this figure.**

force sensors. There was a possibility to use gold dots to covalently anchor nanoparticles. However, for my main project in part II, I opted to use a much simpler but effective approach such as EDC chemistry.

2.5D-LUVI-TFM

Using LUVI-TFM, I could significantly eliminate the acute drift in xyz axes caused by poor handling during trypsinization procedures. It was useful for 2D measurement, in which I acquired an image only in one z position, and for 2.5D-TFM in which I took a z-stack. In 2.5D-TFM, one considers not only tangential components (i.e., x and y) but also the normal component (i.e., z) of traction. In short, it is a 3D force measurement of cells growing on elastic/viscoelastic surfaces where normal components are only measured at the cell-ECM interface.

In general, depending on the application, I could perform the light-based cell detachment protocol using 20x and 40x lenses. To support patterning, I could not use a lens with a phase ring inside as it will block the light path. Figure 1.25A shows LUVI-TFM using 20x lens NA = 0.45 on a micropatterned cell cluster having a diameter of 100 μm on PA with Young's modulus of 1.7 kPa. The clarity of the normal component of stress should be appreciated stress as it was only taken with a 20x lens. In the field of 2.5D-TFM, people typically only look at a single cell using 100x oil NA = 1.45 [28, 78, 107].

The result strongly suggests that 2.5D-LUVI-TFM can also be exploited to study the normal force of multicellular clusters as stresses are also involved in maintaining cell-cell adhesion. It might be useful, for example, to study the jamming-unjamming transition or epidermal growth factor (EGF)-induced collective contractility.

Figure 1.25B shows that 2.5D-LUVI-TFM could be implemented for the single cell force measurements with a 40x lens NA = 0.95. The cell was seeded on PA hydrogel with Young's modulus of 11.3 kPa. In this experiment, I was interested in finding the possible relation between the spatial distribution of AP2 clusters and the normal component of the traction. As I used a widefield microscope, I did not adequately see the spatial distribution of AP2. It motivated me to use QGel920 and TIRF microscopy for 2.5D-LUVI-TFM. Nevertheless, I could visualize an indentation caused by the cell edge (i.e., negative z stress value). This finding was one of the bases of my main project in part II.

3D-LUVI-TFM

I performed a quick test to prove that LUVI-TFM had the potential to be applied for 3D force measurements. I let MCF10A spheroids grow inside a gelatin methacrylate hydrogel of Young's modulus of 0.3 kPa. To kill the cell spheroid with a diameter around 100 μm (Figure 1.26A), I used 40000 mJ/mm^2 of near UV light using the 40x air lens NA = 0.95, which was 6.6 times higher than the typical dose I used for 2D and 2.5D-LUVI-TFM. The spheroids seemed resistant to 6000 mJ/mm^2 of near UV light. After illumination, I compared the force release at different time points to determine if the spheroid was already dead. I found that the release after 15 minutes was already sufficient. In Figure 1.26B, I merged the

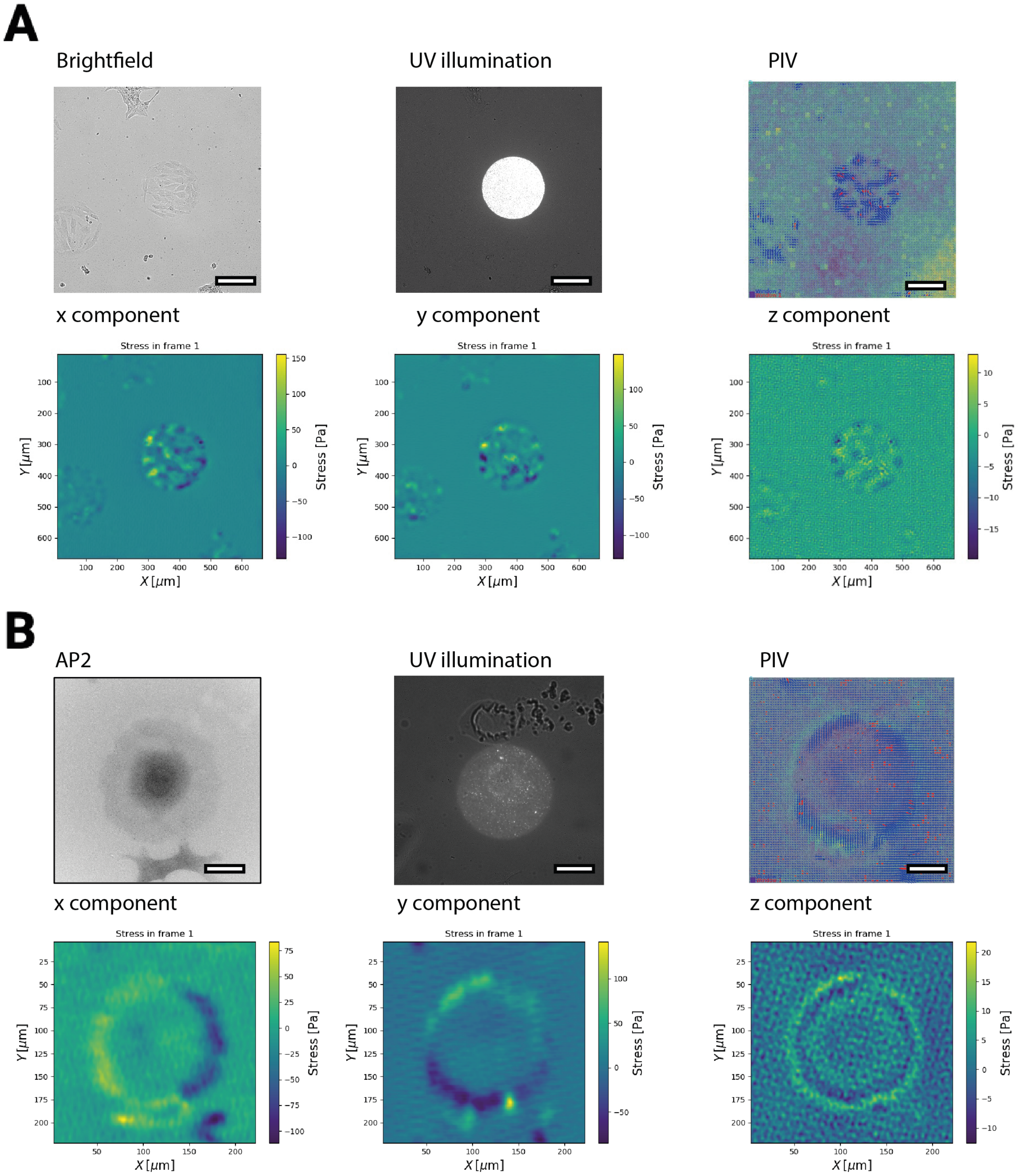

Figure 1.25: (**A**) Micrographs showing LUVI-TFM performed on micropatterned cells seeded on PA (A4B0.1, E = 1.7 kPa) using a 20x NA = 0.45 air objective lens. Tangential components (i.e., x and y) and a normal component (i.e., z) were acquired by comparing the 3D deformation of beads between undeformed and deformed image stacks. Scale bar = 100 μm. (**B**) Micrographs showing LUVI-TFM performed on a single cell seeded on PA (A5B0.3, E = 11.3 kPa) using a 40x NA = 0.95 air objective lens. Scale bar = 50 μm. The image of UV illumination seems brighter on the 20x setup because I used green fluorescent beads that were excited using a blue light. In comparison, in the 40x setup, I used far-red fluorescent beads that were excited using a red light. **Please click here to view a full size version of this figure.**

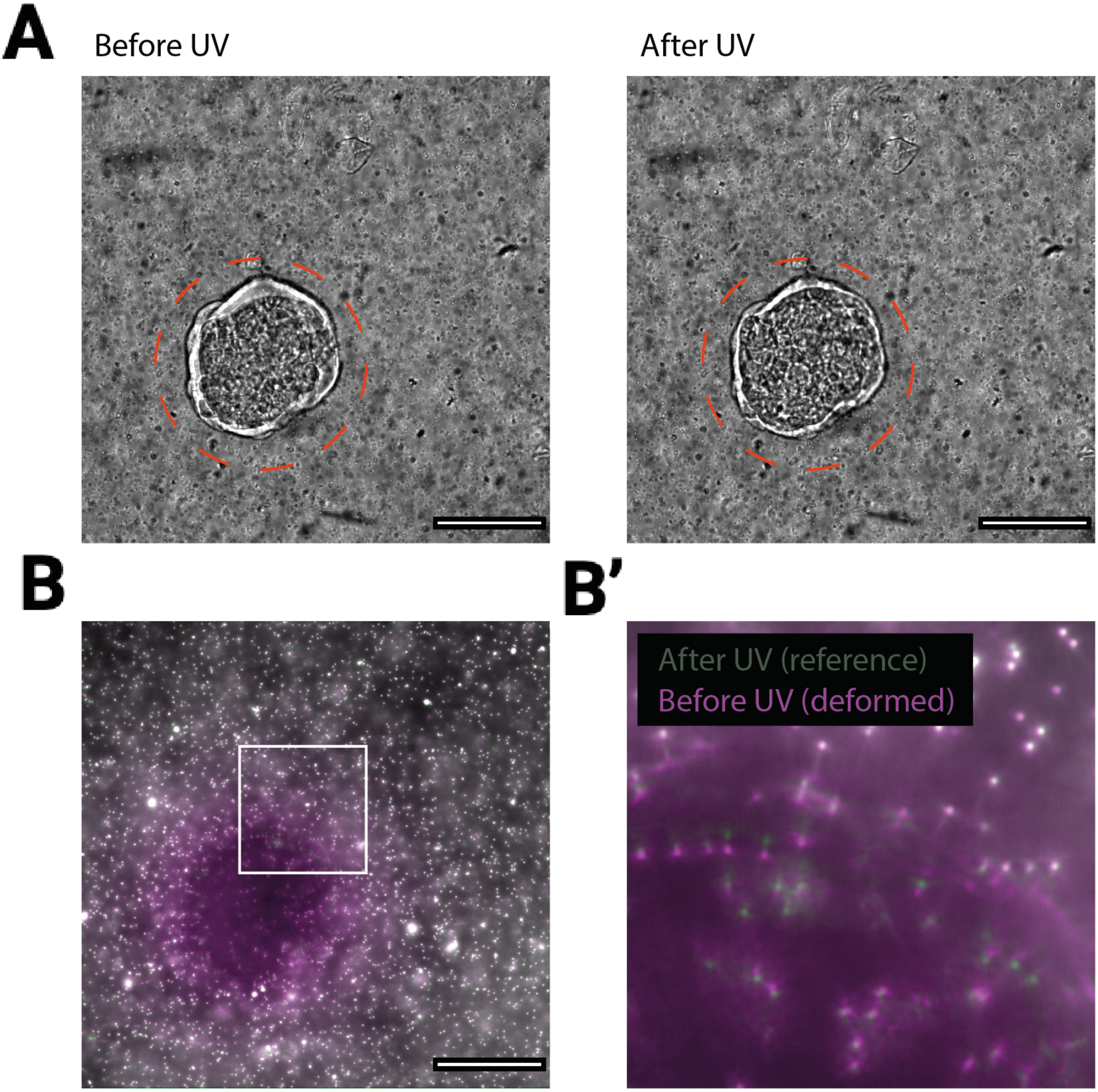

Figure 1.26: LUVI-TFM was performed on a cell spheroid in a hydrogel. **A**) Micrographs showing a 3D cell cluster before and after the exposure of high dose near UV (UVA) light (40000 mJ/mm^2) followed by 15 minutes of waiting. The imaging and illumination were performed using a 40x NA = 0.95 air objective lens. Scale bar = 100 μm. (**B**) Fluorescent micrographs (maximum intensity projection) showing the embedded beads before and after the exposure of the high-dose UVA laser. Scale bar = 100 μm. (**B'**) The bead movement indicated the cell cluster exerted traction forces inside the gelatin methacrylate hydrogel (Young's modulus = 0.3 kPa). Cell spheroids courtesy G. Lemahieu. **Please click here to view a full size version of this figure.**

maximum intensity projection image of both undeformed and deformed states. From the inset shown in Figure 1.26B', we can see the release of traction forces indicated by the shift of several fluorescent beads around the spheroid.

Although it has potential in 3D TFM, in the near future, one has to conduct a more comprehensive study of the impact of light illumination on the 3D hydrogel. So far, I relied on Young's modulus that was acquired from nanoindentation experiments which gave me the stiffness of the surface. Mechanical characterization using rheology or Brillouin microscopy could be the options [79, 99]. More information about the material properties could help increase the accuracy of force measurement and, therefore, better understand the mechanotransduction of cells in a 3D environment.

1.5 Summary

Table 1.8: Overview about the existing TFM methods in the lab.

	Conventional TFM	**LUVI-TFM**
How to acquire reference images?	Trypsin	Laser illumination (High-dose)
Mechanism	Break down cellular adhering proteins	Kill cells by over-expressing ROS
Effect of treatment	Global	Local
Advantage of technique	Fast Big cell clusters	Low sample loss risk Single cell, High SNR Easy handling
Drawback of technique	High sample loss risk Low SNR Difficult handling	Need calibration Slow Specialized microscope

Table 1.9: Overview about substrates used in this work.

	PA	**QGel920**
Type	Elastic hydrogel	Viscoelastic silicon organic polymer
Ref. index	1.33	1.49
Polymerisation time	20-30 mins at RT	Overnight at 70 degrees Celsius
Advantage	(1) Easy and fast to produce (2) Cheap materials (3) Established micro/ nanopatterning protocols (4) Stiffness remains upon UV illumination	(1) Able to be imaged by TIRF and RICM (2) Similar biofunctionalisation protocol to glass (3) Poisson's ratio = 0.5 [64]
Drawback	(1) Toxic monomers (2) Not reliable for colocalization studies (3) Poisson's ratio varies depending on monomer concentration [64]	(1) Expensive (2) Requires a spincoater and an oven (3) Stiffness increases due to UV illumination

In part I, I developed a novel method called "local ultraviolet illumination traction force microscopy" or LUVI-TFM that I could combine with surface patterning. I developed this method because later in part II, I would study the influence of cellular adhesion strength on the matrix during CME of nanoparticles from the cellular ventral side. The strength of the cellular adhesion is typically measured by TFM. Having worked using the trypsin-based single cell TFM already for several years, I realized that single-cell experiments were cumbersome to be conducted with this conventional TFM method. Many labs have come up with solutions regarding high-throughput TFM methods. However, I felt that it was more encouraging to build my own setup based on the available equipment in the lab rather than applying established protocols from other labs, which sometimes required some advanced devices and specific skills to operate.

Table 1.8 shows the overview about TFM protocols which were used in the lab.

I started with the mechanical characterization of elastic PA and viscoelastic QGel920 substrates in part I. Table 1.9 shows the overview of these two substrates. Then I continued with surface patterning of the substrates. I could perform micropatterning on both PA and QGel920 surfaces. In the case of nanopatterning, I could apply only on some rigid PA. Lastly, I performed some examples of 2D, 2.5D, and 3D-LUVI-TFM.

To summarize, part I aimed to provide a toolbox in which users can choose a single tool or a combination of multiple tools to study cellular forces. I used several tools in the s part of my thesis, in which I studied the role of traction forces in initiating CME of nanoparticles at the cellular ventral side.

1.6 Outlook

As shown in Figure 1.27, the bioengineering toolbox provides wide potential applications in studying 2D, 2.5D, and 3D cellular forces. The incorporation of nanopatterning and micropatterning also increases the versatility. However, several aspects could be improved, including the choice of microscopy, the strength of the light source, and the substrate.

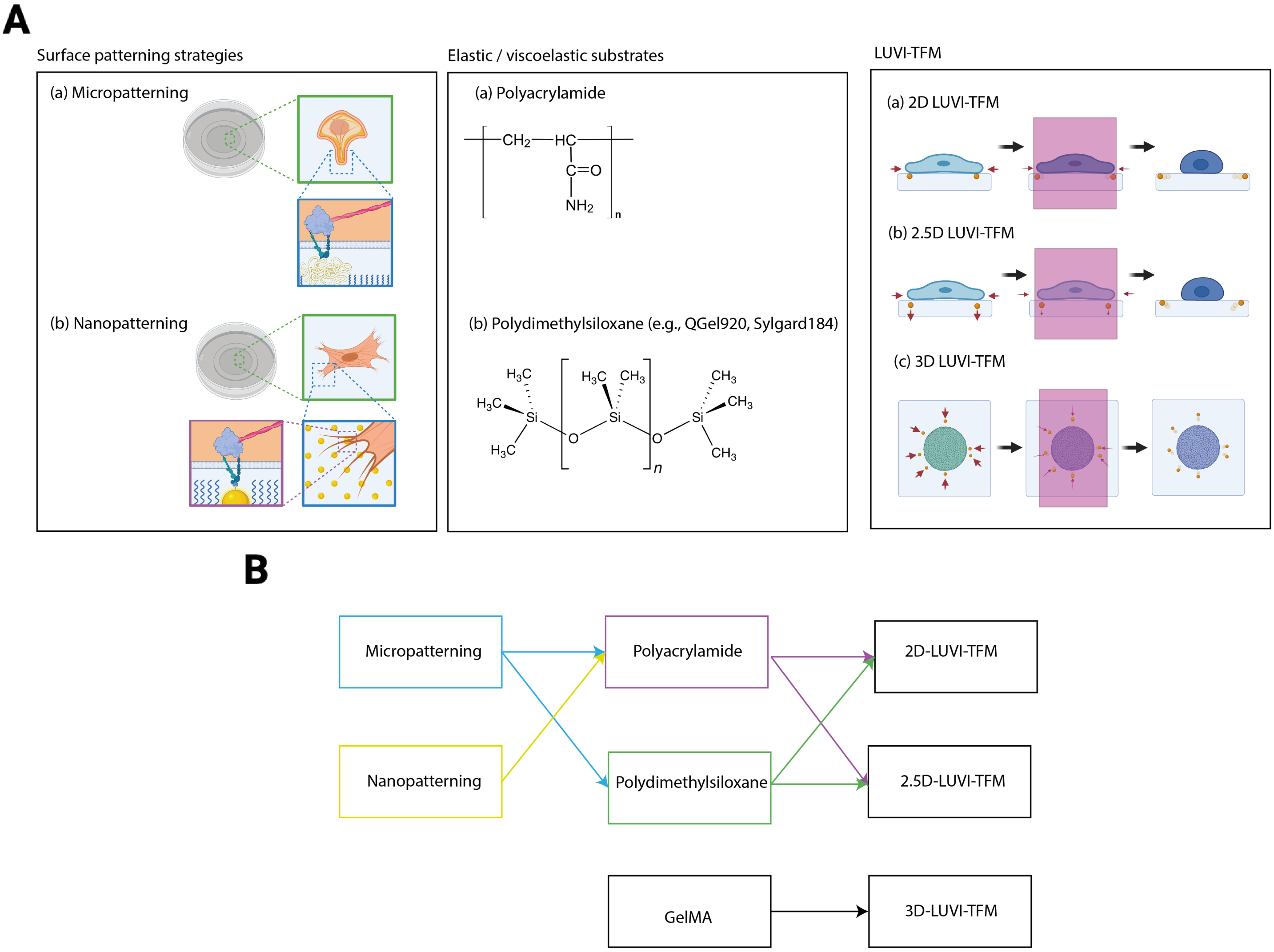
A
Surface patterning strategies
(a) Micropatterning
(b) Nanopatterning
Elastic / viscoelastic substrates
(a) Polyacrylamide
CH2
HC
C=O
NH2
n
(b) Polydimethylsiloxane (e.g., QGel920, Sylgard184)
H3C
CH3
Si
O
n
LUVI-TFM
(a) 2D LUVI-TFM
(b) 2.5D LUVI-TFM
(c) 3D LUVI-TFM
B
Micropatterning
Nanopatterning
Polyacrylamide
Polydimethylsiloxane
GelMA
2D-LUVI-TFM
2.5D-LUVI-TFM
3D-LUVI-TFM

Figure 1.27: Integrated bioengineering toolbox to study the cell-matrix interaction. (**A**) The toolbox includes surface patterning strategies, substrates production protocol, and LUVI-TFM protocol. All images were created with BioRender.com. Micropatterning and nanopatterning images are reproduced with permission from Ref. [26]. Copyright 2022 Royal Society of Chemistry. 2D-LUVI-TFM schematic is reproduced with permission from Ref. [25]. Copyright 2022 the Journal of Visualized Experiments. (**B**) Every box represents a single tool that can be used to study the cell-matrix interaction. A single solid line connecting two boxes indicates a combination of both tools that has be used in this work. **Please click here to view a full size version of this figure.**

2

Part II : Role of Traction Forces in Initiating Clathrin-Mediated Endocytosis of Nanoparticles at the Cellular Ventral Side

2.1 Introduction

2.1.1 Related previous discoveries

Integrin-mediated molecular adhesion between the cell membrane and nanoparticles increased the uptake of non-covalently bound nanoparticles at the cellular ventral side

A recent study from Wiegand et al. described the influence of integrin-mediated molecular adhesion on the nanoparticle uptake at the cellular ventral side [121]. They reported relatively enhanced uptake of immobilized, pre-coated cRGD or integrin $\alpha_5\beta_1$ ligand nanoparticles compared to immobilized, non-coated nanoparticles. The size of a single nanoparticle was 100 nm. Interestingly, cells removed those nanoparticles preferentially at the cell periphery, where cells exerted traction forces on the underlying substrate through integrin-cytoskeleton linkages. They also reported the use of pharmacological treatments to inhibit actin polymerization and resulted in a diminished number of particles removed from the surface.

Let us imagine a cell growing on a surface presenting immobilized nanoparticles. As surface-bound particles are present on the surface, a nanoparticle will immediately cause a membrane deformation on the lipid membrane at the cellular ventral side. This condition initiates the uptake. According to the model from Wiegand et al. [121], the forces generated by the adhesion energy between surface-bound nanoparticles and lipid membranes were enough to exceed the energetic cost of increasing membrane area during membrane bending. The adhesion energy increased when nanoparticles were coated with integrin ligands.

Interaction between the cell membrane and covalently bound nanoparticles triggered the recruitment of clathrin machinery at the cellular ventral side

Regarding the possible involvement of clathrin machinery on the uptake from the ventral side, Fratini et al. described that the recurrent recruitment of clathrin adaptor protein (i.e., AP2) on immobilized nanoparticles was dependent on the particle size [43]. Specifically, they immobilized labeled alkyne beads of different sizes (i.e., 20, 100, 300, and 1000 nm) using click-reaction on the surface of the nanopatterned glass and backfilled the void area with cRGD. After letting cells expressing fluorescent AP2 adhere to the surface, they observed that 100 and 300 nm surface-bound nanoparticles recruited relatively more AP2 clusters than 20 and 1000 nm. By normalizing the AP2 fluorescent intensity above a nanoparticle of each time point to the average of maximum intensity of AP2 fluorescent intensity not above a nanoparticle of a similar cell, they reported that the lifetime of AP2 above 100 and 300 nm resembled that of clathrin-coated pits. It tells us that CME at the cellular ventral side can be mechanically triggered.

2.1.2 What is the gap in previous discoveries? Why is it important?

Integrin-mediated cellular adhesion might influence the uptake of nanoparticles at the cellular ventral side, however it was less studied

Wiegand et al. used integrin ligands to coat nanoparticles [121]. They aimed to increase the adhesion energy between the cell membrane mediated by integrin receptors and integrin ligand-coated nanoparticles to overcome the energetic cost of membrane tension. Indeed, they observed an increase in uptake upon coating the nanoparticles with integrin ligands. They also reported the vital role of the actin-cytoskeleton as they observed the diminished number of particle uptake when the actin polymerization was inhibited using a pharmacological treatment (i.e., Cytochalasin D and Latrunculin A). However, the information regarding whether the uptake was clathrin-dependent was not explored.

Wiegand et al. used integrin ligands to study the molecular adhesion that led to the uptake of nanoparticles at the cellular ventral side. However, based on the effects of Cytochalasin D (actin polymerization inhibitor) on cellular adhesion, I could inevitably build a rationale that the integrin-mediated cellular adhesion strength might also influence nanoparticle uptake at the cellular ventral side. The strength of cellular adhesion could be tuned using soft substrates and measured by traction force microscopy. To my knowledge, no specific study has been performed to answer this. In my opinion, this study is vital to challenge to what extent *in vitro* experimental results could be transferred to *in vivo* studies. All these experiments were performed on a glass substrate, which is mechanically stiff and flat. Inside tissues, ECM is much softer than glass and consists of fibrous proteins like collagen and fibronectin.

As mentioned before, Fratini et al. reported that CME at the cellular ventral side could be mechanically triggered [43]. However, as nanoparticles were covalently bound to the surface, they did not report whether more clathrin machinery recruitment leads to more particle removal. As the nanoparticle size used by Wiegand et al. matched the size that triggered clathrin machinery recruitment (i.e., 100 nm), some of those nanoparticles might be internalized *via* CME.

2.1.3 Motivation

Why did I have an interest in studying the influence of integrin-mediated cellular adhesion on clathrin-mediated endocytosis of nanoparticles at the cellular ventral side?

Why the ventral side? To my knowledge, few *in vitro* studies have been performed to study nanoparticle uptake mechanisms at the cellular ventral side. In comparison, general nanoparticle uptake experiments were typically performed by putting nanoparticles in suspension. This way, nanoparticles would eventually interact mainly with the apical/dorsal membrane and be internalized. This study was mainly motivated by developing efficient nanoparticle-based drug carriers to combat diseases [31].

The biologically-relevant motivation behind the second part of my doctoral thesis work was not related to any study about drug carriers. The main reason why I was interested studying the uptake at the ventral side was the fact that several viruses gain entry at the ECM/cell interface by hijacking cell receptors such as integrins (reovirus, adenovirus) and are subsequently internalized by cells *via* CME [85]. Furthermore, reovirus infection of human airway epithelia is more efficient after adsorption to the basolateral surface than the apical surface [41].

The ventral side of the cell is the interface between the cell-ECM where one could quantify 2D or 2.5D traction forces, especially at the cell periphery. Furthermore, since nanoparticles could be immobilized on the surface, one could efficiently study the correlation of nanoparticle uptake with putative proteins using advanced light microscopy techniques.

Why using nanoparticles? The initial interest was to work directly with the virus. However, as the laboratory safety regulations did not allow me to work with viruses such as reoviruses, I shifted to 200 nm fluorescent carboxylated nanoparticles as the most practical solution. Fluorescent carboxylated nanoparticles were commercially available and could be used in a biosafety level 1 lab. Furthermore, the size was in the range of nanoparticles that were used to trigger CME (i.e., 100 - 300 nm) [43].

Why CME? CME is the major endocytic pathway in mammalian cells and is well-recognized for mediating the entry of some viruses, including reoviruses [85]. Although it has been 50 years since the initial discovery of the clathrin protein, the study of CME still generates high research interest, for example, in the mechanobiology field.

Why studying the influence of cellular adhesion? Clathrin-coated structures seem to vary significantly between a soft and rigid matrix in terms of their structure and functionality [124, 7]. Baschieri et al. described a subset of long-lived and flat clathrin-coated structures assembled in response to increasing substrate rigidity [7]. Furthermore, the assembly of this mechanosensitive structure was found to be independent of focal adhesions, actin, and myosin II activity. Integrin $\alpha V\beta 5$ colocalized strongly with clathrin-coated structures on glass but not on softer substrates. On the glass, $\alpha V\beta 5$ was tightly engaged, thus leading to the frustrated endocytosis. They also confirmed that inhibiting either αV or β5 integrins using siRNAs also resulted in a loss in large and static clathrin-coated structures.

From another study, Yu et al. reported that the reduction in traction force in integrin-mediated cellular adhesion regulated the recruitment of an adaptor protein (i.e., Dab2) on β3 integrin clusters followed by endocytosis of β3 integrin clusters [124]. Yu et al. described that on a softer substrate coated with RGD, β3 integrin clusters recruited Dab2 through its phosphotyrosine-binding (PTB) domain. In comparison, they observed no colocalization on a glass coated with RGD. When they inhibited cellular adhesion on glass coated with RGD by the ROCK inhibitor (Y27632), β3 integrin clusters recruited Dab2 and talin, a classical focal adhesion protein. However, Dab2 clusters were excluded from talin clusters.

2.2 Theoretical Background

2.2.1 Integrins

The linkage of ECM to the cell requires transmembrane proteins to act as receptors. Integrins are the principal receptors in metazoan cells for binding most ECM proteins, including bone matrix proteins, collagen, fibronectin, fibrinogen, laminin, thrombospondin, vitronectin, and von Willebrand factor [96]. A single integrin molecule is a heterodimeric transmembrane glycoprotein consisting of α- and β- subunits. The α- and β- subunits vary in size between 120 - 180 kDa and 90 - 100 kDa, respectively. Each subunit is organized into a globular ligand-binding N-terminus head, a single-spanning transmembrane domain, and a short cytoplasmic tail interacting with the F-actin through multiple adapters and signaling proteins making up the adhesome [46]. There are 24 distinct integrins comprising 8 β and 16 α subunits [61]. Distinct $\alpha\beta$ integrin pairs are grouped together based on their receptor-ligand specificity (Figure 2.1). A very well-known integrin recognition sequence, the RGD sequence, was originally identified as the sequence in fibronectin that engages the fibronectin receptor, integrin $\alpha_5\beta_1$. However, it is also known as the recognition sequence for several different integrins [96].

2.2.2 Clathrin-mediated endocytosis

Clathrin-mediated endocytosis (CME) is crucial for the vesicular trafficking that transports a wide range of cargo molecules including proteins and lipids from the cell surface into the cell interior [70]. Clathrin-coated vesicles are found in all nucleated cells, from yeasts to humans. The major protein, clathrin, is a trimer of 190-kDa heavy chains. Each heavy chain is associated with a 25 kDa light chain and together they trimerize with other heavy-light chains to form a three-armed structure known as a triskelia. Another important protein in a coated vesicle associated with the plasma membrane is the heterotetrameric adaptor protein called AP2 (α, β2, μ2, σ2). AP2 proteins are well described to direct CME of transferrin receptors from the plasma membrane into endosome [83].

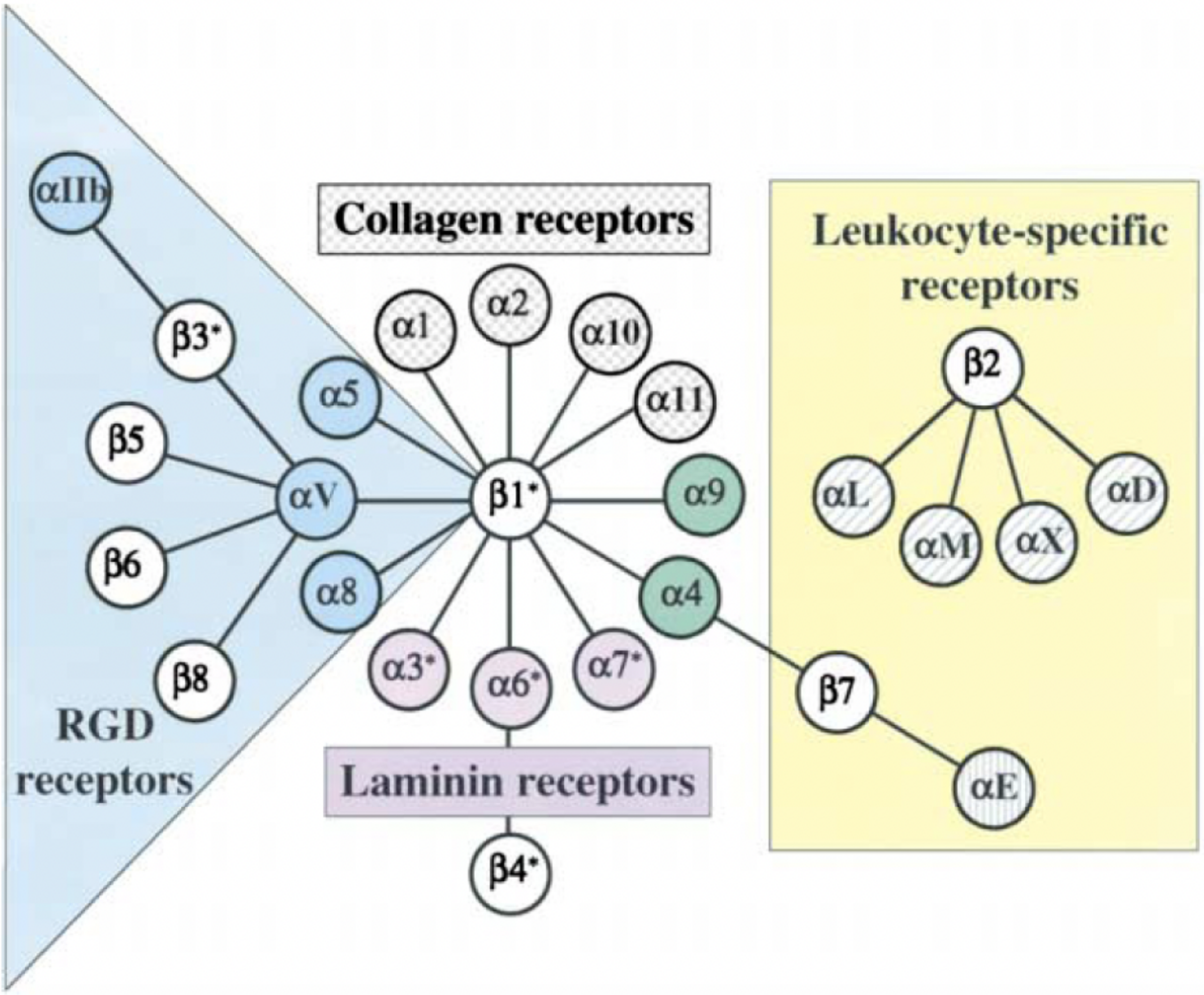
αIIb
β3*
β5
β6
β8
αV
α5
α8
RGD receptors
Collagen receptors
α1
α2
α10
α11
β1*
α9
α4
α3*
α6*
α7*
Laminin receptors
β4*
Leukocyte-specific receptors
β2
αL
αM
αX
αD
β7
αE

Figure 2.1: The family of integrin receptors. There are known 24 distinct integrins comprising of 8 β and 16 α subunits. Integrin pairs are restricted into several groups based on their receptor-ligand specificity. Reproduced with permission from Ref. [61]. Copyright 2002 Elsevier.

As shown in Figure 2.2, the proposed steps of CME begin with the nucleation step where F-BAR domain-containing proteins bind PtdIns(4,5)P_2 or PIP_2 -rich zones in the plasma membrane followed by the recruitment of EPS15-EPS15R, intersectins, and AP2 through its μ2-adaptin domain [12, 88]. Then the cargo selection step where AP2, through its μ-subunit and σ-subunit, recruits several classes of receptors to the AP2 hub. Afterward, the coat assembly step where clathrin triskelia are recruited by the AP2 hub, followed by polymerization of the clathrin trimers forming the clathrin coat around the nascent pit. Then the scission step where the GTPase dynamin is recruited to the neck of the emerging clathrin-coated vesicle by polymerized BAR-domain-containing proteins. The membrane scission is induced by GTP hydrolysis. Actin polymerization at the neck of the pit is required to aid vesicle production. Finally, the clathrin coat is disassembled by recruiting proteins such as auxilin, cyclin G-associated kinase (GAK), and HSC70 to form an endocytic vesicle containing the cargo molecules

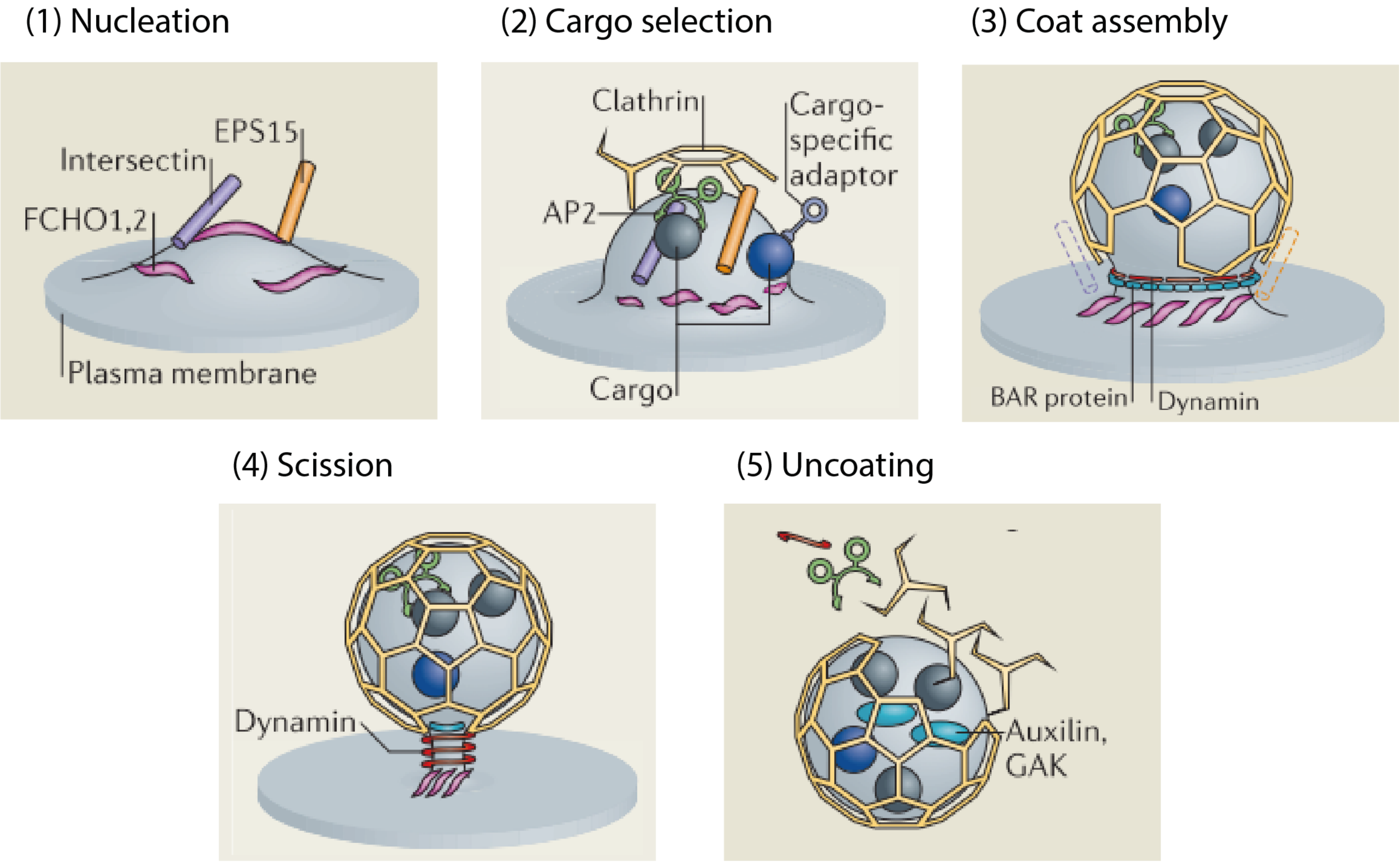
(1) Nucleation
EPS15
Intersectin
FCHO1,2
Plasma membrane
(2) Cargo selection
Clathrin
Cargo-specific adaptor
AP2
Cargo
(3) Coat assembly
BAR protein
Dynamin
(4) Scission
Dynamin
(5) Uncoating
Auxilin, GAK

Figure 2.2: Steps of clathrin-coated vesicles production in CME. Adapted with permission from Ref. [88]. Copyright 2011 Springer Nature.

2.2.3 Role of integrin-mediated cellular adhesion in the formation of clathrin coated structures

During cellular migration, cells actively regulate their adhesion to the underlying substrate mainly through the actin-integrin linkage. Actin polymerization regulates the assembly of nascent adhesions in the leading edge [47]. The dynamic cross-linking of actin filaments triggers adhesion maturation and the disassembly process is dictated by the breaking of these physical linkages.

The formation of clathrin-coated pits is vital for recycling disassembled integrins [21]. It is known that CME is involved in the turnover of β1 integrin during the diassembly of focal adhesions. Furthermore, Chao et al. reported that knockdown of dynamin 2 or clathrin adaptors (i.e. AP2 and Dab2) impaired the disassembly of focal adhesions and cell migration. Meanwhile, the role of integrin is known to facilitate the formation of clathrin-coated pits. β1 integrins were reported by Maginnis et al. to engage CME of mammalian reovirus in HeLa cells from the dorsal side [85].

β1 integrins are known to be present on both dorsal and ventral surfaces in adherent cells [106, 24, 85]. However, integrin-mediated adhesions are more relevant for ventral surfaces as the dorsal surfaces do not interact with the underlying substrate. Underlying adhesion sites do not only provide the adhesion stability but can also translate mechanical cues into biochemical signals that determine the cell behaviour.

Reticular adhesome : clathrin-containing adhesion complexes

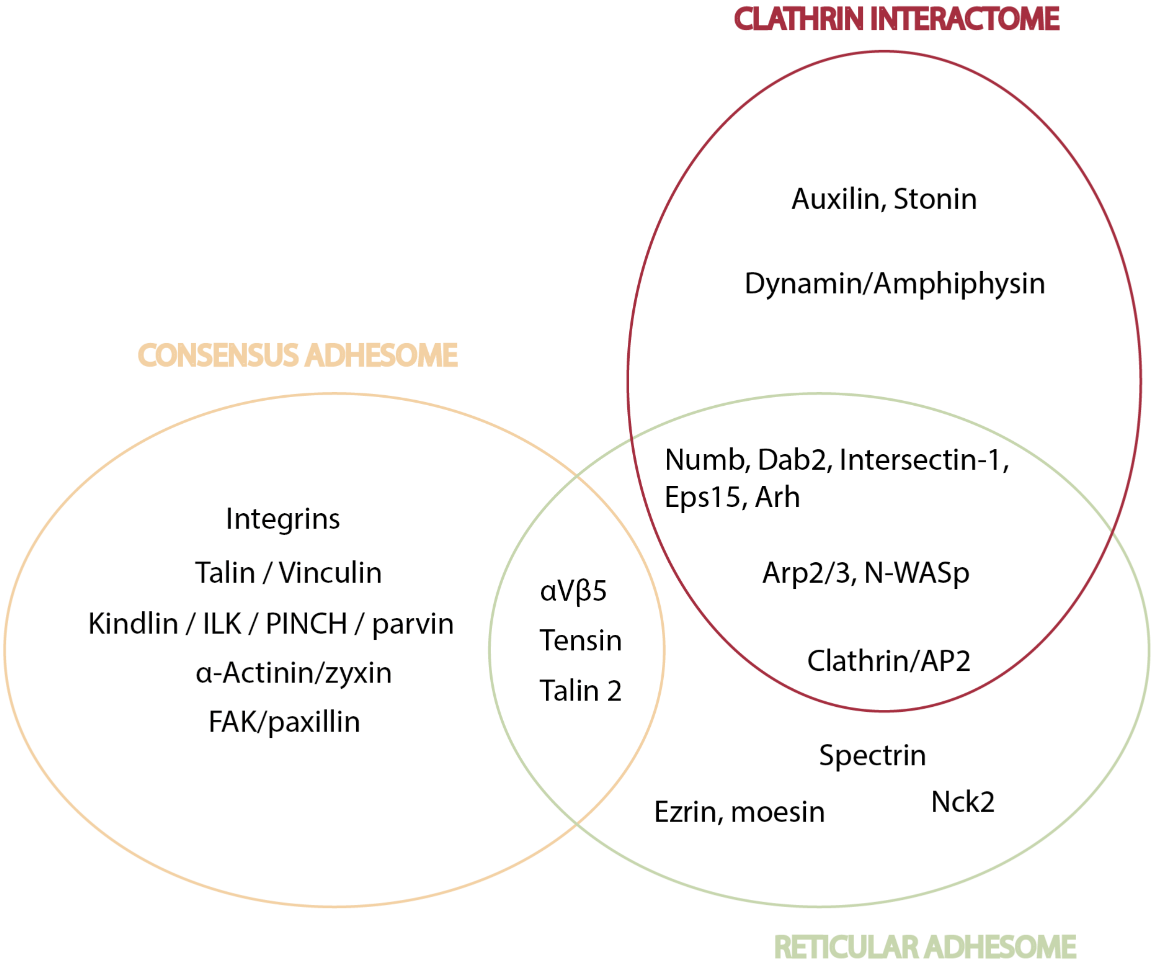
CLATHRIN INTERACTOME
Auxilin, Stonin
Dynamin/Amphiphysin
CONSENSUS ADHESOME
Integrins
Talin / Vinculin
Kindlin / ILK / PINCH / parvin
α-Actinin/zyxin
FAK/paxillin
αVβ5
Tensin
Talin 2
Numb, Dab2, Intersectin-1, Eps15, Arh
Arp2/3, N-WASp
Clathrin/AP2
Spectrin
Ezrin, moesin
Nck2
RETICULAR ADHESOME

Figure 2.3: Comparing the consensus adhesome of canonical adhesion complexes to the reticular adhesome and the clathrin interactome. Most proteins in the consensus adhesome are distinct from the other adhesomes. However, the reticular adhesome and the clathrin interactome share many proteins. Therefore, they are highly analogous. Adapted with permission from Ref. [81]. Copyright 2019 Rockefeller University Press.

Pioneered by Heuser et al. in 1980, several groups have reported the long-lived and large clathrin coated structures that were in close proximity to the substratum and associated with integrin receptors [55, 87, 30, 74]. Initially, the structures were viewed as endocytic intermediates with a primary function of receptor distribution [30]. However, as Baschieri et al. reported in 2018, the structures were anchored to the substrate by $\alpha V\beta 5$ integrins leading to the failure in budding and the formation of extended plaques [7]. They introduced it as the frustrated endocytosis. In the same year, Lock et al. reported that $\alpha V\beta 5$ integrins dominated the adhesion of cells in long-term culture and mitosis [82]. The adhesion was found to be lacking of actin and most components of the consensus adhesome. They termed the adhesion complexes responsible for the adhesion the reticular adhesome. Proteomic cataloging of the reticular adhesome revealed many components of clathrin machinery, and subsequent ultrastructural and kinetic analyses confirmed their similarity, if not identity, to clathrin plaques (Figure 2.3).

Along with $\alpha V\beta 5$ integrins, it was also reported that reticular adhesions/clathrin plaques were enriched with PIP_2 [77, 7, 82, 126]. The depletion of enzyme that generates PIP_2 was reported to decrease the level $\beta5$ integrins [82]. Furthermore, the use of Neomycin, PIP_2 binding inhibitor also reduced the level $\beta5$ integrins. These findings indicate that PIP_2 promotes reticular adhesions.

2.3 Materials and Methods

2.3.1 Cell Culture

Mouse embryonic fibroblast-AP2 lox clath-RFP/AP2-eGFP MEF cells stably expressing clathrin-light chain A (CLTA) tagged with RFP and AP2-$\sigma 2$ domain tagged with eGFP (kindly provided by Sigismund's group) were cultured in Dulbecco's Modified Eagle Medium (DMEM) (Thermo Fisher, #41965) supplemented with 10 % Fetal Bovine Serum (FBS) South America Origin (Biowest, #S181T) and 1 % penicillin streptomycin (Gibco, #15140-122).

Mouse embryonic fibroblast myosinVI-eGFP MEF cells stably expressing myosinVI tagged with eGFP (kindly provided by Polo's group) were cultured in DMEM (Thermo Fisher, #41965) supplemented with 10 % FBS South America Origin (Biowest, #S181T) and 1 % penicillin streptomycin (Gibco, #15140-122).

HeLa AP2-eGFP HeLa cells (immortal cervical cancer cells) stably expressing AP2 tagged with eGFP (generated and kindly provided by Ms. Federica Pennarola) were cultured in DMEM (Thermo Fisher, #41965) supplemented with 10 % FBS (Sigma Aldrich, #F7524) and 1 % penicillin streptomycin.

All cells were cultured inside an incubation chamber with 37 degrees Celsius, 5 % CO_2, and 95 % relative humidity (RH). For all experiments, cells were rinsed with PBS, trypsinized with 0.05 % trypsin, resuspended in medium with serum, and seeded on substrates. All cells tested negative for the mycoplasma contamination.

2.3.2 Immunostaining

For staining, cells were washed once with PBS followed by the fixation using 4 % paraformaldehyde (PFA) for 10 minutes. Next, cells were washed with 0.1 % v/v Triton X-100 in PBS (3 x 5 mins). Afterward, cells were treated with 1 % m/v BSA in PBS for 1 h at RT. Cells were then washed with PBS followed by the incubation with the primary antibodies diluted in 1 % m/v BSA in PBS for 1 h at RT. Afterward, cells were washed again with 0.1 % v/v Triton X-100 in PBS (3 x 5 mins). Cells were washed with PBS followed by incubation with the secondary antibodies diluted in 1 % m/v BSA in PBS for 1 h at RT or overnight at 4 degrees Celsius. Finally, cells were washed with PBS. Each coverslip was mounted on a microscopy glass slide by using Mowiol and let dry at RT overnight.

List of antibodies

Lists of primary, secondary antibodies, and fluorescent affinity binders are shown in Table 2.1 and 2.2.

Table 2.1: Primary antibodies.

Name	Details	Manufacturer
anti-Paxillin	Monoclonal mouse IgG #610620, 1:500	BD Biosciences Germany
anti-Zyxin	Polyclonal rabbit IgG #Z4751, 1:400	Sigma Aldrich Germany
anti-β1 integrin (CD29)	Monoclonal rat IgG2a #550531, 1:400	BD Biosciences Germany
anti-β3 integrin chain	Monoclonal rat IgG2a #M030-0 Luc.A5, 1:400	Emfret Analytics Germany
anti-Dab2	Polyclonal rabbit IgG #HPA028888, 1:400	Merck Germany
anti-PIP$_2$	Monoclonal mouse IgG2b #ADI-915-052-020, 1:400	Enzo Germany

Table 2.2: Secondary antibodies and fluorescent affinity binders.

Name	Details	Manufacturer
goat anti-mouse Alexa680	#A-21058, 1:200	Thermo Fischer Scientific Germany
goat anti-rat Alexa647	#A-21247, 1:200	Thermo Fischer Scientific Germany
goat anti-rabbit TRITC	#T6778, 1:200	Sigma Aldrich Germany
anti-phalloidin Alexa555	#A-34055, 1:400	Sigma Aldrich Germany
DAPI	1:1000	Roth, Germany

2.3.3 F-actin labelling for the fluorescent live imaging

To label F-actin for the live fluorescent imaging 1 hour before observing on the microscope, cells were washed once with warm PBS followed by adding 1 μl of SiR-actin (Spirochrome) in Dimethyl sulfoxide (DMSO) per 1 ml of warm imaging medium. This corresponded to 1 μM of SiR-actin. Additionally, 1 μl of verapamil in DMSO per 1 ml of warm imaging medium was also added. This corresponded to 10 μM of verapamil. The cells were kept at 37 degrees Celsius, 5% CO$_2$, and 95% RH for 1 hour before imaging.

2.3.4 Image acquisition

Confocal Laser Scanning Microscope Confocal images were acquired using an Axio Observer Z1 inverted microscope. The microscope was equipped with laser scanning confocal module (Zeiss, #LSM880), the Airyscan module GaAsP (Zeiss), fluorescent and transmission light filterblocks (38 GFP RL, 43 DsRed RL, 49 DAPI RL, and Pol TL), a Plan APO 63x oil immersion objective NA = 1.4, and several laserlines including 405 nm, 561 nm, and 633 nm (Zeiss).

Total Internal Reflection Fluorescence Microscope

Olympus Delta Vision IX81 TIRF images were acquired using an IX81 inverted microscope (Olympus). The microscope was equipped with an incubation chamber (Life Imaging Services Reinach), the IX2-RFACEVA TIRF attachment (Olympus), a 60x TIRF oil immersion objective NA = 1.49 (Olympus, #APON60X0TIRF), dichroic fluorescence filter sets including DAPI, GFP, RFP, and Cy5 (Chroma), a CCD camera (Quantix 57), and an argon laser source model I77 (lines 488 nm, 514 nm) (Spectra Physics).

Nikon H-TIRF TIRF imaging was performed with the help of Dr. Ulrike Engel at Nikon Imaging Center (NIC), Heidelberg University. TIRF images were acquired using an Eclipse Ti2 inverted microscope with the perfect focus system feature (Nikon). The microscope was equipped with H-TIRF module (Nikon), an on-stage incubation chamber (TokaiHit), Apo TIRF 60x NA = 1.49 (Nikon), and Andor iXon Ultra DU-897U EMCCD camera (Oxford Instruments)

Reflectance Interference Contrast Microscope RICM images were acquired using an Axio Observer Z1 inverted microscope with the definite focus feature (Zeiss). The microscope was equipped with a 63x Plan Neofluar Antiflex oil immersion objective NA = 1.25 (Zeiss, #420489-9900), fluorescent and transmission light filterblocks (38 GFP RL, 43 DsRed RL, 49 DAPI RL, and Pol TL), a RICM filter cube with beam splitter (50R/50T VIS), a polarization filter (AHF), a Colibri LED light source (Zeiss), and a dual CCD camera system (Zeiss, AxioCam HRM).

Widefield Microscope

Leica DMi8 Images were acquired using a DMi8 inverted microscope (Leica). The microscope was equipped with an incubation chamber (Pecon, Incubator8), a LED light source X-Cite 200DC (Lumen Dynamics), Heating and CO_2 controller (Pecon), fluorescence filter sets including DAPI, FITC, rhodamine, Y5, and QSP-T (Chroma), a HC PL APO 63x oil immersion objective NA = 1.4 (Leica, #11506349), and an sCMOS camera (Leica, #DFC9000GT).

Nikon Eclipse Ti2 Images were acquired using an Eclipse Ti2 inverted microscope (Nikon). This microscope was equipped with an incubation chamber (EMBLEM), a CFI Plan FLuor ELWD 20x air objective NA = 0.45 (Nikon, #MRH08230), a CFI P-Apo 40x lens NA = 0.95 (Nikon, #MRD00405), a fluorescence filter sets including GFP, Cy3, and Cy5 (Chroma), and an sCMOS camera (Hamamatsu, #C11440 - 42U30).

2.3.5 Biofunctionalization of the surface

Biofunctionalization of the glass/PDMS surface 200 μl of solution containing 25 μg/ml of fibronectin in PBS was pipetted dropwise onto the the surface of glass/PDMS elastomer. Finally, the surface was rinsed thrice with PBS and stored in PBS at RT.

Biofunctionalization of the PA surface 250 μl of 1 mg/ml sulfo-SANPAH (Sigma Aldrich, stock solution = 25 mg/ml in DMSO) was pipetted onto the surface of PA. Next, the hydrogel was illuminated with a UV light ($\lambda = 365$ nm, 7.5 mJ/mm^2). Upon illumination, phenylazide groups form nitrene groups reacting to PA. Next, the hydrogel was rinsed multiple times with ddH$_2$O. Next, 200 μl of solution containing 25 μg/ml of fibronectin in PBS was pipetted dropwise onto the the surface of PA hydrogel. Finally, the surface was rinsed thrice with PBS and stored in PBS at RT.

2.3.6 Immobilization of nanoparticles on the surface

Covalent immobilization of nanoparticles on the PA surface For the covalent immobilization of nanoparticles on the surface of PA, As described in part I for the micropatterning of PA, oxidized HEA solution was prepared by mixing 50 mg/ml of N-Hydroxyethyl Acrylamide and 20 mM sodium (meta)periodate in ddH$_2$O and stirred for 4 hours in dark at RT before use. The fluorescent nanoparticles stock solution (200 nm, aminated) (Invitrogen, #F8764) was diluted 1 % v/v in PBS, pipetted dropwise onto a clean glass coverslip, and incubated for 1 h at RT. Afterward, the coverslip was gently rinsed with PBS and dried with the air gun. Then, a hydrogel precursor prepared by mixing 98.3 μl of the stock solution (see Figure 1.2), 1 μl of oxidized HEA, 0.5 μl of APS 10 %, and 0.2 μl of TEMED was pipetted dropwise on a methacrylated coverslip (see Figure 1.16). After that, the coverslip presenting aminated nanoparticles was placed on the droplet. Finally, the top coverslip was detached by a scalpel. The hydrogel was rinsed thrice with PBS and stored in PBS at RT.

Covalent immobilization of nanoparticles on the glass/PDMS surface The attachment solution was prepared by mixing 0.1 mg/ml EDC and 1 % v/v carboxylated fluorescent beads (Invitrogen, #F8805/ #F8848/ #F8810/ #F8807) in ddH$_2$O. Glass/elastomer substrates were cleaned using the oxygen plasma (100 W, 0.4 mbar) for 20 s. Then, the surface of the elastomer was conjugated with 10 % v/v of 3-aminopropyl trimethoxysilane in ethanol for 5 minutes, followed by rinsing with ethanol once and twice with ddH$_2$O. The attachment solution was placed on the surface of the elastomer and was incubated for 30 minutes. Finally, the elastomer was rinsed multiple times with ddH$_2$O and stored in ddH$_2$O at RT.

Electrostatically immobilization of nanoparticles on the glass/PDMS/PA surface For the non-covalent (i.e. electrostatically) immobilization of nanoparticles on the surface of glass/PDMS elastomer, 1 % v/v fluorescent nanoparticles solution (200 nm, carboxylated) (Invitrogen, #F8805/ #F8848/ #F8810/ #F8807) was pipetted dropwise onto the biofunctionalized glass/PDMS surface and incubated for 1 h. Finally, the hydrogel was rinsed thrice with PBS and stored in PBS at RT.

2.3.7 SEM imaging of critical point dried cells

To image cells using SEM without destroying the structure of the surface, cells were first fixed (i.e. protein crosslinking to increase mechanical and thermal stability) using 2 % glutaraldehyde in PBS for 15 mins followed by the dehydration process (i.e. replacing the water content in the cell by ascending concentration of liquid) in which cells were incubated in graded ethanol (1x 25 %, 1x 50 %, 1x 75 %, 2x 95 %, and 3x 100 %). Next, cells were transfered into the pressure chamber of a critical point dryer (Leica, #CPD300) *via* a holder followed by fully immersing the holder in 100 % ethanol and sealing the chamber. Then, the chamber was set to 10 degreess Celsius and 50 bar to allow liquid CO_2 filling in. The purging process (liquid CO_2 influx, mixing, efflux of CO_2-exchange fluid) was done up to 14 times until all exchanging fluid was replaced with liquid CO_2. Then, the chamber temperature and pressure were slowly raised to 40 degrees Celsius and 80 bar to generate supercritical CO_2. Then, the supercritical CO_2 was set to form gaseous CO_2 by maintaining constant temperature 31 degrees Celsius followed by slowly getting the gas out by reducing the pressure to 1 bar (i.e. atmospheric pressure). The criticial point dried cells were recovered followed by carbon-coating to increase the conductivity before SEM imaging.

2.3.8 TEM sample preparation and imaging

TEM sample preparation and imaging were conducted with the help of Dr. Charlotta Funaya at the Electron Microscopy Core Facility (EMCF), Heidelberg University. First, the surface of a sapphire disk (3 mm in diameter) was patterned using maskless photolithography, followed by biofunctionalization with fibronectin and cell seeding overnight. Afterward, cells were rapidly chilled to liquid nitrogen temperature and exposed to very high pressure (i.e., 2300-2600 bar) using a high-pressure freezer (Abra HOM-010) followed by freeze substitution. Dehydration was performed in steps of 10 minutes inside an ethanol gradient, followed by Spurr resin embedding and polymerization at 60 degrees Celsius. The blocks were sectioned using an ultramicrotome (Leica UC7), providing ultrathin sections for TEM imaging. Sections were imaged using Jeol JEM-1400 (Jeol Ltd.).

2.4 Results and Discussion

2.4.1 Traction forces exerted by cells result in removal of electrostatically immobilized nanoparticles from the surface

As reported by Wiegand et al. and supported by preliminary experiments, cells preferentially removed immobilized nanoparticles at the periphery where cells link to the underlying matrix through focal adhesions [121]. To prove that nanoparticles at the cellular ventral side were internalized under cellular traction forces, HeLa cells were seeded on a PA substrate (E = 5.74 kPa) pre-coated with fibronectin and subsequently coated with electrostatically immobilized carboxylated nanoparticles (Figure 2.4A). At 4 hours post-seeding, I picked up a single cell and recorded the movement of fiducial beads underneath the cell every 5 s for 20 minutes. The concomitant movement of electrostatically immobilized beads was also recorded. Using live 2D-LUVI-TFM, I could observe that the electrostatically bound nanoparticles were removed under cellular traction forces exerted at the cell edges as depicted in Figure 2.4B and C. In Figure 2.4B, the regions of interest (ROI) showing a nanoparticle under the traction forces and a nanoparticle that was not under the traction forces were labeled as "1" and "2". As shown in Figure 2.4C, there are four kymographs. The x-axis and y-axis of the kymograph represent the spatial length (i.e., measured in μm) and the elapsed time (i.e., measured in s). The upper kymographs describe movements of the different nanoparticles inside the ROI 1 and 2. The lower kymographs describe the traction force values inside the ROI 1 and 2. The electrostatically immobilized nanoparticle in the ROI 2 did not move as it was not under traction force. Meanwhile, the electrostatically immobilized nanoparticle in the ROI 1 was under cell traction.

Interestingly, the nanoparticle in the ROI 1 was not spontaneously removed by the cell despite being under constant stress. Within 20 minutes of observation, I observed that the traction above the particle experienced two significant drops. The longest traction drop was recorded for 160 seconds. The cell edge moved and therefore went outside and returned to the observation window is one possible reason behind the drop and the recovery. The observation window was small (i.e., 4 μm^2) and spatially fixed for the nanoparticle (i.e., a white box number 1 in Figure 2.4B). Unfortunately, I did not record any image of the cell edge to prove this. After the traction recovered, it took around 260 seconds of relatively constant stress until the particle was removed. It remained obscure why it took so long to remove, let alone internalize a nanoparticle even though it was already under the subcellular area that should contain rich adhesion proteins like integrins and endocytic proteins like clathrin.

Adhesion dynamics of a single cell is shown by plotting traction forces over time (Figure 2.4D). I observed that the total forces exerted by the cell fluctuated over time and did not show any declining trend. It indicated that the cell was healthy despite being exposed to light every 5 s for 20 minutes. Furthermore, the fluctuation in the global force was believed to be caused by several factors, including

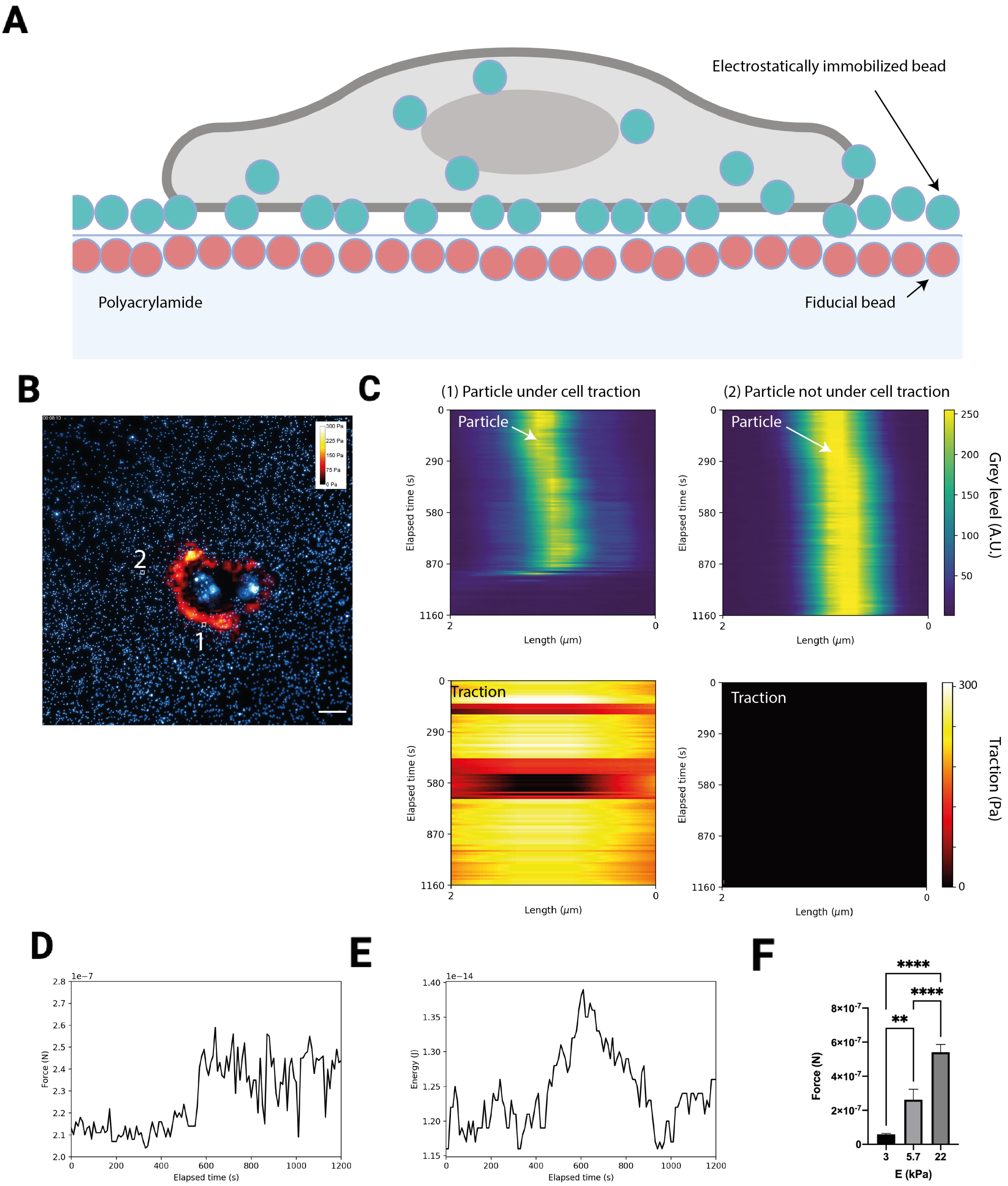

Figure 2.4: (**A**) Schematic of live 2D-LUVI-TFM during the uptake of nanoparticles at the cellular ventral side. Fiducial beads for tracking the deformation were embedded inside PA close to the surface. Beads for uptake were immobilized electrostatically on the surface. Image is created with BioRender.com (**B**) Traction force heatmap during particle uptake around 4 hours post seeding. A single HeLa cell was seeded on a 5.7 kPa PA substrate coated with fibronectin. The electrostatically immobilized particles are shown in cyan. (**C**) Kymographs show the movements of different nanoparticles in the region of interest 1 and 2. Two upper kymographs describe the movement of the different nanoparticles inside the ROI 1 and 2, whereas the lower kymographs describe the traction force values inside the ROI 1 and 2. In ROI 1, an electrostatically immobilized nanoparticle was removed from the surface under cellular traction forces. (**D**) The graph showing total forces exerted by the cell over 1200 s. (**E**) The graph showing the energy transferred from the cell to the substrate over 1200 s. (**F**) Traction forces exerted by a single HeLa cell on 3 kPa ($n = 25$), 5.7 kPa ($n = 20$), and 22 kPa ($n = 22$) substrates. Bars show mean ± S.E.M (ordinary one-way ANOVA, **** $P < 0.0001$, *** $P < 0.001$, ** $P < 0.01$, * $P < 0.05$, ns $P \leq 0.5$). **Please click here to view a full size version of this figure.**

F-actin and integrin turnover [5, 66]. The energy transferred from the cell to the substrate is shown in Figure 2.4E. Interestingly, it seemed that the cell invested some energy (i.e., from 11.6 femtojoules (fJ) to 13.8 fJ, around 2.2 fJ) to build more traction forces (i.e., from 2.15 nanonewtons (nN) to 2.45 nN, around 0.3 nN) on the substrate as the energy ramped up at around 400-600 s after the imaging started. After the traction force was raised, the cell seemed to return to its initial energy state (i.e., the energy from 0-400 s after the imaging started). I argue that cells might need to invest more energy in reinforcing their adhesion forces. To maintain the adhesion forces, cells might require less energy. However, the process governing the events remained unclear in this experiment.

Finally, the traction forces of a single HeLa cell on different substrate stiffnesses are shown in Figure 2.4F. According to the mechanosensitive molecular clutch model, cells on softer substrates exert lower traction forces due to the lower loading rate of the clutch compared to the lifetime of integrin-ECM bond [38]. The bond fails before any forces can reach talin. In comparison, as the loading rate is higher than the lifetime of integrin-ECM beyond a specific rigidity threshold, the resistive force from the matrix can activate talin and reinforce adhesion. The response of HeLa cells to varied stiffness values of PA hydrogels (i.e., 3, 5.7, and 22 kPa) confirms the molecular clutch model.

2.4.2 Controlled distribution of focal adhesion and endocytic clusters by micropatterning

Crossbow pattern to mimic a cell that displays leading edges

The previous results show that electrostatically immobilized nanoparticles were removed from the surface under cellular traction forces. It seemed that the bead was ruptured from the surface, dragged along the ventral membrane to the area closer to the cell center, and possibly was internalized there. Therefore, the link between traction force and the internalization of nanoparticles remained obscure. To elucidate it, I employed micropatterning in which I could dictate the shape and size, thereby the traction hotspots of a single cell. I chose the crossbow pattern to mimic a cell that displays leading edges. Leading edges are the hotspot of cellular traction forces and are typically rich with adhesion proteins like integrins and endocytic proteins like clathrin machinery.

Mature focal adhesion clusters in the side arc and tail regions of the crossbow

Before performing TFM, I performed experiments to investigate the spatial distribution of clathrin adaptor protein 2 (AP2) and some focal adhesion proteins on the micropattern. I used mouse embryonic fibroblast (MEF) expressing AP2-eGFP. To detect the distribution of focal adhesion proteins, I performed immunostaining of β3-integrin, paxillin, and β1-integrin.

As shown in Figure 2.5A, I observed that the density of AP2 clusters was significantly higher in the pattern area than in the non-pattern area. The pattern area was the area of integrin ligands such as

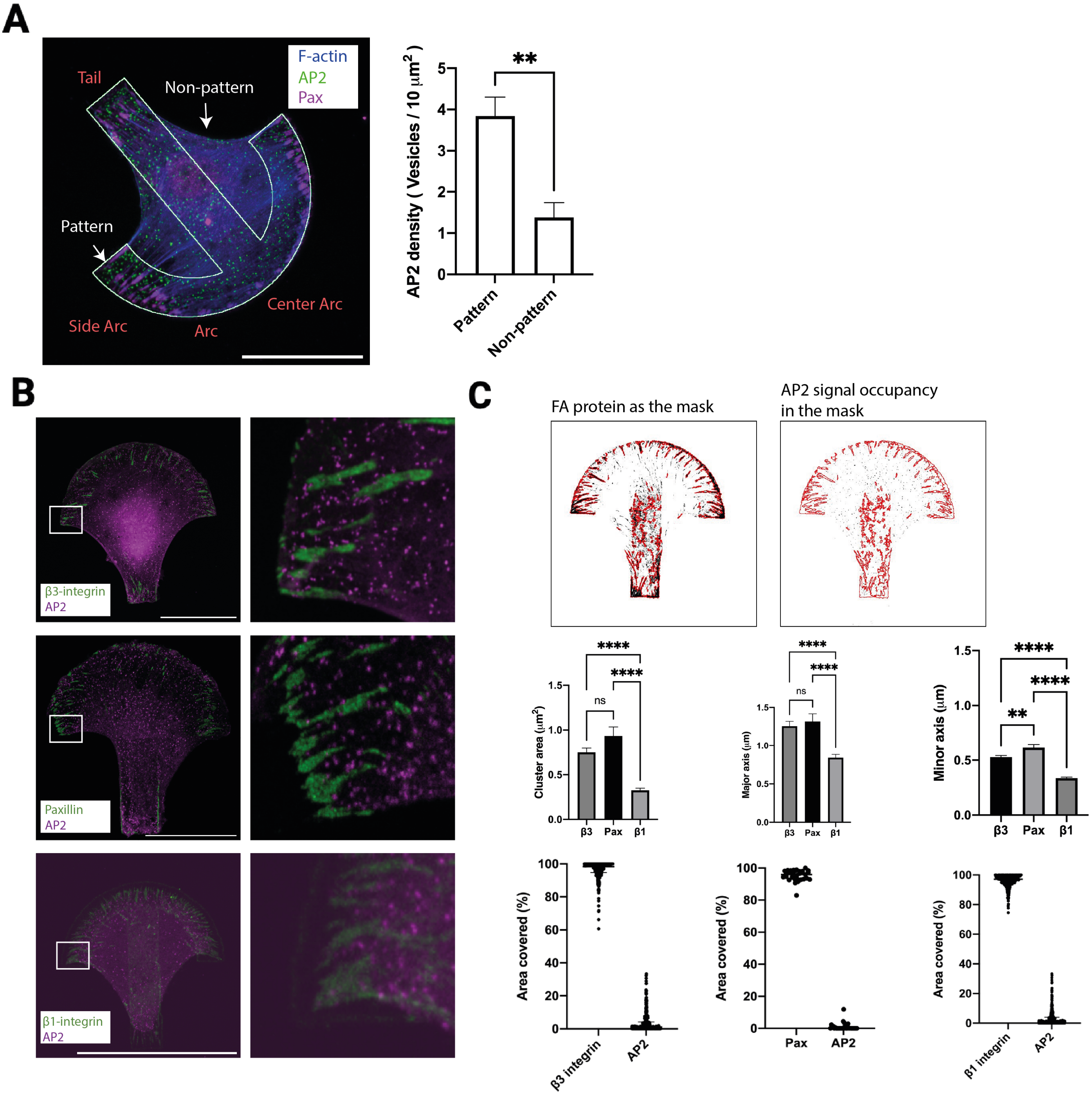
A
F-actin
AP2
Pax
Tail
Non-pattern
Pattern
Side Arc
Arc
Center Arc
AP2 density (Vesicles / 10 μm^2)
**
Pattern
Non-pattern
B
β3-integrin
AP2
Paxillin
AP2
β1-integrin
AP2
C
FA protein as the mask
AP2 signal occupancy in the mask
Cluster area (μm^2)
Major axis (μm)
Minor axis (μm)
****
ns
**
β3
Pax
β1
Area covered (%)
β3 integrin
AP2
Pax
β1 integrin

Figure 2.5: (**A**) Fluorescent micrograph of a micropatterned MEF cell expressing stable AP2 tagged with eGFP and clathrin light chain A (CLTA) (CLTA signals were not shown because they were very low in this image). AP2 density was higher in the patterned region. Scale bar = 50 μm. (**B**) Fluorescent micrographs, including the insets, showing AP2 clusters were excluded from focal adhesion clusters signified by β3-integrin, paxillin, and β1 integrin. MEF cells were seeded on the patterns coated with vitronectin (1 μg/cm^2) for β3-integrin staining. For paxillin and β1-integrin, MEF cells were seeded on the patterns coated with fibronectin (1 μg/cm^2). Scale bar = 50 μm. (**C**) (**C**) FA protein clusters (i.e., β3-integrin (n=423), paxillin (n=155), and β1 integrin(n=509)) were used as the masks, whose the area, the major, and the minor axis were quantified. Furthermore, by detecting the AP2 signal occupancy inside the mask, the area covered by AP2 could be quantified. Focal adhesion clusters excluded AP2 clusters since less than 5 % of the mask was covered by the AP2. Bars show mean ± S.E.M (ordinary one-way ANOVA, **** P < 0.0001, *** P < 0.001, ** P < 0.01, * P < 0.05, ns P ≤ 0.5). **Please click here to view a full size version of this figure.**

fibronectin. A possible reason for high AP2 density in the pattern area might be related to integrin turnover. As the cell had to maintain the adhesion constantly, integrin proteins had to be constantly recycled. In Figure 2.5A, focal adhesion clusters were labeled with canonical focal adhesion protein, paxillin. The clusters were prominently formed in the arc and tail regions. However, massive clusters were found mainly in the side arc regions and typically supported long actin stress fibers.

Focal adhesions to the ECM exclude AP2

As shown in Figure 2.5B, I investigated other focal adhesion proteins such as β3-integrin and β1-integrin. For β3-integrin and β1-integrin, I used vitronectin and fibronectin as the ligand. Like the measurement done with paxillin, I observed massive clusters of focal adhesion proteins at the side arc, and AP2 clusters were proximal to focal adhesion clusters. To quantify the spatial correlation between AP2 and focal adhesion proteins, I created a mask image by using an image of the focal adhesion protein and applied the mask to the counterpart AP2 image as shown in Figure 2.5C.

Meanwhile, I quantified the cluster area, major axis, and minor axis of focal adhesion clusters with the mask. Regarding the area and the cluster length (i.e., major axis), both paxillin and β3-integrin clusters were the largest and non-significantly different. β1 clusters were the smallest. Meanwhile, the width (i.e., minor axis) of paxillin clusters was the largest, followed by β3-integrin and β1-integrin clusters.

The area, major, and minor axis of paxillin clusters were the largest among all focal adhesion proteins. Since all forms of adhesion (i.e., focal complexes, focal adhesions, and fibrillar adhesions) were detected by paxillin [47], Those high values might be attributed to the fibrillar adhesions staining. For β1-integrin, the cluster sizes visually seemed similar to paxillin even though they were smaller after the quantification. The smaller clusters might be caused by the staining and the deficiency in the image-processing routine. β1-integrin clusters were stained using a monoclonal antibody specifically binds to a 130 kDa β1-integrin subunit (CD29). However, the antibody does not only bind to the activated integrin but also to the inactivated integrin.

Despite their non-significant difference from paxillin clusters in terms of area and length, β3-integrin clusters were exceptionally established on MEF cells seeded on micropatterns coated with vitronectin as it is widely known as the ligand for the β3-integrin [59]. Therefore, I refrained from over-interpreting the data from paxillin and β3-integrin clusters. Similarly, I refrained from over-interpreting the data from β3-integrin and β1-integrin clusters as the cells were not seeded on a surface with a similar ECM protein.

According to the initial aim, this experiment was not planned to compare the behavior of paxillin, β1-integrin, and β1-integrin clusters. The aim of this experiment was to investigate the spatial relation between focal adhesions and AP2 clusters to elucidate the link between integrin-mediated traction forces and the uptake of nanoparticles at the cell periphery that possibly be mediated by CME.

By mirroring the mask of focal adhesion clusters to the counterpart AP2 image, I could quantify the AP2 occupancy inside focal adhesion clusters as shown in Figure 2.5C. The result shows that focal adhesion clusters excluded AP2 clusters since less than 5 % of the mask was covered by the AP2. The finding confirmed the consensus in the adhesion field that clathrin machinery is widely known not to be associated with canonical adhesion complexes [82].

2.4.3 Controlled distribution of traction forces by micropatterning

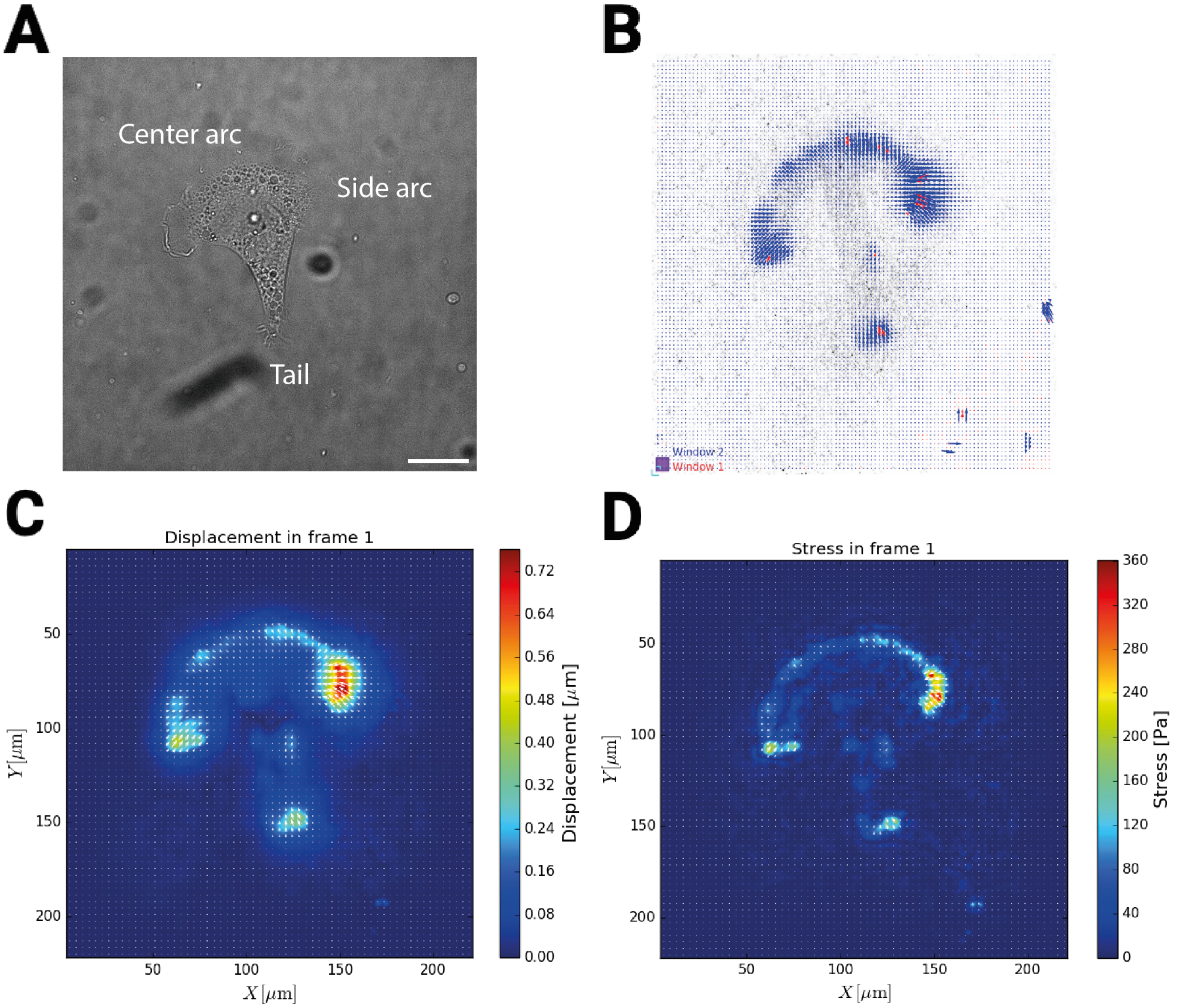

Figure 2.6: High traction forces in the side arc and tail regions. (**A**) Phase contrast image of micropatterned MEF on a 5.4 kPa PA hydrogel. Scale bar = 20 μm. (**B**) After releasing the traction forces *in situ* with a near UV (UVA) light, the substrate deformation was tracked with PIV. (**C**) The displacement field. (**D**) The reconstructed stress field. **Please click here to view a full size version of this figure.**

High traction forces in the side arc and tail regions of the crossbow

Figure 2.6 shows a single MEF cell on a micropatterned PA hydrogel coated with fibronectin (A). After releasing the traction forces *in situ* with a near UV (UVA) light, the substrate deformation was tracked with particle imaging velocimetry (PIV) generated by a program from Schwarz's group (B). Figure 2.6C and D show the successful displacement and the stress fields reconstruction.

By performing 2D-LUVI-TFM on a 5.4 kPa PA hydrogel, high traction hotspots were observed in the side arc and tail regions, where massive clusters of focal adhesion proteins like β3-integrin, paxillin, and β1-integrin were also previously discovered on glass. I chose 5.4 kPa because the rigidity threshold in which the matrix resistive force can activate talin before the integrin-ECM bond fails is around 5 kPa according to the molecular clutch model [38]. Therefore, I assumed that traction forces on the 5.4 kPa PA hydrogel were mediated by talin unfolding and vinculin binding.

The reason for high traction forces in the side arc and tail regions could lie in the fact that as the cell was static, massive focal adhesion clusters should transmit higher traction forces to the matrix than small clusters, as big clusters were connected to long and dense actin stress fiber *via* adhesion proteins such as talin and vinculin (Figure 2.5B).

2.4.4 Traction forces alone were insufficient to remove nanoparticles

Nanoparticles along the crossbow arc could not be removed by the cell

After characterizing the distribution of endocytic protein clusters, focal adhesion protein clusters, and traction force hotspots of the micropatterned cell, I focused on the side arc regions of the micropatterned cell as they presented a high density of AP2 clusters, focal adhesion clusters, and high traction forces. To do this, I performed micropatterning of fibronectin on a glass surface followed by electrostatic immobilization of nanoparticles. Finally, cells were seeded on the micropatterns overnight. As I expected, cells internalized nanoparticles. Interestingly, some nanoparticles remained along the arc, as shown in Figure 2.7A and Figure 2.8. It was still unclear how those nanoparticles formed a line of bead clusters along the arc curvature.

One might argue that the repellent PEG brushes at the pattern boundary played a role. However, the nanoparticles were 200 nm in diameter, whereas PEG brushes were typically only several nanometers in height. It could also be that there were still some uncovered positive-charged PLL at the area close to the arc boundary that interacted with negative-charged nanoparticles. As mentioned in part I, the light-based micropatterning uses UV light to cleave PEG polymer brushes from the surface. The chemical composition of UV exposed and UV non-exposed areas was assessed with X-ray photoelectron spectroscopy (XPS) by Azioune [4]. He reported that UV exposure led to the disappearance of PEG-carbon and the appearance of carboxyl groups contributing to the strong attachment of proteins. Compared to the extreme decrease of PEG carbon (C-O-C), the decrease of PLL backbone (C-C/C-H) was milder. Thus, the other possibility that nanoparticles were trapped at the arc boundary might be due to uncovered positive-charged PLL.

The possibility of uncovered positive-charged PLL should not be limited to the arc boundary but also to all patterned areas. However, as shown in Figure 2.7A, only nanoparticles at the arc boundary remained attached under a spreading cell. It seems that the cell could not remove them.

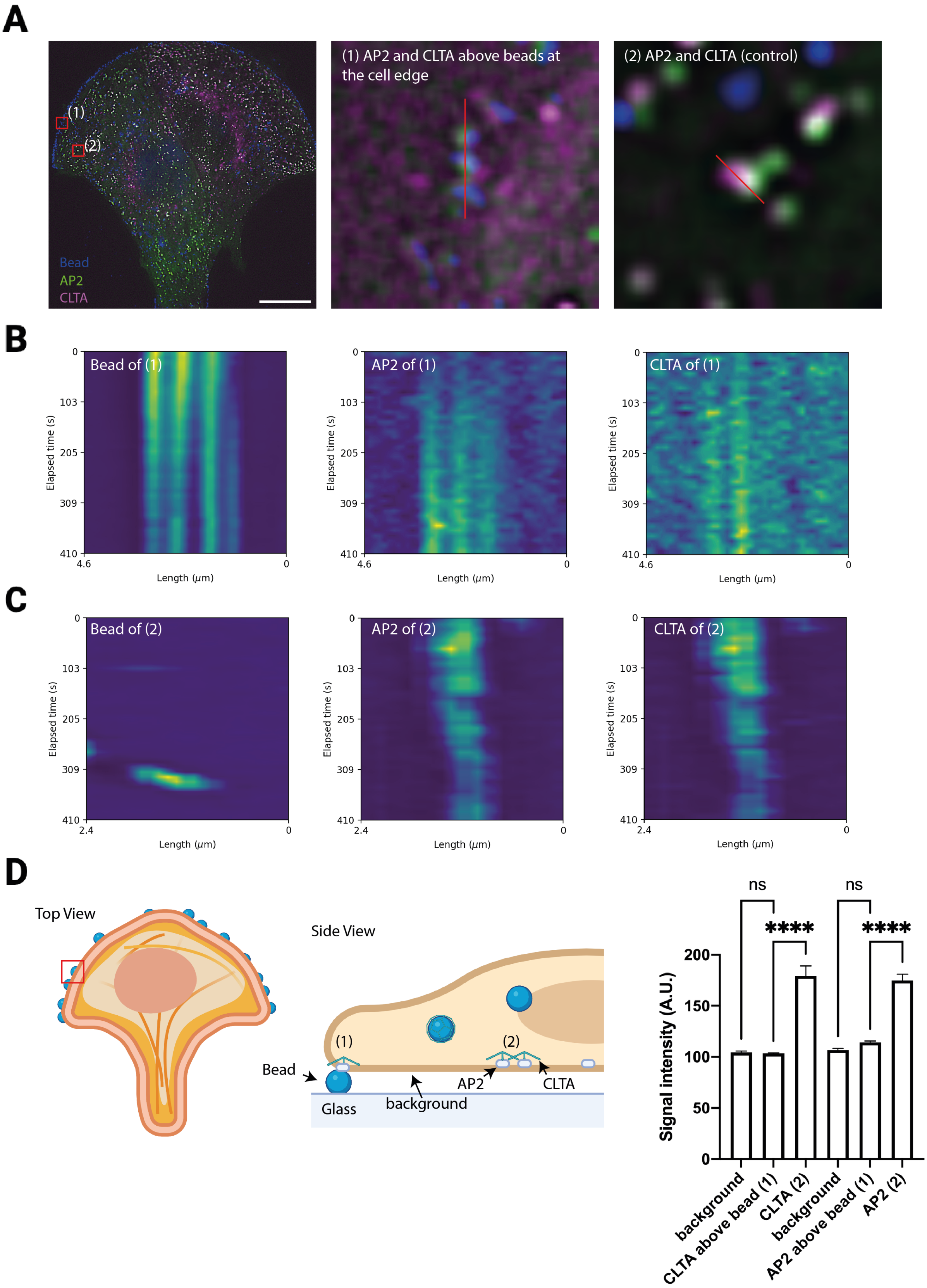
A
(1)
(2)
Bead
AP2
CLTA
(1) AP2 and CLTA above beads at the cell edge
(2) AP2 and CLTA (control)
B
Bead of (1)
AP2 of (1)
CLTA of (1)
Elapsed time (s)
0
103
205
309
410
4.6
0
Length (μm)
C
Bead of (2)
AP2 of (2)
CLTA of (2)
2.4
D
Top View
Side View
Bead
Glass
background
AP2
CLTA
(1)
(2)
ns
ns
****
****
Signal intensity (A.U.)
200
150
100
50
0
background
CLTA above bead (1)
CLTA (2)
background
AP2 above bead (1)
AP2 (2)

Figure 2.7: (**A**) Fluorescent micrographs of a micropatterned MEF expressing AP2 tagged with eGFP and CLTA tagged with RFP cell taken with live-TIRF. Scale bar = 20 μm. Inset (1) shows AP2 (green) and clathrin-light chain A CLTA (magenta) clusters above immobilized nanoparticles in the side arc region. Inset (2) shows random AP2 (green) and CLTA (magenta) clusters. (**B**) Kymograph showing the recruitment of AP2 and CLTA clusters above immobilized nanoparticles in the side arc region. (**C**) Kymograph showing the kinetics of random AP2 and CLTA clusters. (**D**) Quantification of signal intensity of the background (n=10), AP2 and CLTA clusters above immobilized nanoparticles in the side arc region (n=10), and arbitrary AP2 and CLTA clusters (n=10). Schematics were created with BioRender.com. Bars show mean ± S.E.M (ordinary one-way ANOVA, **** $P < 0.0001$, *** $P < 0.001$, ** $P < 0.01$, * $P < 0.05$, ns $P \leq 0.5$). **Please click here to view a full size version of this figure.**

Despite no removal, CME was initiated above immobilized nanoparticles in the arc regions

As the cell was fully grown on the micropattern, I checked if nanoparticles in the arc regions could recruit clathrin machinery. Using kymograph analysis, I observed the recruitment of very weak AP2 and clathrin-light chain A (CLTA) signals above those nanoparticles (Figure 2.7B) were very noisy compared to control AP2 and CLTA signals (Figure 2.7C). Unfortunately, I could not compare with AP2 and CLTA signals above beads in the center as most beads were already internalized, perhaps while the cell was spreading on the pattern. As shown in Figure 2.7D, I compared the signal intensity of AP2 and CLTA when they were above nanoparticles in the arc regions versus arbitrary AP2 and CLTA signals. The result shows that AP2 and CLTA were so weak when they were above nanoparticles in the arc regions as the average value was non-significantly different from the background. Nevertheless, as shown in Figure 2.7B, the recruitment of those weak AP2 and CLTA indicated that CME might be initiated several times but never reached productive endocytosis.

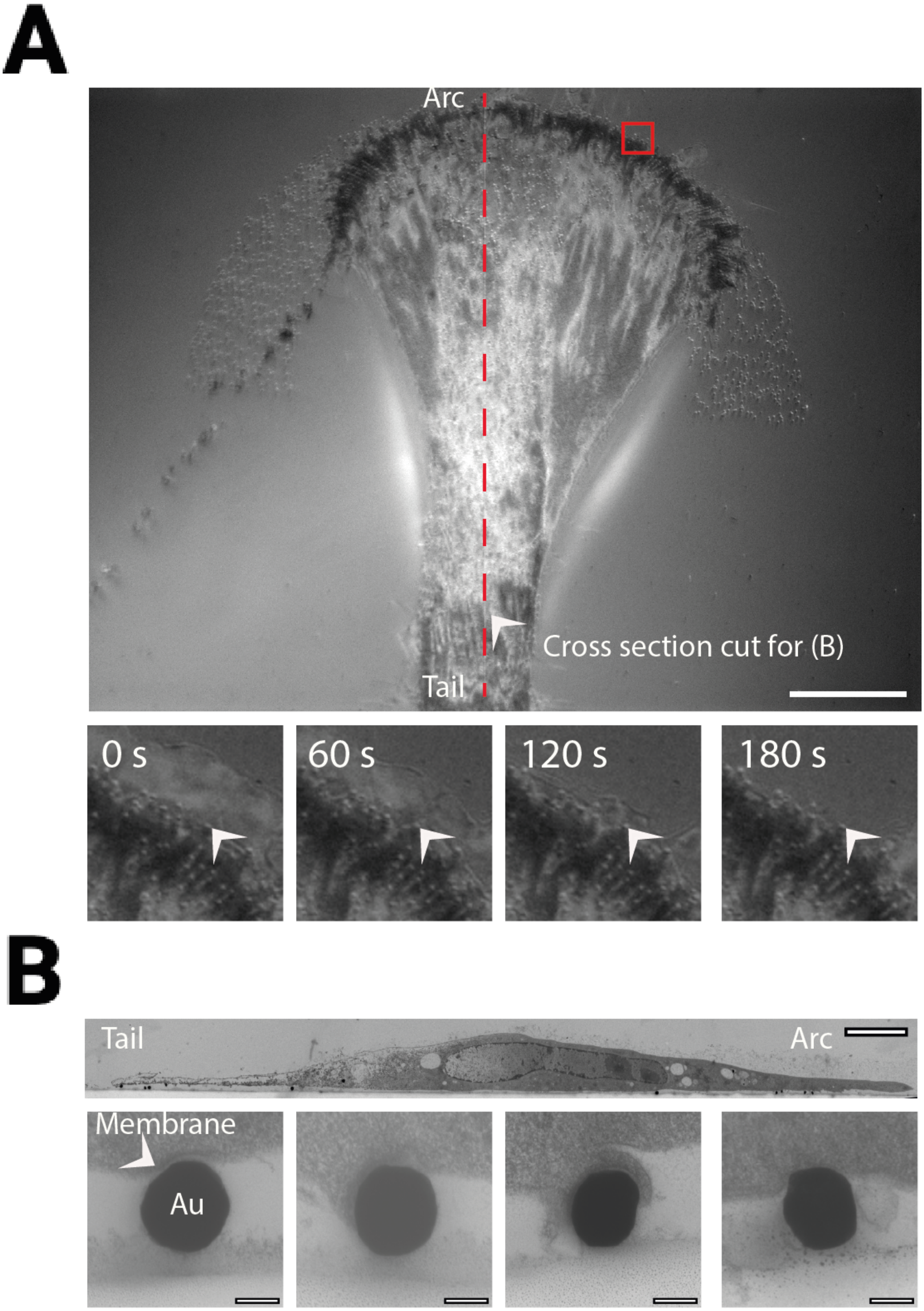

Figure 2.8: (**A**) Micrographs of a micropatterned MEF cell above electrostatically immobilized nanoparticles were taken with live-RICM. A darker RICM signal along the crossbow arc indicated that the ventral membrane (marked with the red square) was intimately linked to the matrix. Scale bar = 20 μm. Insets show that a nanoparticle was linked to the membrane but could not be removed from the surface. (**B**) TEM images from ultrathin section of a micropatterned MEF cell that was seeded above electrostatically immobilized 300 nm gold nanoparticles (Au). The cross section was taken from the central part connecting the arc and the tail of the crossbow. Scale bar of the cell cross section = 5 μm. Scale bar of the cross section showing a gold deforming the ventral membrane = 200 nm. **Please click here to view a full size version of this figure.**

According to the results I obtained from experiments using static micropatterned cells, I think that traction forces through integrin-mediated cellular adhesion alone were insufficient to remove nanoparticles as I did not observe any removal of electrostatically immobilized nanoparticles under the area where the cell exerted high traction forces. Another factor, such as the membrane dynamic at the cell edge, might contribute to the removal of electrostatically immobilized nanoparticles.

After finding out that traction forces alone were insufficient to remove electrostatically immobilized nanoparticles, I continued to investigate the role of traction force in initiating particle uptake *via* CME at the cellular ventral side. As shown in Figure 2.7B, AP2 and CLTA were recruited above beads in the side arc regions where the cell exerted high traction forces. In the area of high traction forces, the ventral membrane of the cell edge might be more pushed against the underlying matrix by the actin cytoskeleton compared to the center/perinuclear area as indicated by Figure 2.8A. The insets also confirm that an electrostatically immobilized nanoparticle was linked to the cell membrane in the arc region where the cell exerted high traction forces, but it could not be removed by the cell. Furthermore, in the area of high traction forces (i.e., arc and tail regions), immobilized nanoparticles will intimately interact with the membrane, causing membrane deformation that initiates CME as shown by the insets showing a gold nanoparticle in different locations under the ventral membrane at the cell periphery (Figure 2.8B). For better quality in TEM imaging, I used gold nanoparticles instead of polystyrene nanoparticles.

To elucidate the role of traction force in initiating particle uptake *via* CME at the cellular ventral side, I focused on cells that transitioned between the early adhesion phase (P1) and the initial contractility phase (P2) at around 4 hours post-seeding [98]. As cells still exhibited the shape of a symmetric “bulls-eye egg” (Figure 2.9B), it would be easier to compare with other measurements. In this experiment, nanoparticles were covalently bound to the surface not only to avoid particle removal by cells but also to trigger CME as shown by Fratini et al. [43].

2.4.5 AP2 clusters were highly distributed at the cell edge at 4 hours post-seeding

During the transition between the early adhesion phase (P1) and the initial contractility phase (P2) at around 4 hours post-seeding (Figure 2.9A), a single adherent cell like HeLa or MEF typically displayed the symmetric “bulls-eye egg” shape as depicted in Figure 2.9B. By using TIRF microscopy, I observed that AP2 clusters were highly distributed at the cell edge, forming a ring, irrespective of the presence of immobilized nanoparticles (Figure 2.9C). To quantify the spatial distribution of AP2, AP2 clusters from “cargo” and “without cargo” images were segmented by an image processing software (i.e., ilastik (Kreshuk’s lab)) and were analyzed to measure the distance between each cluster and the cell centroid with a custom-made Matlab script. The result shows that, indeed, AP2 clusters were highly distributed proximal to the cell edges, irrespective of the presence of covalently bound nanoparticles, as shown by the histograms in (Figure 2.9C).

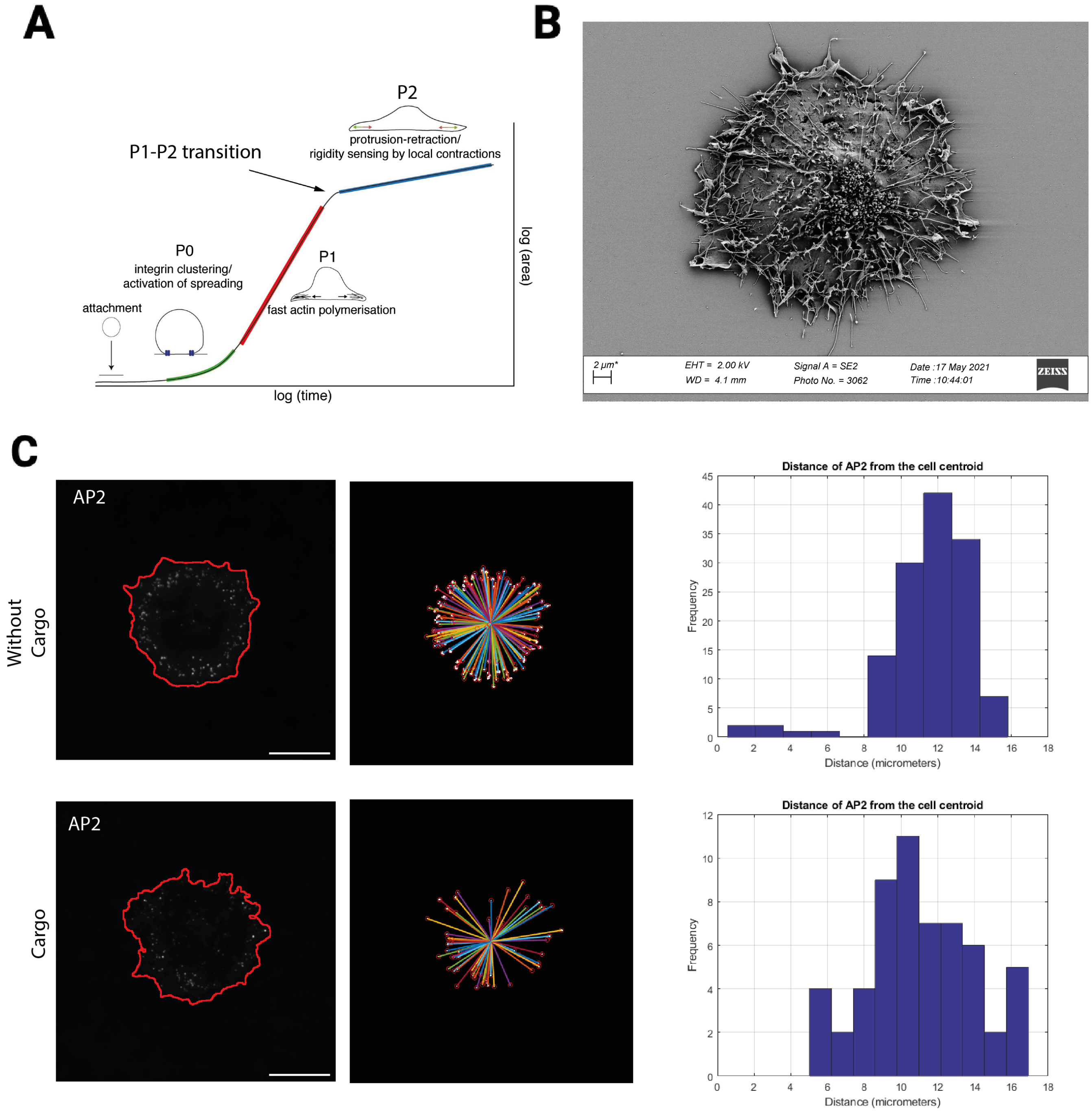

Figure 2.9: (**A**) A spreading fibroblast cell on a fibronectin-coated substrate undergoes several distinct phases. (P0) The formation of initial integrin clusters. (P1) Expanding membrane surface and fast actin polymerization. (P2) The initial contractility (i.e., protrusion-retraction). Adapted with permission from Ref. [122]. Copyright 2014 Elsevier. (**B**) SEM image of a critically dried "bulls-eye egg" cell on the glass around 4 hours post-seeding. (**C**) TIRF images of HeLa cells stably expressing AP2 tagged with eGFP. AP2 clusters were highly distributed at the cell periphery. The upper left image describes the cell adhered to the glass coated with fibronectin (without cargo). The lower left image describes the cell adhered to the glass coated with covalently immobilized nanoparticles and fibronectin (cargo). The red line indicates the shape of the cell. Scale bars = 20 μm. To quantify the spatial distribution of AP2, AP2 clusters from "cargo" and "without cargo" images were segmented by an image processing software (i.e., ilastik) and were analyzed to measure the distance between each cluster and the cell centroid with a custom-made Matlab script. The upper center and lower center images show the output images of the script. The upper right and lower right graphs show the histogram of AP2 clusters as a function of distance from the cell centroid. The spatial distribution of AP2 is mainly at the cell periphery, irrespective of the presence of immobilized nanoparticles (cargo). **Please click here to view a full size version of this figure.**

2.4.6 AP2 lifetime was independent on the substrate rigidity

As I planned to study the role of traction force in initiating particle uptake *via* CME at the cellular ventral side, I had to perform measurements on substrates that can be deformed by cells. To increase the probability of finding fluorescent events very close to the surface, I opted to use a TIRF microscope. TIRF is based on the total internal reflection mechanism. At the critical angle, a light beam from the TIRF source will be transmitted through a high numerical aperture lens, imaging oil, glass, and finally to the cell before being reflected. Typical TIRF experiments use glass with a specific thickness, usually around 170 μm. Therefore, cells are directly on the surface of the glass and the ventral side can be imaged by TIRF. However, glass can not be deformed by cells. PA can be deformed, but it has a refractive index of around 1.33, which is incompatible for TIRF. The light beam passing through the glass will never reach the cell as it will be reflected on the glass-PA interface. In comparison, QGel920 has a refractive index of around 1.49, which is very close to glass (i.e., n=1.5).

To check if AP2 clusters were sensitive to mechanical stimuli such as matrix rigidity, I seeded HeLa AP2-eGFP cells on the surface of a 3 kPa QGel920 and glass, which were already coated with immobilized 200 nm nanoparticles and biofunctionalized with fibronectin. Next, I analyzed the spatial distribution of AP2 with a TIRF microscope at around 4 hours post-seeding. Similar to glass (Figure 2.10A), AP2 clusters were also highly distributed at the cell periphery on the 3 kPa QGel920 substrate (Figure 2.10B). Next, I observed no significant difference between 3 kPa QGel920 substrate and glass concerning the cluster area and the signal lifetime of AP2 (Figure 2.10C). The lifetime was measured by normalizing the AP2 fluorescent intensity (above a nanoparticle) of each time point to the average of maximum intensity of AP2 fluorescent intensity (empty pits or not above a nanoparticle) of a similar cell, according to work done by Fratini et al. [43].

As I used similar nanoparticles on glass and 3 kPa QGel920, I expected the cluster size above a nanoparticle to be similar as Fratini et al. reported that the immobilized nanoparticle imprinted the final size of the clathrin vesicle [43]. My experiments were performed around 4 hours post-seeding, where cells still displayed the symmetric “bulls-eye egg” shape. I avoided waiting longer (e.g., 24 hours) because contractile cells are typically arbitrary in shape and size, making it more challenging to perform a comparison study. Another important reason was that large clathrin-coated structures considered unrelated to endocytosis and mechanically sensitive might emerge if I waited 24 hours, as reported by Baschieri et al. when HeLa cells were grown overnight on collagen-coated glass [7, 82]. Large clathrin-coated structures were observed in my preliminary experiments with HeLa cells seeded on glass coated with fibronectin.

Regarding the lifetime of AP2 clusters, I was aware that the typical lifetime of clathrin-coated pits is around 45-60 s from the study using BSC-1 cells [27]. In this study, I could find few lifetime events around 60 s. However, most AP2 signals above a bead did not have a strong signal peak. This signal typically led to a lifetime of around 120 s in the analysis. I encourage a more extended observation time in the near

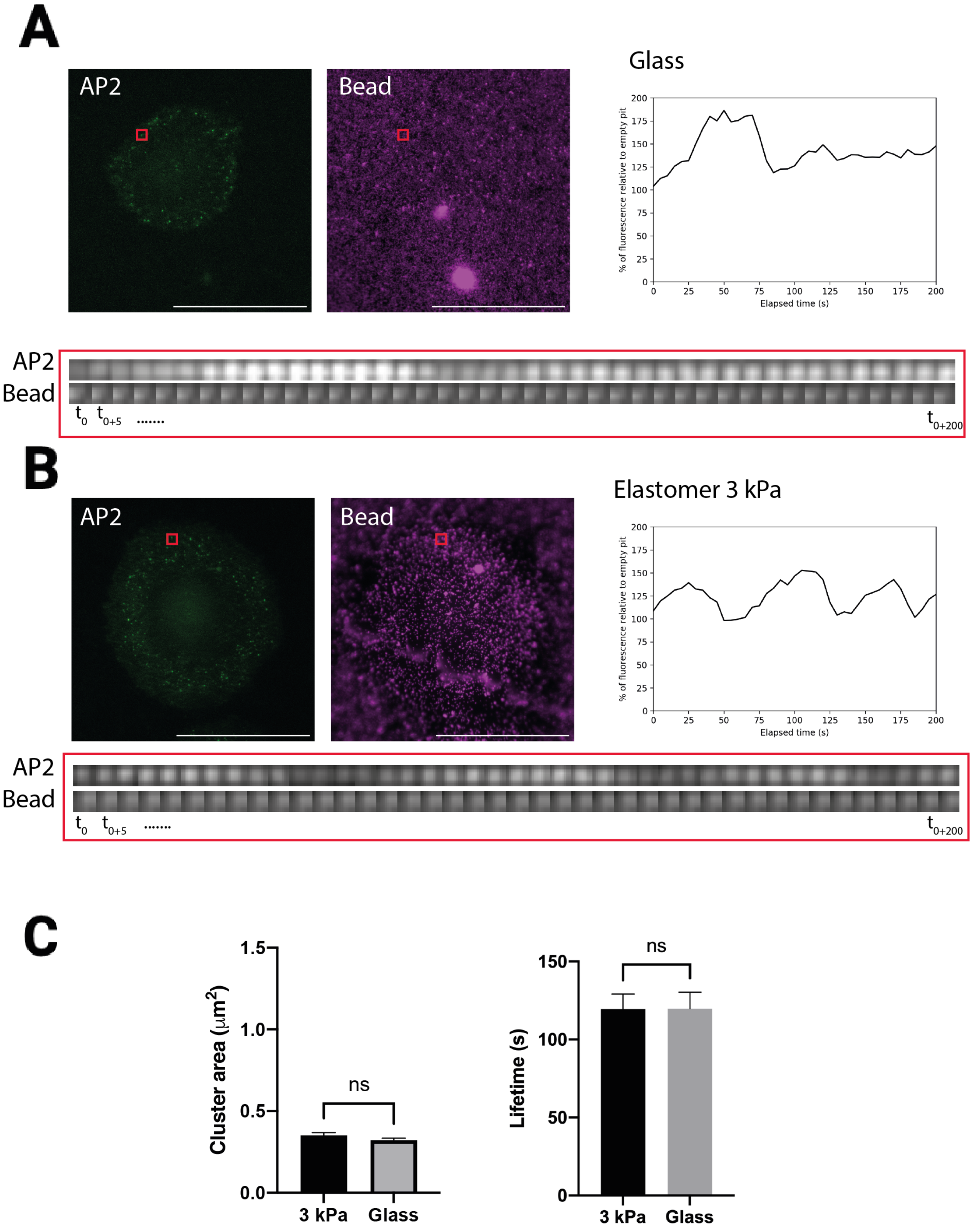

Figure 2.10: (**A**) Fluorescent micrographs of HeLa cells stably expressing AP2 tagged with eGFP (green) at 4 hours post-seeding on the surface of the glass, which was already immobilized covalently with 200 nm nanoparticles (magenta) and biofunctionalized with fibronectin. Scale bars = 50 μm. Red squares on both channels indicate the recruitment of AP2 on a single bead. The insets show the evolution of AP2 intensity above a single bead. The intensity over time is depicted in the graph on the right. (**B**). Similar analysis like (A) but on a 3 kPa QGel920 substrate. (**C**) (Left) Comparison of AP2 cluster area between 3 kPa PDMS elastomer (n=143) and glass (n=243). (Right) Comparison of AP2 cluster lifetime above a nanoparticle between a 3 kPa PDMS elastomer (n=26) and glass (n=22). Bars show mean ± S.E.M (unpaired t-test (two-tailed), **** $P < 0.0001$, *** $P < 0.001$, ** $P < 0.01$, * $P < 0.05$, ns $P \leq 0.5$). **Please click here to view a full size version of this figure.**

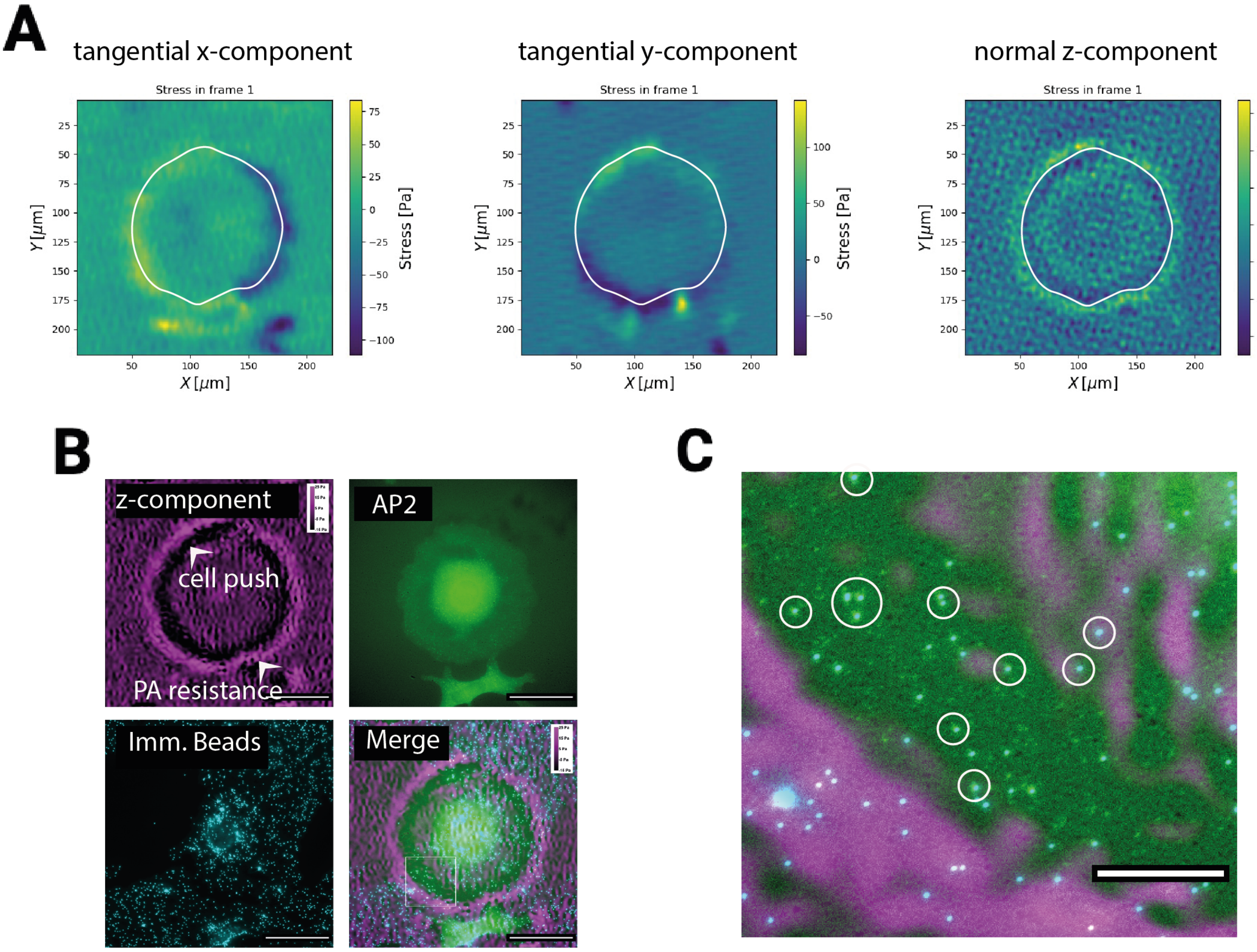

Figure 2.11: (**A**) Tangential (x, y) and normal (z) components of traction forces exerted by HeLa cells on a 3 kPa fibronectin-coated PA hydrogel at around 4 hours post-seeding. (**B**) The normal component of traction forces, fluorescent micrographs of AP2, and electrostatically immobilized nanoparticles. The cell indented the substrate indicated by negative stress values at the cell periphery area. Scale bar = 50 μm. (**C**) Inset shows the spatial correlation between AP2 and electrostatically immobilized beads in the region where the cell indented the substrate. Scale bar = 10 μm. **Please click here to view a full size version of this figure.**

future to detect several signal peaks.

2.4.7 AP2 clusters were spatially-colocalized with the normal component of traction forces

Cell indented the substrate at the cell periphery

Previous experiments showed that AP2 clusters were highly distributed at the cell edge, forming a ring, irrespective of the nanoparticles and matrix rigidity. In this part, I performed an initial check with 2.5D-LUVI-TFM to assess traction force components (i.e., x, y, and z components). As the focus was to assess traction force components, LUVI-TFM was performed on a widefield microscope using a 3 kPa fibronectin-coated PA hydrogel having its surface electrostatically immobilized with nanoparticles. At around 4 hours post-seeding, I performed 2.5D-LUVI-TFM on a single cell. As shown in Figure 2.11A, the symmetric

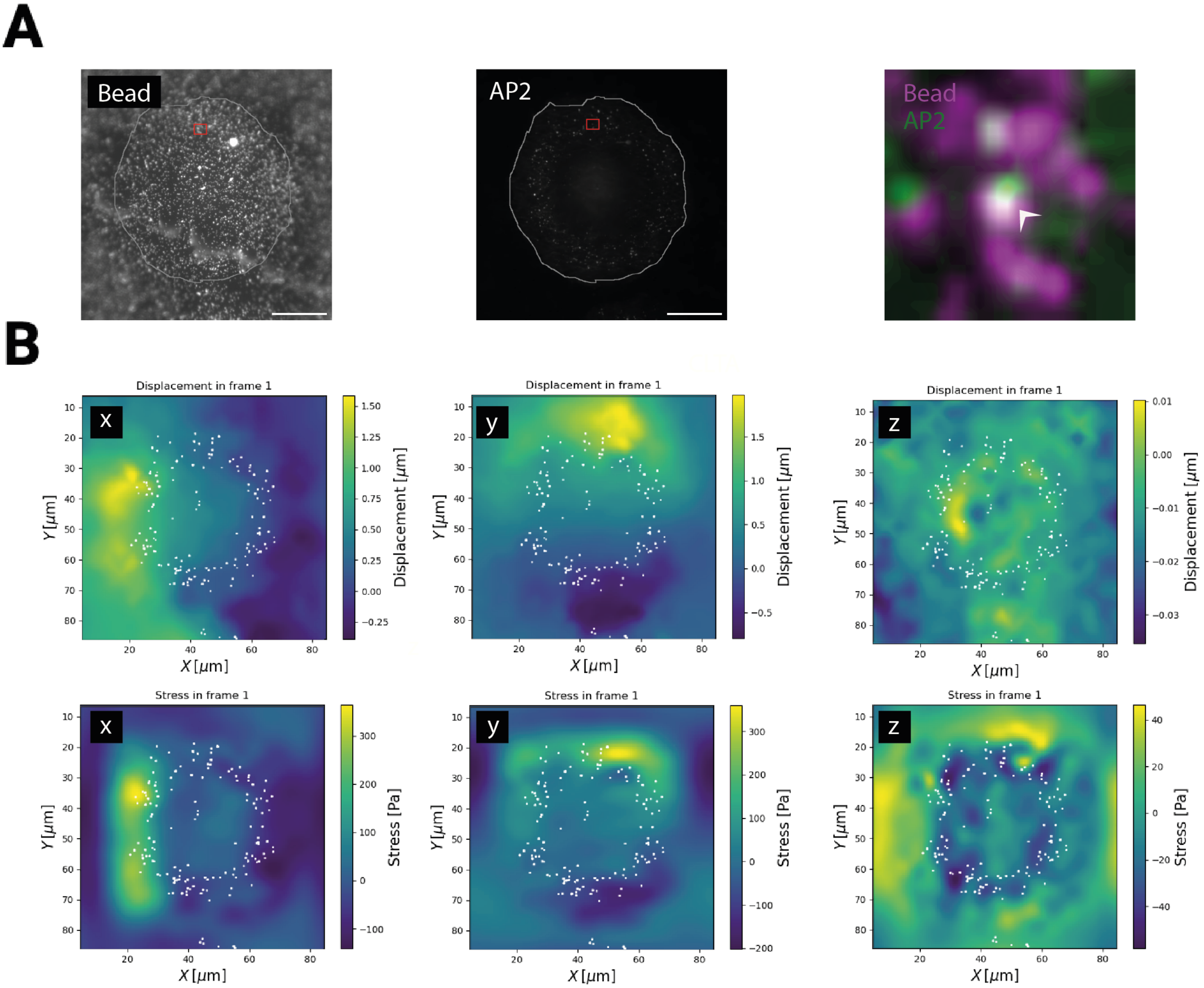

Figure 2.12: (**A**) Fluorescent micrographs of the covalently immobilized nanoparticles and AP2-eGFP of a single HeLa 4 hours post-seeding taken with a TIRF microscope. Scale bar = 20 μm. The inset shows the clustering of AP2 above a covalently bound nanoparticle. (**B**) Displacement and stress fields (x, y, and z) overlaid with AP2 clusters (white, thresholded). The ring of AP2 clusters was spatially-correlated with the normal component (z) of the stress field. **Please click here to view a full size version of this figure.**

"bulls-eye egg" shaped exerted tangential x, y, and normal z components. In the x and y components, positive values indicate that the contracting cells deformed marker beads from left to right and from bottom to up. In the z component, positive values indicate that the contracting cells deformed marker beads from inside to outside (i.e., towards the reader). By looking at the z component, I observed a ring of negative stress values at the cell periphery indicating that the cell indented the substrate at its periphery. Beyond the cell boundary, I also observed a ring of positive stress values. This inside-out movement was due to the elastic property of PA to compensate for the push by the cell. Next, as shown in Figure 2.11B and the inset in Figure 2.11C, I observed that AP2 clusters were recruited above electrostatically immobilized nanoparticles inside the area of indentation at the cell periphery.

TIRF based 2.5D-LUVI-TFM revealed that AP2 cluster were colocalized with the normal component of traction forces

As shown by the AP2 image in Figure 2.11B, by using a widefield microscope, I could not observe the recruitment of AP2 on the ventral plasma membrane due to the high intensity of diffuse AP2-eGFP signal around the cell center. To simultaneously detect AP2 clusters and cellular indentation at the cell periphery, I applied LUVI-TFM in a TIRF microscope using 3 kPa QGel920 as the substrate. Figure 2.12A shows the covalently bound marker beads and the AP2-eGFP clusters at the ventral cellular membrane. As shown in Figure 2.12B, I observed that the ring of AP2 clusters at the cell periphery was colocalized with the normal (z) component of the stress field.

Role of traction forces in initiating CME lies in its normal component

As mentioned, cells generally exert 3D traction forces on the 2D surface. In a continous substrate like PA which is different from discrete elastic pillars, it makes more sense to relate the normal component than tangential components of traction forces to early events of CME. As shown in Figure 2.12B, AP2 clusters were outside x and y components of traction forces. It should be noted that traction hotspots were constructed based on the movement of beads embedded in PA (covalently bound to the surface in case of PDMS like QGel920). Since the substrate is continous, integrin-mediated traction forces did not only move beads close to integrin-matrix linkages. Depending on the strength, it could also move beads located up to several microns from the linkage epicentrum. In my setup, it is more relevant to x and y components as beads were restricted near the surface.

As AP2 clusters were observed inside the negative stress values of the normal component at the cell periphery irrespective of the presence of immobilized nanoparticles and matrix rigidity, it seems that during the transition between the early adhesion phase (P1) and the initial contractility (P2), the cellular indentation at the cell edge triggered the recruitment of AP2 cluster for the adhesion turnover. As the indentation brought the ventral membrane closer to the cargo, the cargo would interact with the membrane, causing membrane deformation that initiated CME. Finally, the results strongly suggest that the normal component of traction forces plays a crucial role in initiating CME.

2.5 Summary

In part II, I observed that cells preferentially removed electrostatically immobilized nanoparticles at the cell periphery. Nanoparticles were removed from the surface under cellular traction forces. However, it was unclear if traction forces caused the particle removal. To elucidate it, I employed micropatterning to control the size and shape, thereby the traction force hotspots of a single cell. I could also immobilize nanoparticles in regions where the cell exerted high traction forces. The result was that traction forces alone were insufficient to remove nanoparticles from the surface. Despite no removal, I observed that immobilized nanoparticles initiated CME in high traction force regions.

Concerning the role of traction force in initiating CME of nanoparticles at the cellular ventral side, I focused on cells that were transitioning between the early adhesion phase and the initial contractility at around 4 hours post-seeding. In this phase, cells exhibited the shape of a symmetric "bulls-eye egg" and were easier to compare. I observed that AP2 clusters were highly distributed at the cell periphery, irrespective of the presence of covalently immobilized nanoparticles and substrate rigidity. Furthermore, I observed no significant difference between 3 kPa elastomer substrate and glass concerning the AP2 cluster area and signal lifetime. Lastly, I observed that the cell pushed down substrate at the cell periphery, and AP2 clusters were found colocalizing with the indentation. I observed that AP2 clusters were recruited above covalently immobilized nanoparticles in the indentation area. This strongly suggests that the normal component of traction forces plays a crucial role in initiating CME.

2.6 Outlook

As shown in Figure 2.13, high throughput analysis using flow cytometry shows that cells internalized more electrostatically immobilized nanoparticles during 4 hours of adhesion when they were on 0.4 kPa than 50 kPa PDMS elastomer. It would be interesting to check in the near future if this was directly related to the normal component of traction forces.

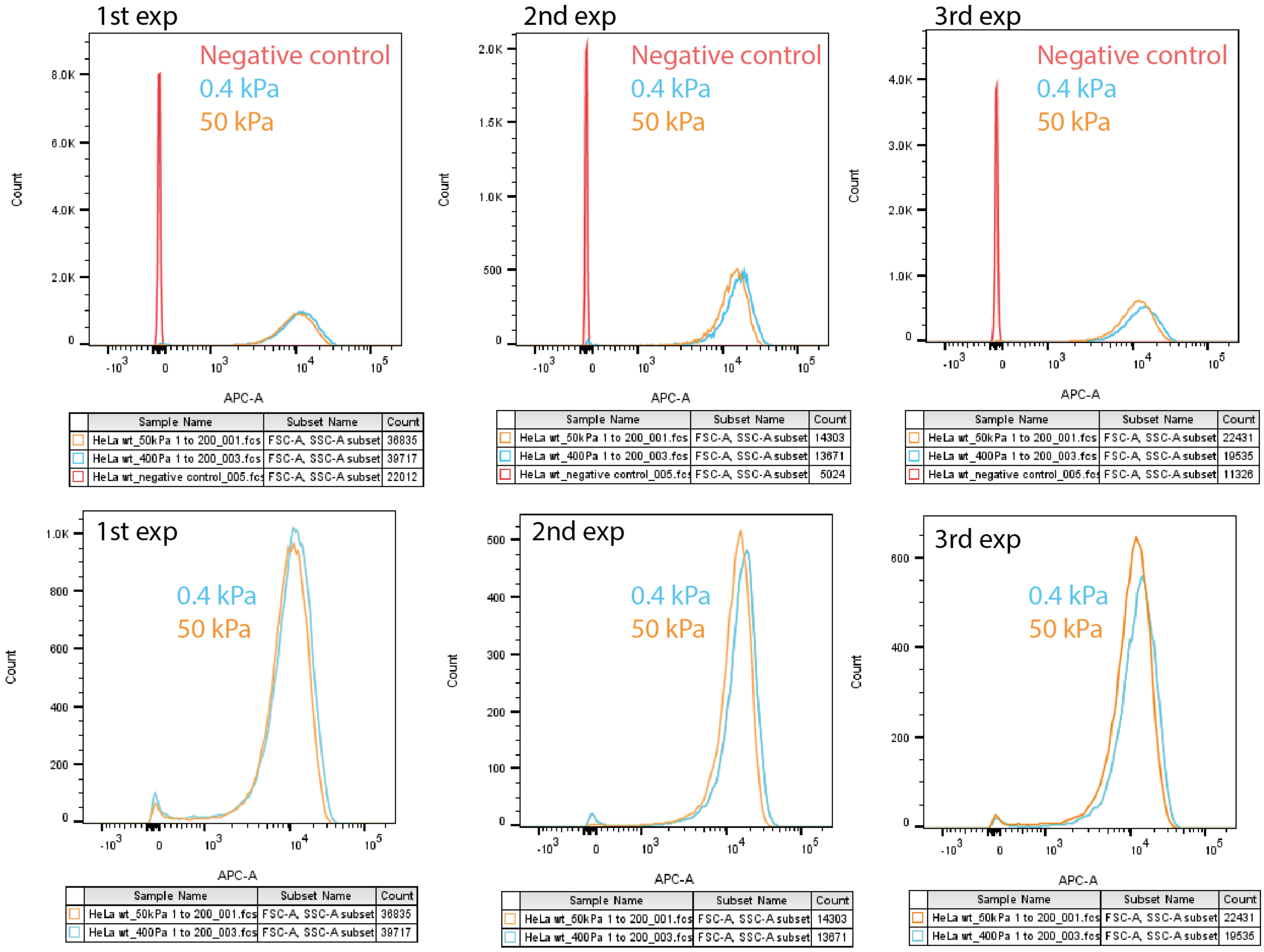

	Sample Name	Subset Name	Count
☐	HeLa wt_50kPa 1 to 200_001.fcs	FSC-A, SSC-A subset	36835
☐	HeLa wt_400Pa 1 to 200_003.fcs	FSC-A, SSC-A subset	39717
☐	HeLa wt_negative control_005.fc	FSC-A, SSC-A subset	22012

	Sample Name	Subset Name	Count
☐	HeLa wt_50kPa 1 to 200_001.fcs	FSC-A, SSC-A subset	14303
☐	HeLa wt_400Pa 1 to 200_003.fcs	FSC-A, SSC-A subset	13671
☐	HeLa wt_negative control_005.fc	FSC-A, SSC-A subset	5024

	Sample Name	Subset Name	Count
☐	HeLa wt_50kPa 1 to 200_001.fcs	FSC-A, SSC-A subset	22431
☐	HeLa wt_400Pa 1 to 200_003.fcs	FSC-A, SSC-A subset	19535
☐	HeLa wt_negative control_005.fc	FSC-A, SSC-A subset	11326

	Sample Name	Subset Name	Count
☐	HeLa wt_50kPa 1 to 200_001.fcs	FSC-A, SSC-A subset	36835
☐	HeLa wt_400Pa 1 to 200_003.fcs	FSC-A, SSC-A subset	39717

	Sample Name	Subset Name	Count
☐	HeLa wt_50kPa 1 to 200_001.fcs	FSC-A, SSC-A subset	14303
☐	HeLa wt_400Pa 1 to 200_003.fcs	FSC-A, SSC-A subset	13671

	Sample Name	Subset Name	Count
☐	HeLa wt_50kPa 1 to 200_001.fcs	FSC-A, SSC-A subset	22431
☐	HeLa wt_400Pa 1 to 200_003.fcs	FSC-A, SSC-A subset	19535

Figure 2.13: Flow cytometry analysis of the cellular uptake of fluorescent 200 nm carboxylated nanoparticles at the ventral side after 4 hours seeding. The median of APC-A in the first experiment, 0.4 kPa = 9014, 50 kPa = 7269. In the s experiment, 0.4 kPa = 14151, 50 kPa = 9470, and third experiment, 0.4 kPa = 13083, 50 kPa = 8281. Flow cytometry data courtesy of Mr. Jonah Voigt.

In part II, I observed a strong indication that the normal component of traction forces has a crucial role in initiating CME of nanoparticles at the cellular ventral side. However, the molecular determinants remained obscure. In a preliminary experiment, colocalizing MyosinVI, Dab2 (clathrin adaptor protein), and PIP_2 clusters were recruited above a covalently immobilized 200 nm nanoparticle as shown in Figure 2.14. As the early stages of CME are indicated by the recruitment of PIP_2 protein, this result strongly suggests that MyosinVI and PIP_2 proteins are involved in CME of nanoparticles at the ventral side. Some preliminary results concerning myosinVI, PIP_2, and cellular uptake responses to varying matrix rigidity

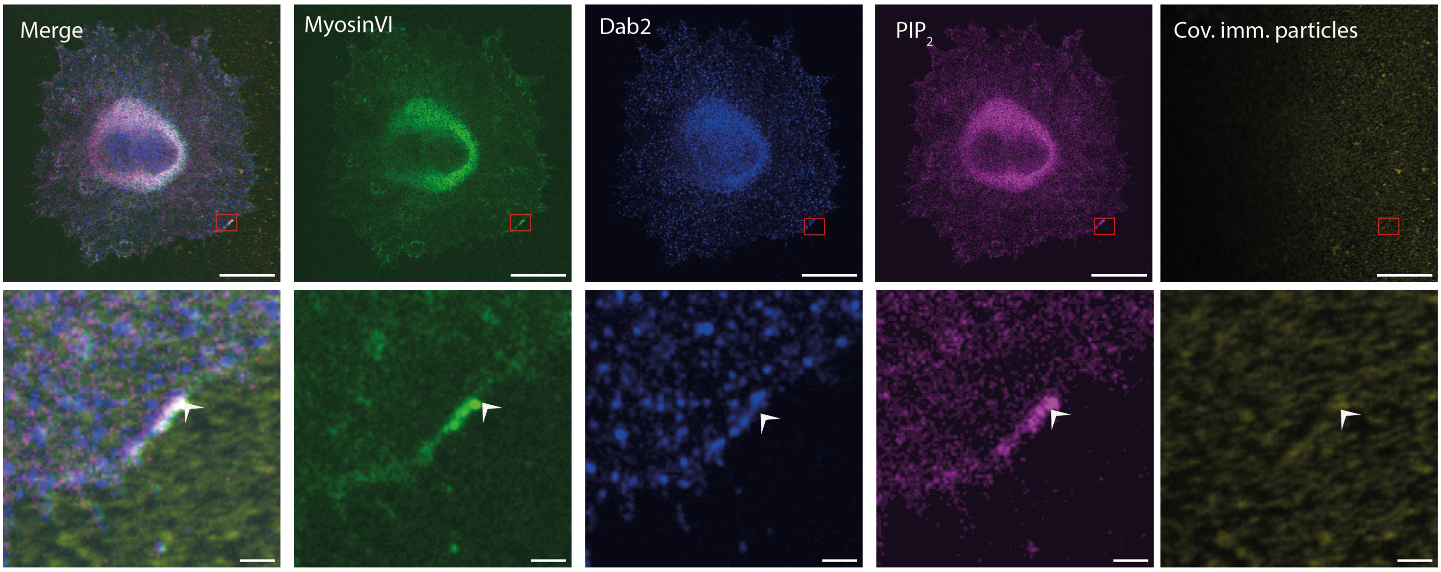

Figure 2.14: Fluorescent micrographs of MyosinVI, Dab2, PIP_2 signals, and 200 nm fluorescent nanoparticles. MEF cells expressing MyosinVI-eGFP were seeded on glass, fixed at 1 hour post-seeding, and stained for Dab2 (clathrin adaptor protein) and PIP_2. Before cell seeding, the glass surface was first covalently immobilized with nanoparticles and coated with fibronectin. Scale bar = 20 μm. Insets show colocalizing MyosinVI, Dab2, and PIP_2 clusters above immobilized nanoparticles. Scale bar = 2 μm.

can be found in the supplementary figures.

In the near future, it would be interesting to perturb those proteins (i.e., MyosinVI and PIP_2) genetically (e.g., knockdown) and biochemically (e.g., inhibitors) and investigate the influence on CME and cellular traction forces.

Appendix - Supplementary Figures

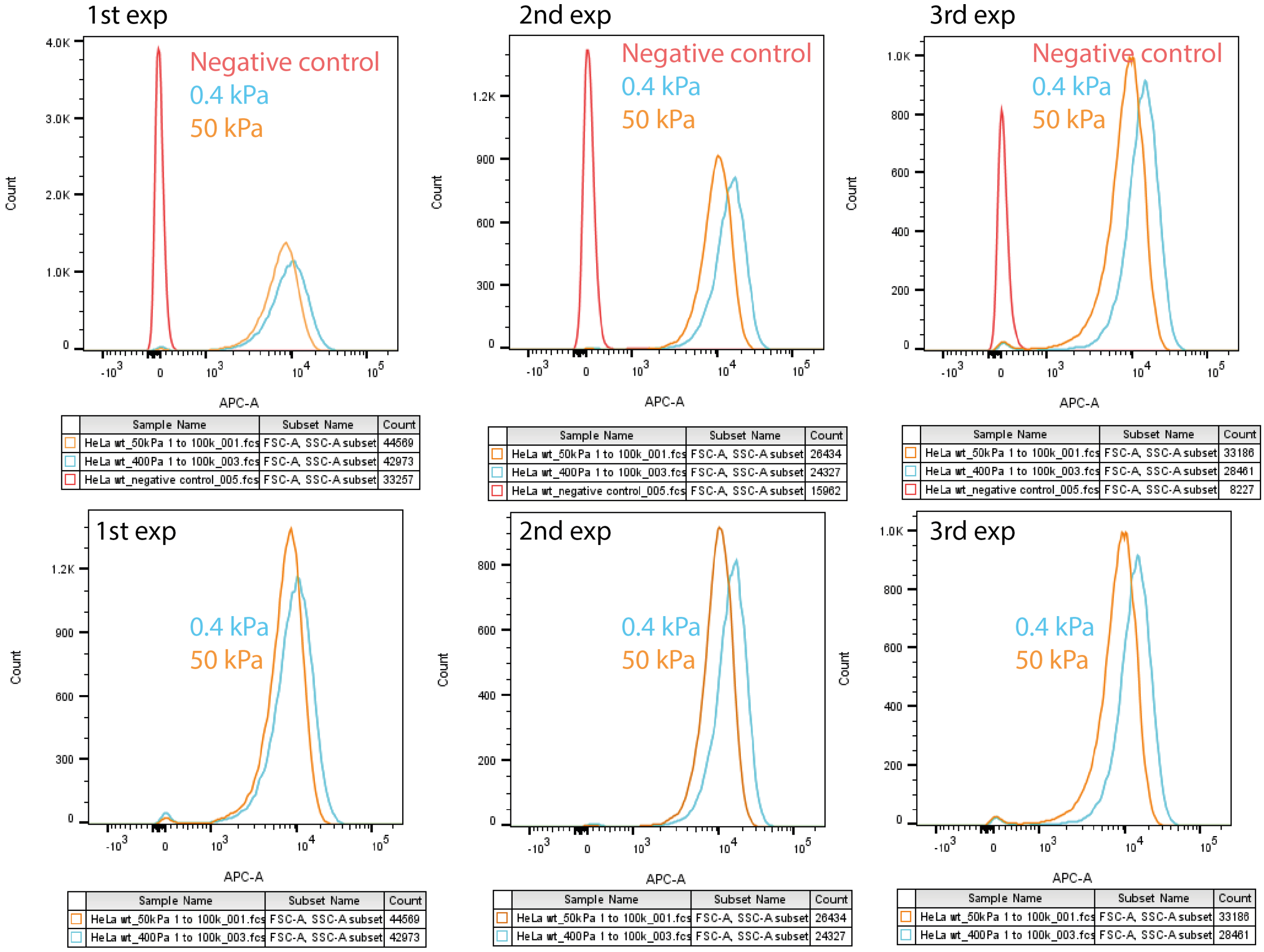

1st exp

	Sample Name	Subset Name	Count
🟧	HeLa wt_50kPa 1 to 100k_001.fcs	FSC-A, SSC-A subset	44569
🟦	HeLa wt_400Pa 1 to 100k_003.fcs	FSC-A, SSC-A subset	42973
🟥	HeLa wt_negative control_005.fcs	FSC-A, SSC-A subset	33257

2nd exp

	Sample Name	Subset Name	Count
🟧	HeLa wt_50kPa 1 to 100k_001.fcs	FSC-A, SSC-A subset	26434
🟦	HeLa wt_400Pa 1 to 100k_003.fcs	FSC-A, SSC-A subset	24327
🟥	HeLa wt_negative control_005.fcs	FSC-A, SSC-A subset	15962

3rd exp

	Sample Name	Subset Name	Count
🟧	HeLa wt_50kPa 1 to 100k_001.fcs	FSC-A, SSC-A subset	33186
🟦	HeLa wt_400Pa 1 to 100k_003.fcs	FSC-A, SSC-A subset	28461
🟥	HeLa wt_negative control_005.fcs	FSC-A, SSC-A subset	8227

1st exp

	Sample Name	Subset Name	Count
🟧	HeLa wt_50kPa 1 to 100k_001.fcs	FSC-A, SSC-A subset	44569
🟦	HeLa wt_400Pa 1 to 100k_003.fcs	FSC-A, SSC-A subset	42973

2nd exp

	Sample Name	Subset Name	Count
🟧	HeLa wt_50kPa 1 to 100k_001.fcs	FSC-A, SSC-A subset	26434
🟦	HeLa wt_400Pa 1 to 100k_003.fcs	FSC-A, SSC-A subset	24327

3rd exp

	Sample Name	Subset Name	Count
🟧	HeLa wt_50kPa 1 to 100k_001.fcs	FSC-A, SSC-A subset	33186
🟦	HeLa wt_400Pa 1 to 100k_003.fcs	FSC-A, SSC-A subset	28461

Figure 2.15: **Flow cytometry experiments indicated that electrostatically immobilized 40 nm nanoparticles were internalized more on the softer than the stiffer PDMS elastomer**. Flow cytometry analysis of the cellular uptake of fluorescent 40 nm carboxylated nanoparticles at the ventral side after 4 hours seeding. The median of APC-A in the first experiment, 0.4 kPa = 10341, 50 kPa = 9385. In the second experiment, 0.4 kPa = 15030, 50 kPa = 12934, and third experiment, 0.4 kPa = 12184, 50 kPa = 10364. Flow-cytometry data courtesy of Mr. Jonah Voigt.

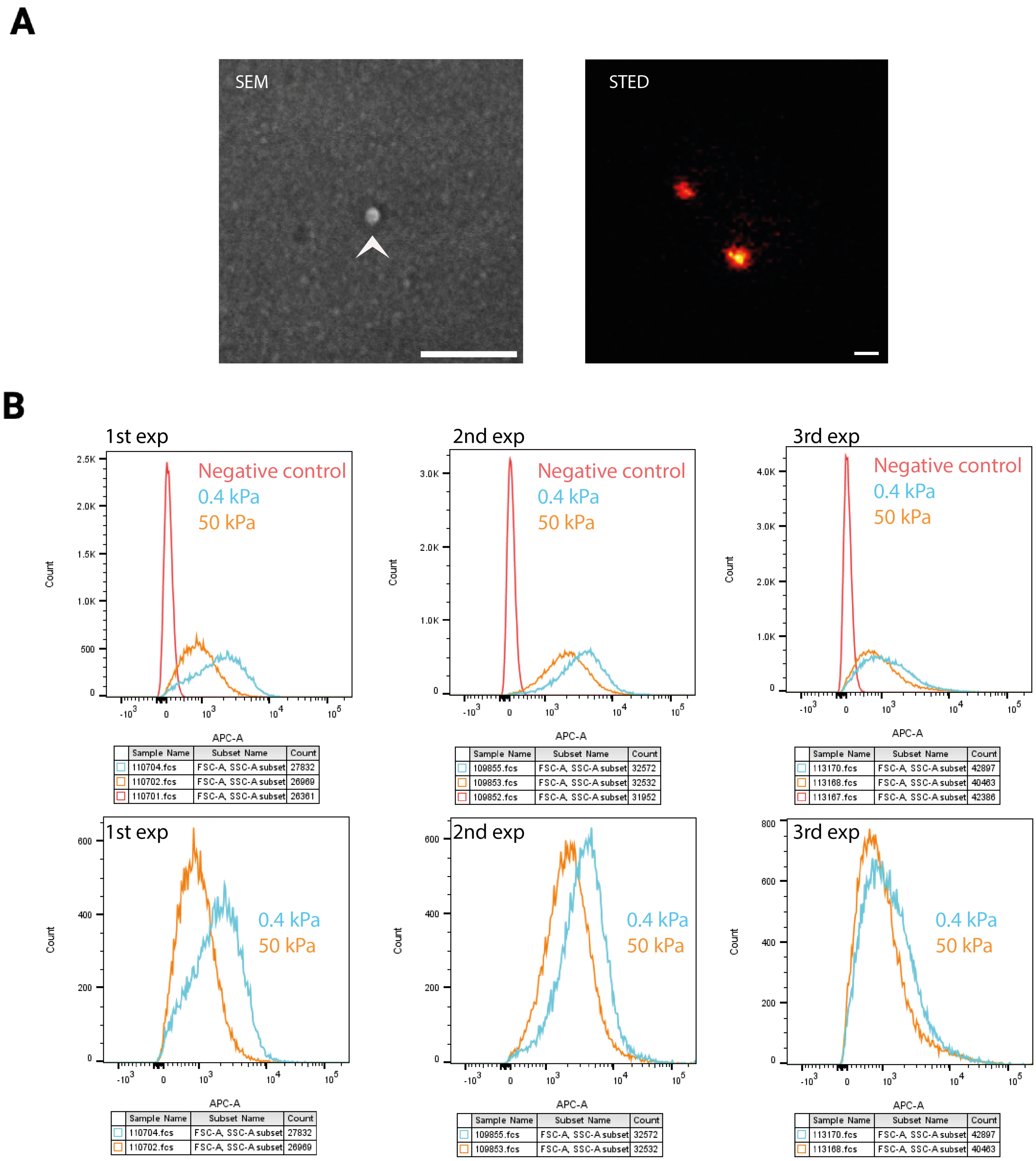

1st exp

	Sample Name	Subset Name	Count
☐	110704.fcs	FSC-A, SSC-A subset	27832
☐	110702.fcs	FSC-A, SSC-A subset	26969
☐	110701.fcs	FSC-A, SSC-A subset	26361

2nd exp

	Sample Name	Subset Name	Count
☐	109855.fcs	FSC-A, SSC-A subset	32572
☐	109853.fcs	FSC-A, SSC-A subset	32532
☐	109852.fcs	FSC-A, SSC-A subset	31952

3rd exp

	Sample Name	Subset Name	Count
☐	113170.fcs	FSC-A, SSC-A subset	42897
☐	113168.fcs	FSC-A, SSC-A subset	40463
☐	113167.fcs	FSC-A, SSC-A subset	42386

1st exp

	Sample Name	Subset Name	Count
☐	110704.fcs	FSC-A, SSC-A subset	27832
☐	110702.fcs	FSC-A, SSC-A subset	26969

2nd exp

	Sample Name	Subset Name	Count
☐	109855.fcs	FSC-A, SSC-A subset	32572
☐	109853.fcs	FSC-A, SSC-A subset	32532

3rd exp

	Sample Name	Subset Name	Count
☐	113170.fcs	FSC-A, SSC-A subset	42897
☐	113168.fcs	FSC-A, SSC-A subset	40463

Figure 2.16: **Flow cytometry experiments indicated that electrostatically immobilized AAV2 particles were internalized more on the softer than the stiffer PDMS elastomer**. (**A**) SEM and STED image of non-labelled and Atto647N-labelled AAV2. Scale bar of the SEM image = 100 nm. Scale bar of the STED image = 200 nm. (**B**) Flow cytometry analysis of the cellular uptake of TFP ester Alexa647 labelled AAV2 at the ventral side after 4 hours seeding. The median of APC-A in the first experiment, 0.4 kPa = 3427, 50 kPa = 2033. In the second experiment, 0.4 kPa = 1828, 50 kPa = 890, and third experiment, 0.4 kPa = 1112, 50 kPa = 839. Flow-cytometry data courtesy of Mr. Jens Timmer.

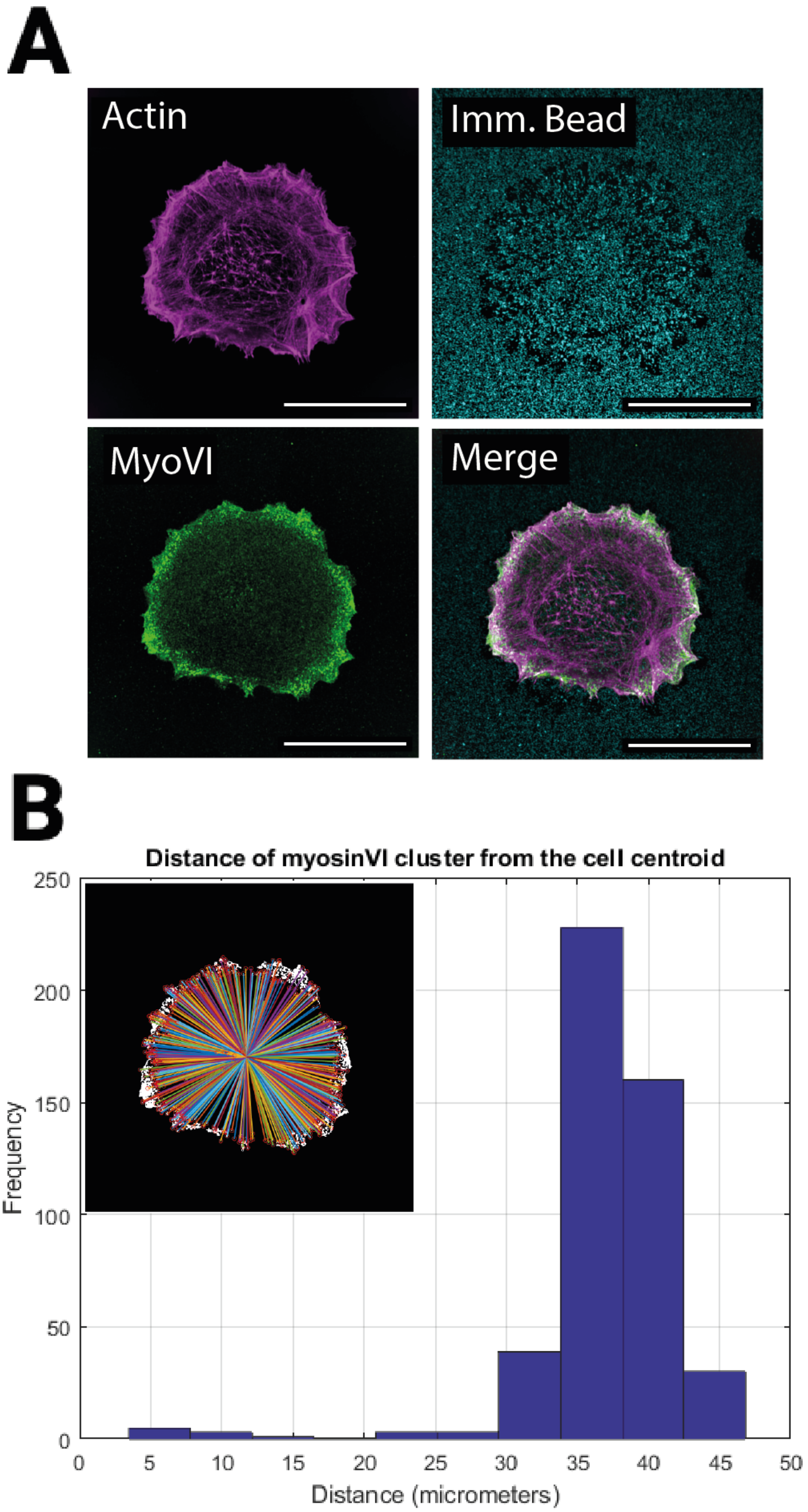

Figure 2.17: **MyosinVI clusters were highly distributed at the cell periphery**. (**A**) Fluorescent micrographs of a HT1080 stained for F-actin and MyosinVI protein. MyosinVI clusters were highly distributed at the cell periphery where the electrostatically particles (cyan) were removed from the surface. Scale bar = 50 μm. (**B**) Quantification of the distance between each MyosinVI cluster from the cell centroid. The graph shows that MyosinVI clusters were highly distributed at the cell periphery.

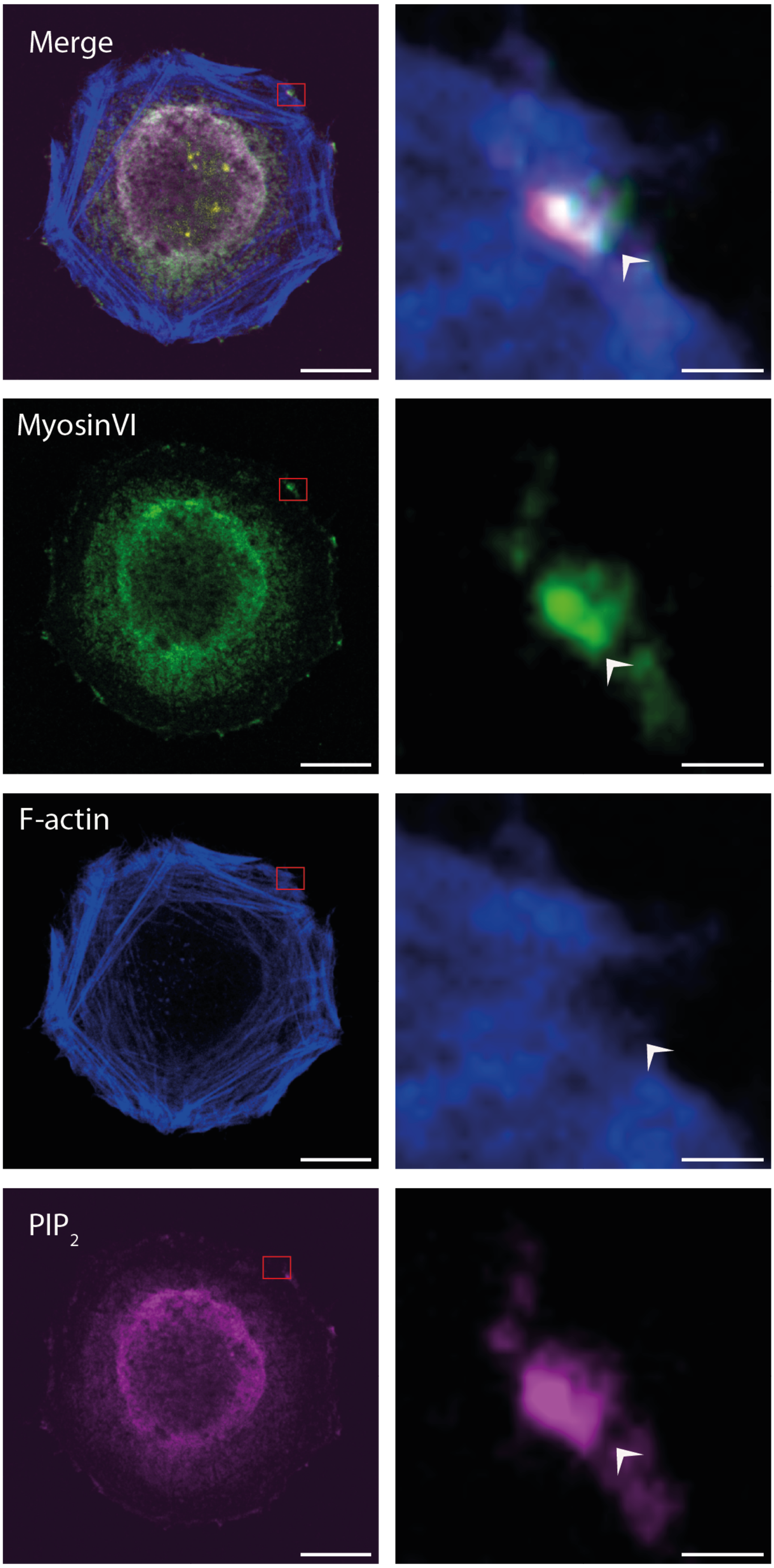

Figure 2.18: **Colocalizing MyosinVI-PIP$_2$ clusters linked to actin stress fibers at the cell periphery**. MEF cells expressing MyosinVI-eGFP were seeded on fibronectin-coated glass, fixed at 1 hour post-seeding, and stained for F-actin and PIP$_2$. Scale bar = 20 μm. Insets show that MyosinVI clusters were colocalized with PIP$_2$. Colocalizing MyosinVI/PIP$_2$ clusters linked to actin stress fibers at the cell periphery. As PIP$_2$ recruitment on the membrane is vital for the early stages for CME (i.e., Dab2-PIP$_2$ colocalization, Figure 2.14), these images strongly indicate that actin, MyosinVI, and PIP$_2$ are the governing proteins for CME of nanoparticles at the cellular ventral side. Scale bar = 2 μm.

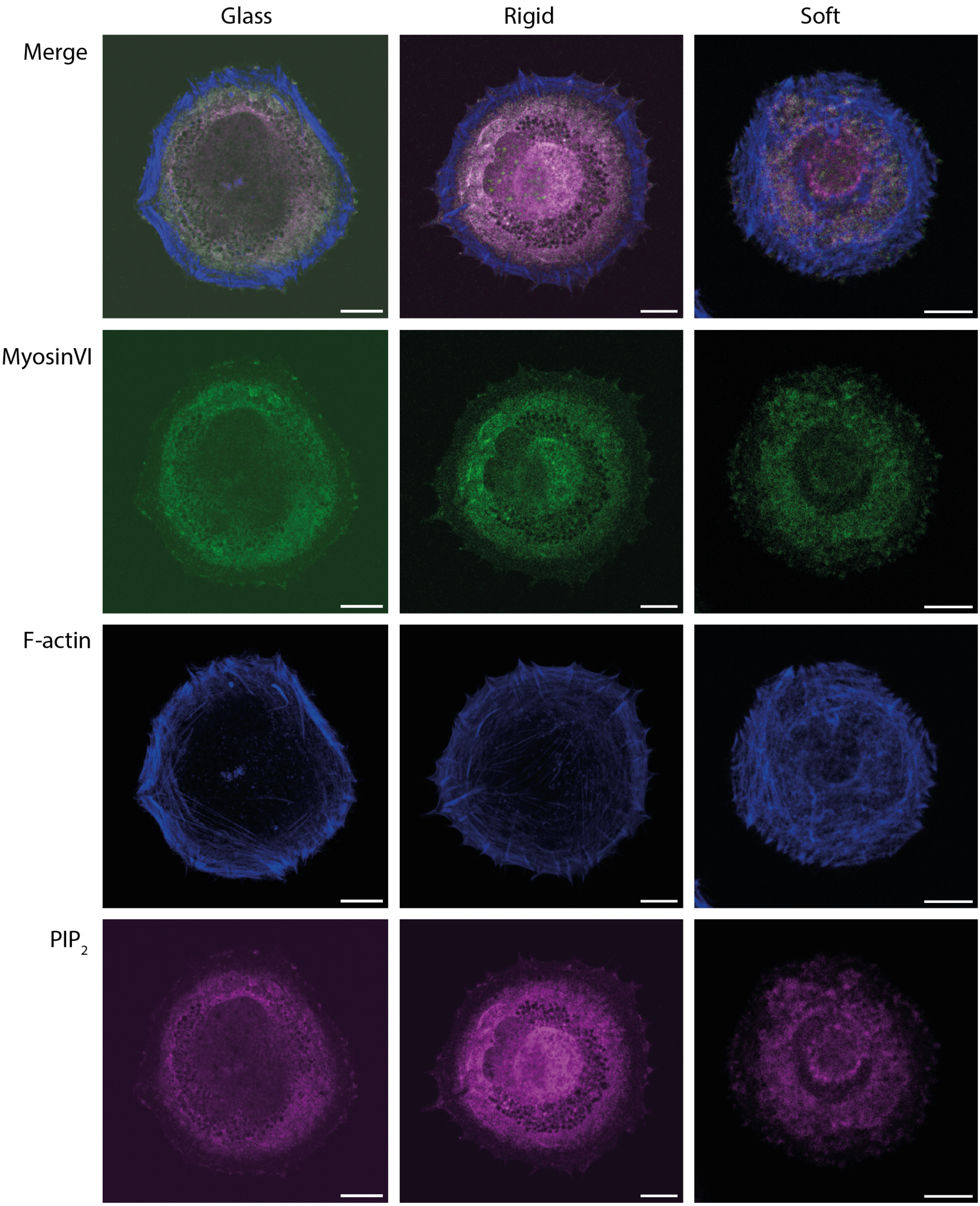
Glass
Rigid
Soft
Merge
MyosinVI
F-actin
PIP
2

Figure 2.19: **MyosinVI-PIP$_2$ clusters seemed to be influenced by matrix rigidity**. MEF cells expressing MyosinVI-eGFP were seeded on fibronectin-coated substrates (i.e., glass, rigid PDMS elastomer = 50 kPa, and soft PDMS elastomer = 0.4 kPa), fixed at 1 hour post-seeding, and stained for F-actin and PIP$_2$. Scale bar = 20 μm.

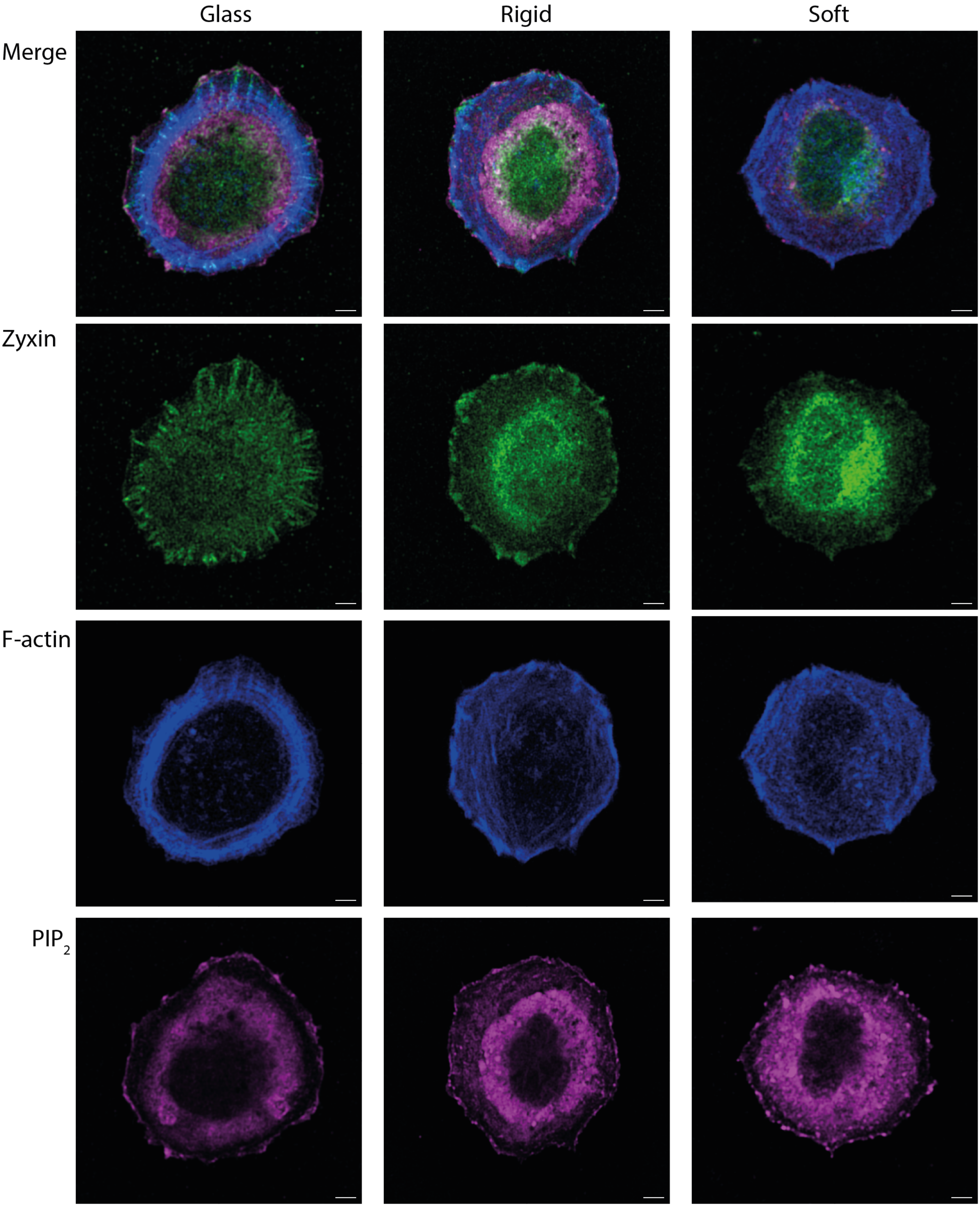
Glass
Rigid
Soft
Merge
Zyxin
F-actin
PIP2

Figure 2.20: **PIP_2 clusters also seemed to be associated with cellular adhesion**. MEF cells were seeded on fibronectin-coated substrates (i.e., glass, rigid PDMS elastomer = 50 kPa, and soft PDMS elastomer = 0.4 kPa), fixed at 1 hour post-seeding, and stained for zyxin, F-actin and PIP_2. PIP_2 clusters colocalize with zyxin clusters at the cell boundary. Scale bar = 20 μm.

Appendix - Script

Quantification of the distance of segmented focal adhesion clusters to the cell centroid

```
clc
clear
close all

I = imread('Image_cell.png');    %cell
I2 = imread('Image_segmented.png');     %FA

pairOfImages = [I2,I];
%imshow(pairOfImages);
imshow(I2);


Ibw = im2bw(I);
Ibw = imfill(Ibw,'holes');
Ilabel = bwlabel(Ibw);
stat = regionprops(Ilabel,'centroid');

hold on;
for x = 1: numel(stat)
    plot(stat(x).Centroid(1),stat(x).Centroid(2),'ro');
end

cell_centroid = [stat(1).Centroid(1),stat(1).Centroid(2)]




Ibw2 = im2bw(I2);
%Ibw2 = imfill(Ibw2,'holes');
Ilabel2 = bwlabel(Ibw2);
stat2 = regionprops(Ilabel2,'centroid');


%%%
s = regionprops('table',Ibw2,'Centroid', ...

'MajorAxisLength','MinorAxisLength','Orientation');
MaA=table2array(s(:,'MajorAxisLength'));
MiA=table2array(s(:,'MinorAxisLength'));
%%%

%Orientation with props measuring the angle between major axis and
%universal x axis

xMajor=s.Centroid(1) + [-1 1].*(s.MajorAxisLength/
2).*cosd(s.Orientation);
yMajor=s.Centroid(2) + [-1 1].*(s.MajorAxisLength/
2).*sind(s.Orientation);

xMinor=s.Centroid(1) + [-1 1].*(s.MinorAxisLength/
2).*sind(s.Orientation);
yMinor=s.Centroid(2) - [-1 1].*(s.MinorAxisLength/
2).*cosd(s.Orientation);

abs(diff(xMajor(1,:)));      %measure the x and y of major axis
abs(diff(yMajor(1,:)));

abs(diff(xMinor(1,:)));
abs(diff(yMinor(1,:)));

%%%%




for x = 1: numel(stat2)
    plot(stat2(x).Centroid(1),stat2(x).Centroid(2),'ro');
    FA_centroid(x,:) = [stat2(x).Centroid(1), stat2(x).Centroid(2)];
    dist_centroids(x) =
pdist2(cell_centroid,FA_centroid(x,:),'euclidean');
    dist_centroids_um(x)=dist_centroids(x)/7.5879;
    image(x)=plot([cell_centroid(1),FA_centroid(x,1)],
[cell_centroid(2),FA_centroid(x,2)],'LineWidth',2);



    %%%%
    tetaa(x)=asind((+FA_centroid(x,2)-cell_centroid(2))/
dist_centroids(x));
    %alphaa(x)=180-(90+tetaa(x));
    rad_angles(x)=s.Orientation(x)-tetaa(x);

    % read the radial angle with respect to axis connecting cell
centroid
    % to all FAs centroid

    if rad_angles(x) > 90
        rad_angles(x)= -180 + rad_angles(x);
    else if rad_angles(x) < -90
           rad_angles(x)= 180 + rad_angles(x);
        end
    end


%vect(x)=quiver(FA_centroid(x,1),FA_centroid(x,2),MaA(x),MiA(x),'LineW
idth',2);
    %vect(x)=quiver(FA_centroid(x,1),FA_centroid(x,2),
(diff(xMajor(x,:))),(diff(yMajor(x,:))),0.5,'LineWidth',2);

end
```

```
figure
bar((1:x),dist_centroids_um)
title('Distance from the cell centroid');
xlabel('Number of FA')
ylabel('Distance (micrometers)')
grid on

figure
hist(dist_centroids_um)
%bar((1:x),dist_centroids_um)
title('Distance of FA from the cell centroid');
ylabel('Frequency')
xlabel('Distance (micrometers)')
grid on

figure
bar((1:x),rad_angles)

title('Radial Angles');
xlabel('Number of FA')
ylabel('Radial Angles (^o)')
grid on

figure
polarhistogram(rad_angles,25)
thetalim([-90 90])
title('Radial Angles (^o)');
%ylabel('Radial Angle (^o)')
grid on

figure
obj1=CircHist(rad_angles,25)
%thetalim([-100 100])
%title('Radial Angles (^o)');
%ylabel('Radial Angle (^o)')
%grid on

obj1.colorBar = 'r';
obj1.scaleBarSide = 'right';
obj1.barWidth = 10;
obj1.polarAxs.ThetaZeroLocation = 'right';
```

Glossary

AgOAc Silver acetate. ix, 43

APS Ammonium Persulfate. 25, 26, 27

AuNP Gold nanoparticle. xviii, 26, 27, 46

BAC Bis-acrolyl cystamine. x, 26, 44, 45

BCMN Block copolymer micellar nanolithography. 1, 21, 23, 24, 43, 44

BCP Block copolymer. 20, 43

CME Clathrin-mediated endocytosis. xii, xvii, 1, 2, 57, 58, 61, 62, 63, 64, 65, 77, 81, 83, 85, 89, 90, 91, 92, IV

cRGD cyclic Arginine-Glycine-Aspartic Acid. xi, xviii, 27, 43, 46, 51, 52

ddH$_2$O Double distilled water. 23, 24, 25, 26, 28, 71

DMD Digital micromirror device. viii, 19, 22, 39, 40, 46

DMEM Dulbecco's modified Eagle's medium. 30, 68

DMSO Dimethyl sulfoxide. 69, 71

ECM Extracellular Matrix. ix, 1, 5, 15, 16, 18, 19, 25, 36, 37, 40, 41, 51, 53, 61, 62, 63, 75, 77, 79

EDC 1-ethyl-3-(3-dimethylaminopropyl) carbodiimide hydrochloride. 28, 71

FBS Fetal Bovine Serum. 30, 68

FN Fibronectin. vii, xi, 31, 50

FTTC Fourier transform traction cytometry. vi, 5, 6, 9

H_2O_2 Hydrogen peroxide. 24

H_2SO_4 Sulfuric acid. 24

$HAuCl_4$ Tetrachloroauric(III) acid. vii, ix, 21, 22, 24, 43

HEA N-Hydroxyethyl Acrylamide. 25, 40, 71

HEPES (4-(2-hydroxyethyl)-1-piperazineethanesulfonic acid). 23, 28

LUVI-TFM Local ultraviolet illumination traction force microscopy. x, xi, xii, xiii, 1, 2, 46, 47, 48, 49, 51, 53, 54, 55, 57, 58, 59, 73, 74, 79, 87, 89

MEF Mouse embryonic fibroblast. 75, 78

$NaBH_4$ Sodium borohydride. x, 26, 44, 45

PA Polyacrylamide. vii, ix, x, xi, xiii, xvi, xviii, 1, 5, 8, 10, 14, 15, 18, 25, 26, 27, 31, 32, 33, 34, 35, 36, 37, 40, 41, 42, 43, 44, 45, 46, 49, 50, 51, 52, 53, 54, 57, 58, 71, 73, 74, 75, 78, 79, 85, 87, 88, 89

PBS Phosphate Buffer Saline. vii, 23, 27, 28, 29, 30, 31, 32, 33, 68, 69, 70, 71, 72

PDMS Polydimethylsiloxane. xv, xvi, xvii, 1, 8, 10, 14, 15, 18, 19, 31, 37, 38, 70, 71, 86, 89, 91, I, II, V, VI

PEG Polyethylene glycol. 79

PFA Paraformaldehyde. 68

PIV Particle image velocimetry. x, xi, xiii, 8, 46, 47, 50, 78

PLL Poly-L-lysine. 79

PS Polystyrene. 21, 24, 44

PVP Poly(2-vinyl pyridine). 21, 24

RGD Arginine-Glycine-Aspartic Acid. 19

RH Relative humidity. 68, 69

RICM Reflectance interference contrast microscopy. 57

ROI Region of interest. xiii, 73, 74

ROS Reactive oxidative species. x, 48, 57

rpm Rotation per minutes. 24, 28

RT Room Temperature. 23, 24, 25, 26, 27, 28, 68, 71

SEM Scanning electron microscopy. viii, ix, x, xv, xvii, xviii, 24, 27, 39, 43, 44, 45, 46, 72, 84, II

SNR Signal to noise ratio. 57

TEMED Tetramethylethylendiamin. 25, 26, 27

TFM Traction Force Microscopy. i, vi, ix, xi, xviii, 1, 5, 6, 7, 8, 9, 15, 16, 25, 26, 40, 41, 42, 43, 46, 48, 49, 51, 53, 56, 57, 58, 75

TIRF Total internal reflection fluorescence. 31, 37, 53, 57

UV Ultraviolet. vii, viii, x, xi, xii, xiii, xviii, 19, 23, 28, 29, 34, 36, 37, 38, 39, 40, 46, 47, 48, 49, 50, 51, 53, 55, 71, 78, 79

Bibliography

[1] Ahmad, S. I. *Ultraviolet Light in Human Health, Diseases and Environment*, vol. 996. 2017.

[2] Arnold, M., Schwieder, M., Blümmel, J., Cavalcanti-Adam, E. A., López-Garcia, M., Kessler, H., Geiger, B., and Spatz, J. P. Cell interactions with hierarchically structured nano-patterned adhesive surfaces. *Soft Matter 5*, 1 (2009), 72–77.

[3] Arnold, M., Schwieder, M., Blümmel, J., Cavalcanti-Adam, E. A., López-Garcia, M., Kessler, H., Geiger, B., and Spatz, J. P. Cell interactions with hierarchically structured nano-patterned adhesive surfaces. *Soft Matter 5*, 1 (2009), 72–77.

[4] Azioune, A., Storch, M., Bornens, M., Théry, M., and Piel, M. Simple and rapid process for single cell micro-patterning. *Lab on a Chip 9*, 11 (2009), 1640.

[5] Ballestrem, C., Hinz, B., Imhof, B. A., and Wehrle-Haller, B. Marching at the front and dragging behind. *Journal of Cell Biology 155*, 7 (dec 2001), 1319–1332.

[6] Barbieri, L., Colin-York, H., Korobchevskaya, K., Li, D., Wolfson, D. L., Karedla, N., Schneider, F., Ahluwalia, B. S., Seternes, T., Dalmo, R. A., Dustin, M. L., Li, D., and Fritzsche, M. Two-dimensional TIRF-SIM–traction force microscopy (2D TIRF-SIM-TFM). *Nature Communications 12*, 1 (2021).

[7] Baschieri, F., Dayot, S., Elkhatib, N., Ly, N., Capmany, A., Schauer, K., Betz, T., Vignjevic, D. M., Poincloux, R., and Montagnac, G. Frustrated endocytosis controls contractility-independent mechanotransduction at clathrin-coated structures. *Nature Communications 9*, 1 (2018).

[8] Bastounis, E., Meili, R., Álvarez-González, B., Francois, J., del Álamo, J. C., Firtel, R. A., and Lasheras, J. C. Both contractile axial and lateral traction force dynamics drive amoeboid cell motility. *Journal of Cell Biology 204*, 6 (2014), 1045–1061.

[9] Bates, F. S., and Fredrickson, G. H. Block copolymer thermodynamics: Theory and experiment. *Annual Review of Physical Chemistry 41*, 1 (1990), 525–557.

[10] Bhadani, R., and Mitra, U. K. Synthesis and Studies on Water Swelling Behaviour of Polyacrylamide Hydrogels. *Macromolecular Symposia 369*, 1 (nov 2016), 30–34.

[11] Blumberg, J. W., and Schwarz, U. S. Comparison of direct and inverse methods for 2.5D traction force microscopy. *PLoS ONE 17*, 1 January (2022), 1–25.

[12] Boucrot, E., Saffarian, S., Massol, R., Kirchhausen, T., and Ehrlich, M. Role of Lipids and Actin in The Formation of Clathrin-Coated Pits. *Exp Cell Res. 312*, 20 (2009), 4036–4048.

[13] Bowden, N., Brittain, S., Evans, A. G., Hutchinson, J. W., and Whitesides, G. M. Spontaneous formation of ordered structures in thin films of metals supported on an elastomeric polymer. *Nature 393*, 6681 (may 1998), 146–149.

[14] Boyen, H. G., Kästle, G., Zürn, K., Herzog, T., Weigl, F., Ziemann, P., Mayer, O., Jerome, C., Möller, M., Spatz, J. P., Garnier, M. G., and Oelhafen, P. A micellar route to ordered arrays of magnetic nanoparticles: From size-selected pure cobalt dots to cobalt-cobalt oxide core-shell systems. *Advanced Functional Materials 13*, 5 (2003), 359–364.

[15] Bridgman, P. C., Dave, S., Asnes, C. F., Tullio, A. N., and Adelstein, R. S. Myosin IIB Is Required for Growth Cone Motility. *The Journal of Neuroscience 21*, 16 (aug 2001), 6159–6169.

[16] Butcher, D. T., Alliston, T., and Weaver, V. M. A tense situation: forcing tumour progression. *Nature Reviews Cancer 9*, 2 (feb 2009), 108–122.

[17] Butler, J. P., Toli-Nørrelykke, I. M., Fabry, B., and Fredberg, J. J. Traction fields, moments, and strain energy that cells exert on their surroundings. *American Journal of Physiology - Cell Physiology 282*, 3 51-3 (2002), 595–605.

[18] Butler, J. P., Tolić-Nørrelykke, I. M., Fabry, B., and Fredberg, J. J. Traction fields, moments, and strain energy that cells exert on their surroundings. *American Journal of Physiology-Cell Physiology 282*, 3 (mar 2002), C595–C605.

[19] Cavalcanti-Adam, E. A., Micoulet, A., Blümmel, J., Auernheimer, J., Kessler, H., and Spatz, J. P. Lateral spacing of integrin ligands influences cell spreading and focal adhesion assembly. *European Journal of Cell Biology 85*, 3-4 (2006), 219–224.

[20] Cavalcanti-Adam, E. A., Volberg, T., Micoulet, A., Kessler, H., Geiger, B., and Spatz, J. P. Cell spreading and focal adhesion dynamics are regulated by spacing of integrin ligands. *Biophysical Journal 92*, 8 (2007), 2964–2974.

[21] Chao, W. T., and Kunz, J. Focal adhesion disassembly requires clathrin-dependent endocytosis of integrins. *FEBS Letters 583*, 8 (2009), 1337–1343.

[22] Chaudhuri, O., Cooper-White, J., Janmey, P. A., Mooney, D. J., and Shenoy, V. B. Effects of extracellular matrix viscoelasticity on cellular behaviour. *Nature 584*, 7822 (aug 2020), 535–546.

[23] Chaudhuri, O., Gu, L., Darnell, M., Klumpers, D., Bencherif, S. A., Weaver, J. C., Huebsch, N., and Mooney, D. J. Substrate stress relaxation regulates cell spreading. *Nature Communications 6*, 1 (may 2015), 6365.

[24] Chen, W., Joos, T. O., and Defoe, D. M. Evidence for β1-integrins on both Apical and Basal Surfaces of Xenopus Retinal Pigment Epithelium. *Experimental Eye Research 64*, 1 (jan 1997), 73–84.

[25] Christian, J., Blumberg, J. W., Probst, D., Lo Giudice, C., Sindt, S., Selhuber-Unkel, C., Schwarz, U. S., and Cavalcanti-Adam, E. A. Control of Cell Adhesion using Hydrogel Patterning Techniques for Applications in Traction Force Microscopy. *Journal of visualized experiments : JoVE*, 179 (2022), 1–17.

[26] Christian, J., and Cavalcanti-Adam, E. A. Chapter 7. Micro- and Nanopatterned Substrates for Studies on the Mechanobiology of Cell–Matrix Adhesions. 2022, pp. 135–151.

[27] Cocucci, E., Aguet, F., Boulant, S., and Kirchhausen, T. The First Five Seconds in the Life of a Clathrin-Coated Pit. *Cell 150*, 3 (aug 2012), 495–507.

[28] Colin-York, H., Javanmardi, Y., Barbieri, L., Li, D., Korobchevskaya, K., Guo, Y., Hall, C., Taylor, A., Khuon, S., Sheridan, G. K., Chew, T. L., Li, D., Moeendarbary, E., and Fritzsche, M. Spatiotemporally Super-Resolved Volumetric Traction Force Microscopy. *Nano Letters* (2019).

[29] Colin-York, H., Shrestha, D., Felce, J. H., Waithe, D., Moeendarbary, E., Davis, S. J., Eggeling, C., and Fritzsche, M. Super-Resolved Traction Force Microscopy (STFM). *Nano Letters 16*, 4 (2016), 2633–2638.

[30] De Deyne, P. G., O'Neill, A., Resneck, W. G., Dmytrenko, G. M., Pumplin, D. W., and Bloch, R. J. The vitronectin receptor associates with clathrin-coated membrane domains via the cytoplasmic domain of its β5 subunit. *Journal of Cell Science 111*, 18 (1998), 2729–2740.

[31] De Jong, W. H., and Borm, P. J. Drug delivery and nanoparticles: Applications and hazards. *International Journal of Nanomedicine 3*, 2 (2008), 133–149.

[32] Dee, K. C., Puleo, D. A., and Bizios, R. *An Introduction to Tissue-Biomaterial Interactions.* John Wiley and Sons, 2003.

[33] del Campo, A., Nogales, A., Ezquerra, T. A., and Rodríguez-Hernández, J. Modification of poly(dimethylsiloxane) as a basis for surface wrinkle formation: Chemical and mechanical characterization. *Polymer 98* (2016), 327–335.

[34] Denisin, A. K., and Pruitt, B. L. Tuning the Range of Polyacrylamide Gel Stiffness for Mechanobiology Applications. *ACS Applied Materials and Interfaces 8*, 34 (2016), 21893–21902.

[35] Di Russo, J., Young, J. L., Balakrishnan, A., Benk, A. S., and Spatz, J. P. NTA-Co3+-His6 versus NTA-Ni2+-His6 mediated E-Cadherin surface immobilization enhances cellular traction. *Biomaterials 192*, July 2018 (2019), 171–178.

[36] Duane Brown, W. Reduction of protein disulfide bonds by sodium borohydride. *Biochimica et Biophysica Acta 44* (jan 1960), 365–367.

[37] Efimenko, K., Wallace, W. E., and Genzer, J. Surface Modification of Sylgard-184 Poly(dimethyl siloxane) Networks by Ultraviolet and Ultraviolet/Ozone Treatment. *Journal of Colloid and Interface Science 254*, 2 (oct 2002), 306–315.

[38] Elosegui-Artola, A., Oria, R., Chen, Y., Kosmalska, A., Pérez-González, C., Castro, N., Zhu, C., Trepat, X., and Roca-Cusachs, P. Mechanical regulation of a molecular clutch defines force transmission and transduction in response to matrix rigidity. *Nature Cell Biology 18*, 5 (2016), 540–548.

[39] Engler, A. J., Sen, S., Sweeney, H. L., and Discher, D. E. Matrix Elasticity Directs Stem Cell Lineage Specification. *Cell 126*, 4 (2006), 677–689.

[40] Ethirajan, A., Wiedwald, U., Boyen, H. G., Kern, B., Han, L., Klimmer, A., Weigl, F., Kästle, G., Ziemann, P., Fauth, K., Cai, J., Behm, R. J., Romanyuk, A., Oelhafen, P., Walther, P., Biskupek, J., and Kaiser, U. A micellar approach to magnetic ultrahigh-density data-storage media: Extending the limits of current colloidal methods. *Advanced Materials 19*, 3 (2007), 406–410.

[41] Excoffon, K. J. D. A., Guglielmi, K. M., Wetzel, J. D., Gansemer, N. D., Campbell, J. A., Dermody, T. S., and Zabner, J. Reovirus Preferentially Infects the Basolateral Surface and Is Released from the Apical Surface of Polarized Human Respiratory Epithelial Cells. *The Journal of Infectious Diseases 197*, 8 (apr 2008), 1189–1197.

[42] Frantz, C., Stewart, K. M., and Weaver, V. M. The extracellular matrix at a glance. *Journal of cell science 123*, Pt 24 (dec 2010), 4195–4200.

[43] Fratini, M., Wiegand, T., Funaya, C., Jiang, Z., Shah, P. N., Spatz, J. P., Cavalcanti-Adam, E. A., and Boulant, S. Surface Immobilization of Viruses and Nanoparticles Elucidates Early Events in Clathrin-Mediated Endocytosis. *ACS Infectious Diseases 4*, 11 (2018), 1585–1600.

[44] Friedland, J. C., Lee, M. H., and Boettiger, D. Mechanically activated integrin switch controls $\alpha 5\beta$ 1 function. *Science 323*, 5914 (2009), 642–644.

[45] Geerligs, M., Peters, G. W. M., Ackermans, P. A. J., Oomens, C. W. J., and Baaijens, F. P. T. Linear viscoelastic behavior of subcutaneous adipose tissue. *Biorheology 45*, 6 (2008), 677–688.

[46] Geiger, B., Spatz, J. P., and Bershadsky, A. D. Environmental sensing through focal adhesions. *Nature Reviews Molecular Cell Biology 10*, 1 (2009), 21–33.

[47] Geiger, B., and Yamada, K. M. Molecular architecture and function of matrix adhesions. *Cold Spring Harbor Perspectives in Biology 3*, 5 (2011), 1–21.

[48] Glass, R., Arnold, M., Cavalcanti-Adam, E. A., Blümmel, J., Haferkemper, C., Dodd, C., and Spatz, J. P. Block copolymer micelle nanolithography on non-conductive substrates. *New Journal of Physics 6* (2004), 1–17.

[49] Glatz, B. A., Tebbe, M., Kaoui, B., Aichele, R., Kuttner, C., Schedl, A. E., Schmidt, H.-W., Zimmermann, W., and Fery, A. Hierarchical line-defect patterns in wrinkled surfaces. *Soft Matter 11*, 17 (2015), 3332–3339.

[50] Golub, G. H., Heath, M., and Wahba, G. Generalized cross-validation as a method for choosing a good ridge parameter. *Technometrics 21*, 2 (1979), 215–223.

[51] Haes, A. J., Chang, L., Klein, W. L., and Van Duyne, R. P. Detection of a Biomarker for Alzheimer's Disease from Synthetic and Clinical Samples Using a Nanoscale Optical Biosensor. *Journal of the American Chemical Society 127*, 7 (feb 2005), 2264–2271.

[52] Haes, A. J., Hall, W. P., Chang, L., Klein, W. L., and Van Duyne, R. P. A Localized Surface Plasmon Resonance Biosensor: First Steps toward an Assay for Alzheimer's Disease. *Nano Letters 4*, 6 (jun 2004), 1029–1034.

[53] Hamill, K. J., Kligys, K., Hopkinson, S. B., and Jones, J. C. R. Laminin deposition in the extracellular matrix: a complex picture emerges. *Journal of cell science 122*, Pt 24 (dec 2009), 4409–4417.

[54] Herth, G., Schornick, G., and Buchholz, F. *Polyacrylamides and Poly(Acrylic Acids)*. 2015, pp. 1–16.

[55] Heuser, J., and Evans, L. Three-dimensional visualization of coated vesicle formation in fibroblasts. *Journal of Cell Biology 84*, 3 (1980), 560–583.

[56] Hickey, A. S., and Peppas, N. A. Solute diffusion in poly(vinyl alcohol)/ poly(acrylic acid) composite membranes prepared by freezing/thawing techniques. *Polymer 38*, 24 (1997), 5931–5936.

[57] Hillborg, H., Ankner, J., Gedde, U., Smith, G., Yasuda, H., and Wikström, K. Crosslinked polydimethylsiloxane exposed to oxygen plasma studied by neutron reflectometry and other surface specific techniques. *Polymer 41*, 18 (aug 2000), 6851–6863.

[58] Hofman, A. H., ten Brinke, G., and Loos, K. Hierarchical structure formation in supramolecular comb-shaped block copolymers. *Polymer 107* (dec 2016), 343–356.

[59] Horton, M. A. The $\alpha v\beta 3$ integrin "vitronectin receptor". *The International Journal of Biochemistry & Cell Biology 29*, 5 (may 1997), 721–725.

[60] Hu, X. H., and Xiong, S. Fabrication of Nanodevices Through Block Copolymer Self-Assembly. *Frontiers in Nanotechnology 4*, February (2022), 1–19.

[61] Hynes, R. O. Integrins: bidirectional, allosteric signaling machines. *Cell 110*, 6 (sep 2002), 673–687.

[62] Janmey, P. A., Amis, E. J., and Ferry, J. D. Rheology of Fibrin Clots. VI. Stress Relaxation, Creep, and Differential Dynamic Modulus of Fine Clots in Large Shearing Deformations. *Journal of Rheology 27*, 2 (apr 1983), 135–153.

[63] Järveläinen, H., Sainio, A., Koulu, M., Wight, T. N., and Penttinen, R. Extracellular Matrix Molecules: Potential Targets in Pharmacotherapy. *Pharmacological Reviews 61*, 2 (jun 2009), 198–223.

[64] Javanmardi, Y., Colin-York, H., Szita, N., Fritzsche, M., and Moeendarbary, E. Quantifying cell-generated forces: Poisson's ratio matters. *Communications Physics 4*, 1 (2021), 1–10.

[65] Jennings, T. L., Singh, M. P., and Strouse, G. F. Fluorescent lifetime quenching near d = 1.5 nm gold nanoparticles: Probing NSET validity. *Journal of the American Chemical Society 128*, 16 (2006), 5462–5467.

[66] Ji, L., Lim, J., and Danuser, G. Fluctuations of intracellular forces during cell protrusion. *Nature Cell Biology 10*, 12 (dec 2008), 1393–1400.

[67] Kandow, C. E., Georges, P. C., Janmey, P. A., and Beningo, K. A. Polyacrylamide Hydrogels for Cell Mechanics: Steps Toward Optimization and Alternative Uses. 2007, pp. 29–46.

[68] Kapp, T. G., Rechenmacher, F., Neubauer, S., Maltsev, O. V., Cavalcanti-Adam, E. A., Zarka, R., Reuning, U., Notni, J., Wester, H. J., Mas-Moruno, C., Spatz, J., Geiger, B., and Kessler, H. A comprehensive evaluation of the activity and selectivity profile of ligands for RGD-binding integrins. *Scientific Reports 7*, January (2017), 1–13.

[69] Kestin, J., Sokolov, M., and Wakeham, W. A. Viscosity of liquid water in the range minus 8 to 150 degrees Celcius. *Journal of Physical and Chemical Reference Data 7*, 3 (jul 1978), 941–948.

[70] Kirchhausen, T. Clathrin. *Annual Review of Biochemicals* (2000), 699–727.

[71] Knapp, D. M., Barocas, V. H., Moon, A. G., Yoo, K., Petzold, L. R., and Tranquillo, R. T. Rheology of reconstituted type I collagen gel in confined compression. *Journal of Rheology 41*, 5 (sep 1997), 971–993.

[72] Kong, F., García, A. J., Mould, A. P., Humphries, M. J., and Zhu, C. Demonstration of catch bonds between an integrin and its ligand. *Journal of Cell Biology 185*, 7 (jun 2009), 1275–1284.

[73] Kumar, J., Das, S., and Teoh, S. L. Dietary Acrylamide and the Risks of Developing Cancer: Facts to Ponder. *Frontiers in nutrition 5* (2018), 14.

[74] Lampe, M., Vassilopoulos, S., and Merrifield, C. Clathrin coated pits, plaques and adhesion. *Journal of Structural Biology 196*, 1 (2016), 48–56.

[75] Landau, L. D., Lifshitz, E. M., Sykes, J. B., Reid, W. H., and Dill, E. H. Theory of Elasticity: Vol. 7 of Course of Theoretical Physics. *Physics Today 13*, 7 (jul 1960), 44–46.

[76] Levental, I., Georges, P. C., and Janmey, P. A. Soft biological materials and their impact on cell function. *Soft Matter 3*, 3 (2007), 299–306.

[77] Leyton-Puig, D., Isogai, T., Argenzio, E., Van Den Broek, B., Klarenbeek, J., Janssen, H., Jalink, K., and Innocenti, M. Flat clathrin lattices are dynamic actin-controlled hubs for clathrin-mediated endocytosis and signalling of specific receptors. *Nature Communications 8*, May (2017), 1–14.

[78] Li, D., Colin-York, H., Barbieri, L., Javanmardi, Y., Guo, Y., Korobchevskaya, K., Moeendarbary, E., Li, D., and Fritzsche, M. Astigmatic traction force microscopy (aTFM). *Nature Communications 12*, 1 (2021), 1–10.

[79] Liu, J., Zhang, L., Cao, D., and Wang, W. Static, rheological and mechanical properties of polymer nanocomposites studied by computer modeling and simulation. *Physical Chemistry Chemical Physics 11*, 48 (2009), 11365.

[80] Liu, Z., and Bilston, L. On the viscoelastic character of liver tissue: experiments and modelling of the linear behaviour. *Biorheology 37*, 3 (2000), 191–201.

[81] Lock, J. G., Baschieri, F., Jones, M. C., Humphries, J. D., Montagnac, G., Strömblad, S., and Humphries, M. J. Clathrin-containing adhesion complexes. *Journal of Cell Biology 218*, 7 (2019), 2086–2095.

[82] Lock, J. G., Jones, M. C., Askari, J. A., Gong, X., Oddone, A., Olofsson, H., Göransson, S., Lakadamyali, M., Humphries, M. J., and Strömblad, S. Reticular adhesions are a distinct class of cell-matrix adhesions that mediate attachment during mitosis. *Nature Cell Biology 20*, 11 (2018), 1290–1302.

[83] Lodish, H., Berk, A., Kaiser, C. A., Krieger, M., Bretscher, A., Ploegh, H., Amon, A., and Scott, M. P. *Molecular Cell Biology Seventh Edition*, 7 ed. W. H. Freeman and Company, New York, 2013.

[84] Lötters, J. C., Olthuis, W., Veltink, P. H., and Bergveld, P. The mechanical properties of the rubber elastic polymer polydimethylsiloxane for sensor applications. *Journal of Micromechanics and Microengineering 7*, 3 (1997), 145–147.

[85] Maginnis, M. S., Forrest, J. C., Kopecky-Bromberg, S. A., Dickeson, S. K., Santoro, S. A., Zutter, M. M., Nemerow, G. R., Bergelson, J. M., and Dermody, T. S. 1 Integrin Mediates Internalization of Mammalian Reovirus. *Journal of Virology 80*, 6 (2006), 2760–2770.

[86] Masuda, H.-t., Ishihara, S., Harada, I., Mizutani, T., Ishikawa, M., Kawabata, K., and Haga, H. Coating extracellular matrix proteins on a (3-aminopropyl)triethoxysilane-treated glass substrate for improved cell culture. *BioTechniques 56*, 4 (apr 2014), 172–179.

[87] Maupin, P., and Pollard, T. D. Improved preservation and staining of HeLa cell actin filaments, clathrin-coated membranes, and other cytoplasmic structures by tannic acid glutaraldehyde saponin fixation. *Journal of Cell Biology 96*, 1 (1983), 51–62.

[88] McMahon, H. T., and Boucrot, E. Molecular mechanism and physiological functions of clathrin-mediated endocytosis. *Nature Reviews Molecular Cell Biology 12*, 8 (2011), 517–533.

[89] Missirlis, D., Baños, M., Lussier, F., and Spatz, J. P. Facile and Versatile Method for Micropatterning Poly(acrylamide) Hydrogels Using Photocleavable Comonomers. *ACS Applied Materials and Interfaces 14*, 3 (2022), 3643–3652.

[90] Miwa, S., Ohtake, Y., and Kawahara, S. Characterization of ozone-degraded composite of crosslinked polydimethylsiloxane with silica in water. *Polymer Degradation and Stability 128* (jun 2016), 193–199.

[91] Munevar, S., Wang, Y. L., and Dembo, M. Traction force microscopy of migrating normal and H-ras transformed 3T3 fibroblasts. *Biophysical Journal 80*, 4 (2001), 1744–1757.

[92] Oria, R., Wiegand, T., Escribano, J., Elosegui-Artola, A., Uriarte, J. J., Moreno-Pulido, C., Platzman, I., Delcanale, P., Albertazzi, L., Navajas, D., Trepat, X., García-Aznar, J. M., Cavalcanti-Adam, E. A., and Roca-Cusachs, P. Force loading explains spatial sensing of ligands by cells. *Nature 552*, 7684 (2017), 219–224.

[93] Ouyang, M., Yuan, C., Muisener, R. J., Boulares, A., and Koberstein, J. T. Conversion of Some Siloxane Polymers to Silicon Oxide by UV/Ozone Photochemical Processes. *Chemistry of Materials 12*, 6 (jun 2000), 1591–1596.

[94] Patek, S. N., and Caldwell, R. L. Extreme impact and cavitation forces of a biological hammer: strike forces of the peacock mantis shrimp Odontodactylus scyllarus. *Journal of Experimental Biology 208*, 19 (oct 2005), 3655–3664.

[95] Plotnikov, S. V., Sabass, B., Schwarz, U. S., and Waterman, C. M. High-Resolution Traction Force Microscopy. vol. 25. 2014, pp. 367–394.

[96] Plow, E. F., Haas, T. A., Zhang, L., Loftus, J., and Smith, J. W. Ligand binding to integrins. *Journal of Biological Chemistry 275*, 29 (2000), 21785–21788.

[97] Polacheck, W. J., and Chen, C. S. Measuring cell-generated forces: A guide to the available tools. *Nature Methods 13*, 5 (2016), 415–423.

[98] Pontes, B., Monzo, P., Gole, L., Le Roux, A. L., Kosmalska, A. J., Tam, Z. Y., Luo, W., Kan, S., Viasnoff, V., Roca-Cusachs, P., Tucker-Kellogg, L., and Gauthier, N. C. Membrane tension controls adhesion positioning at the leading edge of cells. *Journal of Cell Biology 216*, 9 (2017), 2959–2977.

[99] Prevedel, R., Diz-Muñoz, A., Ruocco, G., and Antonacci, G. Brillouin microscopy: an emerging tool for mechanobiology. *Nature Methods 16*, 10 (2019), 969–977.

[100] Reinhart-King, C. A., Dembo, M., and Hammer, D. A. Endothelial cell traction forces on RGD-derivatized polyacrylamide substrata. *Langmuir 19*, 5 (2003), 1573–1579.

[101] Ribeiro, A. J., Denisin, A. K., Wilson, R. E., and Pruitt, B. L. For whom the cells pull: Hydrogel and micropost devices for measuring traction forces. *Methods 94* (2016), 51–64.

[102] Roca-Cusachs, P., Conte, V., and Trepat, X. Quantifying forces in cell biology. *Nature Cell Biology 19*, 7 (2017), 742–751.

[103] Sabass, B., Gardel, M. L., Waterman, C. M., and Schwarz, U. S. High resolution traction force microscopy based on experimental and computational advances. *Biophysical Journal 94*, 1 (2008), 207–220.

[104] Sabatier, L., Chen, D., Fagotto-Kaufmann, C., Hubmacher, D., McKee, M. D., Annis, D. S., Mosher, D. F., and Reinhardt, D. P. Fibrillin Assembly Requires Fibronectin. *Molecular Biology of the Cell 20*, 3 (feb 2009), 846–858.

[105] Sarker, B., Walter, C., and Pathak, A. Direct Micropatterning of Extracellular Matrix Proteins on Functionalized Polyacrylamide Hydrogels Shows Geometric Regulation of Cell-Cell Junctions. *ACS Biomaterials Science and Engineering 4*, 7 (2018), 2340–2349.

[106] Schoenenberger, C. A., Zuk, A., Zinkl, G. M., Kendall, D., and Matlin, K. S. Integrin expression and localization in normal MDCK cells and transformed MDCK cells lacking apical polarity. *Journal of Cell Science 107*, 2 (1994), 527–541.

[107] Schürmann, H., Abbasi, F., Russo, A., Hofemeier, A. D., Brandt, M., Roth, J., Vogl, T., and Betz, T. Analysis of monocyte cell tractions in 2.5D reveals mesoscale mechanics of podosomes during substrate-indenting cell protrusion. *Journal of cell science 135*, 10 (2022).

[108] Schwab, E. B. *Directing Osteogenic Signaling and Differentiation by Surfaces Modified with Adhesive Proteins and Immobilized Bone Morphogenetic Protein 2.* PhD thesis, Ruprecht-Karls-Universitaet Heidelberg, 2015.

[109] Schwarz, U. S., Balaban, N. Q., Riveline, D., Bershadsky, A., Geiger, B., and Safran, S. A. Calculation of forces at focal adhesions from elastic substrate data: The effect of localized force and the need for regularization. *Biophysical Journal 83*, 3 (2002), 1380–1394.

[110] Schwarz, U. S., and Soiné, J. R. Traction force microscopy on soft elastic substrates: A guide to recent computational advances. *Biochimica et Biophysica Acta - Molecular Cell Research 1853*, 11 (2015), 3095–3104.

[111] Schwieder, M. *Hierarchical Nanopatterns for Cell Adhesion Studies.* PhD thesis, Ruprecht-Karls-Universitaet Heidelberg.

[112] Shoulders, M. D., and Raines, R. T. Collagen Structure and Stability. *Annual Review of Biochemistry 78*, 1 (jun 2009), 929–958.

[113] Sies, H., and Jones, D. P. Reactive oxygen species (ROS) as pleiotropic physiological signalling agents. *Nature Reviews Molecular Cell Biology 21*, 7 (2020), 363–383.

[114] Smith, M. L., Gourdon, D., Little, W. C., Kubow, K. E., Eguiluz, R. A., Luna-Morris, S., and Vogel, V. Force-induced unfolding of fibronectin in the extracellular matrix of living cells. *PLoS Biology 5*, 10 (2007), 2243–2254.

[115] Spencer, P. S., and Schaumburg, H. H. Nervous system degeneration produced by acrylamide monomer. *Environmental health perspectives 11* (jun 1975), 129–133.

[116] Strale, P. O., Azioune, A., Bugnicourt, G., Lecomte, Y., Chahid, M., and Studer, V. Multiprotein Printing by Light-Induced Molecular Adsorption. *Advanced Materials 28*, 10 (2016), 2024–2029.

[117] Suh, K. Y., Seo, S. M., Yoo, P. J., and Lee, H. H. Formation of regular nanoscale undulations on a thin polymer film imprinted by a soft mold. *The Journal of Chemical Physics 124*, 2 (jan 2006), 024710.

[118] Théry, M. Micropatterning as a tool to decipher cell morphogenesis and functions. *Journal of Cell Science 123*, 24 (2010), 4201–4213.

[119] Wang, J. H.-C. Cell Traction Forces (CTFs) and CTF Microscopy Applications in Musculoskeletal Research. *Operative Techniques in Orthopaedics 20*, 2 (jun 2010), 106–109.

[120] Wang, K., Meng, X., and Guo, Z. Elastin Structure, Synthesis, Regulatory Mechanism and Relationship With Cardiovascular Diseases. *Frontiers in Cell and Developmental Biology 9* (nov 2021).

[121] Wiegand, T., Fratini, M., Frey, F., Yserentant, K., Liu, Y., Weber, E., Galior, K., Ohmes, J., Braun, F., Herten, D. P., Boulant, S., Schwarz, U. S., Salaita, K., Cavalcanti-Adam, E. A., and Spatz, J. P. Forces during cellular uptake of viruses and nanoparticles at the ventral side. *Nature Communications 11*, 1 (2020).

[122] Wolfenson, H., Iskratsch, T., and Sheetz, M. P. Early events in cell spreading as a model for quantitative analysis of biomechanical events. *Biophysical Journal 107*, 11 (2014), 2508–2514.

[123] Yoo, P. J., Suh, K. Y., Kang, H., and Lee, H. H. Polymer Elasticity-Driven Wrinkling and Coarsening in High Temperature Buckling of Metal-Capped Polymer Thin Films. *Physical Review Letters 93*, 3 (jul 2004), 034301.

[124] Yu, C. H., Rafiq, N. B. M., Cao, F., Zhou, Y., Krishnasamy, A., Biswas, K. H., Ravasio, A., Chen, Z., Wang, Y. H., Kawauchi, K., Jones, G. E., and Sheetz, M. P. Integrin-beta3 clusters recruit clathrin-mediated endocytic machinery in the absence of traction force. *Nature Communications 6* (2015), 1–12.

[125] Yun, C. S., Javier, A., Jennings, T., Fisher, M., Hira, S., Peterson, S., Hopkins, B., Reich, N. O., and Strouse, G. F. Nanometal Surface Energy Transfer in Optical Rulers, Breaking the FRET Barrier. *Journal of the American Chemical Society 127*, 9 (mar 2005), 3115–3119.

[126] Zuidema, A., Wang, W., Kreft, M., Te Molder, L., Hoekman, L., Bleijerveld, O. B., Nahidiazar, L., Janssen, H., and Sonnenberg, A. Mechanisms of integrin αVβ5 clustering in flat clathrin lattices. *Journal of Cell Science 131*, 21 (2018).